Direct Ink Writing of Polycaprolactone-Based Scaffolds for Interfacial Tissue Engineering

Bin Zhang

A thesis submitted in partial fulfilment

of the requirements for the degree of

Doctor of Philosophy

of

University College London.

Department of Mechanical Engineering

University College London

March 27, 2021

I, Bin Zhang, confirm that the work presented in this thesis is my own. Where information has been derived from other sources, I confirm that this has been indicated in the work.

Acknowledgements

Firstly, I would like to express my deepest gratitude to my supervisor Dr Jie Huang who trusted and gave me the opportunity to undertake this PhD research. She has offered constructive suggestions, encouragements, and supports throughout my PhD. I would also like to express my gratefulness towards my second supervisor, Dr William Suen, for his advice and support.

I am thankful to Prof Roger J. Narayan, who offered me the opportunity to work in his group in the joint Department of Biomedical Engineering at the University of Chapel Hill and North Carolina State University in the USA in the final year of my PhD. This opportunity has expanded my horizon and helped me to accomplish this study. I would also thank Dr Qi Sheng for providing me with the opportunity as a research assistant in the School of Pharmacy of the University of East Anglia.

I would like to acknowledge Prof Stavroula Balabani and Dr Ryo Torii for examining my transfer viva and offered valuable suggestions for my thesis. I am also like to thank Prof Duncan Craig, Prof Susan Barker, Dr Liwei Guo, Dr Saeid Movahed, and Dr Rebecca Yuan for their valuable suggestions and insightful discussions. Also, thanks to JiaJie Yang for the cooperation building direct ink writing printer together in my research. My best friends Jia, Rui, Peng, Kang, Dan, Ejie, Chak, and Kamila for their companion and making my PhD life colourful.

Finally, I give my gratitude to the financial supports from China Scholarship Council (CSC) - UCL joint research scholarship and the Charles M. Vest US Na-

tional Academy of Engineering (NAE) Grand Challenges for Engineering International Scholarship Programme.

Last, but most importantly, my utmost gratitude is accorded to my parents for their unconditional support and love during these years.

List of Publications

Journal publications

- **Zhang, B.**, Guo, L., Chen, H., Ventikos, Y., Narayan, R.J. and Huang, J., 2020. Finite element evaluations of the mechanical properties of polycaprolactone/hydroxyapatite scaffolds by direct ink writing: Effects of pore geometry. Journal of the Mechanical Behaviour of Biomedical Materials, 104, p.103665.

- **Zhang, B.**, Chung, S.H., Barker, S., Craig, D., Narayan, R.J. and Huang, J., 2020. Direct ink writing of polycaprolactone/polyethylene oxide based 3D constructs. Progress in Natural Science: Materials International.

- **Zhang, B.**, Huang, J. and Narayan, R.J., 2020. Gradient scaffolds for osteochondral tissue engineering and regeneration. Journal of Materials Chemistry B, 8(36), pp.8149-8170.

- **Zhang, B.**, Nguyen, A., Narayan, R.J. and Huang, J., 2020. Direct ink writing of vancomycin loaded polycaprolactone/ polyethylene oxide/ hydroxyapatite 3D scaffolds. Submitted to Journal of the American Ceramic Society.

- **Zhang, B.**, Huang, J. and Narayan, R., 2020. Nanostructured biomaterials for regenerative medicine: Clinical perspectives. In Nanostructured Biomaterials for Regenerative Medicine (pp. 47-80). Woodhead Publishing.

- **Zhang, B.**, Cristescu, R., Chrisey, D.B. and Narayan, R.J., 2020. Solvent-

based extrusion 3D printing for the fabrication of tissue engineering scaffolds. International Journal of Bioprinting, 6(1).

- Kostecki, R., **Zhang, B.**, El Habti, A., Arman, A., Hutchinson, M.R., Tricker, P.J., Fleury, D., Narayan, R.J. and Ebendorff-Heidepriem, H., 2019, December. Optical fiber based in-vivo oxidative stress biosensor. In Biophotonics Australasia 2019 (Vol. 11202, p. 112020R). International Society for Optics and Photonics.

- Kostecki, R., **Zhang, B.**, El Habti, A., Arman, A., Hutchinson, M.R., Tricker, P.J., Fleury, D., Narayan, R.J. and Ebendorff-Heidepriem, H., 2019, June. Reversible Protein Carbonylation In-Vivo Biosensor. In Optical Sensors (pp. STu2D-3). Optical Society of America.

- Kostecki, R., Arman, A., **Zhang, B.**, Yang, K.H., Narayan, R.J., Hutchinson, M.R. and Ebendorff-Heidepriem, H., Dynamic In Vivo Protein Carbonyl Biosensor for Measuring Oxidative Stress. Medical Devices and Sensors, p.e10135.

- Alqahtani, F., Belton, P., **Zhang, B.**, Al-Sharabi, M., Ross, S., Mithu, M.S.H., Douroumis, D., Zeitler, J.A. and Qi, S., 2020. An investigation into the formations of the internal microstructures of solid dispersions prepared by hot melt extrusion. European Journal of Pharmaceutics and Biopharmaceutics, 155, pp.147-161.

- Machekposhti, S.A.,**Zhang, B.**, Sachan, R., Vanderwal, L., Stafslien, S.J. and Narayan, R.J., 2021. Patterned surfaces with the controllable drug doses using inkjet printing. Journal of Materials Research, pp.1-12.

Key conference contributions

- **Zhang, B.**, Nguyen, A., Narayan, R.J. and Huang, J. Direct ink writing of polycaprolactone/hydroxyapatite scaffolds loaded with vancomycin for bone

repair. Oral presentation at British Orthopaedic Research Society (BORS) Annual Meeting, Bath, United Kingdom, September 2020.

- **Zhang, B.**, Nguyen, A.K., Narayan, R.J. and Huang, J. Direct ink writing of Vancomycin loaded polycaprolactone/ polyethylene oxide/ hydroxyapatite scaffolds: influence of material composition on drug release. Poster presentation at World Biomaterials Congress (WBC), Glasgow, United Kingdom, December 2020.

- Kostecki, R., **Zhang, B.**, El Habti, A., Arman, A., Hutchinson, M.R., Tricker, P., Fleury, D., Narayan, R.J. and Ebendorff-Heidepriem, H. Reversible Protein Carbonylation In-Vivo Biosensor. Oral presentation at Optical Sensors and Sensing Congress, San Jose, California, United States, June 2019.

- Chung, S.H., **Zhang, B.**, Barker, S. and Huang, J. Fabrication of drug-loaded medical devices by a novel three-dimensional printing method. Poster presentation at 3rd European Conference on Pharmaceutics, Bologna, Italy, March 2019.

- **Zhang, B.**, Yang, JJ., Shepherd, J., Best, S. and Huang, J. Prediction of effects of pore architecture on cell differentiation in TE scaffolds: a finite element study. Poster accepted at Society For Biomaterials (SFB) Annual Meeting, Atlanta, Georgia, United States, April 2018.

- **Zhang, B.**, Zhang, SG., Tiwari, M. and Huang, J. Finite element analysis of scaffold architecture on the distribution of fluid shear stress for bone tissue engineering. Poster presentation at World Congress of Biomechanics (WCB), Dublin, Ireland, July 2018 .

- **Zhang, B.**, Chung, S.H., Wang, B.L., Yuan, R., Chang, M.W., Barker, S. and Huang, J. Fabrication of DIW scaffolds functionalized with drug release for tissue regeneration. Poster presentation at European Society of Biomaterials (ESB) Conference, Maastricht, Netherlands, September 2018.

Abstract

Engineering interface tissues (e.g. cartilage-to-bone) is a complex process requiring specific designs and organisation of materials, cells and biomolecules. Polycaprolactone (PCL) is a widely applied biomaterial in tissue engineering for its mechanical properties and biocompatibility. Direct ink writing (DIW) is a promising 3D technique to fabricate personalised scaffolds in a heat-free environment by ink deposition. However, it is challenging to develop PCL-based scaffolds using DIW as PCL is water-insoluble. This study aims to develop PCL-based inks to fabricate customised scaffolds with improved properties and functionality for DIW printing.

Two types of filament-based scaffolds were designed: single lay-down angle scaffolds and a complex scaffold with layers of different lay-down angles. Finite element simulation results indicate the orthotropic effect increased when the angle decreased from 90° to 15°. Gradient strain magnitudes were achieved in a complex structure with various lay-down angles, mimicking the gradient mechanical characteristics of natural tissue.

PCL-based inks were formulated by blending hydrophilic polyethylene oxide (PEO), nano-hydroxyapatite (HAp) comprising acetone and dichloromethane. Ink rheology results indicate that acetone inks had more pronounced shear-thinning behaviour than the dichloromethane inks but had inferior viscosity recovery performance. The addition of PEO and HAp had improved the ink shear-thinning behaviour, viscosity recovery performance, and the scaffold surface wettability. With the varying HAp concentration (55–85%w/w) and lay-down angle, the scaffold with 65%w/w HAp and 90° lay-down angle exhibited the highest elastic modulus and

yield strength. 65% w/w HAp concentration is close to the inorganic composition of natural bone tissue. Vancomycin as a model drug was embedded in the PCL/PEO/HAp scaffold. The release behaviour of vancomycin was assessed with the in vitro dissolution test and the antibacterial activity of the printed scaffold was effectively inhibited *Staphylococcus aureus* in the agar diffusion test.

In conclusion, the combined numerical and experimental studies reported in this thesis mainly contains: (1) the use of FEM in design structures with gradient mechanical property, (2) the development of printable PCL/PEO and PCL/PEO/HAp ink formulations, and (3) the use of DIW in fabricating the predesigned scaffold. This study demonstrates that DIW can be used to fabricate scaffold with desired properties with the proper design of ink formulation and scaffold structures. The ink formulation and methodology developed in this study can be transferred to other hydrophobic biomaterials for DIW scaffold fabrication. The gradient property of the DIW tissue scaffold could be achieved by the optimal combination of ink formulations and inner structures to match with natural interfacial tissue.

Impact Statement

Three-dimensional (3D) printing is a relatively new, but rapid and flexible manufacturing technology that has the potential to revolutionise many fields including tissue engineering. Tissue engineering aims to fabricate tissue scaffolds with the goal of repairing the functions of damaged natural tissue. Although natural tissues have their own complex structures, and it is even more challenging to develop tissue scaffolds for interfacial tissues. 3D printing has the advantage of fabrication 3D constructs using medical imaging to produce personalised tissue engineering scaffolds with controllable complex geometries to match with natural tissue.

This study provides an insightful understanding of the application of direct ink writing (DIW), an ink-based 3D printing technology, for building tissue scaffolds by investigating their ink rheological behaviour and DIW printing process, and evaluation of the printed scaffold properties. A novel structure design focusing on gradient transitions within a wide range of strain magnitudes were achieved in a single construct by assembling layers with different lay-down angles. The proposed novel structure design and developed DIW printed scaffolds are transferable to other biomaterials for scaffold fabrication using DIW printing, which will be useful to develop interfacial tissue scaffolds in the future.

The work presented in this thesis will be beneficial for researchers to develop innovative tissue scaffolds with variable combinations of materials and inner structures to mimicking the gradient transition of natural interfacial tissue. Meanwhile, DIW has the advantage of fabricating scaffolds in a heat-free environment, making it possible to incorporate heat-sensitive growth factors related to tissue regeneration

or drugs for local drug delivery; this is especially beneficial for tumour related tissue repairing. Further, it will strengthen the collaborations between the clinical and industrial fields by enabling personalised tissue engineering scaffolds with controllable complex geometries and materials to obtain optimal therapeutical outcomes, which provides a promising solution to satisfy individual patient needs for tissue repairing.

Contents

List of Figures

List of Tables

Nomenclature

D_1, D_2	Edge length of the scaffold
d_{xy}	Inter-filament spacing in the XY plane
f	Layer overlap
m	Consistency index
n	Power-law index
Q_E	Extrusion rate
Ra	Surface roughness
R^2	Correlation coefficient
T_d	Degradation temperature
T_m	Peak melting temperatures
V_z	Ink velocity alongside the needle
V_{xy}	Printed filament speed in the XY plane
$W_{filament}$	Printed filament width
W_{ZOI}	Width of the clear zone of inhibition
$\dot{\gamma}$	Shear rate
ΔP	Extrusion pressure along the needle
ΔH_f	Enthalpy of fusion
η	Viscosity
$\sigma_{filament}$	Relative filament deviation

Abbreviations

2-Bu	2-butoxyethanol
3D	Three-dimensional
ACE	Acetone
BMP-2	Bone morphogenetic protein-2
CAD	Computer-aided design
CNT	Carbon nanotube
CaP	Calcium phosphate
CA	Contact angle
DCM	Dichloromethane
DSC	Differential scanning calorimetry
DBP	Dibutyl phthalate
DSC	Differential scanning calorimetry
DIW	Direct ink writing
ECM	Extracellular matrix
FEM	Finite element method
FTIR	Fourier-transform infrared spectroscopy
GAG	Glycosaminoglycan
HAp	Hydroxyapatite
hMSCs	Human mesenchymal stem cells
hBMSCs	Human bone marrow stromal cells
hAVIC	Human aortic interstitial cells
hMMECs	Human mammary microvascular endothelial cells
hPDC	Human placenta-derived cells
Mg-HAp	Magnesium-hydroxyapatite
MRI	Magnetic resonance imaging
OC	Osteochondral

PXRD	Powder X-ray powder diffraction
PCL	Polycaprolactone
PEO	Polyethylene oxide
PLGA	Poly(lactic-co-glycolic acid)
PGA	Polyglycolide
PEG	Poly(ethylene glycol)
PLA	Polylactic acid
PLLA	Poly-L-lactic acid
P. aeruginosa	*Pseudomonas aeruginosa*
S. aureus	*Staphylococcus aureus*
SEM	Scanning electron microscope
TGF-β3	Transforming growth factor-beta 3
TCP	Tricalcium phosphate
Ti	Titanium
TGA	Thermogravimetric analysis
VAN	Vancomycin
WHO	World Health Organization
XPS	X-ray photoelectron spectroscopy

Chapter 1

Introduction

1.1 Motivation

Tissue engineering aims to fabricate biological tissue scaffolds with the goal of repairing or regenerating the functions of diseased or damaged natural tissue. Design and production of tissue scaffolds that mimic the complex structural and functional features of natural tissues are the most key issues of tissue engineering strategy (Seidi et al., 2011). Although natural tissues have their own complex structure, an even more complex case in terms of developing tissue scaffold would encounter at the interfacial tissues, where two distinct tissues come together (Seidi et al., 2011; Rao et al., 2016). For example, osteochondral (OC) tissue is one of the common interfacial tissues that compose of cartilage and bone, which is especially susceptible to injury and tear when high strain fields are present (Bayrak and Yilgor Huri, 2018). Engineering OC tissue still remains a challenge due to their complexities such as biochemical composition, structure and mechanical property.

OC tissue defect can lead to joint malfunction and the development of degenerative diseases such as osteoarthritis. It has been estimated by the World Health Organization (WHO) that 9.6% of men and 18.0% of women over the age of sixty suffer from symptomatic osteoarthritis. There are 80% of osteoarthritis patients

have limitations in mobility, and 25% of them are unable to perform most daily activities (March et al., 2016). OC defects have a limited capacity for spontaneous healing due to the poor healing capabilities of cartilage; these defects can lead to catastrophic degenerative arthritis (Chiang and Jiang, 2009). Clinical findings have indicated that there is no existing medication substantially promotes the healing process (Martín et al., 2019; Chiang and Jiang, 2009). As such, surgical replacement is required for OC tissue repair. However, among surgical treatments, repair using autograft or allograft is limited due to the insufficient supply of autograft material and potential risk of viral transmission with allograft material (Bauer and Muschler, 2000; Miron et al., 2016).

Tissue engineering is regarded as a promising approach for OC tissue regeneration, which overcomes the limitations associated with the use of allograft and autograft tissue (Bittner et al., 2019; Chen et al., 2019b; Kosik-Kozioł et al., 2020; Nowicki et al., 2020; Li et al., 2018; Zhou et al., 2019; Kang et al., 2018; Ansari et al., 2019; Mohan et al., 2011; Dormer et al., 2010). As the OC defect often involves damage to both the cartilage and the underlying subchondral bone, tissue scaffolds must have a discrete gradient or a continuous gradient in terms of cell type, growth factor, material composition, structural and mechanical properties. It has been indicated that engineered scaffolds with discrete or continuous gradient properties are superior to single-phase tissue scaffolds for OC defect repair (Kang et al., 2018; Ansari et al., 2019). Some studies developed discrete gradient scaffolds by fabrication of two or three phases separately, which are subsequently integrated with suturing, glue, or press-fitting. However, most of these scaffolds exhibit insufficient bonding strength, which increases the risk of phase delamination after implantation (Nooeaid et al., 2012; Schaefer et al., 2000). Other studies (Dormer et al., 2010; Mohan et al., 2011) proposed a continuous gradient scaffold with the freeze-drying approach; the scaffold structure changed in a linear gradient manner in terms of pore size and porosity. This design is less prone to delamination and can facilitate stress transfer within the scaffold. The continuous gradient scaffold has the potential to provide a smooth transition between cartilage and bone; moreover,

it can avoid instability at the interface and can better mimic the natural structure of the OC tissue. Although the development of OC tissue scaffolds has yielded satisfactory results in terms of OC regeneration in vitro and in vivo, longer-term follow-up clinical studies were less appealing. Further studies into gradient tissue scaffolds for OC regeneration are required.

Many types of scaffolds have been developed using conventional methods such as solvent-casting (Eltom et al., 2019; Lee et al., 2016), gas-forming (Loh and Choong, 2013; Hutmacher and Cool, 2007), freeze-drying (Levingstone et al., 2014; Shi et al., 2019; Korpayev et al., 2020; Parisi et al., 2020) and electrospinning (Zhang et al., 2013; McCullen et al., 2010; Rebollar et al., 2011). These approaches offer flexibility in terms of selection of biomaterials as well as control over scaffold pore size and porosity. Recently 3D printing methods have been used for the OC scaffold fabrication for their ability to fabricate interconnected porous scaffolds with well-controlled pore geometries. The scaffold structure could be designed to exhibit appropriate mechanical properties, matching the host tissue. Various 3D printing techniques, including liquid, powder and solid-based methods, have been used to fabricate gradient scaffolds with several types of biomaterials, structural features and mechanical properties for OC tissue regeneration (Bittner et al., 2019; Chen et al., 2019b; Kosik-Kozioł et al., 2020; Nowicki et al., 2020; Li et al., 2018; Zhou et al., 2019). Among the 3D printing methods, direct ink writing (DIW) technique, has been widely applied to fabricate tissue scaffolds thanks to the advantage of the heat-free fabrication environment. So that heat-sensitive component, e.g. anti-inflammatory drug and growth factor, can be incorporated into the printing process. Due to DIW fabrication characteristics, it has stringent requirements on the ink properties, e.g. filament formation capability, shear-thinning feature and high recovery behaviour.

Drug delivery using biodegradable polymers has an advantage, since there is no need for the second surgery to remove the tissue scaffold once the drug supply is depleted. Existing research efforts have developed drug-loaded tissue scaffolds using DIW, mostly focusing on the hydrogel-based inks since they are water-soluble

which is relatively easy to formulate as inks (Cheng et al., 2020; Shin and Kang, 2018; Zhou et al., 2020). However, the application of DIW for hydrophobic biomaterials such as polycaprolactone (PCL) remains limited. This is unfortunate as PCL is known for its propensity to form blends and composites that enable modulations of the physical properties of the scaffold (Yeo and Kim, 2012; Lin et al., 2014; Dong et al., 2017). Meanwhile, PCL is one of the promising biomaterials used in drug delivery. One advantage is its moderate drug release rate and creation of a minimum acidic environment during degradation as opposed to other hydrophobic biodegradable polymers like polylactic acid or poly (lactic-co-glycolic acid). Thus, more biomaterial inks, particularly hydrophobic biomaterials (i.e. PCL-based), are to be developed for tissue scaffold fabrication using DIW.

Additionally, biological experiments have been used to investigate the relations among tissue scaffold material, structure and tissue regeneration (Lin et al., 2014; Hung et al., 2004; Xue et al., 2019). However, tissue regeneration is a complicated metabolic process. Parameters such as scaffold, cells, growth factors and cultural environment, would influence tissue regeneration, and they are not independent. It is time-consuming and costly to evaluate so many parameters affecting tissue regeneration in vitro or in vivo. Computational modelling shows excellent potential in biomedical engineering research. For example, data from modelling and experiments can be used to understand the correlation between the scaffold structure and cellular responses for bone and cartilage formation.

1.2 Aim and objectives

This research aims to formulate PCL-based inks and to use DIW technique to fabricate scaffolds with controllable material compositions, structures and mechanical properties for interfacial tissue engineering. The aim can be distributed into the following objectives:

1. Propose the design of the computer-aided design (CAD) scaffolds with variable pore geometries, i.e. pore size, porosity and pore shape, and investigate

their mechanical properties with computational modelling method.

2. Develop PCL-based inks with feasible properties to fabricate predesigned structures using DIW.
3. Evaluate the structural, surface, material and mechanical properties of the DIW printed 3D scaffold.
4. As proof of concept, a model drug can be incorporated into the developed scaffolds to achieve controlled drug release and anti-inflammation.

To realise the above objectives, the CAD scaffold structures are to be predesigned and their mechanical properties should be investigated. The PCL-based inks should be formulated, and ink rheology properties and filament formation need to be investigated before the scaffold fabrication with DIW technique. Then, the anti-inflammation drug for bone-related infection reduction can be loaded in the inks to fabricate the DIW composite scaffolds with multiple material compositions, structures and mechanical properties. The flow chart of thesis is shown in Figure 1.1.

1.3 Thesis structure

This thesis comprises seven chapters. The first chapter introduces the main problem faced, outlining the need of biomaterial inks for DIW technique to build tissue scaffold with controllable material compositions, structures and mechanical properties for interfacial tissue repair.

Chapter 2 consists of a literature review where the biochemical composition, structure and mechanical property of interfacial tissue (i.e. OC tissue) are summarised whilst tissue engineering for OC tissue regeneration are introduced. Particularly, the DIW technique - a solvent-based extrusion 3D printing method, is detailly discussed regarding the ink materials, ink rheology behaviours, fabrication parameters and the evaluation of the printed tissue scaffolds.

Chapter 3 provides a detailed description of the simulative details of the finite

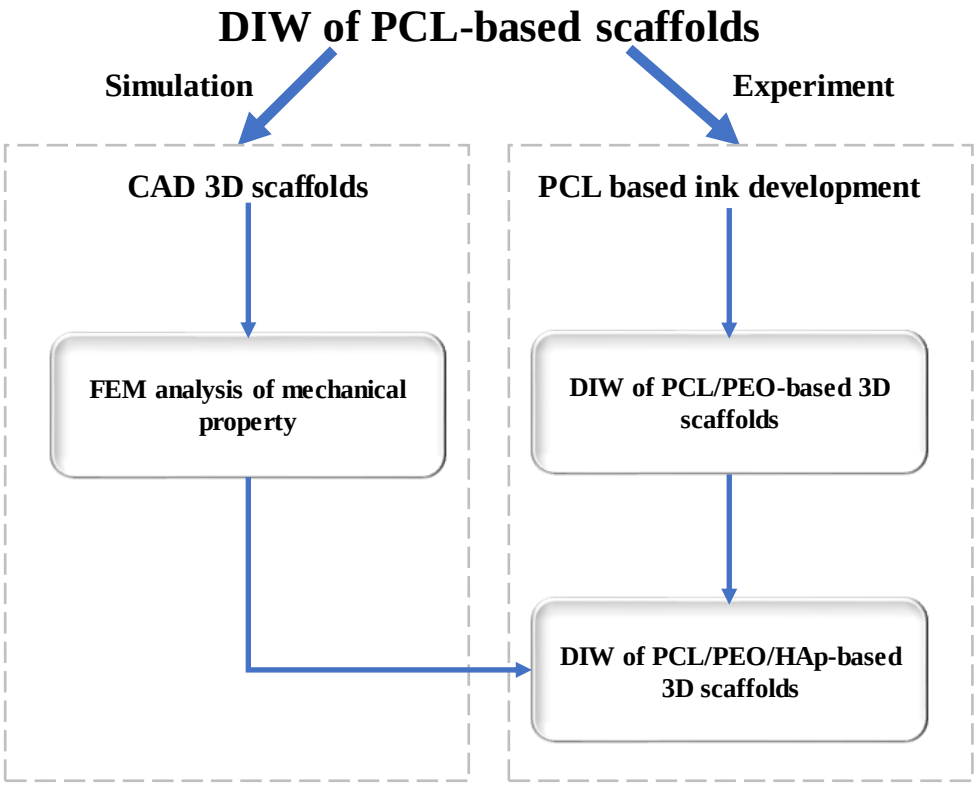

Figure 1.1: Flow chart of thesis. There are two main sections - simulation and experiment. The CAD designs were proposed for tissue scaffold and their mechanical property were analysed in the simulation section. The experimental section focuses on inks development, two new inks were developed for scaffold fabrication using DIW. The PCL/PEO scaffold was developed to mimic the cartilage tissue layer of the OC tissue, while the PCL/PEO/HAp scaffold was developed to mimic the bone tissue layer of the OC tissue, which aims for the gradient property from cartilage to bone tissue.

element modelling (FEM) methods, experimental methods for the formulation of inks and the scaffold fabrication using the DIW. The characterisation techniques for the evaluation of the printed scaffold are detailed. Meanwhile, the standard protocols for drug dissolution procedure, mechanical property evaluation and agar diffusion experiment on the DIW fabricated scaffolds are outlined.

Chapter 4 details the designed computer-aided design (CAD) scaffold specimens with different filament diameters, inter-filament spacing, layer overlaps, and single lay-down angles. Meanwhile, a gradient scaffold structure with multiple lay-down angles from 90° to 15° was created. FEM was applied to investigate the

influence of designed CAD scaffold structures on their mechanical properties.The development of a complex structure with variable lay-down angles that can form gradient mechanical properties.

Chapter 5 introduces the details about the application of DIW methods to fabricate those above pre-designed scaffold structures. The selection of the solvents for formulation PCL-based inks and the influence of material compositions and solvents on ink rheology, material characterisation and surface property of DIW printed 3D constructs were investigated. The DIW printed PCL-based scaffold aims to mimic the cartilage layer.

Chapter 6 describes hydroxyapatite (HAp) nanoparticles formulated in the PCL-based inks to fabricate the 3D scaffolds to closely mimic the material composition of nature bone tissue. The influence of HAp concentrations and scaffold structures on the scaffold mechanical properties were investigated. The DIW printed PCL/HAp-based scaffold is to mimic the bone layer. The anti-inflammation drug was incorporated into the developed biocomposite inks for the scaffold fabrication. The drug release profile and anti-bacteria property were evaluated.

Chapter 7 concludes the research. Future work is proposed based on the results and findings.

Chapter 2

Literature review

Overview

Tissue engineering approach for repairing interfacial tissue defects involves the fabrication of a biological tissue scaffold that mimics the physiological properties of natural interfacial tissue. For example, osteochondral (OC) tissue, one of interfacial tissue in the body, has the gradient transition between the cartilage surface and the subchondral bone. The OC tissue scaffolds described in many research studies exhibit a discrete gradient (e.g. a biphasic or tri/multiphasic structure) or continuous gradient to mimic OC tissue attributes such as biochemical composition, structure, and mechanical properties. One advantage of a continuous gradient scaffold over biphasic or tri/multiphasic tissue scaffolds is that more closely mimics natural OC tissue since there is no distinct interface between each layer. Although research studies to this point have yielded satisfactory results related to OC regeneration with tissue scaffolds, differences between engineered scaffolds and natural OC tissue remain; due to these differences, current clinical therapies to repair OC defects with engineered scaffolds have not been successful.

This literature review provides an overview of both discrete and continuous gradient OC tissue scaffolds in terms of scaffold material, microscale structure,

mechanical properties and manufacture methods. Fabrication of gradient scaffolds with three-dimensional (3D) printing is given special emphasis due to its ability to control scaffold structure accurately. Moreover, the application of computational modelling in OC tissue engineering is considered; for example, efforts to optimise scaffold structure and mechanical properties to match with the host tissue are considered. Finally, challenges associated with the repair of OC defects and recommendations for future directions in OC tissue regeneration are proposed.

2.1 Interfacial tissue organisation

Nature tissue can be either homogeneous properties in terms of cell types and matrix components or heterogeneous distributions of cell types and matrix components with gradients of architecture and various other properties to fulfil their complex functions (Seidi et al., 2011). Typically, heterogeneous tissues represent as "soft to hard" interfacial tissue, which is ubiquitous in the body and critical for joint motion and stabilisation, such as osteochondral tissue (Patel et al., 2018). The soft tissues (e.g. cartilage) connect and support other structures of the body, while hard tissues (e.g. bone) primary determine the shape of the body and provide mechanical strength required for the movement. These interfaces are characterised by gradual changes in biochemical composition, structural organisation and mechanical property from one tissue to another, which allows for integration between soft and hard tissues (Rao et al., 2016).

2.2 Biochemical composition, structure, and mechanical property of OC tissue

Osteochondral (OC) tissue, one of classical "soft to hard" interfacial tissue, which comprises two main components, i.e. cartilage and bone. As shown in Figure 2.1 (a), OC tissue exhibits a transition from hard bone to soft cartilage; this transition exhibits gradient characteristics. The cartilage can be further divided into calcified cartilage and noncalcified cartilage; the "tidemark" serves as the interface between

noncalcified cartilage and calcified cartilage. The natural OC tissue gradient is defined by changes in the biochemical composition, structure and mechanical properties from the surface of the cartilage to the subchondral bone. The properties of the cartilage, calcified cartilage and subchondral bone components are summarised in Table 2.1.

The noncalcified cartilage contains three zones, which are the deep zone (on top of the calcified cartilage (30–40%)), the middle zone (centrally located in noncalcified cartilage tissue (40–60%)), and the superficial zone (interfacing with the synovial fluid and the joint surface (10–20%)) (Di Luca et al., 2015; Martin et al., 2007). Cartilage mainly comprises water (60%–80%), extracellular matrix components (mainly collagen II fibres) and chondrocytes (Sophia Fox et al., 2009). The diameter and orientation of collagen fibrils vary from the superficial zone to the deep zone of cartilage. The superficial zone contains the thinnest collagen fibrils (30–35 nm), which are arranged in a highly parallel orientation to the joint surface. The collagen fibrils diameter increases in the middle zone of cartilage; fewer parallel arrangements are observed in the middle zone than in the superficial zone. The diameter of collagen fibrils is 40–80 nm in the deep zone of cartilage; the fibrils are oriented perpendicular to the joint surface to enhance the strength of the bonds between the cartilage and the bone (Zhang et al., 2009). The superficial zone contains the largest number of chondrocytes; these cells exhibit flattened morphologies and alignment parallel to the joining surface in the superficial zone. In the middle zone, chondrocytes exhibit a rounded shape and a lower number of cells. The fewest number of chondrocytes appear in the deep zone where the cells exhibit rounded and ellipsoid shapes (Zhang et al., 2009; Panadero et al., 2016).

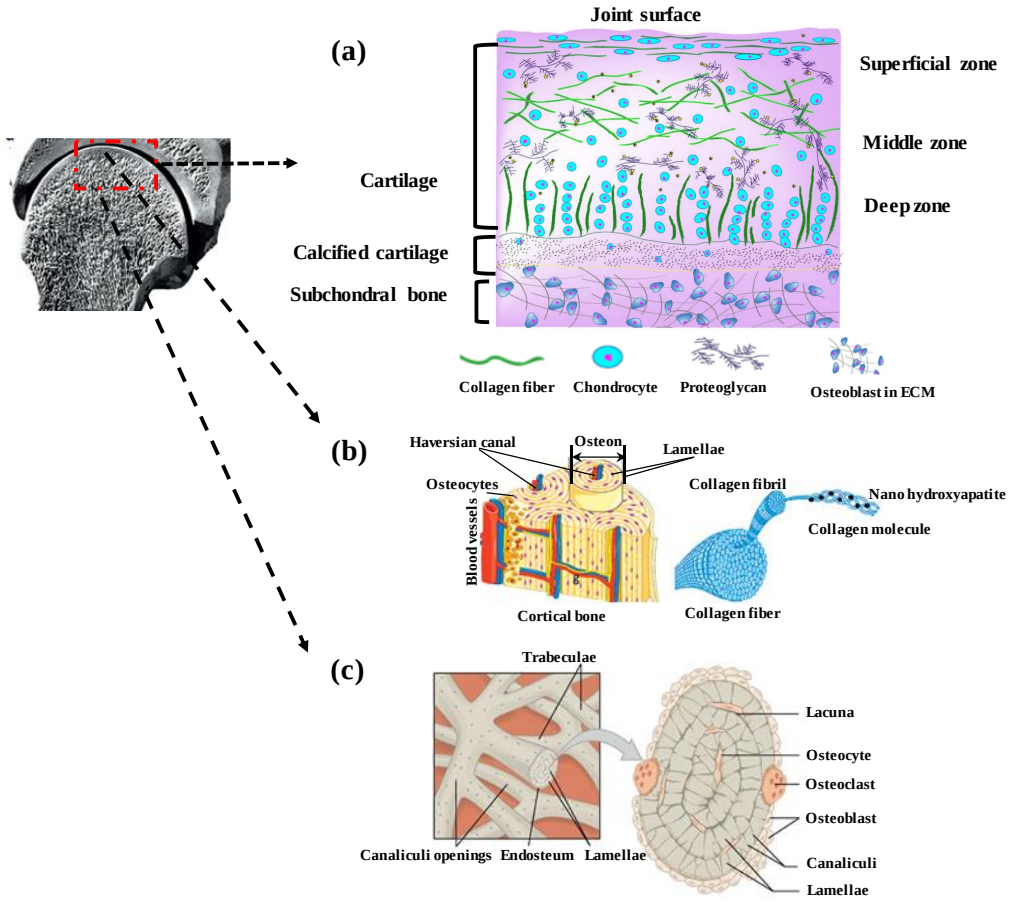

Figure 2.1: Images of the gradient characteristics of natural OC tissue. (a) A schematic diagram of the OC unit, which includes cartilage, calcified cartilage, and subchondral bone (Zhang et al., 2009). (b) The material composition of cortical bone tissue (Gong et al., 2015). (c) The material composition of trabecular bone tissue (Betts et al., 2013).

Table 2.1: The gradient biochemical composition, structure, and mechanical property of OC natural tissue.

	Biochemical composition		**Structure**	**Mechanical property**
	Cells	Materials		
Cartilage (Comper, 1996; Ansari et al., 2019; Korpayev et al., 2020; Antons et al., 2018)	Chondrocyte morphology is flattened in the cartilage surface zone and gradually becomes a round and ellipsoid shape in the deep zone	Type II collagen fibrils are parallel to the joint surface in the cartilage surface zone and gradually become perpendicular to the joint surface in the deep zone	Cartilage is a highly interconnected tissue with a porosity of 60-85% and a pore size of 2–6 nm	The compressive modulus of cartilage increases from the superficial to the deep zone from 0.2 to 6.44 MPa
Calcified cartilage (Khanarian et al., 2012; Zhang et al., 2020b; Steele et al., 2014)	Chondrocyte size in calcified cartilage is higher than in cartilage	Collagen fibrils are anchored to the subchondral bone and hold the cartilage and subchondral bone	Calcified cartilage is located in the transition zone from cartilage and bone; its pore size and porosity gradually vary	The compressive modulus values of cartilage, calcified cartilage, and bone exhibit anisotropic properties and vary in a depth-dependent manner
Subchondral bone (Zhang et al., 2020c; Tripathy et al., 2019; Lee et al., 2012; Zhang et al., 2012; Molino et al., 2020)	Osteoblasts, osteoclasts, osteocytes, and MSCs	Hydroxyapatite crystalline plate-shaped particles with length of 20-50 nm, width of 15 nm, and thickness of 2–5 nm are deposited on type I collagen fibrils	Subchondral bone contains cortical bone (top) and trabecular bone (bottom). The pore size varies from 0.1–2000 μm and the porosity changes from 5-90% from the top to the bottom of the subchondral bone	Compressive modulus values for cortical bone and trabecular bone are 18–22 GPa and 0.001–0.9 GPa, respectively

Calcified cartilage locates in the transition region of OC tissue where contains fewer chondrocytes than the noncalcified cartilage zones. The collagen fibrils in this zone are anchored to the subchondral bone and serve to hold the cartilage and subchondral bone. Features of bone tissue (e.g. the presence of alkaline phosphatase) can be found in the calcified cartilage zone (Li et al., 2013; Ng et al., 2017). Below the calcified cartilage is subchondral bone which contains cortical bone and trabecular bone. The material composition of this layer is shown in 2.1 (b) and (c). The cortical bone locates immediately underneath the calcified cartilage, whereas the trabecular bone is below the cortical bone. Bone is composed of water (10%), organic components (30%–mainly collagen I), and mineral components (60%-mainly hydroxyapatite (HAp)). The HAp crystalline nanoparticles, which exhibit a plate shape with a thickness of 2–5 nm, a length of 15–150 nm, and a width of 10–80 nm, are located on the collagen I fibrils (30–300 nm) (Gong et al., 2015; Kalia et al., 2014; Nikolov and Raabe, 2008). The cells in the bone tissue include osteoblasts, osteoclasts, osteocytes, and mesenchymal stem cells (MSCs). Osteoblasts are the cells that form new bone; these cells are also responsible for HAp synthesis. Osteoclasts are associated with bone resorption. Osteocytes are the most common cell type in bone; they regulate the interaction between osteoblasts and osteoclasts. MSCs are multi-potential stromal cells that are able to differentiate into many cell types such as osteoblasts and chondrocytes (Hadjidakis and Androulakis, 2006).

The structure and mechanical properties of the OC tissue vary from the surface of the cartilage to the subchondral bone. The cartilage within OC tissue has a gel-like structure with the porosity of 60–85%; the cells in the articular cartilage are fed by articular fluid that moves across the cartilage pores. The cortical bone has high stiffness; its porosity ranges from 5% to 30%. The stiffness decreases from the cortical bone to the trabecular bone as the porosity increases; the porosity of trabecular bone ranges from 30% to 90%. Porous structures in the subchondral bone tissue are filled with vessels and nerve fibres that provide bone cells with nutrients and remove waste (Ansari et al., 2019; Sabree et al., 2015; Loh and Choong, 2013). The mechanical properties of OC tissue vary from cartilage to subchondral

bone; this variation is primarily associated with changes to the material composition and structure. The compressive modulus of cartilage shows a depth-dependent change due to variations in the cellular and molecular composition from the superficial zone to the deep zone. The compressive modulus and compressive strength of cartilage gradually increase from the superficial to the deep zone; the compressive modulus increases from 0.2 to 6.44 MPa, and the compressive strength increases from 0.005 to 4 MPa (Boschetti et al., 2004; Walther et al., 2012; Ansari et al., 2019; Gao et al., 2014). Bone tissue consists of organic and inorganic components; the arrangement of these organic and inorganic components gives bone tissue its anisotropic properties. For instance, the transverse elastic modulus and longitudinal modulus of cortical bone are 10.1 ± 2.4 GPa and 17.9 ± 3.9 GPa, respectively. The tension and compression strength of cortical bone in the longitudinal direction are 135 ± 15.6 MPa and 205 ± 17.3 MPa, respectively; the tension and compression strength of cortical bone in the transverse direction are 53 ± 10.7 MPa, and 131 ± 20.7 MPa, respectively (Qu et al., 2019). Trabecular bone performs better under compression than tension, and its compressive elastic modulus and compressive strength are range from 1–900 MPa and 1–10 MPa, respectively (Athanasiou et al., 1994; Boschetti et al., 2004; Gibson, 1985; Sabree et al., 2015; Antons et al., 2018; Helguero et al., 2017).

2.3 OC tissue defects

OC defects often include the destruction of articular cartilage and alterations to the underlying subchondral bone. Heinegård and Saxne (2011) compared the matrix in healthy OC tissue and osteoarthritis-affected defected OC tissue (Figure 2.2 (a and b)). The cartilage compartments in the defect-containing OC tissue exhibit cloning and multiplication of cells at the early stages. This phenomenon results in cartilage destruction, thicker subchondral bone, and decreased trabecular volume. The immunohistochemistry staining data indicate that the degradation of the interterritorial matrix (solid arrow) and changes to the pericellular matrix (dashed arrow) in the cartilage. Those changes in the cartilage and the underlying subchondral bone

can lead to chronic pain and dysfunctional joint movement.

The current surgical treatments for OC defects depend on the lesion size and severity (Figure 2.2 (c)). Microfracture is often used for the treatment of cartilage defects smaller than 1 cm^2, which stimulates MSCs from subchondral bone to repair cartilage tissue (Gill et al., 2006). Autograft or allograft is used to treat lesions in the range of 1–4 cm^2 (Jones and Peterson, 2006); a total joint replacement is required for severe degeneration (Tibor and Weiss, 2013). While these treatments are evolving, the limitations of conventional treatments continue to spur the development of new therapies. The drawbacks of conventional treatments include the quality and consistency of the tissue obtained from microfracture (Minas, 2001), limitations to the supply of autograft tissue, and the possible risk of microbial transmission from allograft tissue (Bauer and Muschler, 2000; Miron et al., 2016; for Disease Control , CDC et al.(1988), as well as wear and loosening of prostheses (Bauer and Schils, 1999; Williams et al., 2010). Tissue engineering therapies are attractive due to their potential to create biological substitutes that can maintain, replace, or regenerate OC tissue (Loh and Choong, 2013).

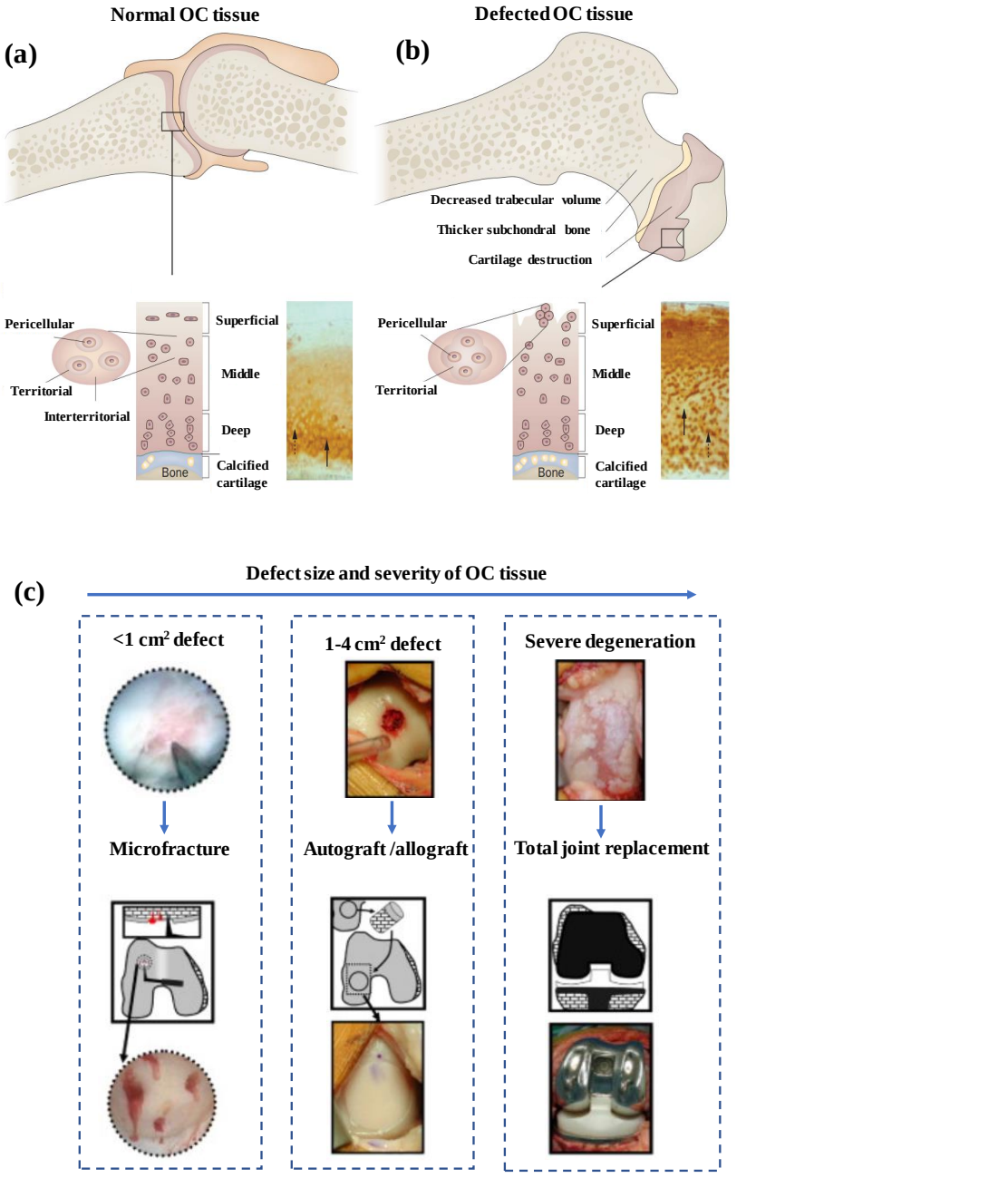

Figure 2.2: (a) A healthy OC tissue with normal cartilage, which is organized into pericellular, territorial, and interterritorial matrices. The immunohistochemistry results show that there was no cartilage oligomeric matrix protein present in the territorial and pericellular matrices (black dashed arrow). Interterritorial matrix staining showed the presence of the cartilage extracellular matrix molecule (solid black arrow). (b) A defected OC tissue in the osteoarthritic joint that shows partial loss of cartilage, subchondral bone thickening, and a decrease in trabecular bone volume. There were alterations in the cartilage compartments from cell cloning and multiplication. The immunohistochemistry results showed the loss of cartilage oligomeric matrix protein in the interterritorial matrix (solid black arrow); there was new synthesis of the molecule in the pericellular matrix of cartilage (black dashed arrow) (Heinegård and Saxne, 2011). (c) Current clinical treatment options for OC defects and the treatment options depend on defect size and severity (Williams et al., 2010).

2.4 Commercial gradient OC scaffolds in clinical trials

To this point, very few scaffold designs have been evaluated in clinical trials. Commercially available tissue scaffolds for OC regeneration are mainly biphasic or triphasic scaffolds that mimic the entire OC unit (Figure 2.3). For instance, the TruFit plug from Smith & Nephew is a classic biphasic scaffold consisting of porous poly(lactic-co-glycolic acid) (PLGA)/polyglycolide (PGA) and calcium phosphate. Although the clinical findings of TruFit plug did demonstrate stable cartilage-like repair over a short term (less than one year), the long-term results (more than two years) were questionable; this result is attributed to delayed and inadequate integration with the surrounding tissue (Verhaegen et al., 2015; Longley et al., 2018). Dell'Osso et al. (2016) indicated that the scaffold would exhibit better performance if the design more closely mimicked the surrounding OC tissue rather than the biphasic approach.

One recently developed scaffold that is undergoing clinical trials is the triphasic MaioRegen from Fin-Ceramica Faenza SpA; this scaffold attempts to more closely mimic the structure of OC tissue. The cartilage layer consists of equine type I collagen; the calcified cartilage layer consists of type I collagen (60% of total weight) and magnesium-hydroxyapatite (Mg-HAp) (40% of total weight). The bone layer consists of a mineralized blend of type I collagen (30% of weight) and Mg-HAp (70% of weight). A clinical study by Kon et al. (2014b) indicated that subchondral bone formation occurred with complete resorption of the biomaterial. The cartilage tissue was not only repaired but also participated in an ongoing maturation process over six months. They performed an analysis five years post-surgery with the MaioRegen treatment and magnetic resonance imaging (MRI) evaluation and demonstrated revealed significant improvement in both cartilage and subchondral bone (Kon et al., 2014a). However, a study by Christensen et al. (2016) observed opposite and adverse outcomes; incomplete cartilage repair and poor subchondral

bone repair after ankle and knee joint treatments with the MaioRegen scaffold were noted. Thus, the available commercial products indicate the advantages of a gradient structure that closely mimics the natural structure of the OC tissue. However, significant efforts in tissue engineering research still required to increase the regenerative capacity of OC replacements (Li et al., 2015; Christensen et al., 2016; Wang et al., 2019).

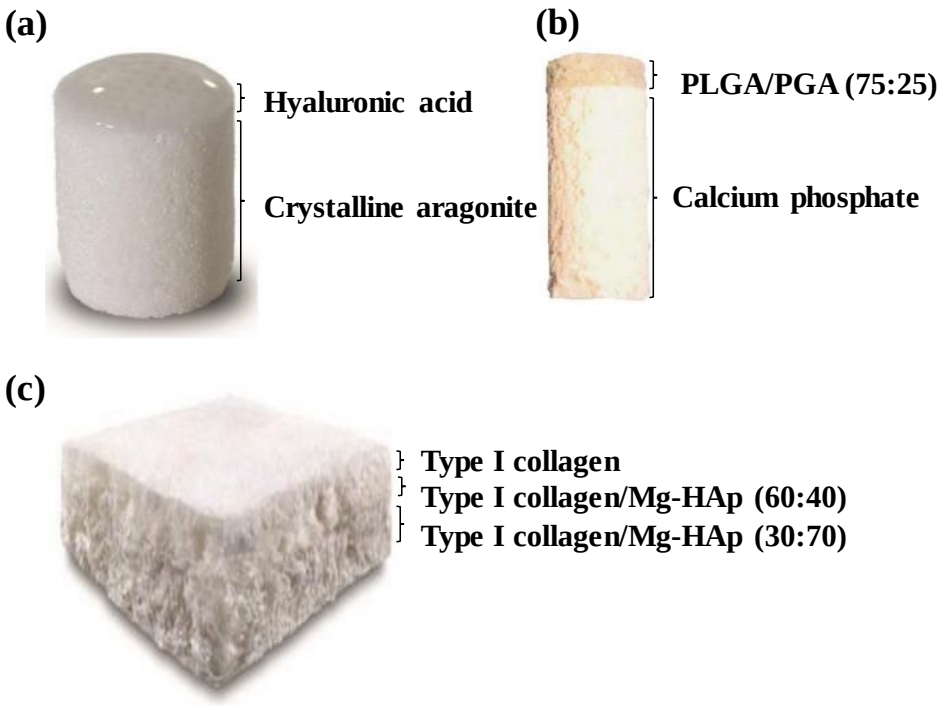

Figure 2.3: Images of gradient scaffolds that reached clinical trials. (a) Crystalline aragonite based biphasic scaffold (Agili-C, CartiHeal, Israel). (b) Polymeric PLGA/PGA and calcium sulfate biphasic scaffold (Trufit, Smith & Nephew, USA). (c) Collagen type I and HAp triphasic scaffold (MaioRegen, Finceramica, Italy) (Longley et al., 2018).

2.5 Tissue engineering for OC tissue regeneration

As indicated earlier, the biochemical composition, structure and mechanical properties of natural OC tissue exhibit gradient transitions from the surface of the cartilage to the subchondral bone. To closely mimic the gradient transition of OC tissue, the cell type (Yousefi et al., 2015; Gadjanski, 2018; Han et al., 2019), growth factor (Du

et al., 2015; Trachtenberg et al., 2017; Gao et al., 2018), scaffold material (Stratton et al., 2016; Dash et al., 2011; Bittner et al., 2019), scaffold structure (Van Bael et al., 2012; Gao et al., 2018; Nowicki et al., 2016), mechanical properties (Kosik-Kozioł et al., 2020; Zhang et al., 2020b; Sabree et al., 2015) should exhibit a gradient transition. The fabrication methods for gradient OC tissue scaffold are also introduced in this section. 3D printing techniques enable control over the pore geometry within the scaffold to obtain scaffolds with appropriate mechanical properties. The application of 3D printing techniques for OC scaffold fabrication are summarised.

2.5.1 Cells, growth factors and material composition in OC tissue engineering

Tissue engineering typically involves the use of porous tissue scaffolds in which cells can adhere, proliferate, differentiate, and migrate to enable tissue regeneration. Although it may be possible to use cell-free scaffolds to repair OC tissue containing minor defects, the scaffold alone cannot usually initiate appropriate biological responses for OC tissue regeneration (Yousefi et al., 2015). Cells used for the OC tissue repair, either in vitro or in vivo, include chondrocytes, osteoblasts and MSCs. Chondrocytes and osteoblasts are often seeded in separate layers of the cartilage and bone components of the OC tissue scaffold. However, the limited presence of chondrocytes in natural OC tissue (around 5% of total cartilage volume) restricts the application of chondrocytes in OC tissue engineering. Additionally, the isolation of collagen from the extracellular matrix (ECM) requires the use of collagenase, which can harm the chondrocytes. It has also been suggested that chondrocytes lose appropriate phenotypic expression in the culture environment (Gadjanski, 2018). MSCs have been used for OC tissue regeneration since they have the capability to differentiate into chondrocytes and osteoblasts; MSCs are seen as an alternative to overcome the limited supply of chondrocytes (Han et al., 2019). In addition, growth factors play an essential role in directing MSCs differentiation into target cells. The sequential addition of growth factors to a scaffold is useful for stimulating chondrogenesis. For instance, chondrocytes seeded in

agarose gels to transforming growth factor-beta 3 (TGF-β3) for two weeks showed better cartilage formation and mechanical properties than chondrocytes seeded in agarose gels without TGFβ3 (Byers et al., 2008). Similarly, the exposure of MSCs in poly(ethylene glycol) (PEG) hydrogels to TGF-β1 resulted in enhanced proliferation and proteoglycan production (Buxton et al., 2011).

Abrahamsson et al. (2010) fabricated polycaprolactone (PCL) tissue scaffolds, seeded the scaffolds with human MSCs, and cultured the scaffolds in a medium containing human TGF-β3. The formation of cartilaginous tissue was observed after culture for 21 days in vitro; moreover, the construct showed mechanical properties similar to those of native articular cartilage after culture for 45 days. Similarly, the use of growth factors is essential for osteogenesis. The most commonly used inducing factor for osteogenesis is bone morphogenetic protein-2 (BMP-2), which is usually immobilized on scaffolds to promote osteoblast differentiation (Du et al., 2015; Loozen et al., 2013). Additionally, calcium phosphate and HAp nanoparticles are used as osteogenic regulators in tissue engineering; these materials promote osteogenic differentiation of MSCs and change the physical properties of the scaffold (Loozen et al., 2013; Trachtenberg et al., 2017). Porous alginate constructs incorporating the osteogenic growth factor BMP2 and calcium phosphate particles were able to efficiently transfect encapsulated MSCs over fourteen days and promote their differentiation towards the osteogenic lineage (Loozen et al., 2013). In general, chondrogenic growth factors (e.g. TGF- β family) supplied to the cartilage layer of the OC scaffold are beneficial for chondrogenesis. Osteogenic growth factors (e.g. BMPs or HAp nanoparticles) are incorporated within the bone layer of the OC scaffold for osteogenesis (Gadjanski, 2018).

A range of biocompatible materials, including natural polymers, synthetic polymers, inorganic materials, and metallic materials, have been used to fabricate OC tissue scaffolds. Natural polymers such as collagen, gelatin, chitosan, alginate, and silk have been used for OC scaffold fabrication because of their similarity to the structure of the extracellular matrix and their biocompatibility (Liao and Ho, 2011; Dash et al., 2011; Abarrategi et al., 2010). Collagen is the most commonly

used natural polymer for OC scaffold fabrication since it is the main component of connective tissue; however, it is unstable. Due to its rapid degradation rate, the scaffold is unable to maintain structural integrity. Crosslinking treatments can be performed to extend the durability and mechanical strength of this material (Zanetti et al., 2013; Zhou et al., 2011). Gelatin has also been used for cartilage repair for its low cost and facile preparation. However, due to its poor mechanical properties, gelatin is usually used in combination with other materials such as HAp, bioactive glass, and chitosan. Silk materials have also been for OC scaffold since they are stable, flexible, and highly resistant in tension and compression (Wang et al., 2006); the main disadvantage of silk is the relatively low speed of its production by spiders (Gervaso et al., 2013). In general, although natural polymers closely mimic natural cartilage tissue, shortcomings such as limited supply, low stable, high degradation rate, and low mechanical strength limit their use for OC scaffold fabrication.

Synthetic polymers such as PCL, poly(lactic-co-glycolic acid) (PLGA), polyglycolic acid, PEG, polylactic acid, polydioxanone, and poly (propylene fumarate) have been used for the fabrication of OC scaffolds (Rezwan et al., 2006). Since most synthetic polymers are hydrophobic, limitations in terms of cell attachment and differentiation may occur due to an insufficient number of interaction sites (Stratton et al., 2016). Blends of hydrophobic and hydrophilic polymers are often used to enhance hydrophilicity and promote cell attachment (Baker et al., 2012; Park et al., 2018). Bioceramics such as HAp, tricalcium phosphate (TCP), and bioglass are capable of stimulating biomineralization for bone tissue repair; the biodegradability of calcium phosphate materials can be controlled by altering the calcium-to-phosphorus ratio (Zhang et al., 2020c; Hench, 2006). Although bioceramic based scaffolds have high bioactivity, they are brittle and cannot resist mechanical stresses. Therefore, scaffolds containing composites of natural or synthetic polymers and bioceramics may exhibit better mechanical properties than bioceramic scaffolds (Zhang et al., 2020c; Liu et al., 2019).

To mimic the gradient of cartilage, calcified cartilage, and bone within natural OC tissue, two main categories of scaffolds, i.e. discrete and continuous gradi-

ent scaffolds, have been developed (Figure 2.4). Discrete gradient scaffolds can be categorised as biphasic or tri/multiphasic. For a biphasic OC scaffold, individual bone and cartilage scaffolds can be joined together. As shown in Figure 2.4 (a), Schaefer et al. (2000) fabricated a polyglycolic acid (PGA) scaffold for the cartilage layer and a PLGA/PEG scaffold for the bone layer; bovine calf articular chondrocytes and bone cells were seeded on those scaffolds separately. The two components were then sutured together. The in vitro results at two weeks show increased glycosaminoglycan (GAG) production on the cartilage side of the scaffold as well as apparent mineralization of the ECM on the bone side of the scaffold. As shown in Figure 2.4 (b), Chen et al. (2011a) developed a biphasic OC scaffold containing TGF-β1 activated chitosan/gelatin for the chondrogenic layer and BMP-2 activated HAp/chitosan/gelatin for the osteogenic layer. The structures were separately seeded with MSCs and fused with fibrin glue. The in vivo results indicate that the scaffold supported the regeneration of cartilage and subchondral bone after twelve weeks of implantation in a rabbit knee defect. Zhao et al. (2013) fabricated porous PLGA and titanium (Ti) scaffolds; a pressing method was applied to join two scaffolds together to create a biphasic construct (Figure2.4 (c)). The in vivo results showed that there were better cartilage and subchondral bone repair in the PLGA/Ti biphasic scaffold than in the PLGA or Ti scaffold. Moreover, the tri/multiphasic scaffolds were shown to closely mimic the cartilage, bone, and transition zone of calcified cartilage in natural OC tissue. Figure2.4 (d) shows tri-phasic scaffolds developed by Jiang et al. (2010); PLGA and bioactive glass seeded with osteoblasts were used to create the bone layer. Agarose hydrogel seeded with chondrocytes was used to create the cartilage phase; the calcified cartilage phase was created using a combination of PLGA and agarose hydrogel. The in vitro results indicate that the appropriate tissue in each layer was formed; chondrocytes were observed within the calcified cartilage zone. Figure2.4 (e) shows multiphasic scaffolds prepared by Nooeaid et al. (2014) which contain alginate for the cartilage layer, bioglass for the bone layer, an alginate/bioglass hybrid adhesive layer at the interface of cartilage and bone. The three layers were joined together by press-fitting manually. The re-

sults showed that the multiphasic scaffolds had appropriate porosity, pore size, and mechanical properties for use as an OC tissue scaffold. Levingstone et al. (2014) developed a multiphasic scaffold; the construct contained three types of layers. As shown in Figure2.4 (f), the bone layer was composed of type I collagen and HAp, while the calcified cartilage layer was composed of type I collagen, type II collagen, and HAp. The cartilage layer was composed of type I collagen, type II collagen and hyaluronic acid. The in vitro tests involving this scaffold showed a homogeneous cellular distribution throughout the entire construct.

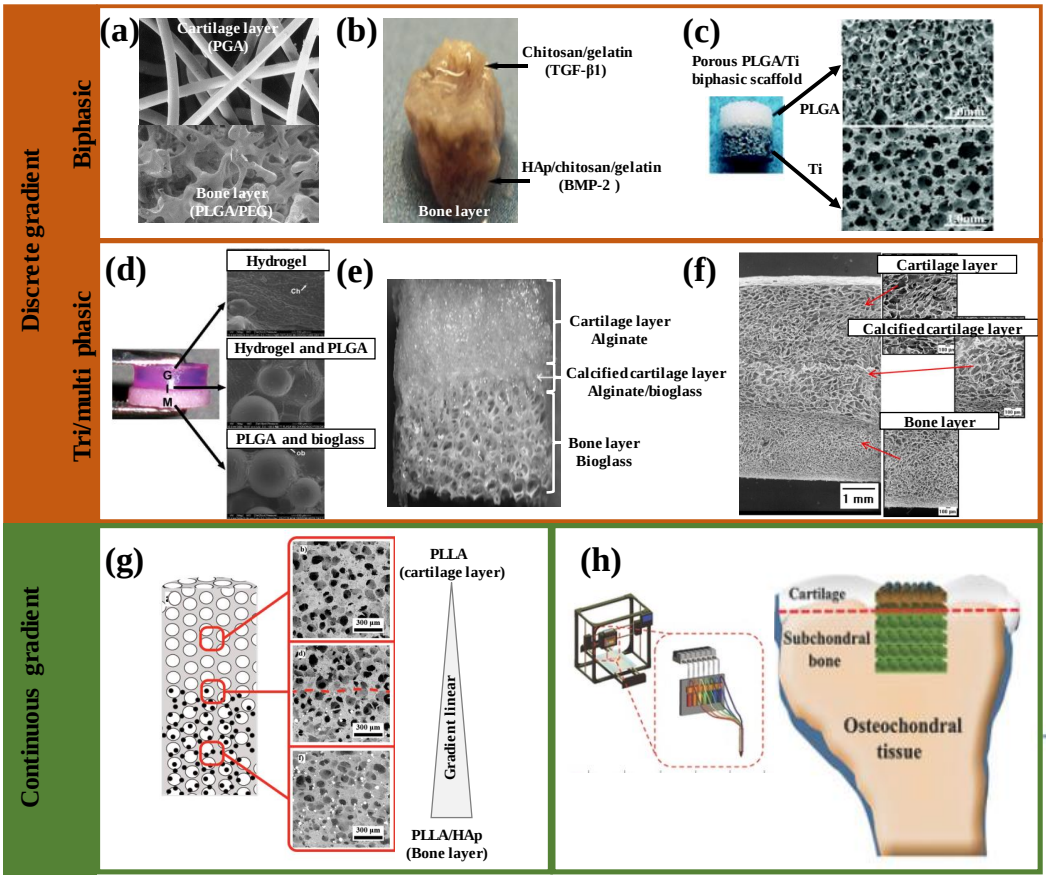

Figure 2.4: Discrete and continuous gradient scaffolds for OC tissue regeneration. (a) biphasic scaffold containing PGA and PLGA/PEG for the cartilage and bone layer, respectively (Schaefer et al., 2000). (b) Biphasic scaffold made of chitosan/gelatin and HAp/chitosan/gelatin (Chen et al., 2011a). (c) Biphasic scaffold made by PLGA and porous Ti blocks (Zhao et al., 2013). (d) Tri-phasic scaffold containing a cartilage phase consisting of agarose hydrogel, a calcified cartilage phase consisting of agarose hydrogel/PLGA/bioglass, and a bone phase containing PLGA/bioglass (Jiang et al., 2010). (e) Tri-phasic scaffold with alginate as the cartilage layer, alginate/bioglass composite as the calcified cartilage layer, and bioglass as the bone layer (Nooeaid et al., 2014). (f) Tri-phasic scaffolds with a cartilage layer composed of type I collagen/type II collagen/hyaluronic acid, a calcified cartilage layer composed of type I collagen/type II collagen/HAp, and a bone layer composed of type I collagen/HAp (Levingstone et al., 2014). (g) Continuous gradient scaffolds with PLLA in the cartilage layer and PLLA/HAp in the bone layer (La Carrubba et al., 2018). (h) Proof of concept of developing continuous gradient scaffold with bioinks using the 3D printing technique (Liu et al., 2017; Gao et al., 2018).

Researchers fabricated a continuous gradient scaffold to more closely mimic the gradient characteristics of OC tissue (Dormer et al., 2010; La Carrubba et al.,

2018; Parisi et al., 2020; Liu et al., 2017). Compared with discrete gradient scaffolds, the continuous gradient scaffold has the potential to induce a smooth transition between the cartilage and bone component, avoiding instability at the interface. Dormer et al. (2010) developed continuous gradient PLGA scaffolds using programmable pumps to control the flow rate; they created a gradient in terms of microsphere size and distribution. The top quarter and the bottom quarter of the scaffold contained TGF–β1 and BMP–2, respectively. The transition region from TGF–β1 to BMP–2 constituted the middle half of the scaffold. MSCs were seeded on the gradient scaffold; the in vitro results showed that there were improved GAG production and alkaline phosphatase activity. La Carrubba et al. (2018) created Poly-L-lactic acid (PLLA)/HAp scaffolds with a continuous gradient in microsphere size and distribution. The HAp concentration was gradually increased from the cartilage region to the bone region within the scaffold (Figure 2.4 (g)). Parisi et al. (2020) developed a continuous gradient scaffold using a freeze-drying process by varying the ratio of collagen to HAp from the bottom to the top of the scaffold; the bottom of the scaffold had the highest HAp content, whilst the top of the scaffold had no HAp. Physicochemical studies were used to examine the chemical composition and the distribution of mineral in the scaffold. By changing the biomaterial composition from the cartilage region to the bone region, the mechanical properties of the scaffold were modulated in a gradient manner. The in vitro results show that the composition and stiffness gradients increased cell proliferation in different sub-regions of the scaffold according to their chondrogenic or osteogenic characteristics. As shown in Figure 2.4 (h), a 3D printing method was used to develop a continuous gradient scaffold for OC tissue repair. A scaffold with the desired gradient was prepared with independent or simultaneous control over more than seven distinct bioinks (Liu et al., 2017). Details about the use of 3D printing for OC tissue scaffold processing are described in Section 2.5.3.2.

2.5.2 Structure and mechanical properties in OC tissue engineering

An efficient OC scaffold design should provide a porous gradient structure with appropriate mechanical properties to match with the host tissue. The scaffold pore size should be larger than the dimensions of the relevant cells so that the cells can readily migrate into the scaffold; the pore size and porosity have significant effects on chondrogenesis and osteogenesis. A scaffold structure with a porosity higher than 50% and pores larger than 300 μm is recommended to achieve direct osteogenesis with enhanced vascularization (Karageorgiou and Kaplan, 2005). On the other hand, 90–120 μm pores are favourable for chondrogenesis (e.g. MSCs proliferation and cartilage tissue formation on the scaffold) (Kim et al., 2010). This difference in pore size is attributed to the fact that bone and cartilage tissue exhibits different levels of metabolism activity. Since oxygen is supplied mostly by the synovial fluid on the surface of the cartilage, chondrocytes consume a lower amount of oxygen than other cell types. While oxygen for subchondral bone is supplied by blood vessels, the pore size of the bone scaffold should enable the growth of blood vessels in the scaffold for exchanging nutrients, oxygen, and metabolic waste (Marrella et al., 2018).

Many studies discussed balancing the relationships among scaffold pore size, porosity, cell penetration, nutrient supply, and the mechanical properties of the scaffold. When scaffold pore size and porosity increase, cell penetration and nutrient supply generally increase. However, the scaffold mechanical strength decreases when the pore size and porosity increase (Figure2.5 (a)). Wang et al. (2014) fabricated bi-layered scaffolds with cartilage ECM and HAp; various scaffold pore sizes and porosities were obtained by optimising the HAp/cartilage ECM ratio. The scaffold pore size decreased from 128.2 $\pm$ 20.3 μm to 21.2$\pm$ 3.1 μm with the addition of HAp. The addition of HAp to the cartilage ECM construct increased the compressive modulus but decreased the permeability of the chondrocytes. Korpayev et al. (2020) developed a chitosan/collagen/HAp based continuous gradient

scaffold using freeze-drying; the HAp content in the scaffold was decreased from the bottom to the top of the scaffold. The top layer of the scaffold contained chitosan/collagen; no HAp was present on the top layer. The pore size varied along the vertical axis; the elastic modulus for the bottom layer exhibited the highest modulus value of 42.95 kPa. Xiao et al. (2019) fabricated a silk fibroin/chitosan/HAp scaffold in which the HAp concentration increased gradually from the upper part of the scaffold to the lower part of the scaffold. The pore size gradually decreased from 152.6 μm to 74.66 μm in this scaffold. Shi et al. (2019) fabricated a gradient alginate/dopamine/HAp scaffold using the freeze-drying technique; its porosity increased between the bottom and the top from 70.5% to 77.5%. The bottom layer in this scaffold contained the highest amount of HAp. Apart from the scaffold pore size and porosity, pore interconnectivity is a critical factor for OC tissue. The interconnections between pores should be suitably large to support cell migration, proliferation, and subsequent ECM infiltration; as such, pore interconnectivity is a more important parameter than the pore size. Scaffolds should ideally have a 100% interconnecting pore volume, which maximizing the exchange of nutrients and metabolic waste throughout the entire scaffold pore volume (Ansari et al., 2019; Choi et al., 2010).

The scaffold material stiffness also influences cell morphology, attachment, and differentiation. Figure 2.5 (b) shows changes in the cell shape and differentiation of native MSCs that are directed by materials with different elasticities. Metal-polymer (Zhao et al., 2013) and ceramic-polymer (Chen et al., 2011a; Jiang et al., 2010) compositions have been used to create structures with gradient mechanical properties. Metal alloys (e.g., Ti alloy), ceramics (e.g., HAp and TCP), and bioglass are used for bone regeneration; the polymers (e.g., PLGA, PCL) and alginate are used for cartilage regeneration. Piezoelectricity has been used for transduction of mechanical loading into electrical energy, which affects tissue regeneration. After placement of the scaffold at the OC tissue site, the dipole moments of the scaffold materials may be altered, creating an electric charge on the surface of cells. The signal reaches the cell membrane and activates calmodulin, calcineurin, and nuclear

factor, which leads to the expression of genes for bone or cartilage production (e.g., cartilage-related gene expression of TGF–β and bone–related gene expression of BMP–2) (Ansari et al., 2019).

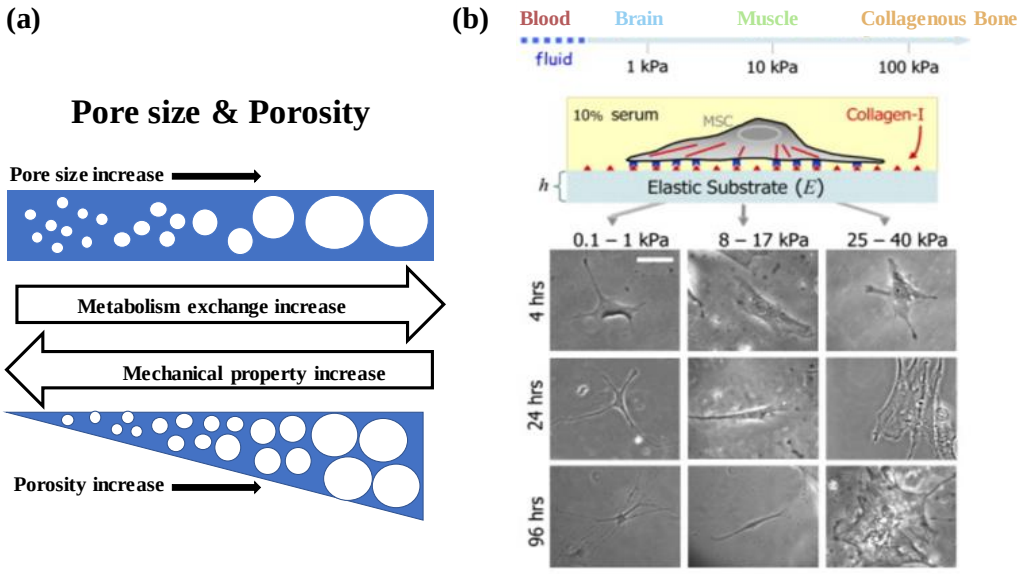

Figure 2.5: (a) Schematic images showing an optimal level of porosity and maintenance of high mechanical strength in a tissue scaffold. (b) The effect of material stiffness on cellular adhesion, differentiation behaviour, and cell shape; the cells show small, branched, and spindle shapes. The scale bar is 20 µm (Engler et al., 2006).

2.5.3 Fabrication methods in OC tissue engineering

The methods used fabricate OC tissue constructs can be divided into conventional and 3D printing methods. Conventional techniques for scaffold fabrication are generally cost-effective that provide some control over scaffold porosity and pore size. 3D printing techniques allow for independent control over macroscale and microscale features as well as enable the development of customised tissue scaffolds.

2.5.3.1 The application of conventional methods for OC scaffolds

Conventional fabrication methods such as solvent casting, gas forming, freeze-drying, and electrospinning have been used to create OC tissue scaffolds (Loh and Choong, 2013; Hutmacher and Williams, 2006; Eltom et al., 2019). Solvent casting,

a solvent combined with uniformly distributed particles of a certain size is used to dissolve the polymer solution. The matrix is then submerged in the solvent; the particle is leached away to form a porous structure. It is a relatively straightforward and low-cost technique (Eltom et al., 2019). Studies (Lin et al., 2019; Lee et al., 2016) have used this technique to create OC scaffolds out of a combination of synthetic polymers; bioactive compounds may be incorporated within the scaffold using this technique (Giannoni et al., 2015). One of the drawbacks of solvent casting is that this approach is compatible with thin membranes or 3D specimens with very thin wall sections; while in other cases, it is not possible to remove the soluble particles from within the polymer matrix (Eltom et al., 2019).

In the gas foaming technique, the polymer granules are plasticised due to the employment of a gas such as nitrogen or carbon dioxide at high pressure. The advantage of the gas forming technique is that it enables the incorporation of heat-sensitive pharmaceuticals and biological agents within the scaffold. However, scaffold fabrication using gas forming is characterised by an incompletely interconnected pore network, which limits cell infiltration (Hutmacher and Williams, 2006; Loh and Choong, 2013).

Freeze-drying of porous scaffolds is based on the conversion of frozen solvents into the gas phase; this approach can fabricate scaffolds with porosity greater than 90% and median pore sizes ranging from 15 to 35 μm (with larger pores greater than 200 μm); the scaffold pores exhibit relatively high interconnectivity. This technique has been used to create OC scaffolds out of natural polymers (Levingstone et al., 2014), synthetic polymers (Dormer et al., 2010), and bioactive composites (Parisi et al., 2020; Korpayev et al., 2020; Shi et al., 2019). The freeze-drying method uses cytotoxic solvents; as such, the scaffold needs to be washed repeatedly to remove the solvent and minimize cytotoxicity (Eltom et al., 2019).

Electrospinning is a technique for the fabrication of fibrous scaffolds, particularly scaffolds with a nanofibrous morphology. In this technique, a polymer solution ejected through a needle to form fibres under a strong electric field. Nanofibrous

scaffolds can be modified by controlling the process parameters (e.g., voltage and fluid rate). Electrospinning fabricated scaffolds typically exhibit small pore sizes of less than 300 μm; these small pore sizes can hamper osteogenesis (Zhang et al., 2013). Post-fabrication procedures have been used to make pores larger than 300 μm in electrospun scaffolds. For example, laser ablation has been used to generate pore sizes up to 500 μm (Rebollar et al., 2011; McCullen et al., 2010).

2.5.3.2 The application of 3D printing methods for OC scaffolds

3D printing has emerged as a new technology for OC scaffold fabrication. In 3D printing, a layer-by-layer fabrication process is guided by a CAD model; excellent control over pore geometry can be achieved by this process. 3D printing enables fabrication of fully interconnected pore structures and optimisation of the mechanical properties of the scaffold (Gloria et al., 2009). The 3D printing techniques that are used to create OC scaffolds are summarised in Table 2.2. There are three main categories of 3D printing techniques are used to develop tissue scaffolds, including solid-based techniques (e.g. fused deposition modelling), powder-based techniques (e.g. selective laser sintering and selective laser melting), and liquid-based techniques (e.g. inkjet printing, stereolithography, direct ink writing).

Table 2.2: The application of 3D printing technologies for the fabrication of gradient OC scaffolds to be used in OC tissue repair.

	Technique	**Scaffold materials**	**Scaffold structure**	**Gradient approach**	**In vitro/in vivo testing**	**Advantage/disadvantage**
Solid-based 3D printing methods (Di Luca et al., 2015; Nowicki et al., 2016)	Fused deposition modelling	PCL	Woodpile structure with pore size gradients on the vertical direction	Pore size/porosity	The osteogenic lineage was improved in gradient scaffolds compared with non-gradient structures	+ Easily fabricate physical gradients - Cannot incorporate cells or bioactive molecules
		Poly (ethyleneglycol)	Pore size gradient lead to varying porosity in layers of scaffolds	Pore size/porosity	MSCs adhesion and proliferation on the 3D printed scaffolds with gradient pore size were improved when compared to uniform porous structures	
Powder-based 3D printing methods (Van Bael et al., 2012; Du et al., 2017)	Selective laser sintering	PCL/HAp, and HAp gradient change from the cartilage layer to the bone layer	A cylindrical scaffold with a pore size of 500 µm	Material composition	The gradient scaffolds induced the formation of cartilage and accelerated the early subchondral bone regeneration in rabbit model in vivo	+ No support structures and toxic solvents required - Cannot achieve horizontal compositional gradients
	Selective laser melting	Ti_6Al_4V	Scaffolds with different pore shape (triangular, hexagonal and rectangular) and pore size (500 µm and 1000 µm)	Pore size and pore shape	The gradient changing pore size and shape enhanced human placenta-derived cells (hPDC) seeding. The in vitro results indicate that the differentiation of hPDC was dependent on both pore shape and pore size	+ Building high quality and complex metal parts and a large range of metal materials - High power consumption
Liquid-based 3D printing methods (Woodfield et al., 2005; Phillippi et al., 2008; Melchels et al., 2011; Trachtenberg et al., 2017; Gao et al., 2018)	Stereolithography	Poly(D,L-lactic acid)	A gradient in both porosity and pore size of the horizontal direction	Pore size/porosity	Gradients in pore size and porosity influence the distribution of seeded human articular chondrocytes and anisotropic adherent cell densities	+ Can create high resolution and complex internal structures - The limited application of biomaterials - Cannot achieve horizontal compositional gradients.
	Inkjet printing	BMP-2 and fibrin	Fibrin film	Growth factor	Provide proof-of-concept of engineering spatial control over stem cell fates by controlling the printed patterns of BMP-2 immobilised to fibrin	+ Can fabricate both cells and bioactive molecules gradient - Only feasible for low viscosity materials
	Solvent-based extrusion printing	Porous poly (ethylene glycol)-terephthalate–poly (butylene terephthalate) copolymer	Pore-size gradients by varing fibre spacing from 0.5–2.0 mm	Pore size	Pore-size gradients promoted an inhomogeneous bovine chondrocyte seeding within the scaffold and affected the inhomogeneous distributions of GAG and collagen type II	+ Can print a wide range of materials + Allow for the printing of,cells/bioactive factors + Can fabricate both physical and compositional gradients - Cannot achieve complex scaffold structure - Difficulty for ink formulation
		The top layers of scaffold fabricated with the PNT and TGF-β1 hydrogel, while the bottom layers were loaded with PNT and β-TCP hydrogel	Filament deposition-based woodpile structure	Material composition	The gradient hydrogel scaffolds promoted the regeneration of both cartilage and subchondral bone in vivo	

3D printing techniques are driving a shift toward personalised scaffolds. For example, personal scans of joints can be converted into computer-aided design files, which are then used to design patient-specific scaffolds. Such personalised scaffolds will not only provide a continuous gradient between bone and cartilage but also provide a continuous transition between the scaffold and the host tissue (Klein et al., 2009; Tamaddon et al., 2018). During the layer-by-layer 3D printing process, it is possible to incorporate several types of living cells, growth factors, and biomaterials within a scaffold (Figure 2.6 (a)). As such, 3D printing provides a mechanism for recapitulating the gradient characteristics of the OC unit (Klein et al., 2009). The gradient scaffold that fabricated by 3D printing includes the material gradient, the structure gradient, and the gradient of both material and structure. As shown in Figure 2.6 (b), Gao et al. (2018) formulated poly(N-acryloyl glycinamide)/poly(N-[tris(hydroxymethyl) methyl] acrylamide) co-polymer hydrogel (PNT) bioinks; they fabricated a gradient scaffolds with the bioinks using a bioprinting method. The top layers of the scaffold contained a hydrogel with PNT and TGF-β1; the bottom layers of the scaffold contained a hydrogel with PNT and β-TCP. The in vitro results indicated that the incorporation of β-TCP improved cell proliferation and differentiation of hBMSCs. The in vivo animal study indicated that the gradient hydrogel scaffolds could promote the regeneration of both cartilage and subchondral bone.

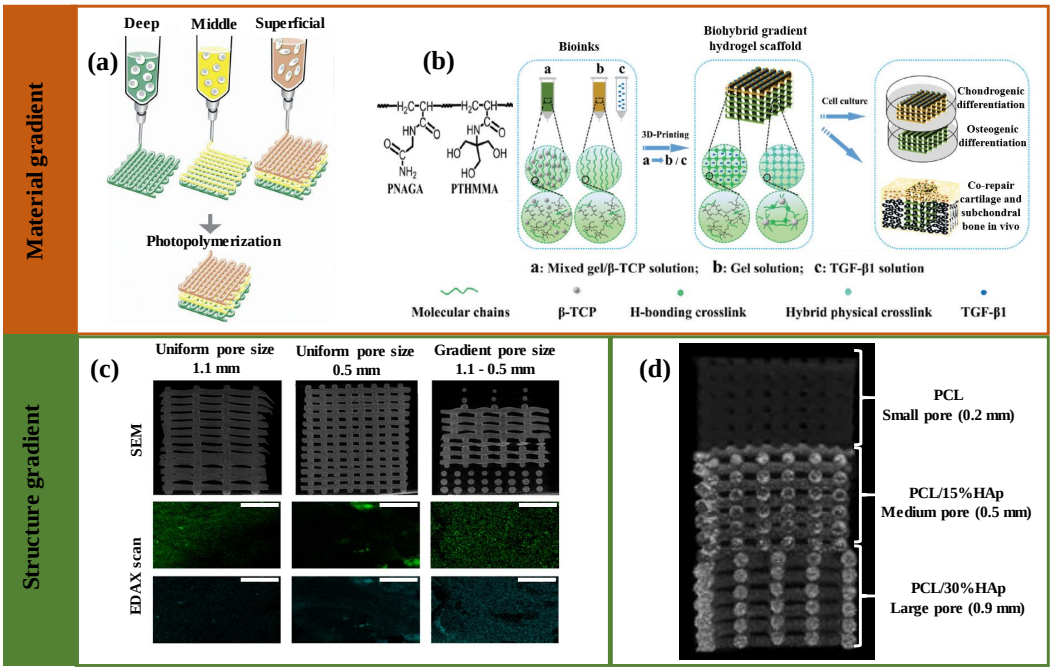

Figure 2.6: The application of 3D printing for a gradient OC tissue scaffold. (a) Schematic of the concept for 3D printing constructs in which chondrocytes from the deep, middle, and superficial zones are suspended in distinct hydrogel precursors and printed in defined geometries (Klein et al., 2009). (b) Schematic illustration of the molecular structure and hydrogen bonding interactions in the PNT hydrogel and biohybrid gradient scaffolds produced with extrusion 3D printing (Gao et al., 2018). (c) SEM image of a scaffold with pore sizes of 0.5 mm, 1.1 mm, and a gradient pore size from 1.1 to 0.5 mm; an energy-dispersive X-ray spectroscopy (EDAX) scan at day 35 also shown, which reveals the presence of calcium (blue) and phosphate (green) in the scaffolds (Di Luca et al., 2015). (d) Gradient scaffold with material (HAp concentration) and structure (pore size change from 0.2–0.9 mm) (Bittner et al., 2019).

The effect of scaffold structure on cellular response has also been investigated. Di Luca et al. (2015) studied the influence of the pore size gradient on the osteogenic differentiation of hMSCs in fused deposition modelling-processed PCL scaffolds (Figure 2.6 (c)). The results indicated that differentiation of hMSCs toward the osteogenic lineage in mineralisation media was improved in gradient scaffolds structures than in scaffolds with non-gradient structures. Nowicki et al. (2016) used fused deposition modelling to fabricate PEG/PEG–diacrylate scaffolds with isotropic and anisotropic pore distributions. The anisotropic structure was fabricated by varying the porosity of the scaffold layers. The in vitro results show

that there was enhanced hMSC proliferation and differentiation within anisotropic 3D printed scaffolds than the 3D printed scaffolds with isotropic porous structures. Bittner et al. (2019) created PCL/HAp scaffolds with gradients of structure and materials (Figure 2.6 (d)). The structural gradient was created by changing the scaffold pore size from top to bottom using 0.2 mm, 0.5 mm, and 0.9 mm fibre spacing; the material gradient was created by changing the HAp concentration from 0 wt% to 30 wt%. Mechanical property analysis results indicated that the large pore size in the gradient scaffolds was more deformed than the other sections; in addition, the gradient scaffolds exhibited compressive modulus in the range of human trabecular bone.

Various 3D printing methods have their advantages and restrictions. For instance, fused deposition modelling can be used to create a gradient structure; however, cells and bioactive molecules cannot be incorporated during the printing process due to the high processing temperature. Similarly, cells and bioactive molecules cannot be incorporated during selective laser sintering or selective laser melting processes, which involve sintering or melting of powder precursors. On the other hand, droplet-based and extrusion bioprinting processes could be used to process scaffolds containing growth factors and cells at ambient or human body temperature. However, it is difficult to fabricate scaffolds with complex pore geometries using these processes.

2.6 Direct ink writing 3D Printing of tissue scaffold

Direct ink writing, one of solvent-based extrusion 3D printing methods, has the advantages of enabling researchers to produce scaffolds in a heat-free environment. The solvent-based extrusion 3D printing can be classified as pneumatic-driven, piston-driven and screw-driven. The piston-driven based 3D printing is also named as direct ink writing (DIW). Table 2.3 summarises their working scheme and advantages and disadvantages for tissue scaffold fabrication. In pneumatic-driven based printing, the inks are forced through the nozzle by controlling the compressive air

pressure. While, the piston and screw-driven based 3D printing, inks are extruded by regulating the motor rotation speed. The volume of material extrusion is dictated by the extrusion rate. Among of the three solvent-based extrusion printing classes, the pneumatic-driven based 3D printing is more suitable for printing ink with cells as the sterilised air can minimise the contamination. The piston and screw-driven based 3D printing can provide larger deposition force compare with the pneumatic-driven based 3D printing, and they are feasible for the printing of relatively high viscosity inks. However, the screw-driven based 3D printing is not suitable for cell involvement printing, as the shear stress generated on the blade may cause cell damage.

The DIW printing technique can extrude continuous filament of inks containing biomaterial with or without cells or biomolecules through a nozzle to form 3D woodpile structures layer-by-layer. The DIW printer mainly includes a three-axis position system, print head, and print platform. The print head can be controlled by the three-axis position system to deposit inks that extruded from the syringe on the print platform in the X, Y and Z directions. The printed filament resolution is depended on the inner nozzle diameter of the print head, which can be achieved in the range of 20–1000 μm.

Table 2.3: Schematic of solvent-based extrusion 3D printing methods and their advantages and disadvantages.

Solvent-based extrusion 3D printing	Advantages	Disadvantages
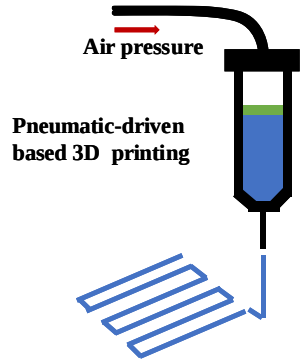	• Sterilised air pressure– suitable for cell printing • Monitor pressure changes in the syringe during the printing	• Not suitable for high viscosity inks
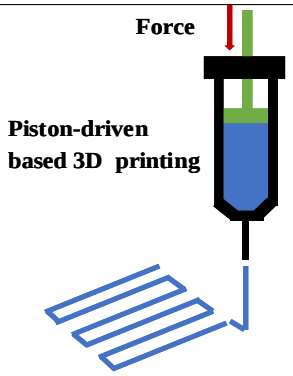	• Motor drive force control is relatively easy to be achievable • Can be used for higher viscosity ink than pneumatic-driven based printing	• Direct control may cause contamination
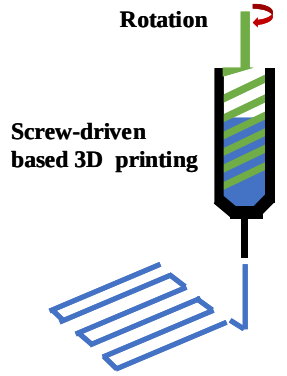	• Can be used for higher viscosity ink than motor-driven based printing • The printed ink can be mixed uniformly during the printing	• Not suitable for cell mixed application • Easy to form bubble inside the biomaterial solutions

2.6.1 Ink biomaterial

Generally, biomaterials applied for scaffold fabrication with solvent-based extrusion 3D printing should be mixed with solvents as ink forms. The applied materials can be classified as incorporated with cells and without cells. The biomaterials can be applied to incorporate with cells - mostly are water-soluble material. In this section, the materials applied with cells and without cells will be separately discussed. Table 2.4 summarises the application of solvent-based extrusion 3D printing, with

or without living cells for tissue scaffold fabrication.

• Ink materials with cells

Biomaterials used in scaffold fabrication are mixed with solvents to create the liquid feedstock for DIW printing. Biomaterials used with living cells in scaffold fabrication should not only provide an appropriate environment for cell survival but also should be compatible with the printing process. The formulated biomaterial solution is often called a bioink, and the processing approach is referred to as bioprinting. The biomaterials most commonly used for bioprinting are hydrogels (either natural or synthetic hydrogels); these biomaterials can provide cells a mild aqueous environment during the printing process. The hydrogels used in solvent-based extrusion 3D printing with cells include alginate, hyaluronic acid, collagen, gelatin, and silk (Lee et al., 2009; Schacht et al., 2015; Gao et al., 2015; Müller et al., 2015; Duan et al., 2014).

Duan et al. (2014) formulated hydrogel inks with hyaluronic acid and gelatin; they incorporated human aortic interstitial cells (hAVIC) within these inks for 3D bioprinting of heart valve conduits. An increase in the gelatin concentration resulted in a lower ink stiffness and a higher viscosity; these parameters facilitated cell spreading and maintenance of a better hAVIC fibroblastic phenotype. They described the dependence of the bioprinting accuracy on the hydrogel concentration; optimisation of the ink concentration can enable the fabrication of a heart valve shape that matches the original design. Wüst et al. (2014) evaluated a combination of alginate and gelatin with various amounts of hydroxyapatite (HAp); hMSCs mixed into the hydrogel/HAp inks survived the printing process. The in vitro results show high cell viability, with an 85% cell viability rate after three days. The elastic modulus of the alginate-gelatin composite discs increased with the HAp concentration. The amount of HAp in the hydrogel correlated with the stiffness of the hydrogel disc, with 36 $\pm$ 3 kPa for hydrogel 8% HAp, 32 $\pm$ 2 kPa for hydrogel 4% HAp and 29 $\pm$ 2 kPa for hydrogel no HAp. However, the ink became more viscous as the HAp concentration was increased. As such, it is difficult to print

HAp-containing inks. They indicated that control of the tip temperature affected the viscosity of the bioink; increasing the temperature can convert the ink to the liquid form, eliminating the clogging issues at the dispenser tips. Notably, more viscous inks require larger pressures for extrusion from the nozzle; as such, cells in the bioinks are exposed to process-induced forces (i.e., shear stress). The deformation of the cell membrane can occur if the applied force is too high. Therefore, the shear stress is a key factor that needs to be evaluated during bioprinting. Blaeser et al. (2016) developed a fluid-dynamics model and performed in vitro experiments to understand shear stress at the nozzle site. The results show that the generated shear stress is affected by the hydrogel ink viscosity, extrusion pressure, and nozzle dimensions. Mouse fibroblasts can exhibit cell viability of 96% if exposed to shear stress of less than 5 kPa; viability is decreased to 90% and 75% for the shear stress of 5–10 kPa and more than 10 kPa, respectively.

Table 2.4: The summary of tissue scaffold fabrication using solvent-based extrusion 3D printing.

	Solvent-based extrusion 3D printing	Ink materials	Ink rheology properties	Post-processing mechanisms	Fabrication process parameters	Scaffold characterisation methods	Biological outcomes	Reference
Printing with cells	Pneumatic-driven based 3D printing	Alginate, nanocellulose and human chondrocyte mixed in D-Mannitol solvent	-The shear viscosity from 0.01–1000 s^{-1} was measured shown shear thinning behaviour of all inks -Oscillation amplitude sweeps from 0.1–1000 Pa at a frequency of 1 Hz were performed to define the linear viscoelastic region	$CaCl_2$ solution bath	The print speed was at 20 mm/s	The optimal ink was selected by the measurement of the filament width from microscopy images of the printed scaffold	Human chondrocyte bioprinted with the nanocellulose based ink and the cell viability of 73% and 86% after 1 and 7 days of 3D culture	(Markstedt et al., 2015)
	Pneumatic-driven based 3D printing	Hyaluronic acid, gelatin and hAVIC mixed in cell culture medium	-Ink viscosity measurements were measured at applied shear stress from 1 to 1000 Pa -The elastic modulus of various concentration hydrogels inks was measured	UV light	No specific mentioned	The printing accuracy was assessed by comparing the measured area with the design values	Increasing gelatin concentration facilitated cell spreading, and better maintained hAVIC phenotype	(Duan et al., 2014)
	Piston-driven based 3D printing	Alginate, gelatin, and hMSCs with different concentration HAp mixed in PBS	-Viscosity of inks with different HAp concentration was measured by varying the shear rate from 0.0001 to 100 s^{-1} -Oscillatory tests over a temperature ramp from 50 to 10°C to investigate the gel point	$CaCl_2$ solution bath	The printing speeds was 2 mm/s	HAp enabled the visualization of the printed structures with mirco-CT	hMSCs survived the printing process and showed high cell viability of 85% living cells after 3 days of subsequent in vitro culture	(Wüst et al., 2014)
Printing without cells	Pneumatic-driven based 3D printing	Silk fibroin water solution	-The shear viscosity of silk solution from 0.01–1000 s^{-1} was measured -Oscillation amplitude sweeps from 0.1–1000 Pa at a frequency of 1 Hz were performed to define the elastic and viscous modulus	Methanol-reservoir	The print speed was 2 mm/s	The mechanical property of silk filament was assessed by nanoindentation test	There was enhanced chondrogenic differentiation for hMSCs, indicated with the increased glycosaminoglycan production	(Ghosh et al., 2008)
	Pneumatic-driven based 3D printing	Silk and HAp mixed with distilled water water	-The shear viscosity of silk/HAp solution shown high viscosity of $\sim 1 \times 10^4$ Pa s under low shear conditions -Oscillation amplitude sweeps results indicated elastic modulus of silk/HA solution nearly 1×10^5 Pa	Solvent evaporation	The print speed was 2 mm/s	Scaffold pore size was measured with microscopy images	The 3D silk fibroin scaffolds are used to support the growth of cocultures of hMSCs and hMMECs	(Sun et al., 2012)
	Piston-driven based 3D printing	Alginate and laponite dissolved in distill water	-Viscosity and shear stress was measured with laponite concentration by varying the shear rate from 0.001 to 1000 s^{-1} -The oscillatory shear test was performed to analyze the viscoelastic behavior of inks -Viscosity recovery test was performed to identify the ink recovery percentage to mimic the ink extruded from the nozzle	$CaCl_2$ solution bath	Investigate the relationship between the extrusion rate and printing speed	The print speed and extrusion rate were selected by the measurement of the filament width from microscopy images of the printed scaffold to match with the nozzle diameter	Two patterns of scaffolds were successfully printed, no cells study involved	(Dávila and d'Ávila, 2019)

Table 2.4 continued from previous page

	Solvent-based extrusion 3D printing	Ink materials	Ink rheology properties	Post-processing mechanisms	Fabrication process parameters	Scaffold characterisation methods	Biological outcomes	Reference
Printing without cells	Pneumatic-driven based 3D printing	Polylactic acid and a bioactive CaP glass dissolved in chloroform	CaP glass improved ink viscosity, but no ink rheology test was involved	Solvent evaporation	The print speed was 3 mm/s	-Filament and pores size were accessed from the SEM image and micro-CT generated structure -The compressive modulus of printed scaffolds with different patterns was evaluated by uniaxial compressive test -The porosities of printed scaffolds were compared with the theoretical ones	-The glass particles increased roughness, hydrophilicity, and mechanical property of scaffolds -CaP glass improved MSCs adhesion	(Serra et al., 2013)
	Pneumatic-driven based 3D printing	PCL-hydroxyapatite and CNT dissolved in dichloromethane	By adjusting CNT concertation to achieve an optimum viscosity between 2.5 and 7 Pa s.	Solvent evaporation	No specific mentioned	The compressive modulus of printed scaffolds with different CNT concentrations was evaluated by uniaxial compressive test	HAp improved the bioactivity, the in vitro test showed there was good cell adhesion and spreading at the scaffold surface	(Goncalves et al., 2016)
	Pneumatic-driven based 3D printing	Polycaprolactone and poly (lactic-co-glycolic acid)) and HAp particles mixed in dichloromethane	Reached the optimal viscosity of 30 to 35 Pa s	Solvent evaporation	The print speeds were as 15 $cm\,s^{-1}$, and extrusion rates were as 275 cm^3/h	The compressive modulus of printed scaffolds was evaluated by uniaxial compressive test	Supported cell viability and proliferation and induced osteogenic differentiation of hMSCs cultured in vitro and quickly integrated with surrounding tissues in vivo	(Jakus et al., 2016)

• Ink materials without cells

When the cells are not placed within the inks, the printed scaffolds can serve as a support structure to facilitate tissue regeneration on the inherent recovery properties of the tissue. DIW is a commonly applied method for printing inks that do not contain cells. Ghosh et al. (2008) printed tissue scaffolds and microvascular networks using the DIW technique; they fabricated a scaffold with a silk fibroin solution ink; the extruded filament was deposited in a methanol-rich reservoir for crystallisation. In vitro studies suggest that the scaffolds supported hMSC adhesion and growth as well as higher chondrogenic differentiation under chondrogenic conditions. Miranda et al. (2008) used the DIW technique to produce scaffolds with precise porous features using concentrated β-TCP and HAp inks with suitable viscoelastic properties. The 3D printed ceramic scaffolds have shown promising results for potential use in bone tissue repair. However, their application is limited due to their brittleness. The incorporation of a polymer material with a ceramic ink is a promising approach to overcome this limitation. The combination of polymer and ceramic components can also mimic the organic and inorganic components of natural bone tissue. Sun et al. (2012) developed scaffolds composed of a gradient array of silk/HAp, which supported cocultures of hMSCs and human mammary microvascular endothelial cells (hMMECs). The histology results indicate that the hMSCs and hMMECs form intricate networks of extracellular matrix within the 3D scaffolds.

Some synthetic polymers are not water-soluble and must be mixed with organic solvents to form solutions. These polymers can often provide better mechanical strength than natural polymers. Considering the toxicity of many organic solvents, cells may not be incorporated within synthetic polymer-laden inks. Several synthetic polymers have been used in DIW printing, including polycaprolactone (PCL), polylactic acid (PLA), poly (lactic-glycolic acid) (PLGA), and their copolymers. Serra et al. (2013) used PCL and bioactive calcium phosphate (CaP) glass to fabricate 3D scaffolds with orthogonal and displaced double-layer patterns. Their results indicate that scaffolds containing CaP glass particles exhibited increased roughness

and hydrophilicity. The preliminary cell response of these materials was studied with MSCs. This study revealed that CaP glass improved cell adhesion. Goncalves et al. (2016) fabricated scaffolds out of composites containing PCL, nano-HAp, and carbon nanotubes (CNT). The CNT improved the mechanical behaviour of the scaffolds - compressive modulus of the printed scaffold was 4 MPa, which can be compatible with the trabecular bone. The in vitro results showed that HAp improved bioactivity, and good cell adhesion and spreading were noted on the scaffold surface.

Although the use of DIW printing to create polymer/ceramic composites is promising for tissue engineering applications, only a few studies to this point have investigated the ink printability and processing parameters. Thus, more investigation should be done through careful control of the ink rheology behaviour (e.g. viscosity, rheological behaviour, and ink recovery percentage), and fabrication process parameters (extrusion rate and printing speed), for the scaffolds fabrication. In the next section, these points will be discussed in detail.

2.6.2 Ink rheological behaviour

The biomaterial ink solution should have an appropriate rheology since the printed structure is prone to collapse if the viscosity of the solution is low. Inks with the non-Newtonian flow and shear thinning behavior are preferable. In shear thinning, high shear rate causes the viscosity of the material solutions to decrease so that it easily flows through the needle. The cells within the ink can influence ink rheology; they can be seen as 'non-soluble' microparticles suspended in the solution. Ning et al. (2016) investigated the influence of various types of cells and cell density on the viscosity of alginate ink. The results reveal that the viscosity of pure alginate ink was higher than those of inks containing three types of cells. As the cell density in the alginate inks is increased, a reduction in viscosity can be obtained. The results suggest that cells containing cytoplasm can be seen as a fluid with low viscosity. As such, the interactions among cells likely act as lubricants and reduce the viscosity (Chen et al., 2019a). Dávila and d'Ávila (2019) formu-

lated laponite/alginate inks without cells and analysed the ink rheology in terms of viscosity and ink recovery behaviour. As the laponite concentration increased from 0 to 6 wt%, an increase in viscosity was noted at the same shear rate (Figure 2.7 (a)). Higher laponite concentrations cause strong shear-thinning behaviors. The ink recovery behavior was also investigated to mimic the ink extrusion process from the nozzle. Figure 2.7 (b) shows the results of viscosity recovery studies. It was observed that the ink viscosity recovered almost instantaneously when a high shear load was removed, which was associated with elastic energy stored by the alginate chains. As shown in Figure 2.7 (c), filament formation with several concentrations of laponite was evaluated; filaments were formed at laponite concentrations greater than 5 wt%. The more viscous ink solution is relatively difficult to flow or spread, which can serve to maintain the printed filament shape.

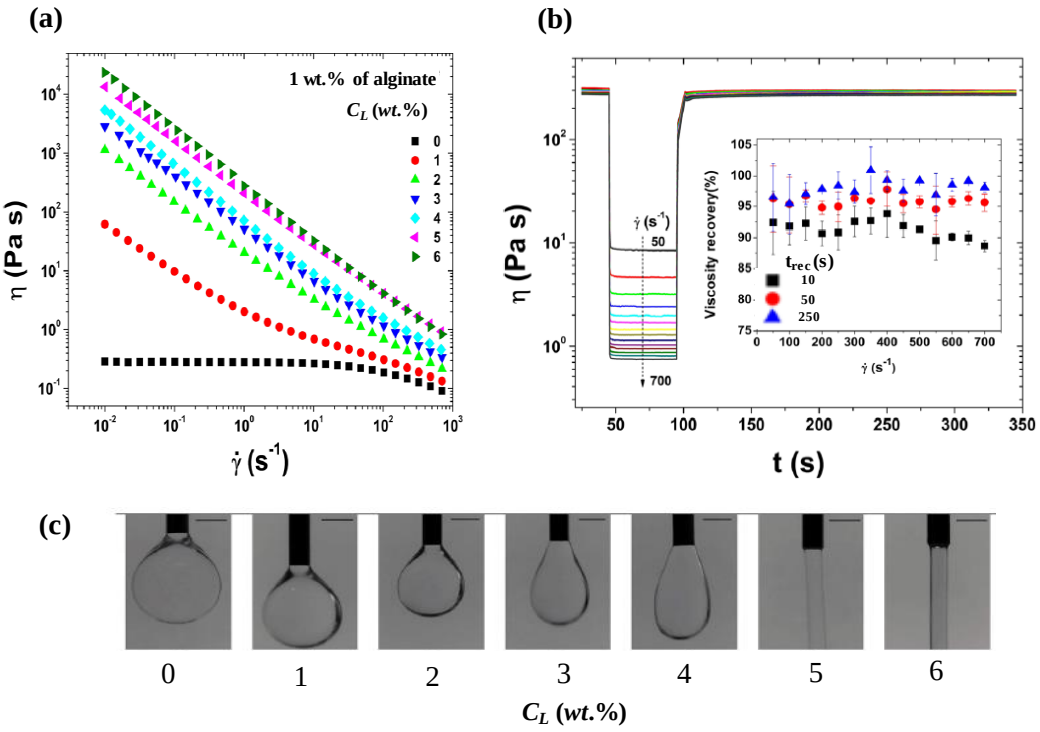

Figure 2.7: (a) The relationship between viscosity (η) and shear rate ($\dot{\gamma}$) for the inks with 1wt% alginate and a laponite concentration (C_L) between 0 and 6 wt%. (b) Viscosity as a function of the time (t) for the ink recovery test. (c) Microscopy images of the extrusion of alginate/laponite inks with the laponite between 0 and 6 wt%. The scale bar is 1 mm (Dávila and d'Ávila, 2019).

2.6.3 DIW printing fabrication process parameters

In addition to the ink material and ink rheology, the process parameters also affect the performance of the DIW printing process. The process parameters in DIW printing include the extrusion rate, needle-moving speed, substrate property and the scaffold design geometries. The extrusion rate can be affected by several factors, including the ink rheology, extrusion rate, and needle parameters. The ink velocity alongside the needle (V_z) follow the power-law equation can be calculated using Equation 2.1:

$$V_z = \int_r^R \gamma dr = \left(\frac{n}{n+1}\right)\left(\frac{\Delta PR}{2mh}\right)^{\frac{1}{n}} R\left[1-\left(\frac{r}{R}\right)^{\frac{n+1}{n}}\right] \tag{2.1}$$

where m is the consistency index and it is associated with the magnitude of the viscosity. n is the power-law index and defines the viscosity behaviour; n is less than 1 for a shear-thinning ink (Morrison et al., 2001). The corresponding extrusion rate (Q_E) can be calculated using Equation 2.2 (Morrison et al., 2001):

$$Q_E = \int_0^R 2\pi R V_z dr = \left(\frac{\Delta PR}{2mh}\right)^{\frac{1}{n}}\left(\frac{n\pi R^3}{3n+1}\right) \tag{2.2}$$

As shown in Figure 2.8 (a), R is the needle radius, h is the length of the needle, and ΔP is the extrusion pressure drop along the needle. Equation 2.1 represents the velocity along the needle length, showing that the velocity distribution of printed inks inside the needle is not constant. The parameter V_z reaches a maximum in the core of the needle and is zero at the needle wall. Equation 2.2 shows that the extrusion rate is associated with the extrusion pressure and needle radius. The filaments are formed depending on the movement of the needle in the XY plane. Ideally, the printed filament diameter should be the same as the nozzle diameter by manipulating the printing speed (V_{xy}) and extrusion rate (Q_E) within a defined range. If the printing speed is higher than the range, the printed filament will be stretched, and the filament diameter will subsequently decrease. If the printing speed lower than

the range, ink accumulation will occur, and the filament diameter will increase.

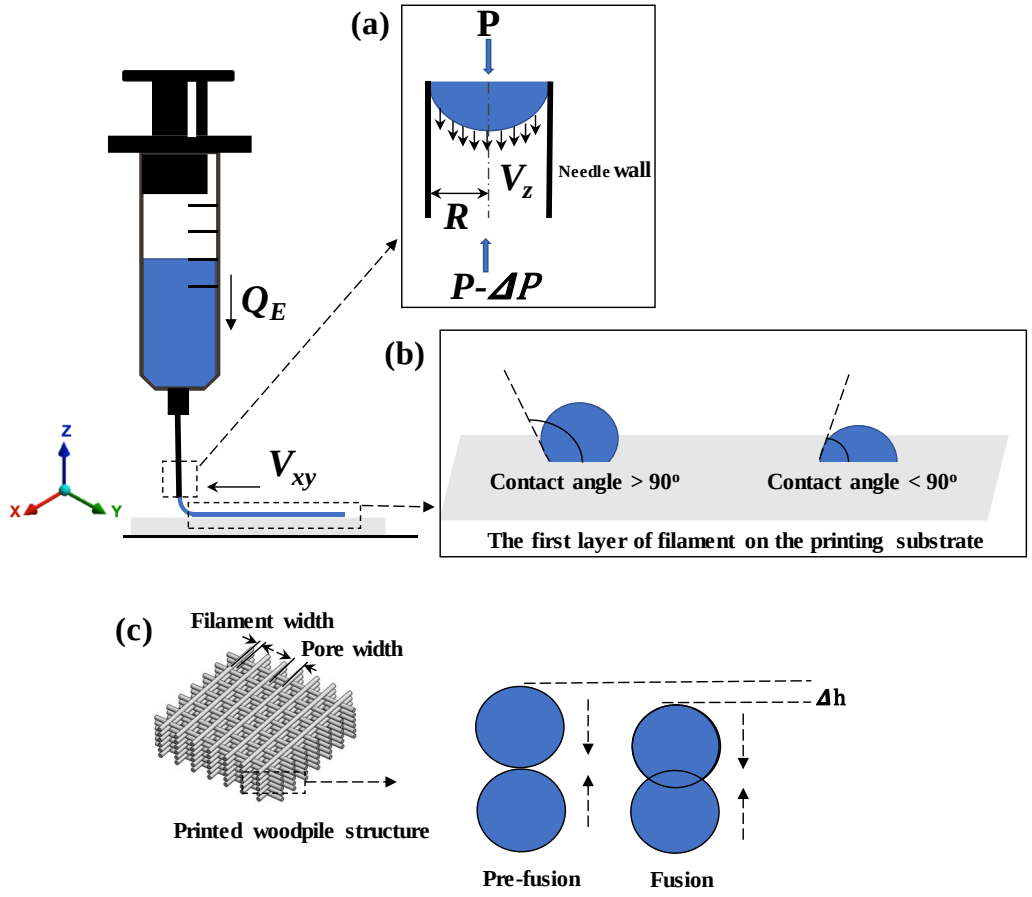

Figure 2.8: (a) The schematic of ink flow inside the printing needle. (b) The first layer of filament formation on the substrate. (c) The fusion process of two filament layers in the vertical direction within the printed woodpile structure.

The substrate can affect filament formation. As shown in Figure 2.8 (b), two filaments were formed with different contact angles on the substrate. The structure of the filament with a large contact angle value can be maintained. While, a small contact angle can improve the stability of the scaffold. In most cases, the substrate (e.g. glass) can have large contact angles with the filament. By coating the substrate with a thin layer of one or more chemicals, e.g., polyethyleneimine, the substrate properties can be modified to decrease the contact angle (You et al., 2017; Chen et al., 2019a). Meanwhile, the pore geometry in the Z direction is more determined by the ink rheology, needle dimensions and needle movement distance in

the Z direction. In Figure 2.8 (c), Δh is caused by two adjacent filament layers that vertically fusion together. Since the scaffold is formed in a layer-by-layer manner, the dripping ink will form at the needle tip if the distance between the needle tip and the substrate is larger; this process interrupts the continuity of filament formation. If the needle tip is too close to the substrate, the extruded filament will be scratched by the needle, and the filament diameter will be increased as a result.

Appropriate maintenance of the shape of the extruded filament is necessary to support the structure without collapsing. He et al. (2016) studied ink printability by investigating filament printing of the first layer and optimised printing parameters. As shown in Figure 2.9 (a), they indicate that diffusion should be considered when designing the scaffold. In Figure 2.9 (b), the lattice structures with various pore width (D_L) values were compared. The results showed that diffusion between two adjacent lines on the same layer could cause overlapping when the D_L was 1 mm. When the D_L was 4 mm, the extent of diffusion was much less.

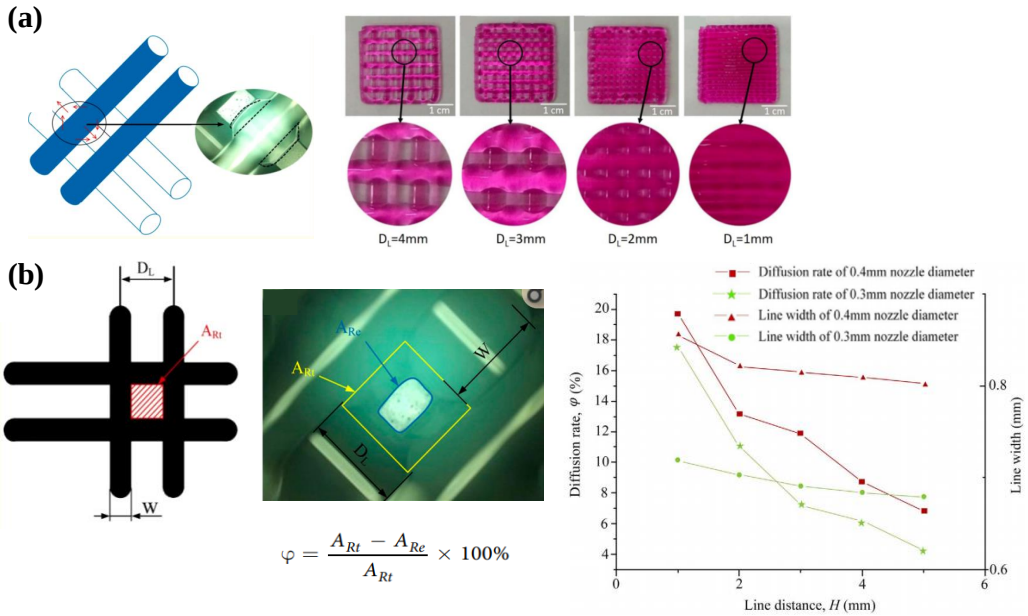

Figure 2.9: (a) The ink diffusion and fusion on the same layer when the D_L was at 1-4 mm; (b) The comparison of lattice area from theory and experiment as well as the relationship among line distance, line width and diffusion rate (He et al., 2016).

The solvents used in DIW printing can cause scaffold shrinkage after drying,

which can result in changes to the scaffold structural and mechanical properties. The 3D printed scaffold structures need to be evaluated before use in vitro or in vivo. There is no standardised method to quantify the difference between the theoretical CAD design and the printed structure. A common evaluation approach involves the measurement of the printed filament diameter and the filament distance from microscopy or SEM images. He et al. (2016) developed a method to measure the intersection area formed by filaments in microscopy images Figure 2.9 (c). They found that the area of the rectangle (A_{Re}) obtained from experiments was much smaller than the theoretical rectangle area (A_{Rt}). They also investigated the relationship between filament distance and diffusion rate (ϕ).

2.7 Computational modelling application in OC tissue engineering

Biological studies have advanced to optimise the scaffold structure, and/or the materials, enabling MSCs differentiation into chondrocytes and osteoblasts for OC repair. However, it is both costly and time-consuming to investigate the influence of each parameter on tissue regeneration in vitro or in vivo. Computational modelling has been applied to predict tissue regeneration within scaffolds. The use of computational simulation methods together with biological experiments can facilitate a better understanding of the interactions among scaffold design and tissue regeneration.

2.7.1 Fundamentals of computational mechanobiology in OC tissue engineering

Various mechanic-regulation algorithms have been developed to describe the effects of mechanical stimulus on cells and tissues. Most recently developed mechano-regulation algorithms are based on a study by Pauwels (1941). The authors proposed that two invariants of mechanical force guide cell differentiation - octahedral shear stress and hydrostatic stress. They noted that high hydrostatic stress induced

chondrogenesis; while, high octahedral shear stress induced fibrous tissue formation. Perren (1979) investigated interfragmentary repair tissues and proposed an interfragmentary strain theory based on the linear elastic behavior of tissue. The strain was defined as 'the interfragmentary movement divided by the initial fracture gap size'. They demonstrated that tissue differentiation is controlled by the resilience of callus tissues to strain. If the interfragmentary strain is higher than 10%, then only fibrous granulation tissue can form. If it is intermediate (2-10%), then cartilage is present; if it is lower than 2%, then bone formation occurs. However, the hypothesis only considered longitudinal strains, and neglected the strain contributions from radial and circumferential strains. Carter et al. (1988) introduced a semiquantitative theory to define the contributions of the hydrostatic stress and the octahedral shear stress to tissue differentiation. The octahedral shear stress was replaced by the octahedral strain in a subsequent study (Carter et al., 1991). Carter et al. (1991) performed an in vivo study, which evaluated the thresholds of strain and stress values based on semiquantitative theory. They found that new bone formation in fracture healing mainly occurs along the existing bone edge. The results suggested that intramembranous bone formation occurs for hydrostatic stresses less than 0.15 MPa and strains lower than 5%. However, endochondral ossification was positively stimulated if hydrostatic stresses were greater than 0.15 MPa and strains were 5-15% (Claes et al., 1998).

The theories mentioned above all considered tissues as solid elastic materials. Prendergast et al. (1997) proposed a mechano-regulatory model for tissue differentiation based on the poroelastic behavior of tissues. They believed that stress on the cell was generated not only by tissue matrix deformation but also by the interstitial fluid flow within the scaffolds. High values of both solid strain and fluid shear stress cause fibrous tissue formation; while, intermediate values lead to cartilaginous tissue. Bone is formed only if the solid strain and fluid shear stress values are sufficiently low. Huiskes et al. (1997) quantified the upper and lower limits of mechanical stimuli for various tissue phenotypes and developed a mechano-regulatory model for tissue differentiation. Over the past decade, the mechano-regulation the-

ory has been used with finite element modelling to predict the influence of scaffold materials, scaffold structures, and culture conditions on cell migration and differentiation (Liu and Niebur, 2008; Geris et al., 2004; Byrne et al., 2007).

2.7.2 The application of finite element modelling in OC tissue engineering

The finite element (FE) modelling method has been used to predict the mechanical properties of 3D scaffolds; with the development of 3D printing techniques, scaffolds can be designed and analysed with FE modelling, enabling researchers to explore the relationships among innovative scaffold topologies, mechanical properties, and tissue regeneration. For example, FE modelling has been used for the analysis of scaffold mechanical properties under mechanical loading. Melchels et al. (2010) designed CAD models with various structures (e.g., cube, diamond, and gyroid); they built the scaffolds out of poly (D, L-lactide)-based resin using the stereolithography approach. The bulk properties of the stereolithography produced solid materials were described mathematically using a constitutive model; the FE simulations results were compared with the mechanical test results. The results indicated that the gyroid structure provided a uniform strain distribution for cells within the scaffold, which would benefit cell growth and differentiation. Several studies have been investigated the effects of various pore sizes and pore shapes on the mechanical properties of extrusion-printed OC scaffolds using the FE approach. For instance, Gleadall et al. (2018) compared the mechanical properties of two types of scaffolds with lattice and staggered filament arrangements under the same mechanical loading parameters, using the Von Mises stress magnitude and distribution were analysed. The FE results demonstrate that lattice structure formed a continuous pillar of filaments that help resist compression. The scaffold with staggered filaments compressed by deformation at hinge points, which were located at regions of high stress concentration. The staggered scaffold collapsed in a concertina manner by a slight bending of the filaments, which resulted in lower stiffness for the staggered scaffold compared to the lattice scaffold with a continuous column of filaments.

Schipani et al. (2020) investigated the effect of 3D printed scaffold geometry on the mechanical properties using the FE method. The results indicate that scaffolds with compressive modulus spanning from the kPa to the MPa range can be obtained by varying filament diameter, spacing and laydown pattern. The FE method combined with 3D printing represents a powerful approach to produce scaffolds that mimic the mechanical properties of a broad range of biological tissues.

The application of FE modelling for the analysis of scaffold mechanical properties under fluid dynamic environment has been evaluated. Olivares et al. (2009) proposed various scaffold structures, including gyroid and hexagonal scaffolds with 55% and 70% porosity as well as gyroid scaffolds with porosity gradient at longitudinal and radial directions. They studied the effect of fluid shear stress distribution on the scaffolds under an inlet fluid flow velocity at 0.1 mm/s using the FE method. The simulation results were analysed using the mechano-regulation theory. The results indicated that the distribution of shear stress induced by fluid perfusion was dependent on the pore distribution within the scaffold. The differentiation process in these scaffold structures was more sensitive to the inlet fluid flow than the compressive strain. Other studies applied FE modelling and in vitro experiments together to investigate the fluid shear stress generated on scaffolds for MSCs differentiation. Melchels et al. (2011) simulated the fluid shear stress within uniform gyroid scaffolds in a perfusing fluid and compared the simulation results with the in vitro experimental results. They fabricated a photo-polymerizable poly-D, L-lactic acid scaffold with 62% porosity using 3D printing and seeded the scaffold with human articular chondrocytes. The results revealed that the highest cell density appeared in the region of the scaffold where the wall shear stress of the fluid flow was the highest (3.8×10^{-3} Pa). Grayson et al. (2010) modelled the flow patterns to determine the relationship between interstitial flow and tissue development. A comparison of mathematical modelling results with in vitro experimental data indicated that the density and architecture of the bone matrix were related to the intensity and pattern of the interstitial flow.

2.8 Challenges and future perspective

This chapter summarises the gradient characteristics of OC tissue from the superficial zone of cartilage to the subchondral bone in terms of biochemical composition, structure, and mechanical properties. The application of tissue engineering and the development of tissue scaffolds to mimic gradient factors for OC repair are discussed. Although most in vitro and in vivo studies yield good results for OC tissue regeneration, longer-term clinical studies did not provide satisfactory results; further studies into tissue scaffolds for OC regeneration are still required. The laboratory studies indicate that a continuous gradient scaffold is more promising than a discrete gradient scaffold since it can mimic the OC tissue structure without abrupt changes between layers; studies of continuous gradient scaffolds for OC repair are currently underway.

Conventional fabrication methods such as solvent-casting, gas forming, freeze-drying, and electrospinning have been used to fabricate tissue scaffolds due to the compatibility of these methods with a wide range of materials, control over scaffold pore size, control over porosity, and low cost. Various 3D printing methods such as solid, powder and liquid-based methods have been used for tissue scaffold processing since they provide a high degree of control over pore geometry and enable processing of highly interconnected pore structures. One of the limitations associated with the use of 3D printing for tissue regeneration is the absence of appropriate materials for the processing of scaffolds. New synthetic or composite materials with non-toxic, biodegradable, chondrogenic, and osteogenic characteristics are required to produce OC tissue. Although DIW printing has been used to create tissue scaffolds, the most applied materials are hydrogel-based and the application of synthetic polymer-based material is relatively limited (particularly hydrophobic based polymer due to they are not water-soluble). The existed researches about DIW printing with hydrophobic based polymers do not have systematical investigation of the ink properties and the fabrication process. Thus, optimisation of the DIW printing process for hydrophobic based polymer scaffold fabrication is needed.

Scaffolds can provide mechanical support for tissue differentiation and generation. However, there are few studies that examine the influence of scaffold pore geometry on tissue generation. Since the collagen fibres within OC tissue have different orientations, an investigation of the relationship between tissue regeneration and filament orientation within 3D scaffolds may facilitate the development of an ideal gradient scaffold for OC tissue repair. The combination of FE simulation and 3D printing brings an important perspective to OC tissue scaffold development. Using the FE modelling is a low-cost and efficient approach for the investigation of the relationship between scaffold structure, mechanical property and tissue regeneration.

Chapter 3

Simulation and experiment details

Overview

This chapter introduces the methods of simulative and experimental details. In the section of simulation details, the computational aid design (CAD) scaffold structures with various porosity and pore shape were designed. The finite element simulation setting up were conducted to analyse the mechanical property of those CAD scaffold structures.

In the section of experimental details, the polycaprolactone/ polyethylene oxide and polycaprolactone/ polyethylene oxide/ hydroxyapatite-based inks were formulated for the scaffold fabrication using direct ink writing (DIW) technique. The ink rheology behaviour and DIW fabrication process were investigated. Thermogravimetric analysis and differential scanning calorimetry were applied to investigate the material thermal property. The material characterisations, i.e. fourier-transform infrared spectroscopy, powder X-ray diffraction analysis, X-ray photoelectron spectroscopy, were conducted to analyse the DIW printed scaffolds. Microscopy images and scanning electron microscopy were used to evaluate the macro and microstructure of the printed scaffolds. The roughness of the printed scaffold surface was also compared. The analysis of contact angle test was used to assess

the scaffold surface wettability. The compressive test was introduced to investigate the influence of material compositions and pore geometries on the mechanical property of the printed scaffolds. Anti-inflammation model drug (i.e. vancomycin) was loaded into the formulated ink for scaffold fabrication. The drug dissolution test profile was applied to investigate the influence of drug concentration on drug release profile. Agar diffusion experiment was conducted to assess the anti-bacteria property of the DIW printed scaffolds.

3.1 Simulation details

3.1.1 Design of the scaffold structure

Two types of scaffolds were designed: the first type is a cubic layered lattice structure with a single lay-down angle. The second type is a complex structure by assembling sections of different lay-down angles.

• Single lay-down angle

The woodpile scaffold was designed as a cubic layered structure, based on the design criteria in the literature (Hulbert et al., 1970; Van Bael et al., 2012). The design criteria are also consistent with the DIW fabrication process, in which the scaffold is printed in a layer-by-layer manner. Each layer of the scaffold is of a square shape and has a lattice structure as shown in Figure 3.1. The entire 3D lattice scaffold forms a porous structure. The edge length of the cubic scaffold is 9 mm ($D_1 = D_2 = H = 9$ mm).

The geometric properties of the lattice scaffold are defined as follows. The scaffold pore size in the XY plane is the inter-filament spacing d_{xy}, i.e. the distance between two adjacent filaments on the same layer, where the filament diameter is d. The scaffold pore size d_z in the direction perpendicular to the XY plane is the distance between two layers of filaments with the same orientation. The layer overlap f refers to the overlapping distance between two adjacent layers. For each layer, the filaments are placed in a parallel arrangement (i.e. they are all arranged in one

direction); the filament orientations between adjacent layers are different in order to form a lattice structure. The angle formed by the two filament orientations between adjacent layers is defined as the lay-down angle (viewed from the XY plane); it is measured with respect to the X direction. Six different lay-down angles, ranging from 15° to 90° (Figure 3.1), are investigated. More specifically, the effects of pore geometry are investigated from two aspects: (a) the porosity, which can be modified by changing the filament diameter d, inter-filament spacing d_{xy} within the same layer, and the layer overlap f between layers, as well as (b) the pore shape, which can be modified by varying the lay-down angle from 15° to 90°.

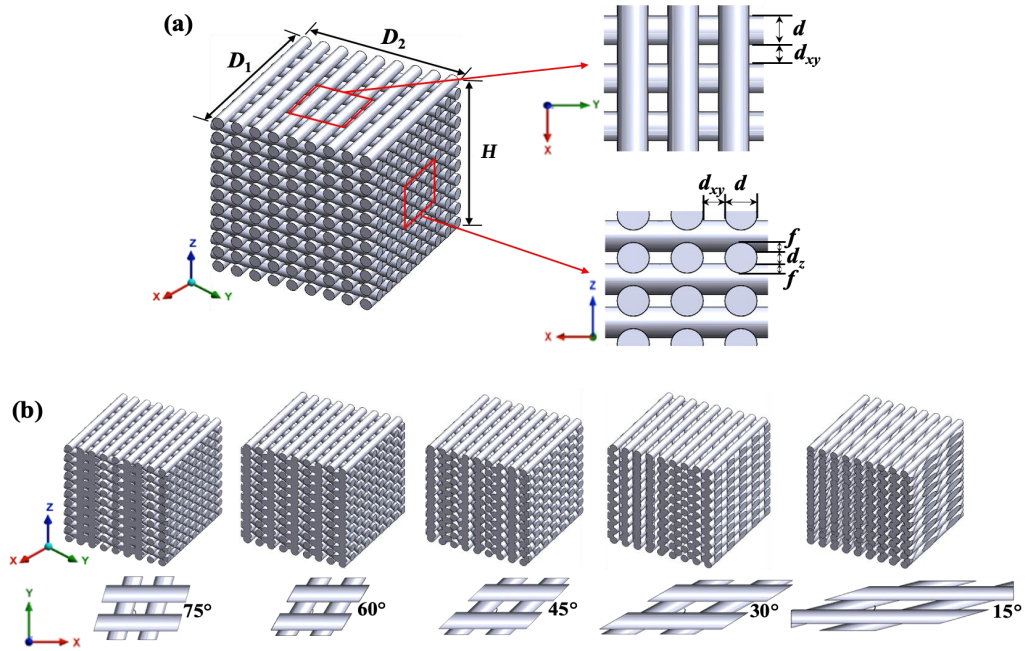

Figure 3.1: (a) A 3D woodpile scaffold with a lay-down angel of 90° and local views to demonstrate the design parameters; (b) Various lay-down angles and associated unit cells in the XY plane.

- **Multiple lay-down angles**

Osteochondral (OC) tissue, one type of natural interfacial tissue, covering the joint surface has a transition from hard bone tissue to soft cartilage; this structure exhibits hierarchical/gradient mechanical characteristics (Dorcemus and Nukavarapu, 2014). A tissue scaffold for the treatment of OC lesion needs to pierce into the hard bone and be in contact with both cartilage and bone; as such, it should mimic the

gradient mechanical properties from cartilage to a transition zone of calcified cartilage and further to bone (Vacanti and Langer, 1999; Hutmacher and Cool, 2007; Reichert et al., 2011). Thus, it is better to achieve the required mechanical properties of the natural OC tissue in a single scaffold construct; benefits of this approach include easier implantation and lower cost in terms of design and fabrication. For this objective, a complex scaffold structure was created by assembling six sections of layered lattices; each section has a single lay-down angle of 15°, 30°, 45°, 60°, 75°, and 90°, respectively (Figure 3.2). All the sections have the same number of layers (i.e. equal height in the longitudinal Z direction). The overall height of the model is 15.34 mm. The cross-section (XY plane) of the scaffold is a square (9 mm $\times$ 9 mm) and remain the same in the Z direction. Other design parameters, including the filament diameter (600 µm), inter-filament spacing (400 µm) and layer overlap (180 µm), remain constant throughout the entire scaffold.

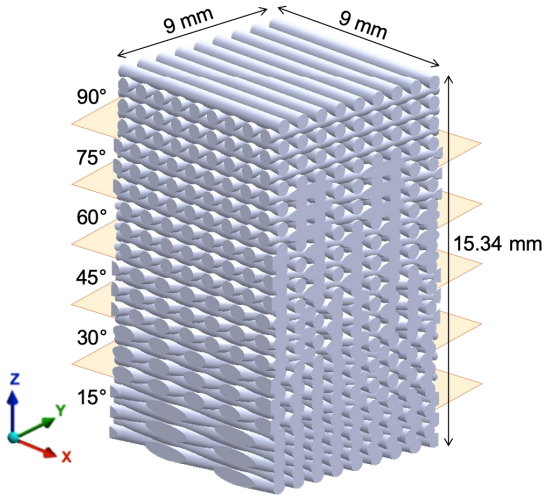

Figure 3.2: A complex scaffold structure assembled by six sections of different lay-down angles in a single construct; each section has same layers.

3.1.2 Finite element model

Finite element simulations were conducted to investigate the effects of pore geometry on Young's modulus (i.e. the apparent elastic modulus of the scaffold), compressive strength, and strain distributions in the lattice scaffolds. All the models

used in finite element modelling are discretised by linear tetrahedral elements. The numerical compression tests are implemented by displacement-controlled boundary conditions. The setup of a compression test in the vertical direction is shown in Figure 3.3. The scaffold specimen is placed between two rigid plates. The bottom plate is fixed; a displacement-controlled boundary condition is applied at the top plate to represent the compressive loading condition. A bonded contact model is applied between the specimen and the loading plates (i.e. no sliding or separation is allowed). The displacement rate is 1 mm/ min, which is a typical quasi-static loading rate for bone and biomaterial testing (Brynk et al., 2011; Luczynski et al., 2013; Feng et al., 2018; Shuai et al., 2020a). The final displacement is set as an equivalent vertical strain of 0.5% in the specimen, which is within the range of elastic deformation for this composite material.

In terms of material properties, the loading plates are assumed to be rigid; as such, the material properties are irrelevant. The material for scaffolds is polycaprolactone (PCL)/nanohydroxyapatite (HAp) composite. For simplicity, a linear elastic isotropic model is used in the simulations. The value of Young's modulus (40 MPa) of the PCL/HAp bulk material is obtained from mechanical compression tests of cylindrical specimens. The corresponding stress-strain curve is in Appendix A.1. It is worth mentioning that other studies (Luczynski et al., 2012, 2013) obtained different values of Young's modulus for similar scaffolds but made of different bulk materials (Poly-L-lactic acid (PLLA)/tri-calcium phosphate (TCP) composite). However, the absolute value of material Young's modulus does not affect the correlation between mechanical properties of scaffolds and structural differences. Poisson's ratio is set as 0.3 (Van Rietbergen et al., 1999; Eshraghi and Das, 2010). The PCL/HAp bulk material is assumed to be homogeneous. All the simulations were conducted using ANSYS Workbench 17.0 (ANSYS, Inc., Canonsburg, Pennsylvania, USA).

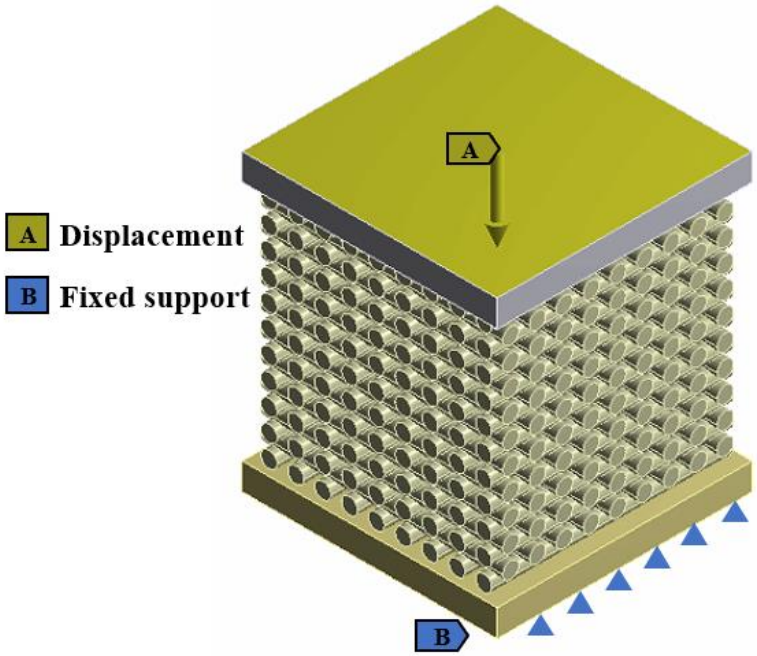

Figure 3.3: Setup for the finite element simulations. An example of compressive loading in the vertical direction is shown. The bottom plate is fixed, and the top plate moves downwards in the vertical direction.

3.2 Experimental details

3.2.1 Ink Materials

Polycaprolactone (PCL; average Mn$\sim$80,000 and density, $\rho = 1.145\ \mathrm{g\,cm^{-3}}$) and polyethylene oxide (PEO; average Mn$\sim$200,000 and $\rho = 1.210\ \mathrm{g\,cm^{-3}}$) were purchased from Sigma-Aldrich (St. Louis, Missouri, USA). Dichloromethane (DCM; stabilised with 0.002% of 2-methyl-2-butene), acetone (ACE), 2-butoxyethanol (2-Bu), and dibutyl phthalate (DBP) were obtained from VWR International Ltd (Radnor, Pennsylvania, USA). Hydroxyapatite (HAp) nanoparticles with particle size less than 40 nm was purchased from SkySpring nanomaterials, Inc (Houston, Texas, USA). All materials were used as received.

3.2.2 Ink formulation procedure

3.2.2.1 Polycaprolactone / polyethylene oxide-based inks

After a preliminary screening of printability for a series of solvents, DCM and ACE were selected for the ink formulations. The polymer concentrations were narrowed down to 7.5% w/w and 15% w/w for the low (L) and high (H) end of the processable range. The PCL inks were prepared by dissolving PCL granules in DCM (D) or ACE (A) at 200 rpm under gentle magnetic stirring at 35°C for 2 h. The DCM-based inks were coded as *L_D_PCL* and *H_D_PCL*, respectively; the ACE-based inks were named as *L_A_PCL*, and *H_A_PCL*, respectively.

PCL/PEO inks were formed by adding PEO to the PCL solutions under stirring conditions of 200 rpm at 35°C for 3 h. For filament formation during extrusion, the formulated inks must be neither too free-flowing nor too viscous. Therefore, only the 1:1 weight ratio of PCL:PEO was chosen for further study. The PCL/PEO inks were designated as *L_D_PCL/PEO* and *H_D_PCL/PEO* for DCM solvent-based systems; *L_A_PCL/PEO* and *H_A_PCL/PEO* refer to the ACE solvent-based systems, respectively.

3.2.2.2 Polycaprolactone/ polyethylene oxide/ hydroxyapatite-based inks

PCL/PEO/HAp-based inks were formulated by dissolve materials into trisolvent mixtures - DCM as an evaporator, 2-Bu as a surfactant and DBP as a plasticiser. Inks were prepared with the aid of manual dispensing assessment after a series of trials and errors. The inks were formulated by dissolving PCL in the DCM, 2Bu, and DBP (2:1:1) mixed solvent with 7.5–15% w/w concentration by gently magnetic stirring at 200 rpm for 2 h at the 35°C temperature. After PCL fully dissolved in the DCM/2Bu/DBP mixed solvent, PEO was added in the PCL solutions with a weight ratio of 0.5–2 to the mixture under a stirring condition for 3 h. Considering the formulated inks cannot be either too liquid or too viscous for the filament formation, the weight ratio of PCL/PEO as 1:1 was finally chosen for the experiment. After that, HAp nanoparticles were gradually added to the polymeric solution with

the weight ratio of 55, 65, 75, and 85% and stirring for 8h at the 35°C temperature to obtain the homogenous solution. Those formulated inks with the HAp concentrations as 55%, 65%, 75%, and 85% w/w were named as *PCL/PEO/55%HAp*, *PCL/PEO/65%HAp*, *PCL/PEO/75%HAp*, and *PCL/PEO/85%HAp*, respectively.

The inks with drug loading were prepared by gradually adding vancomycin (VAN) into the PCL/PEO/HAp solution with low and high concentrations of 3% and 9% w/w and stirring for 4 h at the 35°C temperature to obtain the homogenous solution. The PCL/PEO/HAp composite and drug concentrations are listed in Table 3.1. The formulated inks with the VAN concentrations as 3% and 9% w/w were named corresponding as *PCL/PEO/HAp_3%VAN* and *PCL/PEO/HAp_9%VAN*, respectively.

Table 3.1: The material composition of samples with and without VAN loading.

Scaffold names	HAp conc. (w/w)	VAN conc. (w/w)
PCL/PEO/55%HAp	55%	0
PCL/PEO/65%HAp	65%	0
PCL/PEO/75%HAp	75%	0
PCL/PEO/85%HAp	85%	0
PCL/PEO/HAp_3%VAN	65%	3%
PCL/PEO/HAp_9%VAN	65%	9%

3.2.3 Ink characterisation

3.2.3.1 Polycaprolactone/polyethylene oxide-based inks

The manual dispensing test of PCL/PEO-based inks is shown in Figure 3.4. For each ink sample, a 24 gauge (G) nozzle tip of 20 mm length was attached to the end of the 3 mL syringe. The pressure was manually placed on the plunger until the material extruded and the images were captured by the camera (Canon EOS M50, Canon, Melville, Los Angeles, USA). The rheological properties of the formulated inks were measured using the MCR301 rheometer (Anton Paar, Ostfildern, Germany) with a 25 mm plate-plate (0.5 mm distance) and a solvent trap to minimise solvent evaporation. All the measurements were performed at 25°C and conducted

in triplicate using approximately 0.5 mL of ink. Continuous flow ramps were conducted by varying the shear rate logarithmically from 0.01–100 s^{-1}. To determine the linear viscoelastic region, an oscillatory stress sweep test was performed over the strain range (from 0.01 to 100%). To evaluate the yield stress of the tested samples at a constant frequency of 1 Hz, the stress applied increased from 0.1 Pa until the material yielded. To simulate 3D printing conditions, a creep recovery test was carried out using three intervals. In the rest interval, a low shear rate (1 s^{-1}) was applied for 10 s. Then, a constant high rate (200 s^{-1}) was applied for 1 s. The recovery interval was carried out with a shear rate of 1 s^{-1} for 90 s. The viscosity recovery percentage at the 90 s was calculated by comparing the viscosity to the initial viscosity at the rest interval (10 s).

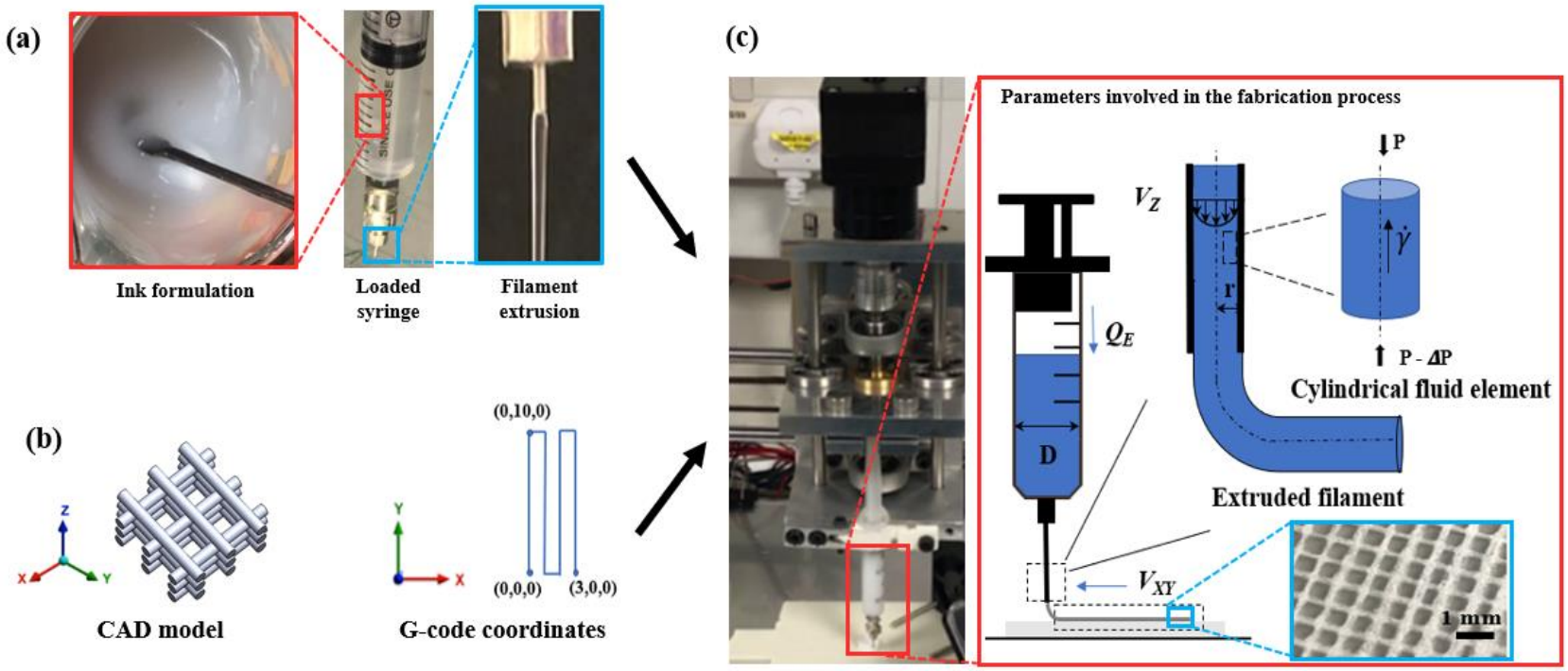

Figure 3.4: Desktop DIW printer and flow chart of the PCL/PEO-based scaffold fabrication process. (a) Material preparation system - inks were formulated to investigate the manual dispensing and ink rheological behaviour. (b) Data processing system-suitable G-code was developed based on the predesigned CAD model. (c) Computer control system-the construct was printed after the investigations of the printing process parameters, including the extruded fluid rate (Q_E) and printing speed on the XY plane (V_{xy}).

3.2.3.2 Polycaprolactone / polyethylene oxide/ hydroxyapatite-based inks

20 G nozzle tip with 20 mm in length were attached to the 3 mL syringe. During the manual dispensing test, inks were consistently extruded under the manual pressure on the plunger and the process was recorded by the Canon EOS M50 camera. The rheological measurements of the formulated inks were measured at 21°C using a Discovery Hybrid Rheometer (DHR-3, TA Instruments, New Castle, Delaware, USA) with a 25 mm plate-plate (0.5 mm distance) and a solvent trap to prevent solvent evaporation during the measurement. 0.5 mL inks were extruded on the plate, and five replicates were taken for each measurement. Considering reducing the influence of the solvents evaporation on the rheological testing results, continuous flow ramps were performed by varying the shear rate logarithmically from 0.1 to 50 s^{-1}. To simulate the 3D printing conditions, the creep recovery test was carried out to characterise the ink recovery behaviour using three intervals - by applying a shear rate 0.1 s^{-1} for 70 s, followed by a high shear rate at 50 s^{-1} for 130 s and then the recovery interval was carried out with a shear rate of 0.1 s^{-1} for 100 s. The ink recovery percentage was calculated by dividing the viscosity at 300 s (after the high shear rate) to the initial viscosity at the rest interval (100 s).

3.2.4 Mathematical model

The DIW operation parameters were studied, as shown in Figure 3.4 (c), including the printing speed on the XY plane (V_{xy}) and ink velocity on Z-axis (V_z), and the extruded fluid rate (Q_E). According to the power law fluid model, the velocity profile along a nozzle tube on the Z-axis is given by Equation 3.1 (Morrison et al., 2001):

$$V_z = \left(\frac{d}{2}\right)^{1+\frac{1}{n}} \left(\frac{\Delta P}{2mh}\right)^{\frac{1}{n}} \left(\frac{n}{n+1}\right) \left[1 - \left(\frac{2r}{d}\right)^{1+\frac{1}{n}}\right] \tag{3.1}$$

where ΔP is the extrusion pressure-the pressure difference between the inlet and outlet of the nozzle tip, r is the radial coordinate, and d and h are the nozzle tip diameter and printed length, respectively.m and n can be obtained by fitting the viscosity curve with the power law model. m is the consistency index, which is

associated with the magnitude of the viscosity, while, the term n is the power law index, defines the viscosity behaviour. The extrusion flow rate Q_E and the generated shear rate ($\dot{\gamma}$) are defined by Equation 3.2 (Morrison et al., 2001) and Equation 3.3 (Macosko and Larson, 1994; Dávila and d'Ávila, 2019):

$$Q_E = \left(\frac{\Delta P d}{4mh}\right)^{\frac{1}{n}} \left[\frac{n\pi d^3}{8(3n+1)}\right] \tag{3.2}$$

$$\left.\frac{\mathrm{d}V_z}{\mathrm{d}d_r}\right|_{\frac{d}{2}} = \dot{\gamma} = \left(\frac{32Q_E}{\pi d^3}\right)\left(\frac{3}{4}+\frac{1}{4n}\right) \tag{3.3}$$

The nozzle tip diameter influences the shear rate. When the extrusion flow rate Q_E is fixed, small nozzle tip diameter requires a higher pressure to dispense the material. If the nozzle diameter d is fixed, the wall shear rate increases with the extrusion flow rate. In this study, the extrusion flow rates were set to resemble the DIW printing process, and the relationship between the solvent selection and the DIW printing parameters were investigated.

3.2.5 3D scaffold fabrication using DIW

3.2.5.1 Polycaprolactone / polyethylene oxide-based scaffold

A five-layer woodpile construct was designed using CAD software (SolidWorks 2005, Dassault Systèmes SolidWorks, Vélizy-Villacoublay, France). Each layer comprising parallel filaments with the width of 311 μm , which is equivalent to the 24 G nozzle diameter. In Figure 3.4 b, the subsequent layers were stacked at 90° in the transverse plane to the prior level. G-codes of the designs were written using MATLAB in accordance with the CAD models, which gave instructions to the printer and controlled the relative positions of the work stage and nozzles in the X, Y, and Z directions as well as the extrusion rates.

The desktop DIW printer used for PCL/PEO scaffold fabrication was modified from a commercial fused deposition modelling (FDM) printer (Prusa i3, Prusa Research, Prague, Czech Republic). The filament print head was replaced with a

customised syringe-based extruder. Figure 3.4 c describes the processes involved in DIW technology. The motion system comprises a print bed and a nozzle. The print bed moves in the Y direction, and the nozzle moves in X and Z directions. Linear actuator stepping motors drive the motion in the Z direction and control the piston with an resolution of 0.001 mm/step and a 1.8° step angle. A 3 mL syringe was used for the extrusion, and the extruded volume resolution was 6×10^{-5} mL/step.

A continuous and consistent extrusion of polymer inks is of great importance during the DIW printing process. The filament extrusion can be affected by the ink rheological behaviour and printing parameters (i.e. printing speed V_{xy} and extrusion rate Q_E). To optimise the DIW printing parameters, the flow rate Q_E of 0.48 to 1.44 mm^3/s and printing speed V_{xy} in the range from 2.5 to 12.5 mm/s were set using Pronterface software (https://pronterface.com). A glass slide was used as a collecting substrate for printing, and the print samples were easily taken off from the substrate after drying.

3.2.5.2 Polycaprolactone / polyethylene oxide/ hydroxyapatite-based scaffold

Woodpile single lay-down angles scaffolds were designed using CAD software and the dimension of the cuboid scaffold is (D_1 x D_2 x H_1 = 14 x 14 x 5 mm^3), as shown in Figure 3.5 b. Each layer comprising parallel filaments with the width of 603 µm. The angle formed by the two filament orientations between adjacent layers is defined as the lay-down angle (viewed the unit cells in the XY plane in Figure 3.1). Three different lay-down angles, ranging from 90° to 45°, were investigated. G-codes of the designs were written using MATLAB in accordance with the designed CAD models.

As mentioned in section 3.3.1, woodpile multiple lay-down angles scaffold structure was designed by assembling three sections of layered lattices. Each section has a single lay-down angle of 45°, 60°, and 90°, respectively. All the sections have the same number of layers (i.e. equal four in the longitudinal Z direction). The overall dimension, the filament diameter, pore width, and layer overlap of multiple lay-down angles scaffold, remain same as the single lay-down angles scaffolds.

The theoretical porosity was calculated as from the percentage of the scaffold solid volume (V_{solid}) to the total volume (V_{total}) of the scaffold using Equations 3.4 and 3.5:

$$Porosity = 1 - \frac{V_{solid}}{V_{total}} \tag{3.4}$$

$$V_{total} = D_1 D_2 H_1 \tag{3.5}$$

where D_1, D_2 are edge length of scaffold and H_1 is the scaffold height. The solid volume (V_{solid}) was obtained from Solidworks software using the 'Mass Property' function. Figure 3.5 shows the flow chart of the DIW printing procedure. The R3bel 3D bioprinter (SE3D, Santa Clara, California, United States), a piston extrusion-based printer, was applied to fabricate the scaffolds. There are three subsystems in the DIW fabrication system, which are the data processing system, material preparation system, and computer control system. In data processing system, G-codes of the designs were generated using MATLAB in accordance with the predesigned CAD models. G-code was developed to control the relative positions of the work stage and nozzle to carry out the developed ink extrusion process forming a 3D scaffold layer by layer.

The continuity and consistency of the PCL/PEO/HAp composite inks extruding process are of great importance during the DIW printing process. The extruding process can be affected by the ink rheology behaviour and configuration of operation parameters. The motion system comprises the work stage and nozzle - the work stage moves in the Y direction, and the nozzle is moving in X and Z directions. Stepping motors drive the motion along the X, Y, Z direction with an resolution of 0.001 mm/step. A 3 mL syringe is used to carry out the extrusion. Glass slide was put on the workbench before extrusion, enabling a smooth and flat surface, and the scaffolds were taken off from glass slides after fully drying. Similar to the discussion of PCL/PEO inks, the extrusion of the PCL/PEO/HAp composite inks can be affected by the ink rheology behaviours and fabrication parameters. To optimise the DIW printing parameters, the flow rate Q_E of 0.8 to 2.4 mm^3/s and printing speed V_{xy} in the range from 2.5 to 12.5 mm/s were set using Pronterface open-source software.

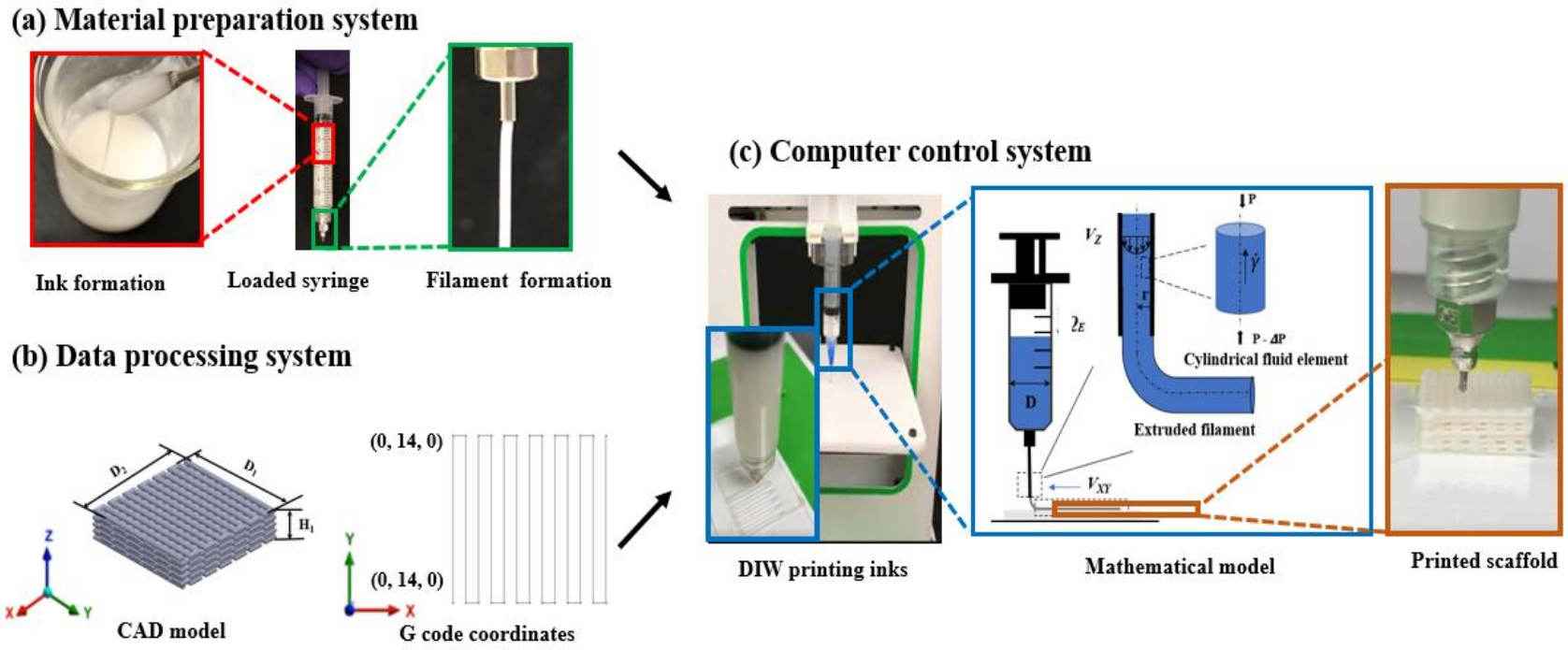

Figure 3.5: Schematic of DIW printing the PCL/PEO/HAp scaffolds. (a) Material preparation system - inks were formulated to investigate the manual dispensing and ink rheological behaviour. (b) Data processing system - G-codes were developed based on the predesigned CAD models. (c) Computer control system - the investigation of ink properties within the nozzle using mathematical model; the scaffolds were printed out after optimising the printing process parameters.

3.2.6 Physicochemical characterisation analysis

3.2.6.1 Fourier-transform infrared spectroscopy

The chemical analysis, looking into the compound of those DIW printed scaffolds and materials, was performed using a Perkin Elmer 2000 Fourier transform infrared (FTIR) spectrophotometer (Perkin Elmer 2000, PerkinElmer, Inc., Waltham, Massachusetts, USA). The pure PCL, PEO, HAp, and DIW printed PCL/PEO and PCL/PEO/HAp-based scaffolds were pressed into disks for FTIR analysis. The spectra were collected over a wavenumber range of 500–4000 cm^{-1}.

3.2.6.2 Powder X-ray diffraction

The crystal structure and phases of the pure materials and DIW printed scaffolds were characterised by powder X-ray diffraction (PXRD) equipment (Siemens D5005, Karlsruhe, Germany). The samples were scanned with a monochromatic CuK radiation (wavelength =1.54056 Å) from a 2θ angle of 15° to 60°, with a scan speed of 2°/min. The scan step was maintained at 0.02° and the collected data were analysed.

3.2.6.3 X-ray Photoelectron Spectroscopy

The chemical bonding states and atomic concentrations in the printed samples were examined to compare the electron binding energy intervals by X-ray Photoelectron Spectroscopy (XPS) equipment (Phoibos 150 analyser, Berlin, Germany). The peak position and atomic concentration of elements (At%) were obtained, and the ratio of oxygen and carbon (O/C) was calculated for quantitative comparison. Each sample was analysed in duplicate and the average was compared.

3.2.7 Surface morphology and property

3.2.7.1 Scanning Electron Microscopy

The surface morphology of the printed samples was observed using a S-3200N (Hitachi, Tokyo, Japan) scanning electron microscope (SEM). The samples were

first sputter-coated with a thin layer of gold (10 nm), and the images were obtained at an acceleration voltage of 5 kV from low to high magnifications (×500 to 10k).

3.2.7.2 Roughness

The surface roughness of the samples was quantified using a profilometer (Keyence VHX 2000, Osaka, Japan). The roughness was measured over an area of 600 µm (length) x 60 µm (width) on the three different filaments on the sample surface. The surface roughness in terms of an arithmetic average (*Ra*) was obtained as a function of the printing conditions.

3.2.7.3 Wettability

Contact angle measurements were performed to evaluate the wettability of the DIW printed surface. A sessile drop method was used to measure the contact angle by depositing ultrapure water on the surfaces of the printed filament using an optical contact angle meter (OCA 15EC; Dataphysics Instruments GmbH, Filderstadt, Germany). To capture the water contact angle on the surface of the single filament, the water droplet volume for the PCL/PEO scaffold was 4×10^{-4} µL and for the PCL/PEO/HAp scaffold was 4×10^{-3} µL. All the measurements were performed at 21°C, and the gradual change of water contact angle was captured with a digital camera at three different places on each sample.

3.2.8 Thermal analysis

The thermal properties of raw polymers and printed scaffolds were characterised with thermogravimetric analysis (TGA) and differential scanning calorimetry (DSC). The model used for TGA and DSC was Hi-Res 2950 and Q1000, respectively, both from TA Instruments (New Castle, Delaware, USA). The tests were conducted after leaving the scaffolds at ambient temperature for 12 h post-printing. TA Universal Analysis 2000 was performed to analyse the collected data. Each sample was analysed in duplicate and the mean value was used to represent the data.

3.2.8.1 Thermogravimetric analysis

For TGA, an open aluminium pan was tared prior to placing the samples in the range of 5–10 mg. All the samples were heated from 30°C to 400°C with a ramp of 10°C/min, and purged under a flux of nitrogen gas. The percentage of weight losses and onset thermal degradation temperatures (T_d) were recorded from the obtained TGA traces.

3.2.8.2 Differential scanning calorimetry

DSC was performed to acquire the peak melting temperatures (T_m) and enthalpies of fusion (ΔH_f) of the raw polymers and printed scaffolds. 5–10 mg of the samples were individually placed in an aluminium DSC pan which was then sealed using a lid with a pin-hole punched through. All samples were equilibrated at 0°C and then heated at a rate of 2°C/min to the desired temperatures. Nitrogen purge gas with a flow rate of 50 µL/min was used throughout the experiments.

3.2.9 DIW printed scaffold evaluation

3.2.9.1 Shape fidelity analysis

A stereomicroscope (SM-3TZZ-54S-10M; AmScope, Irvine, California, USA) was used to observe the DIW printed 2D and 3D patterns. The width of printed filament was quantified by measuring 50 filaments in Image J software (http://rsb.info.nih.gov/ij/); the data was exported for analysis, and the statistical distributions were plotted using Origin software (Origin Lab, Northampton, Massachusetts, USA). The results were presented as the mean ± standard deviation. An index of relative filament deviation ($\sigma_{filament}$) was proposed to evaluate the filament width of DIW printed constructs, it was defined in Equation 3.6:

$$\sigma_{filament} = \frac{W_{filament}}{d} - 1 \tag{3.6}$$

where $W_{filament}$ is the printed filament width and d is the nozzle diameter used. The index of relative filament deviation $\sigma_{filament}$ as a function of the choice of printing parameters was calculated and compared as an assessment of the shape fidelity of printed filaments.

3.2.9.2 Mechanical property analysis

The stress-strain relationships of the DIW printed PCL/PEO/HAp scaffold specimens were tested in uniaxial compression experiments using a universal testing machine - UniVert (CellScale, Waterloo, Canada). Scaffolds with various HAp concentrations (55%–85% w/w) and pore geometries (90°, 60°, 45°, and mixed angle) were tested, and each type of scaffold has four replicates. Before the compression test, the dimensions were measured for samples. In the compression tests, a preload of 1N was applied to each sample, followed by a compression of 1 mm/min. The test was stopped when the load cell reached its rated load of 250 N. The yield point represents the transition from elastic to plastic deformation, was recorded. Elastic modulus of the scaffold samples was calculated from linear region according to ASTM: D695-02a (2002) - the standard test method for compressive properties of rigid plastics with the same method using in literature (Goncalves et al., 2016; Dorj et al., 2013).

3.2.10 Drug loading and release analysis

3.2.10.1 In vitro drug release and release kinetics

Dissolution tests were conducted in a shaking incubator using a KS 3000 i control incubator shaker (IKA, Wilmington, North Carolina, USA) for eight hours. DIW printed scaffolds with vancomycin loaded were weighed before dropping into the preheated glass tubes containing a volume of 100 mL of PBS (pH 7.4). Sink condition was maintained during the drug release period. A constant temperature of 37°C and a rotational speed of 100 rpm has been set throughout the experiments. Samples of 3 mL were taken on time points of 15 min, 30 min, 1 h, 2 h, 4 h, 8 h and each time the same volume of release medium was replaced. The absorbance of collected

samples was measured by UV/VIS spectrophotometry (Cary 4000 UV-Vis, Agilent, Santa Clara, California, USA) at λ = 280 nm, the maximum absorption wavelength of vancomycin. The drug content was calculated according to the calibration curve. Triplicate samples were evaluated for scaffolds loaded with the different amounts of vancomycin, and the mean and standard error for vancomycin concentrations were calculated to generate drug release percentage curves.

3.2.10.2 Agar diffusion test

Agar diffusion test was used to test the antimicrobial activity of the DIW printed samples. The tryptic soy broth, Mueller Hinton agar and phosphate-buffered saline were obtained from VWR (Radnor, Pennsylvania, USA). The microorganisms utilised in the study were acquired from American Type Culture Collection (Manassas, VA, USA); the microorganisms of *Pseudomonas aeruginosa* ATCC 15442 as gram-negative bacteria, and *Staphylococcus aureus* ATCC 6538 as gram-positive bacteria were studied. Cultures were prepared overnight with *Pseudomonas aeruginosa* and *Staphylococcus aureus* in tryptic soy broth. The cultures were pelleted by centrifugation at 4500 rpm for 10 minutes and resuspended in PBS to a cell density of circa 1×10^8 cells mL^{-1}. Sterile swabs were used to inoculate the agar plates with the lawns of the microorganisms. The *Pseudomonas aeruginosa* and *Staphylococcus aureus* lawns were inoculated on Mueller Hinton agar plates for 24 h at 37°C. Inhibition of growth on the plates was evaluated using digital images that were obtained following 24 h of incubation. The assessment was based on the absence or presence of bacterial growth in the contact zone between the agar and the sample and on the eventual appearance of the zone of inhibition which was calculated from Equation 3.7:

$$W_{ZOI} = T - D \tag{3.7}$$

where W_{ZOI} is the width of the clear zone of inhibition in mm, T is the total width of the test specimen and clear zone in mm, and D is the width of the test specimen in mm. Following the standard method, the degree of bacterial growth in the nutrient

medium under the specimen was assessed. The widths of the clear zone of inhibition were quantified by measuring ten times for each sample type in Image J software.

3.2.11 Statistical analysis

All the quantitative data were expressed as the average $\pm$ standard error of the mean. The numerical data were analysed via Student's t-test to determine the differences among the groups. Statistical significance was indicated by (*), which represents a p value < 0.05; (**), which represents a p value < 0.01; and (***), which represents a p value < 0.001. If the p value > 0.05, no difference was noted.

Chapter 4

Finite element evaluations of the mechanical properties of direct ink writing scaffolds: effects of pore geometry

4.1 Introduction

Osteochondral (OC) interfacial tissue is a specialised and integrated structure in the joints between bones in the human body; the interface consists of multiple tissue elements, mainly including cartilage, calcified cartilage, and bone. OC injuries can lead to joint malfunction and ultimately to the development of degenerative diseases such as osteoarthritis (Rodrigues et al., 2011; Mobasheri et al., 2014). OC defects have poor regenerative potential; clinical findings indicate that there is no existing medication to substantially promote the healing process; surgical procedures (e.g. autografts) are normally required for OC tissue repairing (Chiang and Jiang, 2009; Schroeder and Mosheiff, 2011). However, these interventions are limited by the supply of autograft tissue in the human body (Jakob et al., 2002).

To date, tissue engineering approaches have been used to create three-dimensional (3D) porous scaffolds out of biocompatible materials; these porous scaffolds facilitate adhesion, proliferation, differentiation, and migration of cells to facilitate tissue regeneration (Feng et al., 2019; Shuai et al., 2020a). Due to the physiological interfacial transition from cartilage to subchondral bone in natural OC tissue, the most important consideration is that the scaffold features (e.g. pore size and pore shape) should mimic the gradient characteristics to aid nutrient delivery and tissue regeneration, and possess compatible mechanical properties with the host tissue to achieve optimal structural integrity (Athanasiou et al., 1994; Boschetti et al., 2004; Shuai et al., 2020b). Natural OC tissue comprises the cortical bone, the cancellous bone, and the cartilage, which generally become more ductile towards the cartilage region with changed orientation of collagen fibers (Gibson, 1985; Athanasiou et al., 1994; Boschetti et al., 2004; Sophia Fox et al., 2009; Sabree et al., 2015). This complicated structure poses a challenge for scaffold design, especially in terms of mimicking the transition of mechanical properties between different regions (Shuai et al., 2020a).

One method to develop OC tissue scaffolds involves using biphasic, triphasic or multiphasic layers, or gradient structures to mimic the bone and cartilaginous phases of natural OC tissue (Schek et al., 2004). Schaefer et al. (2000) described scaffolds made of polyglycolic acid (PGA), poly-lactic-co-glycolic acid (PLGA) and polyethylene glycol (PEG). Those two constructs were sutured together. Jiang et al. (2010) presented a triphasic scaffold, where the bone phase was based on PLGA and bioactive glass composite; the cartilage phase was created using agarose hydrogel, and the intermediate phase contained a combination of agarose hydrogel, PLGA, and bioactive glass. The three phases were fabricated separately and then pre-integrated as a scaffold using a customised mold.

Previous reseach indicated that biphasic or triphasic scaffolds yielded good repairs of OC defects in vitro or in vivo (Schek et al., 2004; Schaefer et al., 2000; Jiang et al., 2010). However, in most cases, the fabrication of those scaffolds requires joining individual phases together using suturing, glue, or press fitting, which

could result in delamination after transplantation due to insufficient bond strength (Raghunath et al., 2007; Nooeaid et al., 2012). To overcome the problem of delamination and obtain functional gradient in a single construct, Dormer et al. (2010) developed new fabrication methods to produce gradient PLGA scaffolds controlled by a designed program. The in vitro experiments showed increased cell attachment, production of extracellular matrix, glycosaminoglycan, and collagen content, as well as alkaline phosphatase activity of mesenchymal stem cells in gradient scaffolds with pore size increased from 70 to 220 μm in comparison with those having a uniform pore size. However, traditional fabrication methods (e.g. salt leaching, gas forming, and freeze-drying) have limited control of pore geometries, mechanical properties, and interconnectivity. Such limitations may lead to a non-uniform distribution of cells, which can prevent the cells from properly functioning (Wüst et al., 2011; Do et al., 2015).

3D printing has emerged as a new technology in the field of tissue engineering due to its capability to create (a) personalised scaffolds for patients and (b) scaffolds with well-defined porous features Yang et al. (2018). Among many 3D printing methods, direct ink writing (DIW) has been widely used to fabricate tissue scaffolds since this processing approach can be performed at ambient temperature, enabling the incorporation of biomolecule and/or cells (Park et al., 2011; Goncalves et al., 2016; Trachtenberg et al., 2017). Using DIW, the scaffolds can be fabricated according to the design that is specified in CAD models (Athanasiou et al., 1994; Boschetti et al., 2004). Moreover, the scaffold porosity as well as interconnectivity for nutrient delivery and tissue regeneration can be readily modified (Hutmacher and Cool, 2007; Reichert et al., 2011). An example of using DIW to fabricate a polycaprolactone (PCL)/hydroxyapatite (HAp) scaffold based on a CAD model is shown in Figure 4.1. The PCL/HAp ink was formulated by adding nano HAp particles into a PCL solution; the nano HAp particles were prepared in advance by a wet-precipitation method (Huang et al., 2010). The DIW processing approach allows accurate control of the ink extrusion rate and motion of the nozzle by a computer programme.

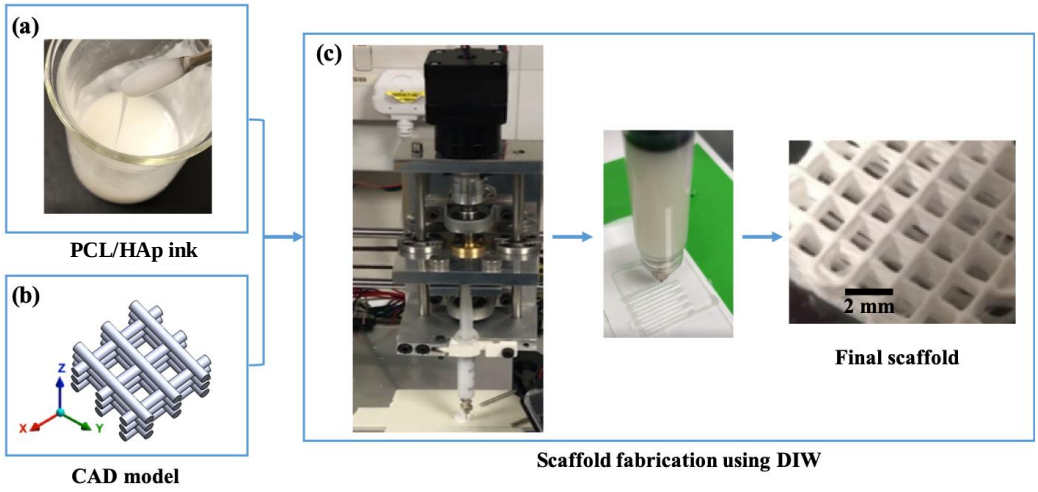

Figure 4.1: Schematic of printing a PCL/HAp scaffold using the DIW technique.

Computational modelling has shown great potential in general biomedical engineering research (Guo et al., 2018; Chen et al., 2018; Guo et al., 2020), such as development of bone scaffolds (Lacroix and Prendergast, 2002; Kaul et al., 2015). It offers a precise and easily adjustable way to compare the mechanical properties of different scaffold designs in a timely and economical manner. Byrne et al. (2007) applied a fully 3D computational modelling approach to simulate tissue differentiation and bone regeneration in scaffolds as a function of porosity, Young's modulus, and dissolution rate. Cahill et al. (2009) used finite element analyses to compare the mechanical properties between 3D printed and CAD designed scaffolds to identify the key factors that affect the mechanical properties of scaffold structures. San Cheong et al. (2018) proposed new finite element algorithms to predict bone ingrowth and model the effect of surface modification on osteoconduction in porous scaffolds. Entezari et al. (2019) developed a simple and efficient computational modelling approach for characterising strain and total strain energy in bond scaffolds.

The finite element method (FEM) is one of the most commonly used numerical methods to simulate the mechanical properties of 3D scaffolds. Sandino et al. (2008) analysed the strain distribution within calcium phosphate scaffolds and biodegradable glass scaffolds. Melchels et al. (2010) designed CAD models with

various structures and evaluated the mechanical properties by simulations of compressive testing. Ali and Sen (2017) analysed the effective elastic modulus, compressive strength, permeability, and fluid flow-induced wall shear stress as functions of porosity. Hendrikson et al. (2017) showed a significant impact of scaffold architecture on mechanical strain distribution. Naghieh et al. (2018) developed both linear and non-linear FE models to predict the elastic modulus of alginate scaffolds. Rodríguez-Montaño et al. (2018) used poroelastic models to investigate the influence of scaffold design parameters on the mechanical response in different load regimes. Wang et al. (2018) evaluated the mechanical properties of porous Ti scaffolds with different pore structures.

Most previous studies focused on the influence of pore size and porosity on the mechanical properties of scaffolds (Lacroix et al., 2006; Diego et al., 2007; Eshraghi and Das, 2010; Naghieh et al., 2016). To the best of the author's knowledge, the effect of pore shape has not been systemically investigated. Hence, the effects of various pore shapes on the mechanical properties of scaffolds are investigated to achieve a gradient of mechanical properties in a single scaffold construct while still maintaining an interconnected pore network. In this chapter, the finite element method is used to evaluate the effects of pore parameters (e.g. porosity and pore shape) on mechanical properties of the scaffolds prior to scaffold fabrication with customised DIW. In addition to the global mechanical properties (e.g. Young's modulus), this study also seeks to understand the local strain distributions in various scaffold structures.It would be helpful for developing scaffold structures with variable inner structures, which can form gradient mechanical properties to mimic the natural interfacial tissue.

4.2 Mesh sensitivity test

The effect of the mesh size on the finite element modelling results was firstly investigated on the scaffold specimens with a lay-down angle of 90° under compressive loading (Figure 3.3). A series of different size meshes are generated for the same

geometry; all the other parameters are identical. The Young's modulus of the scaffold is calculated as an output variable to measure the convergence when the mesh size is decreased. The values of Young's modulus and computational time of different meshes are listed in Table 4.1. The results show that the Young's modulus changes by 12% if the minimum element size is reduced from 0.4 to 0.125 mm; it only changes by 0.7% if the mesh size is further reduced to 0.1 mm. However, using a mesh size of 0.1 mm requires 1.5 times more computational time than using a mesh size of 0.125 mm. Therefore, it is suggested that imposing a minimum edge size of 0.125 mm for the tetrahedral elements generates finite element solutions with good accuracy and an affordable computational time; this mesh size is used in all the simulations.

Table 4.1: Young's modulus and computational time of five different meshes.

	Mesh 1	Mesh 2	Mesh 3	Mesh 4	Mesh 5
Mesh of the 90° lattice scaffold					
Minimum element size (mm)	0.4	0.2	0.15	0.125	0.1
Number of tetrahedral elements	100,701	409,429	889,496	1,379,586	3,047,672
CPU time (min)	25	30	50	80	120
Young's modulus (MPa)	16.2	15.25	14.78	14.2	14.1

4.3 Effects of porosity on Young's modulus

Porosity is an important factor that affects the mechanical properties of scaffolds (Loh and Choong, 2013); it is calculated as the percentage of the void space to the total volume occupied by the outer boundary of the porous scaffold. There are three key parameters that control the porosity of a 3D layered lattice scaffold: the filament diameter d, the inter-filament spacing d_{xy} within the same layer, and the layer overlap f between layers (Figure 3.1). In this section, different combinations of various values for these three parameters are evaluated to create a range of porosities to understand the effects of various porosities on the Young's modulus of scaffolds. All the scaffold specimens simulated in this section have a lay-down angle of 90°.

First, different porosities are achieved by changing the design parameters within the XY plane (parallel to the layers). Nine scaffold specimens with different combinations of filament diameters and inter-filament spacing were created. Three values are chosen for the filament diameter of 600 μm, 400 μm and 300 μm; for each filament diameter, three values of inter-filament spacing are assigned as 400 μm, 700 μm and 1000 μm (Figure 4.2 a). The layer overlap is maintained at a constant value of 180 μm. The filament diameter is fixed at 600 μm, and the inter-filament spacing is fixed at 400 μm; different porosities are obtained by changing the design parameter in the Z direction (perpendicular to the layers). Seven scaffolds were created by varying the layer overlap from 60 to 300 μm (Figure 4.2 b). It can be seen from Figure 4.2 a that the Young's modulus decreases when the filament diameter decreases and the inter-filament spacing increases. This effect can be attributed to the column-like behaviour of filament junctions when undergoing compressive deformation (Domingos et al., 2013). In other words, for a specific area in the XY plane (parallel to the layers), the scaffold with a larger filament diameter or smaller inter-filament spacing has more load-bearing capacity, hence increasing the stiffness of the scaffold. Figure 4.2 b shows that the Young's modulus increases as the layer overlap increases. The overlapping regions between layers provide the main path for load transfer in the Z direction perpendicular to the layers. Therefore, larger overlap means that the layers are more closely bonded, thus making the scaffold structure stiffer.

The porosity values are calculated for the sixteen specimens; the relationship between porosity and Young's modulus is shown in Figure 4.3. The result shows that Young's modulus decreases linearly with increasing scaffold porosity, which is consistent with previous findings for bone (Hellmich et al., 2004) and bone replacement biomaterials (Fritsch et al., 2009, 2010; Kariem et al., 2015). As porosity increases, there are more voids in the lattice structure, making the scaffold less bonded and easier to deform (i.e., lower Young's modulus). Figure 4.3 also shows that the range of Young's modulus values obtained from finite element modelling covers the range of Young's modulus values of natural osteochondral tissue. A porosity value

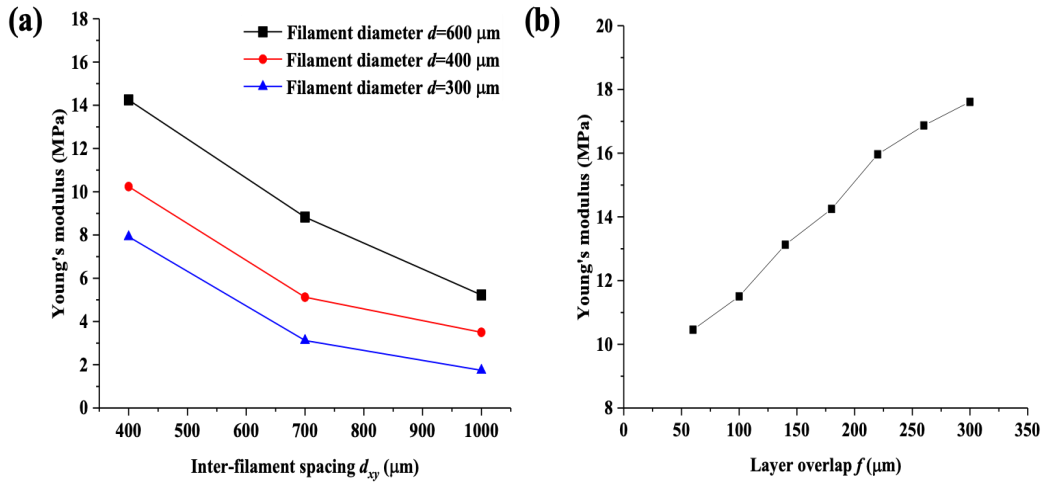

Figure 4.2: (a) Plots of Young's modulus versus the filament diameter and the inter-filament spacing. (b) Young's modulus versus the layer overlap.

of approximately 60% separates the scaffold application between that of cancellous bone repair and that of cartilage repair. By manipulating the parameters used to design the scaffolds, the desired Young's modulus of the scaffold can be customised to match specific osteochondral tissue.

Filament diameter d (µm)	Inter-filament spacing d_{xy} (µm)	Layer overlap f (µm)	Symbol
600	1000	180	
600	700	180	
600	400	180	
400	1000	120	
400	700	120	
400	400	120	
300	1000	90	
300	700	90	
300	400	90	
600	400	300	
600	400	260	
600	400	220	
600	400	180	
600	400	140	
600	400	100	
600	400	60	

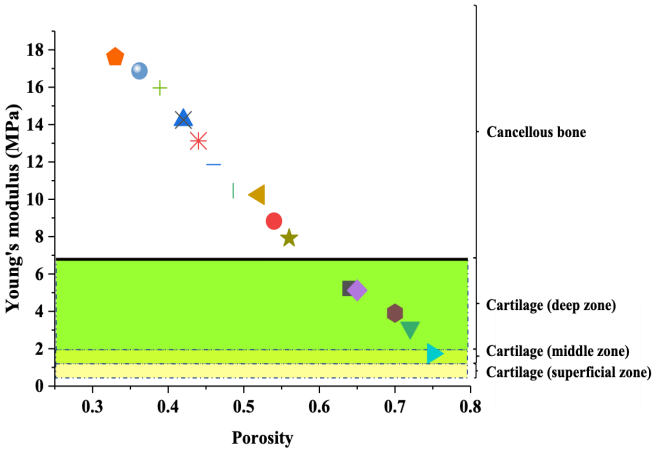

Figure 4.3: Plot of Young's modulus versus porosity.

4.4 Effects of pore shape

The pore shape is characterised by the lay-down angle in the layered scaffold. The focus here is to analyse the correlation between the lay-down angle and the anisotropic property of scaffolds from two perspectives. First, six cubic scaffold specimens were created with a single lay-down angle of 15°, 30°, 45°, 60°, 75°, and 90°, respectively; each layer of all scaffolds has the same number of filaments. The only difference between these scaffolds is the lay-down angle; the other parameters, including the filament diameter (600 μm), inter-filament spacing (400 μm) and layer overlap (180 μm), remain constant. All the specimens have a similar porosity (42%). The anisotropic property is analysed by the difference in Young's modulus when the cubic scaffolds are compressed in three orthogonal directions, respectively, by finite element modelling. Second, a complex layered lattice scaffold was created by assembling six sections with different lay-down angles (15°, 30°, 45°, 60°, 75°, and 90°) in a single construct. The anisotropic property is analysed by the difference in the local strain distributions when the scaffold is simulated under compression loading conditions.

4.4.1 Single lay-down angle

Six cubic scaffold specimens with a single lay-down angle of 15°, 30°, 45°, 60°, 75°, and 90° were compressed in X, Y and Z directions, respectively, using displacement-controlled boundary conditions. Here the Z direction is named as the longitudinal direction because it is perpendicular to the filament layers; the other two directions (X and Y) in the Cartesian coordinate system are named the transverse directions, which are parallel to the filament layers. The lay-down angle is defined with respect to the X direction.

The mechanical properties of scaffolds are normally characterised by stiffness (Young's modulus) and compressive strength (Rezwan et al., 2006; Chen et al., 2011b; Feng et al., 2014; Shuai et al., 2017, 2018), which are presented in Figure 4.4. In the longitudinal Z direction, the Young's modulus slightly decreases

at lower lay-down angles. Filaments with a smaller lay-down angle have more asymmetric alignment of the connecting joints in the Z direction, which affects their force resistance. Hence, under compression in the Z direction, filaments with smaller lay-down angles can more easily slide from each other, thus increasing the deformability of the scaffold. It is also worth pointing out that the Young's modulus value of the 90° scaffold in the longitudinal Z direction is slightly smaller than the values in the two transverse directions (X and Y directions). This result can be explained by the different load transfer mechanisms when the 90° scaffold is compressed in different directions. When compressed in the longitudinal Z direction, the compressive loading is supported by the overlapping regions between layers; when compressed in either the X or Y direction, the loading is mainly supported by the filaments themselves, which are stiffer and behave like columns, therefore generating smaller deformation.

Different lay-down angles mainly affect the pore shape in the XY plane; as such, the anisotropic characteristic is most prominent in the XY plane. When the specimen is compressed in the X direction, the Young's modulus increases when the lay-down angle is reduced from 90° to 15°. More specifically, the Young's modulus is 21.47 MPa at 15°, which is 34% greater than that of the 90° scaffold. When the lay-down angle is small (e.g. 15°), the filaments of all the layers are laid in one dominant direction, which forms a bundle of filaments and behaves like a column structure to sustain the compressive loading. While, when the specimen is compressed in the Y direction, Young's modulus decreases as the lay-down angles is reduced. The lower Young's modulus values at smaller lay-down angles can be attributed to the large deformation of a spring-like structure. When the filaments are arranged almost parallel to the ones in adjacent layers, the load transfer in the direction perpendicular to the filaments follows a spiral path, which can generate large deformation under compressive loading and lead to a relatively low Young's modulus. Moreover, it is worth noting that the Young's modulus of 30° and 15° scaffolds compressed in the Y direction are less than 1 MPa; these values are in the range of the Young's modulus value for cartilage tissue.

The anisotropic nature of the lattice scaffolds in the transverse plane is reflected by the difference in Young's modulus in X and Y directions, so the scaffolds can be classified as orthotropic structures (Sutcu, 1992). The orthotropic effect increases when the lay-down angle decreases from 90° to 15°, indicating that the lattice scaffold can adapt to different requirements of anisotropy simply by rotating the orientation of filaments. In general, the trabecular network is complicated; for example, a highly oriented and columnar architecture is observed in the vertebrae and tibia. This kind of trabecular bone is highly anisotropic, and Young's modulus values can be different in the longitudinal and transverse directions (Williams and Lewis, 1982). In contrast, the cancellous bone can be essentially isotropic in regions such as the proximal part of the bovine humerus (Kaplan et al., 1985). In general, the isotropic nature of scaffold facilitates its use in bone defects regardless of its orientation (Gómez et al., 2013, 2016). The scaffold with a lay-down angle of 90° is more suitable for such an environment where isotropic mechanical properties are necessary. In contrast, if the bone tissue is anisotropic, then the design of the scaffold can be adjusted by tuning the lay-down angle based on the extent of anisotropy.

The compressive strength is recorded as the stress when the scaffold structure reaches yielding on the stress-strain curve. The compressive strength of cubic scaffolds decreases with the lay-down angle varied from 90° to 15° when loaded in the longitudinal Z direction or in the transverse Y direction, whereas the compressive strength has a plateau around 45° when compressed in the transverse X direction. As a layered structure, the scaffold is more stable if the filaments are arranged in orthogonal directions within the layer when compressed in the Z direction (perpendicular to the layers). When compressed in the transverse directions (X or Y), the filaments that are aligned with the compressive direction provide the most support to sustain the loading. Therefore, the compressive strength in the Y direction decreases when the lay-down angle (defined with respect to the X direction) changes from 90° to 15°, as the orientation of filaments rotates from the Y direction to the X direction; when compressed in the X direction, however, the structure lacks constraints in the

lateral direction to maintain compressive stability when all the filaments are aligned dominantly in the X direction (e.g., 15°), so the compressive strength drops after reaching a plateau between 60° and 45°.

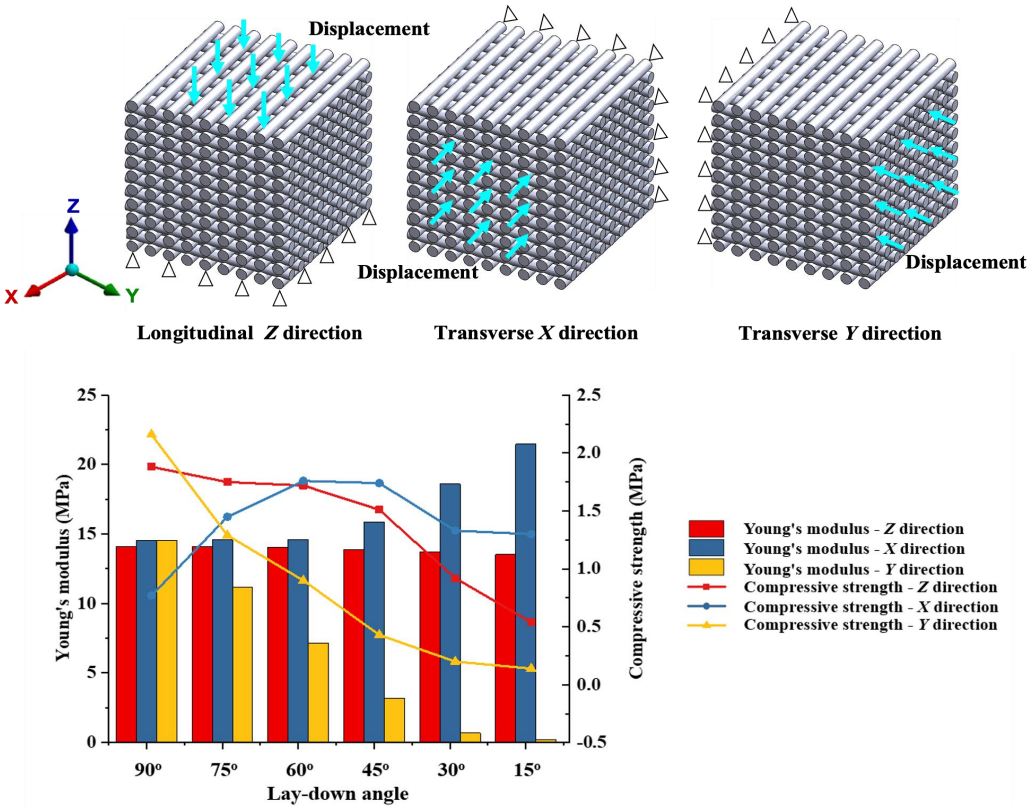

Figure 4.4: Young's modulus and compressive strengths of cubic scaffolds with different lay-down angles compressed in three orthogonal directions, respectively. The lay-down angle is defined with respect to the X direction.

4.4.2 Multiple lay-down angles

In this section, a complex layered scaffold was created by assembling individual sections of six different lay-down angles – 15°, 30°, 45°, 60°, 75°, and 90°. As the anisotropy mainly exists in the transverse XY plane, it is compressed in the transverse X and Y directions, respectively.

In the section 4.4.1, the anisotropic nature of the scaffold is mainly reflected in the difference in Young's modulus between different compressive loading directions. The assembled complex scaffold presented here retains this characteristic

because the local stiffness of each section still depends on the loading direction applied to that individual section; the bonding regions between sections of different lay-down angles behave as transition zones. In this section, the anisotropic property is analysed from another perspective: strain distribution. The strain distribution is also an important factor because the strains generated from mechanical loading are transmitted to cells attached on the surfaces of scaffolds, which in turn stimulate various types of cell differentiation according to the deformation magnitude (Meyer et al., 2006). Different strain magnitudes may lead to chondrogenic or osteogenic differentiation to rebuild the functions of damaged OC tissue (Prendergast et al., 1997; Carter et al., 1988). The assembled scaffold is placed in a uniform loading environment (i.e. no variation of loading between different sections), and the strain distributions from different sections of the scaffold are examined.

Figure 4.5 shows the maximum principal strain on the surface of the central layer in each of the six sections from 90° to 15° at the vertical strain displacement of 0.5%. The light grey filaments in the background represent the underlying layer, where the filaments are arranged in a fixed orientation (i.e. along the X direction) (Figure 3.2). The grey 'holes' within the filaments are the overlapping areas (joints) with adjacent layers in the longitudinal Z direction. Since the strain contours are only visualised on the filament surfaces, these overlapping areas lie within the filaments; as such, the strains are not shown. It can be seen from Figure 4.5 that the strain magnitudes are generally higher around these joints, which is consistent with previous findings of localised stress and strain peaks at the joints (Luczynski et al., 2012; Szlazak et al., 2019). Although the pore shape becomes increasingly skewed as the lay-down angle decreases from 90° to 15°, all the scaffold specimens exhibit periodic strain distributions due to the uniform and repetitive pattern of cell arrangement in the lattice structure. The section with higher strains supports more load than the other lay-down angles. For example, when the specimen is compressed in the X direction, it is the 15° section that has the highest strain magnitude because the filament orientation is the closest to the compressive direction (Figure 4.5 f); when compressed in the Y direction, the 90° section sustains most of the load

and therefore has the largest strain (Figure 4.5 g). As the 45° orientation exhibits the same angle on X and Y directions, the 45° section shows similar patterns of strain distributions when compressed in either X or Y direction (Figure 4.5 d and j).

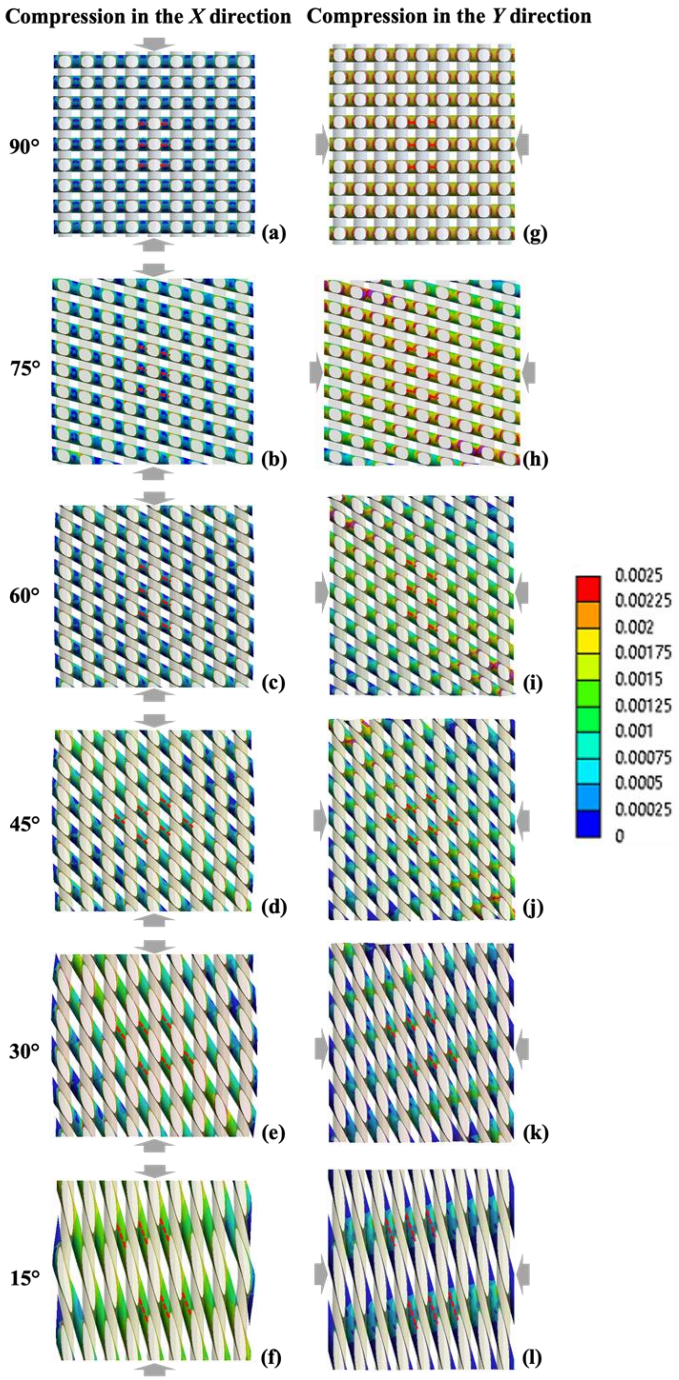

Figure 4.5: Maximum principal strain on the filament surface of the central layer in each section (three layers) of the assembled scaffold specimen when the displacement was set as a vertical strain of 0.5%. The lay-down angle changes from 90° to 15° (top to bottom). The block arrows are used to illustrate the direction of compressive loading. The left column (a–f) shows the strains when the scaffold is compressed in the transverse X direction, and the right column (g–l) shows the strains on the same surface but compressed in the transverse Y direction. The red dashed lines are used to calculate average strain values along these lines.

To further compare the strain distribution and transition between different lay-down angles, three different thicknesses are tested for each lay-down angle. In addition to the assembled scaffold in Figure 3.2, which has three layers in each section of different lay-down angles, two new structures were created, with two and four layers for each section, respectively. The average values of maximum principal strains are calculated along six straight lines on the filament surfaces (red dashed lines in Figure 4.6) for each layer, respectively. The layers are numbered from 90° to 15°.

All the three scaffolds show uniform strain distribution within each section, which is independent of the number of layers of the section. When the scaffold is compressed in the transverse X direction, the maximum principal strain increases with decreasing lay-down angles. However, the opposite trend is found when the loading direction is rotated to the transverse Y direction. It can be seen that the strain magnitudes on transverse directions highly depend on the angle between the direction of compressive loading and the filament orientation; the strain is greater when this angle approaches 0° and decreases when this angle approaches 90° (when the loading is perpendicular to the filaments). When the filaments are aligned with the direction of compressive loading, they provide the most preferable path to sustain the mechanical load. On the other hand, when the filaments are perpendicular to the compressive direction, the load is mainly transferred to neighbour layers, where the filaments are more aligned with the compressive direction.

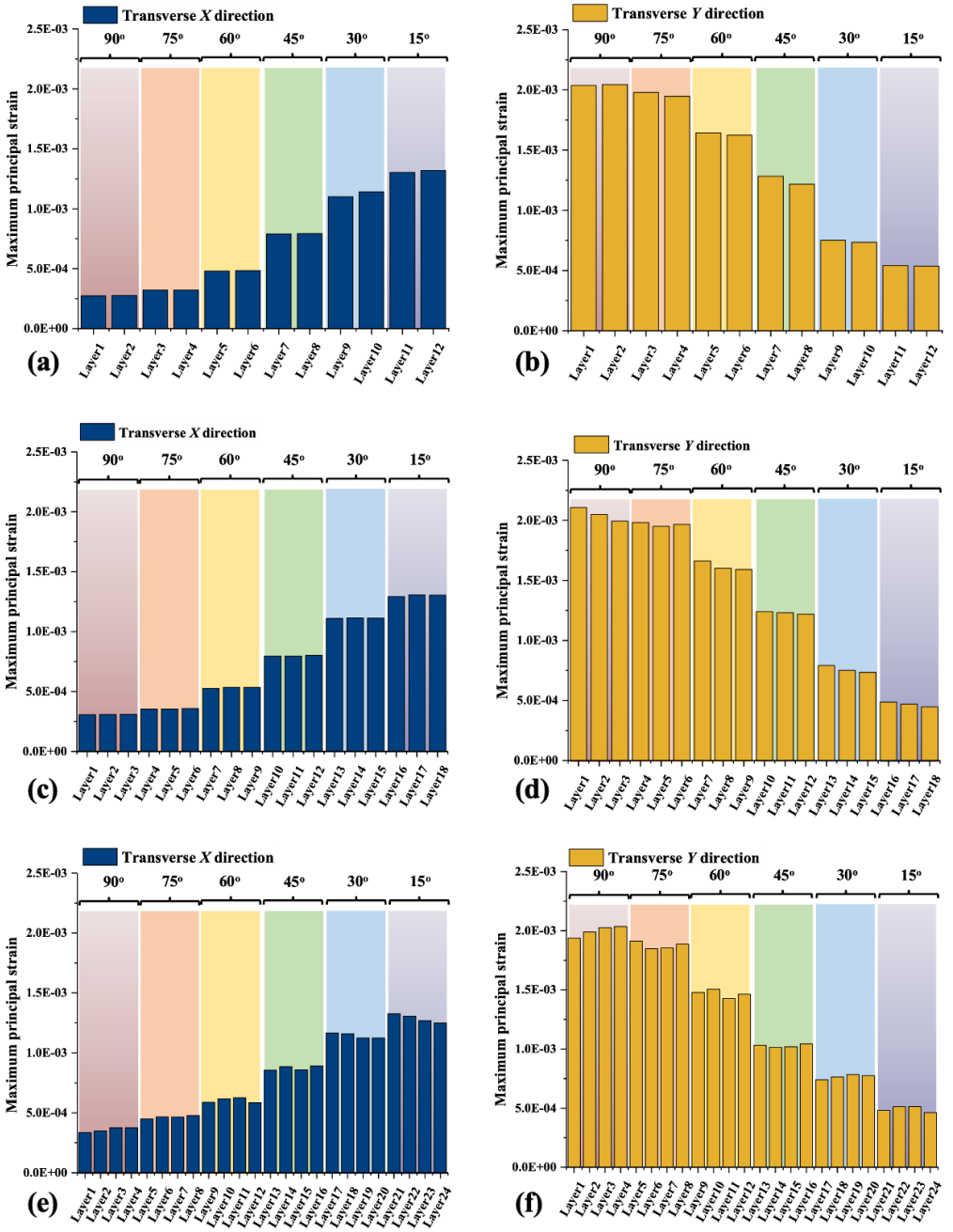

Figure 4.6: Plot of maximum principal strains on filament surfaces compressed in X or Y direction, which are calculated as average values along the red dashed lines defined in Figure 4.5. Three scaffold structures are compared, with two layers (a, b), three layers (c, d), and four layers (e, f) for each section of different lay-down angles, respectively. The layers are numbered from 90° to 15°.

Tunable properties are desirable for bone scaffolds (Feng et al., 2018). The combined results of the assembled scaffold and the individual cubic scaffolds with different lay-down angles show that the deformability of the layered lattice scaffolds

can be tuned by adjusting the lay-down angles which represent the pore shapes in porous scaffolds. The various strain magnitudes in different sections of the assembled scaffold are the result of different stiffness values, measured by Young's modulus, in different parts of the scaffold. This approach also indicates that by assembling sections of different lay-down angles together, the final scaffold retains the distinct Young's modulus values exhibited by the individual sections.

It is known that different strain magnitudes can lead to changes in cell differentiation on bone scaffolds (Sumanasinghe et al., 2006; Delaine-Smith and Reilly, 2011; Michalopoulos et al., 2012). By using an assembled lattice scaffold with multiple lay-down angles, various strain magnitudes and hierarchical/gradient transitions can be achieved in a single construct. A specific strain range at a given location can be accurately adjusted by tuning the local lay-down angle. Using this approach, it is possible to guide cell differentiation in different parts of a given scaffold.

4.5 Conclusions

This chapter has investigated the effects of porosity and pore shape on the mechanical properties of 3D lattice scaffolds using finite element modelling. The results show a linear relationship between scaffold porosity and Young's modulus values in the range of osteochondral bone. Specifically, the Young's modulus decreases with increasing scaffold porosity. The results also suggest a scaffold porosity value of approximately 60% to separate the scaffold application between cancellous bone repair and cartilage repair. The cubic scaffolds with a single lay-down angle exhibit the most pronounced isotropic characteristics when the lay-down angle is 90°; the orthotropic effect increases when the lay-down angle decreases from 90° to 15°. Various strain magnitudes and gradient transitions are achieved in a single construct by assembling individual lattice sections with different lay-down angles. These results demonstrate that the hierarchical mechanical characteristics of natural OC tissue can be mimicked by tuning the porosity and local lay-down angles in specific

parts of the assembled scaffold. The results also provide guidance on the design of personalised scaffolds using 3D printing technology.

Chapter 5

Direct ink writing of polycaprolactone / polyethylene oxide-based 3D constructs

5.1 Introduction

3D printing is a technology that builds objects in a layer-by-layer fashion based on a predetermined digital model. This concept of manufacturing has attracted interest from the biomedical field as a new means of processing biomaterials into functional devices (Hwang et al., 2018). The utilisation of 3D printing allows the rapid construction of complex 3D geometries compared to conventional manufacturing techniques, which require moulding or lithographic masks (Truby and Lewis, 2016). In addition, the digital model in 3D printing is created either in a user-specified way or in compliance with medical imaging data to facilitate the fabrication of patient-specific structures (Morrison et al., 2015). This type of customisability from an architectural perspective has enabled 3D printing to be recognised as a platform for on-demand manufacturing.

A series of 3D printing technologies have been developed over the past decade

that can be classified into two groups, namely light-based and extrusion-based approaches (Hwang et al., 2018)). Although the former group provides higher printing resolution than the latter, the technologies (e.g. stereolithography and selective laser sintering) are limited to processing either photosensitive resins (Gittard and Narayan, 2010) or fine powders of thermoplastic polymers (Drummer et al., 2010). In contrast, extrusion-based platforms such as fused deposition modelling (FDM) and direct ink writing (DIW) may be applied to a greater range of processable materials (Truby and Lewis, 2016) and thus have better versatility for biomedical applications than light-based approaches. FDM involves fusing thermoplastic filaments (Wu and Hsu, 2015). Polycaprolactone (PCL) is a common hydrophobic biomaterials that is processed using the FDM method; it is a major component in US Food & Drug Administration-approved implantable systems (Song et al., 2018). As an example of one such biomedical application, Reichert et al. (2011) used the FDM method to fabricate porous PCL-based scaffolds, which provided defect bridging for long bone repair. The results showed the formation of bone with high mechanical stability in vivo after twelve weeks. Zhou et al. (2018) printed scaffolds containing PCL loaded with vancomycin; agar diffusion studies indicated sustained release and antibacterial activity against *S.aureus* for more than four weeks. Indeed, hydrophobic biomaterials such as PCL have received widespread attention within the biomedical field as tissue grafts or scaffolds, due to their slow degradation rates allow for sustained structural integrity after implantation (Reichert et al., 2011; Song et al., 2018; Sung et al., 2004). Such polymers also tend to be used for sustained release of agents such as anti-inflammatory agents or growth factors over weeks (Malikmammadov et al., 2018; Zhou et al., 2018; Espinoza et al., 2020; Arunkumar et al., 2019). However, FDM requires the use of heat as the printing fidelity relies on solidification after the melt. This feature precludes the use of the platform for the incorporation of thermolabile additives such as cells, growth factors, or heat-sensitive drugs (Jang et al., 2018). Given the requirement to incorporate heat-sensitive materials within scaffolds, the use of FDM in the field of tissue engineering may be subject to significant limitations.

Compared to FDM, DIW can operate in a heat-free environment as it involves extrusion of viscoelastic inks through a nozzle with the aid of a displacement-controlled driving mechanism (Lewis and Gratson, 2004). The ink is technically in the form of a slurry or solution, depending on the component polymers, solvents, and additives. The ink used in the DIW process has to meet the following rheological requirements in order to print with high fidelity: (1) exhibit shear-thinning behaviour (reduction in viscosity with applied shear stress), (2) exhibit uniform flow of filament-like extrusion, and (3) demonstrate the ability to recover more than 80% of its viscosity after deposition (Dávila and d'Ávila, 2019; Barry III et al., 2009; Zhang et al., 2020a). These criteria have been identified from studies that utilised hydrogel-based inks (Malda et al., 2013; He et al., 2016). Hydrogels are an attractive candidate for bioprinting in DIW since they possess similar properties to the natural extracellular matrix; in addition, the high-water content allows the incorporation of cells. However, the applications of DIW for hydrophobic biomaterials such as PCL remains relatively limited. This is unfortunate as PCL is known for its propensity to form blends and composites that enable modulations of the physical properties of the scaffold (Yeo and Kim, 2012; Li et al., 2014; Dong et al., 2017). For example, Remya et al. (2018) blended hydrophobic PCL with a hydrophilic polymer, polyethylene oxide (PEO), and produced hybrid PCL/PEO fibres by electrospinning. The in vitro results showed that, in comparison to a PCL control, the group containing PEO degraded faster in phosphate buffered saline; it also exhibited enhanced cell attachment and proliferation as a result of improved surface wettability and enhanced surface micro-roughness. As PCL and PEO are immiscible, their contributions to the physicochemical properties of the composite may be readily and significantly tailored depending on the incorporation ratio (Qiu et al., 2003). This pair of polymers has not been processed via DIW to date; consequently, both PCL and hybrid PCL/PEO represent systems of interest in this study.

A limited number of studies have processed PCL (alone) via DIW; these studies have utilised volatile solvents such as dichloromethane (DCM) or acetone (ACE) to dissolve the polymer (Dorj et al., 2013; Goncalves et al., 2016). Neither the

rheological behaviour of the inks nor the effect of solvent choice has been extensively studied to date. Nevertheless, a number of studies have evaluated the effect of solvent volatility on the surface properties of polymeric products produced via other bio-fabrication platforms such as solvent casting and electrospinning/spraying (Maleki et al., 2013; Entezari et al., 2019; Shenoy et al., 2005). It is well known that the surface properties of a polymeric matrix depend on both the type of solvent and the manufacturing process. Hence, a similar phenomenon may be expected to occur when polymer solutions are processed via DIW. To the best of the author's knowledge, the properties and their relationship to process parameters have not been investigated yet.

In this chapter, PCL and PCL/PEO inks were prepared based on a strategy of controlling solvent evaporation for processing 3D constructs. The polymer concentrations in the solutions were optimised using rheological measurements; flow was assessed through the nozzle of the printer. The chosen inks were used to fabricate 3D constructs, which were further investigated using a range of microscopic, diffraction, thermal, and wettability measurements. The aims of this study were to: (1) study the rheological properties of processable PCL and PCL/PEO inks, (2) investigate the influence of solvent and PEO incorporation on the surface properties of the printed constructs, and (3) evaluate the applicability of DIW as a tool for fabricating polymeric constructs. This study developed new inks for DIW printing and the DIW printed PCL and PCL/PEO scaffolds were the potential candidates to mimic the cartilage tissue layer of the osteochondral tissue.

5.2 Ink printability assessment

A two-step assessment was proposed to characterise the material properties associated with printability in order to further understand the design factors that facilitate DIW fabrication (Zhang et al., 2020a; Paxton et al., 2017). The first assessment step, manual dispensing, is an initial screening method that focuses on the ability of the inks to form filaments rather than droplets such that the formed filaments stack

in a layer-by-layer manner to obtain the 3D constructs. The second step requires rheological measurements to identify the properties of the inks before, during, and after extrusion in the printing process. Thus, we utilised (a) a shear viscosity test to understand the shear-thinning properties of the material, (b) a shear stress amplitude ramp assessment to obtain the ink linear viscosity region and yield stress, and (c) a recovery test to observe the ink recovery behaviour after being exposed to high shear rates by applying an alteration of high and low shear rates. To understand the influence of various parameters such as the polymer concentration, solvent type, and incorporation of PEO, on the ink printability, the two-step printability assessments were performed on all the ink formulations.

5.2.1 Manual dispensing

The formation of a consistent and cylindrical filament by manual extrusion is a rapid and highly effective way to assess the preliminary printability of an ink. To simulate the DIW printing process, the inner diameter of a nozzle (311 μm) was selected to match the extrusion system used for DIW printing. The dispersing behaviour of PCL and PCL/PEO solutions with low and high concentrations is shown in Figure 5.1. The inks *L_D_PCL*, *L_A_PCL* and *L_D_PCL/PEO* formed droplets while the inks *H_D_PCL*, *H_A_PCL*, *H_D_PCL/PEO*, *L_A_PCL/PEO*, and *H_A_PCL/PEO* were able to form in filaments. This result suggests that the concentration of the polymer is critical for filament formation, as the majority of the inks with lower concentrations were unsuccessful. Those inks that formed filaments passed the first-step printability assessment for extrusion-based printing. Although increasing the polymer concentration can improve the filament formation, the ink viscosity cannot be too high, as it would not be extruded out from the syringe; in addition, the needle will be forced out if higher pressure is applied.

5.2.2 Ink rheology

Rheological properties of the formulated inks were characterised from shear rate-dependent viscosity, yield stress, and recovery behaviour after applying a high shear

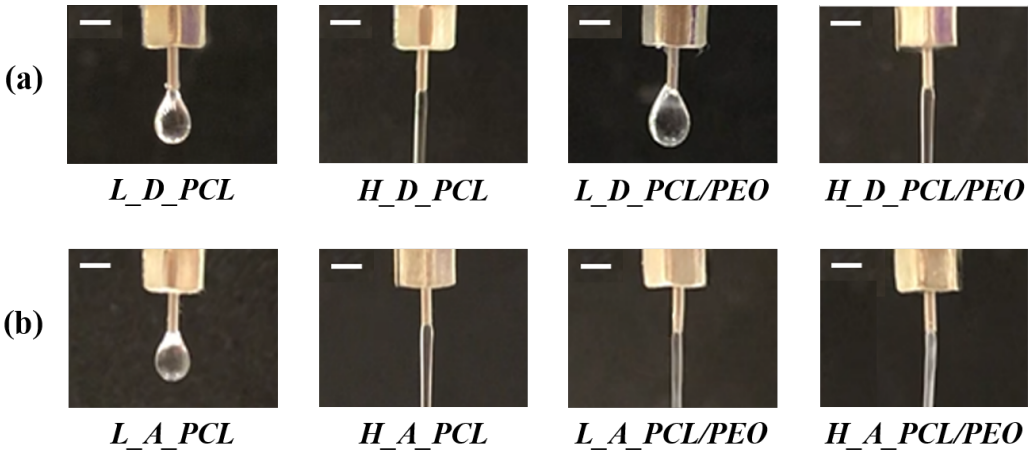

Figure 5.1: Printability assessment with manual dispensing of PCL (a) and PCL/PEO (b) based inks with low and high concentrations. The scale bar represents 1 mm.

rate. The consistency index (m) and the power law index (n) were calculated by applying the power law model to the shear rate-viscosity profiles, so the degree of shear-thinning could be ascertained. The yield stress was determined via shear stress ramps and predicting the extrusion behaviour at DIW printing induced shear rates. Finally, the recovery of the inks after exposure to shear rates similar to those during DIW printing was evaluated.

Firstly, the viscosity of the formulated PCL and PCL/PEO based inks was evaluated through steady-state shear viscosity measurements. Figure 5.2 (a, b) shows the viscosity curves with the shear rate for the PCL and PCL/PEO inks with different concentrations in ACE and DCM solvents.

The viscosity curves were fitted using the power law model (Morrison et al., 2001), which is given by Equation 5.1:

$$\eta(\gamma) = m\gamma^{n-1} \tag{5.1}$$

where m is the consistency index, which is associated with the magnitude of the viscosity. The term n is the power law index, defines the viscosity behaviour: (i) shear-thickening if $n > 1$, (ii) Newtonian if $n = 1$ or (iii) shear-thinning if $n < 1$. The curve of $\ln\eta - \ln\gamma$ was plotted based on the ink viscosity curves. By fitting the

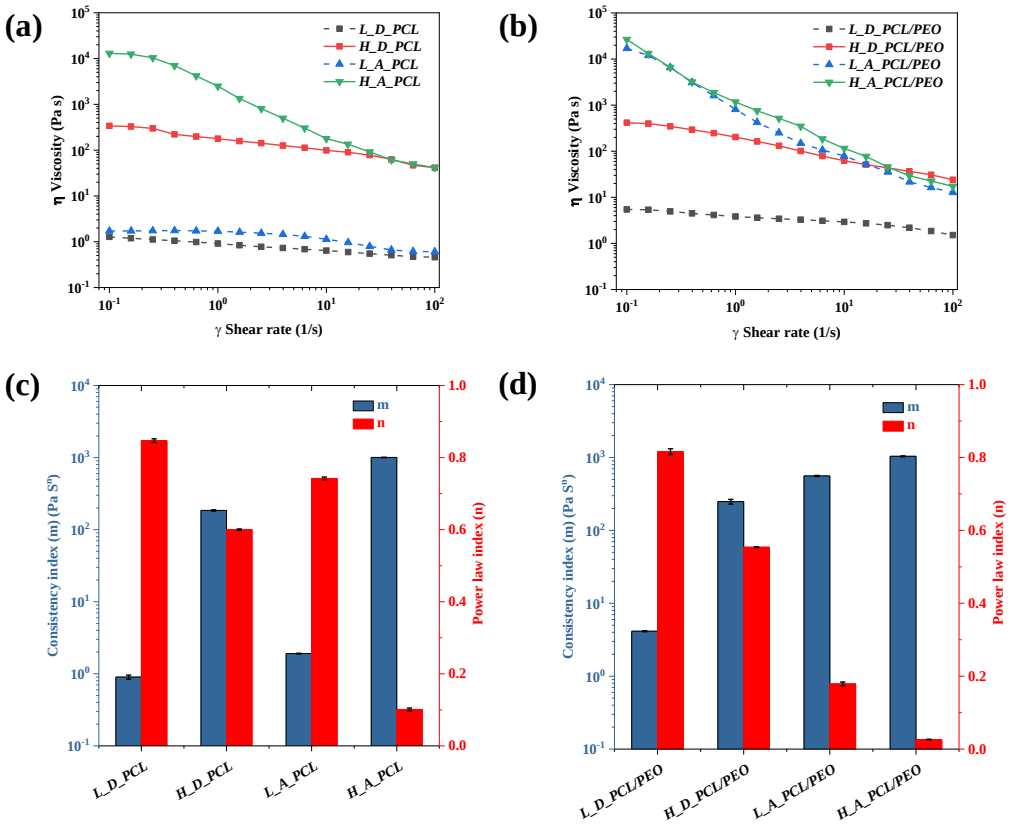

Figure 5.2: Viscosity flow curves of PCL (a) and PCL/PEO (b) based inks in DCM and ACE solvents with low and high concentrations; the consistency index *m* and power law index *n* of PCL (c) and PCL/PEO (d) based inks, obtained from the power law model fitting.

slope and intercept, the consistency index *m* and the power law index *n* of the inks were obtained, respectively. Figure 5.2 (c, d) summarises *n* and *m* results of PCL and PCL/PEO based inks, and their correlation coefficients (R^2) were greater than 0.99. The *n* values of all inks are less than 1, which indicates that all inks are non-Newtonian fluids with shear-thinning behaviour. The larger the deviation of *n* from 1, the more non-Newtonian is the behaviour of the fluid (Blair et al., 1939). All the inks tested are suitable for extrusion-based printing: they pose a high viscosity at the low shear rate and a low viscosity at a high shear rate.

Upon increasing the polymer concentrations from 7.5 to 15% w/w for both PCL and PCL/PEO based inks, the power law index *n* decreased, while the consistency coefficient *m* increases, which indicated more prevalent shear-thinning be-

haviour. The viscosity for the lower concentration of PCL based inks exhibits shear-thinning behaviour after a Newtonian plateau. The power law index n further decreased with the addition of PEO: from 0.60 to 0.55 for the DCM-based ink and from 0.10 to 0.03 for the ACE-based system. The drop in viscosity with shear stress of PCL/PEO inks is greater for the ACE-based inks.

Secondly, an oscillatory stress sweep test was performed on the inks that were able to extrude filaments by manual dispensing so as to evaluate the viscoelastic behavior of these inks. The yield stress was determined using the intersection point of two tangents, one in the linear viscoelastic region in which the inks were deformed elastically, and another in the region in which the storage modulus values dropped. When the ink is at rest, the interacting forces among polymer chains form a stable, three-dimensional network, and the material acts rheologically as a condensed solid-state system. After exceeding the yield stress point, the ink polymer superstructure breaks down, and the material starts to flow.

Both DCM and ACE based PCL inks (*H_D_PCL* and *H_A_PCL*) were prone to flowing away at the shear stress ramp at 0.1 Pa; hence, the yield stress could not be accurately determined. However, those inks with added PEO were able to provide data for the oscillatory stress sweep test when the applied shear stress increased from 0.1 Pa until the yield points were obtained. This result may indicate that the addition of PEO improves the solid-like behaviour of the inks. The yield stress results indicated that the polymer concentration is of clear importance; the low PCL/PEO in ACE ink (*L_A_PCL/PEO*) started to yield when the shear stress was 43.0 Pa, while the yield stress increased with the high polymer concentration; the *H_A_PCL/PEO* ink was approximately eight times higher (347.7 Pa). It was also observed that the choice of solvent had an influence on the yield stress. The yield stress (765.2 Pa) of the DCM-based ink (*H_D_PCL/PEO*) was more than two times higher than the ACE-based ink at the same concentration.

Thirdly, the ability of the inks to recover was examined by the creep recovery test. The results show that the viscosity of all the inks were able to return to

original values with time. This test corresponds to the DIW printing process in that the ink flow through the nozzle tip under shear; thereafter, the viscosity decreases as a function of time to a constant value. For the DCM-based PCL/PEO ink (*H_D_PCL/PEO*), the initial recovery was nearly 93% after the high shear rate removal and became full recovery at circa 100 s; however, ACE based PCL/PEO inks (*L_A_PCL/PEO* and *H_A_PCL/PEO*) were not able to recover fully at 100 s, although the recovery percentage (81%) was higher for the high concentration ink (*H_A_PCL/PEO*) in comparison with that of the low one (44% for *L_A_PCL/PEO*). As the initial viscosity recovery of an ink must be higher than 80% to enable 3D printing (Peak et al., 2018), *L_A_PCL/PEO* ink was deemed to be not suitable for the DIW process, even though it was able to form a filament. Therefore, only high concentration PCL/PEO inks (*H_D_PCL/PEO* and *H_A_PCL/PEO*), with viscosity recovery percentages higher than 80%, were selected for further investigation of the influence of solvents on the DIW printing process.

5.3 Mathematical analysis of ink flow within a printing nozzle

Using the theoretical extrusion pressure, velocity, and shear rate, the theoretical extrusion behaviour of materials inside the needle could be obtained. It is possible to predict spatial distributions of the parameters inside the needle for both DCM and ACE based PCL/PEO inks (*H_D_PCL/PEO* and *H_A_PCL/PEO*). Besides the parameters dictated by the DIW printer setup for dispensing, such as needle radius, needle length, and extrusion rate, the power law index n and the consistency index m obtained from the shear viscosity measurements also play essential roles.

The profiles of velocity on the Z-axis (V_z) of DCM and ACE based PCL/PEO (*H_D_PCL/PEO* and *H_A_PCL/PEO*) inks along a radial axis of 155.5 µm nozzle are shown in Figures 5.3 (a, b), and the parameters were calculated from Equation 3.1. For both inks, with the increasing extrusion fluid rate from 0.48 to 1.44 mm^3/s, the extrusion pressure (ΔP) and induced wall shear rate ($\dot{\gamma}$) were raised; however, the

velocity (V_z) profile along the nozzle tube decreased towards the needle wall. This is similar to the parabolic profile within a pipe of a fully developed fluid; friction is also important in the flows since internal friction resists motion. A fluid with high viscosity has a large amount of internal friction; when a fluid is in contact with a static solid surface (nozzle wall), adhesion can slow the flow of the fluid (Chen et al., 2019a; Zhang et al., 2020a). The results show that the velocity profile of DCM ink gradually decreased from the middle of the needle tip to the wall of the needle tip; while, the velocity (V_z) of the ACE ink kept a similar level within the needle and changed suddenly near the nozzle wall. This result could be associated with the strong shear-thinning behaviour of the ACE ink, which maintains higher viscosity under a low shear rate than the DCM ink. Figures 5.3 (c, d) show that the shear rate of both inks experienced linearly increases as a function of the extrusion flow rate (Q_E). Those profiles were calculated from Equations 3.2 and 3.3. The ink shear-thinning behaviour under conditions of extrusion could be beneficial in allowing the viscosity to decrease at the time of processing, thereby allowing the ink to flow out and deposit. However, when under the same extrusion rate (i.e. 0.48 mm^3/s), the ACE ink (*H_A_PCL/PEO*) exhibited approximately a nine times higher shear rate (1702.9 s^{-1}) than the DCM ink (195.2 s^{-1} for *H_D_PCL/PEO*), predicted from mathematical modelling, as shown in Figures 5.3 (c, d). The higher shear rate for the ACE based ink, as well as the lower initial recovery percentage and slower recovery rate after removing from a high shear rate (i.e. 200 s^{-1}) in the creep recovery test, could explain why the ACE ink may be prone to printing failure while the DCM-based ink (*H_D_PCL/PEO*) could be more suitable for successful extrusion.

5.4 Shape fidelity analysis

5.4.1 Effect of operational parameters

The printing parameters such as the extrusion rate (Q_E) and printing speed in the XY plane (V_{xy}) directly influence the ink deposition. At a fixed the extrusion rate

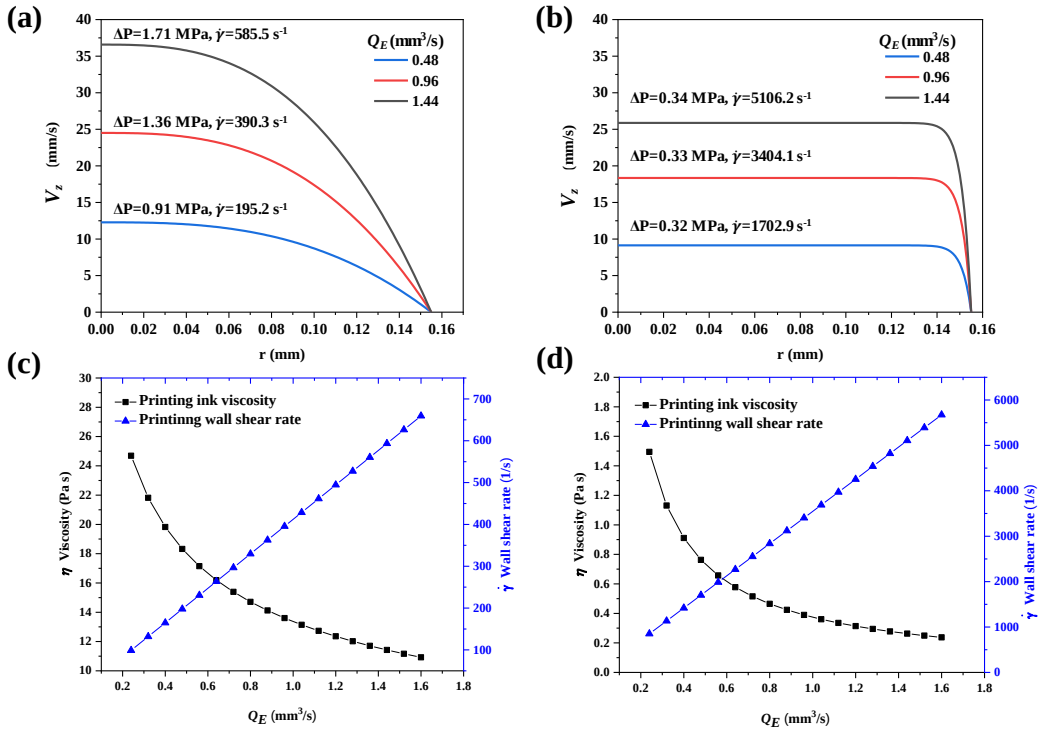

Figure 5.3: The ink velocity (Z-axis) (V_z) profile inside nozzle tip for *H_D_PCL/PEO* (a) and *H_A_PCL/PEO* (b) during the DIW extrusion condition; printing viscosity (η) and wall shear rate ($\dot{\gamma}$) as a function of the extrusion fluid rate (Q_E) for *H_D_PCL/PEO* (c) and *H_A_PCL/PEO* (d).

(i.e. 0.48 mm^3/s), the width of printed filament varied depending on the printing speed, as shown in Figure 5.4 (a) for the DCM based ink *D_PCL/PEO*. When the print speed was 2.5 mm/s, the printed filament width was 400 ± 10.0 µm, which was higher than the nozzle diameter (311 µm). When the printing speed increased to 7.5 mm/s, the printed filament was stretched, and the width of the deposited filament was reduced to 241 ± 12.9 µm, which was lower than the nozzle diameter. Once the velocity increased to 10 mm/s, the deposition was interrupted, and the filaments no longer exhibited a consistent and uniform diameter.

Similar trend was observed for the ACE-based ink (*A_PCL/PEO*), the comparison of the DIW printed filament width of both inks under various extrusion fluid rates (0.48–1.44 mm^3/s) and printing speeds (2.5–12.5 mm/s) is shown in Figures 5.4 (b, c). The width of DIW printed filaments decreased with an increase in print velocity (V_{xy}) or a reduction in extrusion fluid rate (Q_E), and vice versa.

The index of relative filament deviation ($\sigma_{filament}$), calculated from the Equation 3.6, was used to evaluate the DIW printed filaments, it approaches 0 when the filament width ($W_{filament}$) matches the nozzle diameter (d). The deviation indexes at various printing parameters are compared in Figure 5.4 (d, e), the relative filament deviation is closest to 0 at the printing speed V_{xy} of 5 mm/s and the extrusion fluid rate Q_E of 0.48 mm^3/s for the DCM based ink. These operation parameters were used for building 3D constructs subsequently in terms of a better shape fidelity by matching of the nozzle diameter. Similarly, the printing speed V_{xy} of 10 mm/s and the extrusion fluid rate Q_E of 0.48 mm^3/s are considered as the best set up for the ACE-based ink.

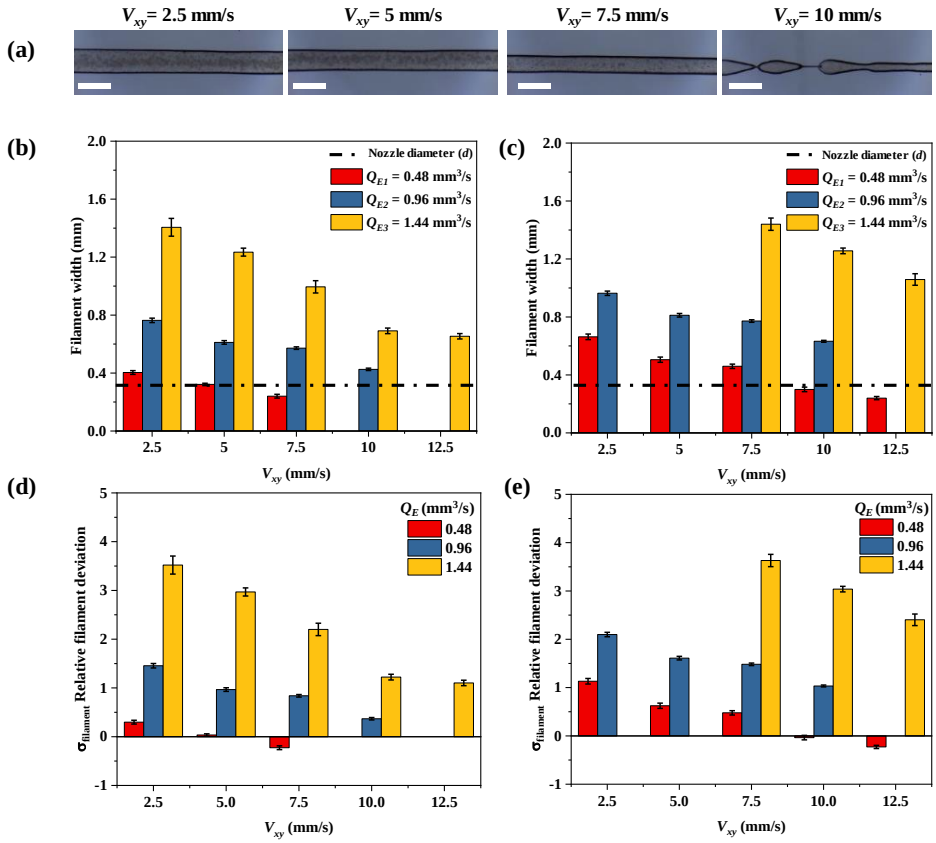

Figure 5.4: (a) Printed filament width of *D_PCL/PEO* changes with various print speed V_{xy} when the extrusion rate $Q_E = 0.48$ mm^3/s, the scale bar is 500 µm; the DIW printed filament width of *D_PCL/PEO* (b) and *A_PCL/PEO* (c) and the relative filament deviation ($\sigma_{filament}$) of *D_PCL/PEO* (d) and *A_PCL/PEO* (e) under the designated printing speed and extrusion rate.

5.4.2 3D constructs

The 3D constructs of PCL and PCL/PEO blend were built in a layer-by-layer manner using DIW from both DCM and ACE based inks. The optical micrographs of printed samples (five layers) are shown in Figure 5.5 a. The width of printed filaments was measured and compared with the applied nozzle diameter, as shown in Figure 5.5 b. The relative filament deviation indexes ($\sigma_{filament}$) were 0.45 ± 0.08, -0.27 ± 0.08, 0.04 ± 0.01, and -0.19 ± 0.09 for the DIW-printed samples *D_PCL*, *A_PCL*, *D_PCL/PEO*, *A_PCL/PEO*, respectively (Figure 5.5 c). The deviation index from *D_PCL/PEO* is closest to 0 when compared to others, it showed that the incorporation of PEO in PCL improved the stability of filament shape after extrusion, and the size was closest to the nozzle diameter. In general, the filaments printed form DCM-based PCL/PEO inks are more uniform than those of the ACE-based inks; this could be resulted from the higher (9 times) shear rate for the ACE-based ink than the DCM system, as simulated from the mathematical modelling (Figures 5.5 c and d). This result combined with the lower ink recovery rate of the ACE ink may be associated with the inherent variability of the extrusion printing process reported by other researchers (Bruyas et al., 2018; Dillon et al., 2019).

5.5 Thermal characterisation

TGA was performed to investigate whether any residual solvents remained in the printed parts after 12 h post-printing. Considering the boiling temperatures of DCM (39.3°C) and ACE (56.2°C), it is evident that all the solvents evaporated within 12 h since no weight loss was observed below 70°C (Figure 5.6 a). The onset T_d value of raw PEO and PCL was 248.3°C and 340.5°C, respectively. Two onset T_d values (259.2°C and 374.6°C) were found in *D_PCL/PEO*, while 244.4 °C and 378.7 °C were in *A_PCL/PEO* samples; the lower T_d represents PEO while the higher corresponds to PCL. The T_d values of the printed samples corresponding to PEO were less than $\pm 5\%$ difference while the onset points representing PCL were visibly higher by 10%. Such shifts in onset temperature suggest that the thermal

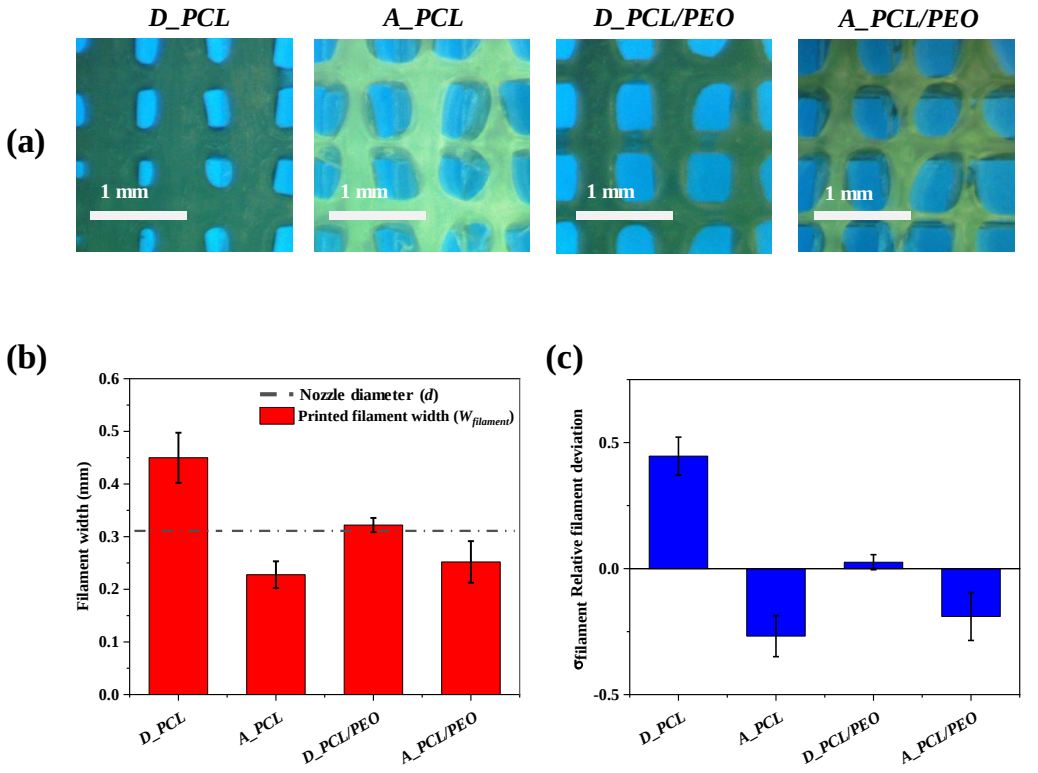

Figure 5.5: (a) Microscopy image. Measurement of filament width (b) and relative filament deviation $\sigma_{filament}$) (c) of DIW printed 3D constructs - *D_PCL*, *A_PCL*, *D_PCL/PEO*, and *A_PCL/PEO*.

stability of PCL improves when blended with PEO.

The resultant thermal DSC traces of the raw polymers and PCL/PEO printed parts are shown in Figure 5.6 b. The observed melting peak (T_m) of raw PCL and PEO was 60.9°C and 70.2°C, respectively. The PCL/PEO blends have shown two distinct peaks clearly; 61.8°C and 67.1°C for *D_PCL/PEO* and 63.9°C and 68.2°C for *A_PCL/PEO*. The closely matching melting peaks of PCL and PEO with the corresponding peaks in the blended parts confirm that the two polymers showed poor miscibility in the matrix.

5.6 Material characterisation

Powder X-ray diffraction (PXRD) was used to determine the phase structure of the biopolymer blends. If two polymers are immiscible, each crystal structure remains

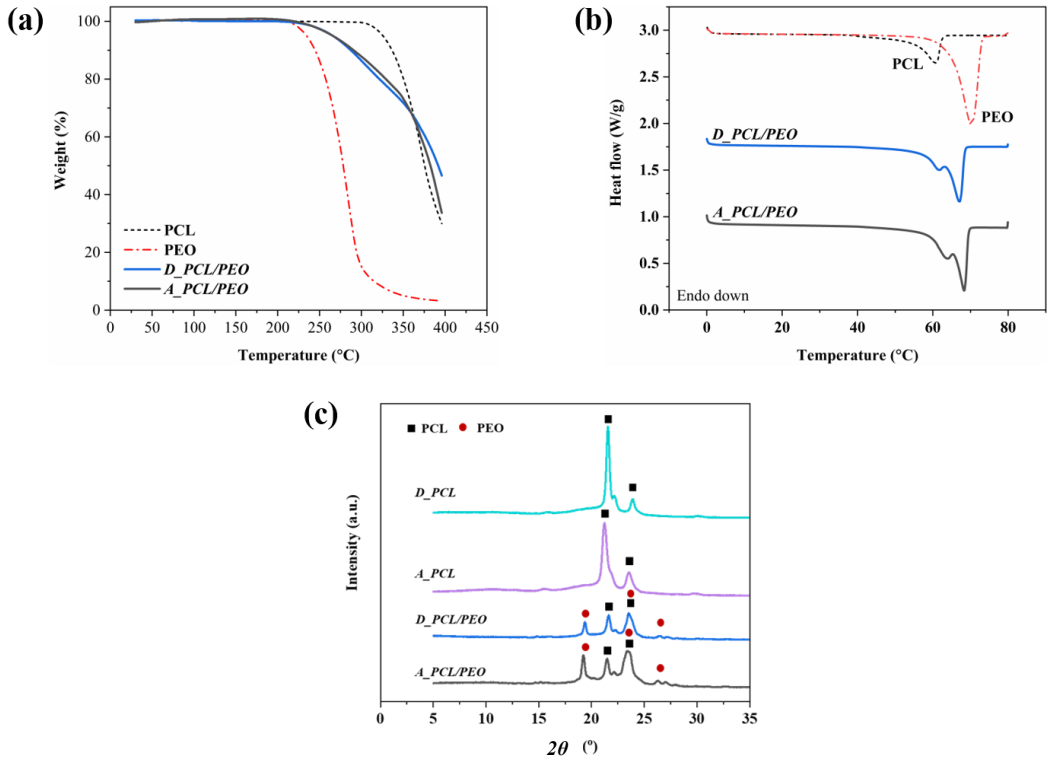

Figure 5.6: Thermogravimetric analysis (a) and differential scanning calorimetry (b) traces of the raw polymers and printed PCL/PEO samples; PXRD patterns (c) of printed samples - *D_PCL*, *A_PCL*, *D_PCL/PEO*, and *A_PCL/PEO*.

in the blends. PXRD patterns of printed *D_PCL/PEO* and *A_PCL/PEO* are depicted in Figure 5.6 c. The peaks at angles $2\theta = 21.4°$ and $23.8°$ correspond to the (110) and (200) crystallographic planes of the semi-crystalline nature of the PCL biopolymer (Abdelrazek et al., 2016), respectively. The pure PEO exhibits two characteristic peaks at angles around $2\theta = 23°$, and $19°$ (Fazli et al., 2005). The decrease in intensity of the PCL peaks is associated with the addition of PEO. The characteristic of peaks of pure PCL were unchanged in both blends, suggesting that the incorporation of PEO did not significantly affect the crystalline structure of PCL.

X-ray photoelectron spectroscopy (XPS) was used to verify the surface elemental composition of the printed samples. Two separated peaks corresponding to C1s (284 eV) and O1s (532 eV) were seen in all the XPS spectra. For a better understanding of the oxygen groups on the sample surface, the C1s and O1s peaks

were further analysed. Three C bonding states at 285.2 eV, 286.5 eV, and 288.6 eV correspond to C-H, C-O, and O-C=O, respectively. The presence of PEO in the sample affected the binding energy and broadening the C1s peaks. The oxygen-containing functional group is vital to surface properties such as hydrophilicity and hydrophobicity (Zhou et al., 2015). Table 5.1 summarised the carbon and oxygen atomic percentage for the *D_PCL*, *A_PCL*, *D_PCL/PEO* and *A_PCL/PEO* samples. With the addition of PEO, the O/C ratio of printed samples increased from 34.7% to 45.2% for the ACE-based ink, and from 36.1% to 50.2% for the DCM-based ink. Wettability is positively related to the surface oxygen content, with increasing of the O/C ratio, the surface becomes more hydrophilic.

Table 5.1: XPS survey data for the atomic component for the printed samples - *D_PCL*, *A_PCL*, *D_PCL/PEO*, and *A_PCL/PEO*.

Samples	Peak designation	Band (eV)	At (%)	O/C ratio (%)
D_PCL	C 1s	285.07	68.8	36.1
	O 1s	532.07	24.8	
A_PCL	C 1s	284.98	70.6	34.7
	O 1s	532.48	24.5	
D_PCL/PEO	C 1s	284.97	63.5	50.2
	O 1s	531.47	31.9	
A_PCL/PEO	C 1s	285.98	66.4	45.2
	O 1s	532.48	30	

5.7 Surface morphology and wettability

The SEM micrographs of the surface morphology of the DIW printed samples are shown in Figure 5.7 (a). The PCL surface printed from the DCM ink was smoother than that from the ACE ink; similarly, the printed PCL/PEO surface from the DCM ink had fewer wrinkles than the ACE system, indicating the influence of solvents on the surface morphology. The addition of PEO resulted in the introduction of bumps onto the filament surface (when compared with the PCL filaments). This happened in samples printed from both ACE- and DCM-based inks. The increase in the surface roughness of the printed PCL/PEO was further confirmed by surface roughness measurements. As shown in Figure 5.7 (b), the arithmetic average

roughness Ra obtained from a quantitative analysis of filaments on the top layers increased from 0.12 ± 0.01 μm to 0.28 ± 0.08 μm for the samples printed from the DCM-based inks; the roughness increased from 0.18 ± 0.02 μm to 0.49 ± 0.11 μm for the samples printed from the ACE-based inks.

The surface roughness (Ra) of printed samples from the ACE-based inks was significantly higher ($p<0.05$) than those from the DCM ones, which indicates that the surface roughness of DIW-printed construct could be controlled by solvent selection. Tang et al. (2004) showed that the surface of the solvent-casted PCL film using chloroform (a hydrophobic solvent) was smoother than that from ACE (a hydrophilic solvent), suggesting that the surface morphology could be dictated by the solubility of PCL in the respective solvent systems.

The contact angle (CA) is a measure of surface wettability (Dubey et al., 2015). The water contact angles on the filaments of the top layer of DIW printed samples are shown in Figure 5.7 (c). The droplet volume used for the CA measurement was 4×10^{-4} μL; the diameter of the droplet was roughly 90 μm, which was smaller than the filament widths (ranging from 200 to 600 μm). Thus, it was possible to place the water droplets on top of a single filament. As shown in Figure 5.7 (d), at the initial contact point of a droplet on the printed filaments, the CAs were $74.3 \pm 0.9°$, $81.7 \pm 4.0°$, $37.0 \pm 0.6°$ and $50.7 \pm 0.3°$ for *D_PCL*, *A_PCL*, *D_PCL/PEO* and *A_PCL/PEO*, respectively ($n = 3$). As the time increased from 0 ms to 800 ms, the CA values for all samples gradually decreased.

The CA values at 200 ms for sample *D_PCL*, *A_PCL*, *D_PCL/PEO* and *A_PCL/PEO* were $67.3 \pm 0.2°$, $77.2 \pm 0.2°$, $33.8 \pm 0.3°$ and $44.5 \pm 0.3°$. At 800 ms, the respective CA values were $55.1 \pm 1.4°$, $70.1 \pm 0.5°$, $28.7 \pm 0.6°$ and $31.6 \pm 0.7°$. After 800 ms, the CA values become too small to be measured as the droplets were fully spread on the surfaces of PCL/PEO samples, indicating that the filaments were wetted completely within less than 1 second.

The DCM-based inks resulted in smaller CA values on the printed samples than those made from ACE-based inks ($p<0.05$); the incorporation of PEO reduced

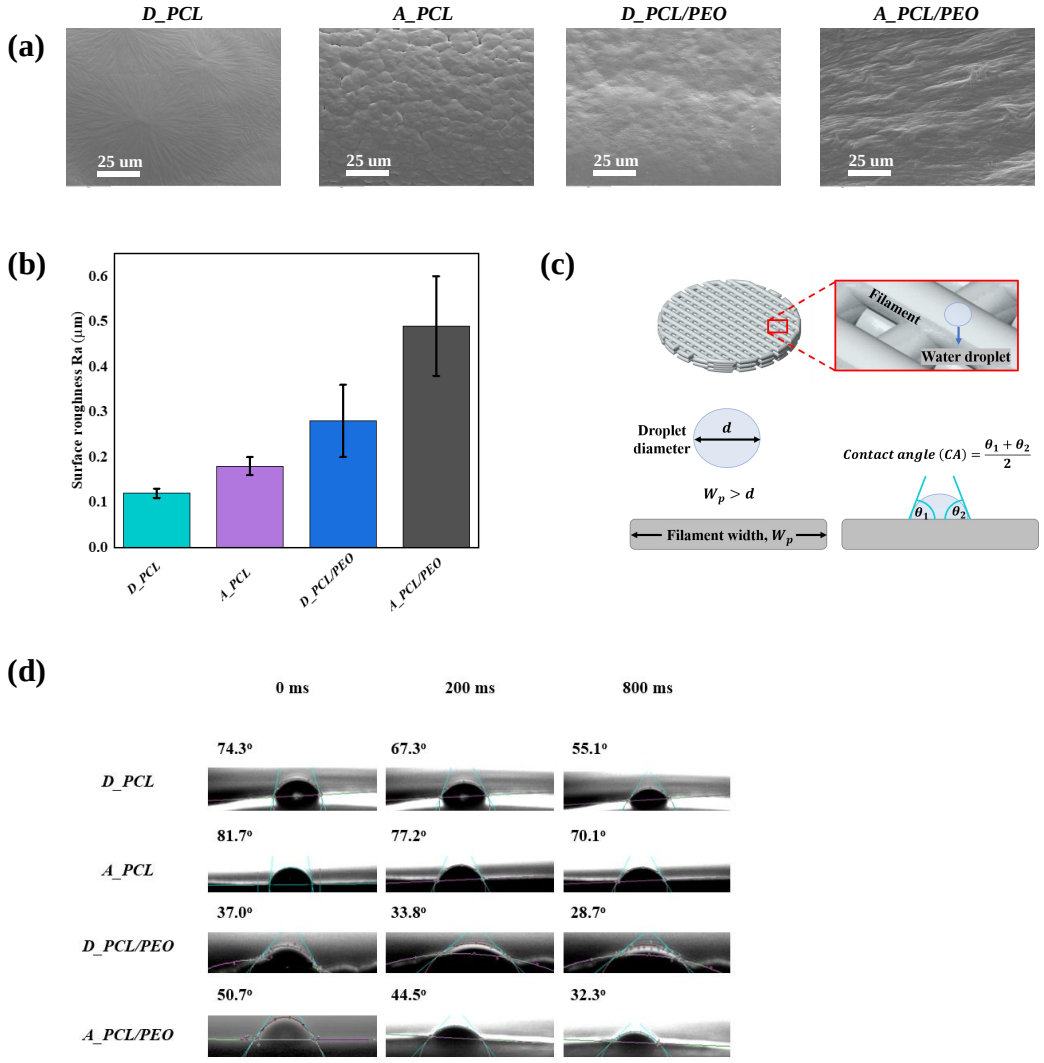

Figure 5.7: (a) SEM micrographs. (b) Surface roughness measurements. (c) The schematic diagram of contact angle. (d) Contact angle results at the time point of 0, 200 and 800 ms on the filament surface of the printed samples - *D_PCL*, *A_PCL*, *D_PCL/PEO*, and *A_PCL/PEO*.

the CA values significantly ($p<0.01$). The results suggest that both the type of solvent system and PEO addition had an impact on the wettability of DIW printed samples. This could be related to the higher O/C ratios measured from XPS. The samples made from the DCM-based inks had a greater O/C ratio than those from ACE-based inks; a further increase of 14% after the addition of PEO into PCL was noted. The results confirmed that the surface oxygen content is a good indicator of the wettability of the DIW-printed structure.

5.8 Discussion

In this chapter, both the type of solvent system and PEO incorporation in PCL ink had a noteworthy impact on the rheological performance. The initial viscosity (when shear rate equals 0.01 s^{-1}) of the ACE-based inks were generally greater than the DCM-based ones (with or without PEO incorporation). This may be resulted from the greater prevalence of interchain bonding in the ACE solvent system compared to the DCM solvent system, which in turn leading to higher viscosity in the ACE-based inks at rest or low shear strains. Moreover, the values of the power law index *n* and the yield stress for all the measurable ACE-based inks were smaller than the DCM-based inks. This result could be related to the difference in solvent polarity between the solvent systems as the ACE is more polar than DCM (Hansen, 2007); the interactions will differ both inter-molecularly (between the polymer chains) as well as between the solvent and solute molecules. In this context, the enhanced shear thinning exhibited by the ACE systems may reflect the greater propensity for temporary disruption of these interactions than is found for the DCM systems, for which there is a lower degree of initial internal bonding; in such systems, the application of stress will not result in the same decrease in viscosity. Although all the formulated inks presented in this study were shear-thinning non-Newtonian fluids, adequate recovery of viscosity (> 80%) with the time-dependent increase was only achievable with PEO incorporation. This also implies that PCL-only inks would not be regarded as an ideal printable material. Therefore, this study demonstrates that incorporation of a polymer such as PEO can aid in processing of PCL by DIW printing.

The thermal results and PXRD patterns shown in Figure 5.6 confirmed the complete evaporation of solvents in the printed outcomes within 12 h, the improved thermal stability of PCL in the blended matrix and the immiscibility of PCL and PEO. The SEM and roughness results in our study corresponded to each other in that both indicated that the printed filaments made out of ACE based inks resulted in a rougher surface than DCM based ones; the addition of PEO further increased the

micro-scale roughness. The results are understandable as both the type of solvent system and the incorporation of PEO would affect the proportion of the polymer-solvent and polymer-polymer interactions in the mixture, which ultimately regulates the entanglements among the polymer chains. It has been reported that a higher degree of polymer entanglements results in a more condensed and smoother surface after the solvent evaporation (Entezari et al., 2019; Tang et al., 2004), which suggests that the entanglements are greater in the DCM-based solvent system than in the ACE-based solvent system and with the PEO incorporation. An interesting aspect of the roughness data is that the PCL filaments processed via DIW in this study were much rougher (Ra of 0.12 μm and 0.18 μm for filaments made from DCM-based and ACE-based inks, respectively) than those prepared using FDM (Ra of 0.02 μm) as reported by Jeon et al. (2014). This result could be attributed to the difference in the solidification between the two techniques. In FDM, the solidification occurs almost immediately after the melt; in DIW, the process depends on a slower solvent evaporation rate, which results in a rougher and uneven surface. Our results suggest that the surface morphology and roughness of a polymeric construct is tuneable when processed via DIW by varying the type of solvent system.

As stated earlier, the hydrophobic biomaterial PCL has been widely applied in tissue engineering field due to its ability to maintain integrity for tissue regeneration as well as facilitate long-term drug release profiles (Reichert et al., 2011; Zhou et al., 2018). Dwivedi et al. (2020) indicate that these advantages are associated with PCL exhibiting a longer degradation time compared to other polyesters due to the presence of five hydrophobic $–CH_2$ moieties in the repeating unit. However, studies also indicate that hydrophobic polymers such as PCL may hinder effective cell attachment and reduce cell affinity; as such, there may be benefits in biological performance via improving the surface wettability (Siddiqui et al., 2018; Dong et al., 2017; Yeo and Kim, 2012).

In terms of the wettability results without PEO, the neat PCL filaments that were processed via DIW were more hydrophilic (initial CA of 74° and 82° on the filaments made out of DCM-based and ACE-based inks, respectively) than those

prepared by other techniques. For instance, Wang et al. (2016) prepared PCL scaffolds using FDM; the reported contact angle was 96.0° after 20 s (using 4 μL of water droplets on filaments that were 330 μm in diameter). Jeon et al. (2014) also used FDM to print PCL scaffolds and placed a 10 μL droplet on the filaments with a diameter of 250 μm. The measured CA was 112.5° after 1 s. Yew et al. (2018) applied electrospinning to fabricate PCL nanofibers; the CAs were around 113° after 1 second using 10 μL of water droplets on PCL nanofibers. Furthermore, the CAs on PCL films that were produced via solvent casting ranged between 89.5° to 101.7° (Jones et al., 2002; Tang et al., 2004). It is important to note that the volume of water droplets used in these studies and the data collection time points were not consistent, which may contribute towards the differences in measured CA. However, our CAs were measured based on the initial contact (the moment the droplet landed on the filaments); more importantly, the droplets wetted the surface of PCL filament completely within 1 s. Hence, the printed PCL constructs have greater hydrophilicity than those made by other fabrication techniques, which could be related to the rougher surface obtained by DIW processing.

As shown from this study, DIW process has a tendency to produce PCL-based constructs with enhanced wettability and surface roughness. This finding could be particularly useful for biomedical applications as the hydrophobicity of PCL is often regarded as a performance weakness. Previous studies have attempted to apply treatments to the PCL surface (Wang et al., 2016) or create a blend with a hydrophilic material (Remya et al., 2018) as a way to improve cell growth and viability. Hence, the surface properties of the PCL-based matrix may be tuned with the aid of hydrophilic polymers such as PEO, thereby enhancing and expanding the usability of the material. In addition, the heat-free printing environment of DIW enables the incorporation of thermo-sensitive components in the ink formulation (Jang et al., 2018). Therefore, the DIW process has the essential attributes to be a successful 3D fabrication tool in the biomedical field.

5.9 Conclusions

In this chapter, the PCL and PCL/PEO polymer inks have been formulated by dissolving PCL and PEO polymers into two solvent systems that are based on DCM and ACE. Upon increasing the concentration of PCL and PEO for both ACE and DCM inks, more marked shear-thinning behaviour has been observed. Although the ACE inks has more pronounced shear-thinning behaviour than the DCM inks, the viscosity recovery performance of the ACE-based inks is inferior to that of the DCM inks. Based on the mathematical modelling of the ink conditions within the needle under the same extrusion rate, the shear rate of the ACE-based ink is nine times higher than the DCM-based one; this parameter can be associated with the inconsistency of the printing process since there is insufficient recovery for the ACE-based inks over the process time window. It therefore suggests DCM over the ACE-based solvent system, particularly when using the PCL/PEO blend for the extrusion-based fabrication process.

Further, the DIW method has been applied to extrude the selected inks to fabricate woodpile structures in a layer-by-layer building sequence. The surface morphology, material characterisation, and wettability of the DIW printed PCL and PCL/PEO constructs are compared. The surface morphology results indicate that the ACE-based samples have a rougher surface than DCM-based ones; the addition of PEO further increases the microscale roughness. The wettability of DCM-based samples is higher than ACE-based ones; the wettability is further improved by blending PCL with PEO in both ACE- and DCM-based samples. Combining these outcomes, the DIW technique offers a new toolkit to develop a 3D construct with tuneable surface characteristics for biomedical application.

Chapter 6

Direct ink writing of polycaprolactone/ polyethylene oxide/ hydroxyapatite-based scaffolds loaded with vancomycin

6.1 Introduction

Bone tissue scaffolds have been intensively studied by researchers as a temporary extracellular matrix, which does not suffer from limitations such as supply restrictions and immune rejection (Farto-Vaamonde et al., 2019). Ideally, a bone scaffold should closely mimic the physiological properties of natural bone tissue; for example, a tissue scaffold should possess mechanical properties that match the host tissue as well as appropriate porosity and interconnectivity for nutrient delivery and tissue regeneration (Reichert et al., 2011; Hutmacher and Cool, 2007). Particularly, bone scaffolds with pores larger than 300 μm facilitate the penetration of mineralised tissue and cell migration towards the scaffold centre, stimulating nutrient supply and waste product removal (Loh and Choong, 2013; Farto-Vaamonde et al.,

2019). In addition, the main chemical components of natural bone tissue are inorganic materials (e.g., calcium phosphate, 50-70% w/w) and organic materials (e.g., collagen, 30-50% w/w); the calcium phosphate mainly exists in the form of crystallized hydroxyapatite (HAp) and bonds with microfibril collagen. Thus, to mimic the chemical composition of natural bone tissue, an appropriate material for bone scaffold fabrication is a bioceramic-polymer composite that consists of both organic and inorganic components.

Over the past decades, extensive efforts have been made towards creating porous bone tissue scaffolds, from the traditional fabrication methods (e.g., freeze-casting, gas-foaming) that result in heterogeneously porous foams, to the 3D printing technologies that can be used to create ordered porosity and user-defined constructs. 3D printing techniques have been used to fabricate porous bone tissue scaffolds such as powder-based printing, liquid-based printing (e.g. DIW printing), and solid-based printing (e.g., fused deposition modelling). In most of these cases, powder-based printing (Chin et al., 2020; Shirazi et al., 2015) or solid-based 3D printing (Shaqour et al., 2020; Azad et al., 2020) requires high temperatures (higher than 100°C), which is not compatible with the incorporation of agents such as heat-sensitive antibiotics or growth factors, which can be used to enhance bone tissue regeneration. The DIW method has the advantage of operating without the addition of heat, enabling the platform to accommodate inks with thermolabile additives (Jang et al., 2018). DIW printing involves the extrusion of pre-formulated inks through a nozzle with a displacement driving system; inks should in form of a slurry or solution depending on the comprising polymers, solvents, and additives (Lewis and Gratson, 2004). Inks should meet specific rheological requirements for the scaffold fabrication with DIW printing: (1) extrusion in ink form as a filament shape, (2) inks should possess shear-thinning phenomenon, and (3) ink viscosity recovery behaviour should be greater than 80% after extrusion (Dávila and d'Ávila, 2019; Barry III et al., 2009; Zhang et al., 2020a).

Polycaprolactone (PCL) is a synthetic biodegradable polymer that has been widely used as a major component of bone tissue scaffolds (Song et al., 2018; Jiao

et al., 2019). PCL is known for its ease of forming of blends and composites, which can be used to modulate physical properties to enhance and expand its usability. Remya et al. (2018) blended hydrophobic PCL with PEO, a hydrophilic polymer, to fabricate PCL/PEO hybrid fibres using electrospinning. The in vitro results show that the PCL/PEO sample degraded faster in phosphate buffer saline than PCL alone; in addition, there was enhanced cell attachment and proliferation on the PCL/PEO samples as a result of improved surface wettability. Hydroxyapatite (HAp) a bioactive ceramic that is similar to the inorganic material found in natural bone (Turner-Walker, 1993; Bruyas et al., 2018). It has been demonstrated to possess osteoconductive properties (Ma et al., 2001). The combination of PCL/PEO/HAp based materials has been investigated in previous studies (Cui et al., 2012; Bruyas et al., 2018; Zhang et al., 2020b; Qu et al., 2017); the bone tissue scaffolds have been tested in vitro and in vivo. The previous results demonstrate that the PCL-based polymer and HAp can mimic the organic and inorganic phases of natural bone tissue, respectively (Park et al., 2011; Shor et al., 2007; Salerno et al., 2011; Li et al., 2017, 2019; Raney and Lewis, 2015). However, the combination of PCL/PEO/HAp has not been investigated via DIW printing to date; furthermore, there is no systematic investigation of the ink optimisation progress. Thus, PCL/PEO/HAp based composite ink system is of interest in this study.

Vancomycin (VAN) is a glycopeptide antibiotic usually utilised against Gram-positive bacteria, including *Staphylococcus aureus* bacteria that is responsible for infection of the bone tissue (osteomyelitis). Considering its ototoxicity and nephrotoxicity via intravenous administration, localized and controlled deployment of this antibiotic offers a unique opportunity to deliver this antibiotic at the desired therapeutic concentration (Bailie and Neal, 1988; Weng et al., 2017). Previous studies have shown that bone tissue scaffolds containing VAN accelerated bone repair (Weng et al., 2017; Rai et al., 2016). In this paper, PCL/PEO/HAp composite inks with various HAp concentrations were used to prepare for 3D scaffold fabrication via DIW printing. VAN was incorporated within the inks to fabricate composite scaffolds and the antibacterial properties of the composites were investigated.

The aims of this study were to (1) study the influence of HAp concentration of PCL/PEO/HAp inks on ink rheology behaviours and DIW scaffold fabrication, (2) investigate the influence of HAp concentrations and inner structures on the mechanical properties of the DIW printed 3D scaffolds, and (3) evaluate the drug release and antibacterial properties of the PCL/PEO/HAp composite scaffolds. This study seeks the optimal PCL/PEO/HAp ink formulation using for DIW fabrication. The DIW printed PCL/PEO/HAp scaffolds with variable inner structures were developed, which aims for the gradient mechanical property to mimic the bone tissue layer of the osteochondral tissue.

6.2 Ink printability assessment

The formulated inks for DIW scaffold fabrication were studied using a two-step printability assessment (Zhang et al., 2020a; Paxton et al., 2017). Manual dispensing is the first assessment step, which evaluates whether the ink can form as filament and whether the formed filament can assemble as a scaffold in a layer by layer manner. The second assessment step involves rheological measurements using shear viscosity tests to investigate the shear-thinning properties of the formulations and recovery tests that involve applying alterations of high and low shear rates to the inks to compare their recovery behaviour after being exposed to high shear rates.

6.2.1 Manual dispensing

Manual dispensing testing can rapidly and effectively determine the ability for a potential ink to demonstrate the basic requirements for DIW printing by assessing whether the ink can form as a cylindrical filament. A 20 G stainless steel nozzle was used for the manual dispensing testing, which corresponds to an inner nozzle diameter of 603 μm. The dispensing behaviour of inks with HAp concentration from 55-85% w/w is shown in Figure 6.1. The inks *PCL/PEO/55%HAp*, *PCL/PEO/65%HAp*, *PCL/PEO/75%HAp*, and *PCL/PEO/85%HAp* were able to form as filament shapes. The results imply that these inks could meet the first assessment step for DIW printing.

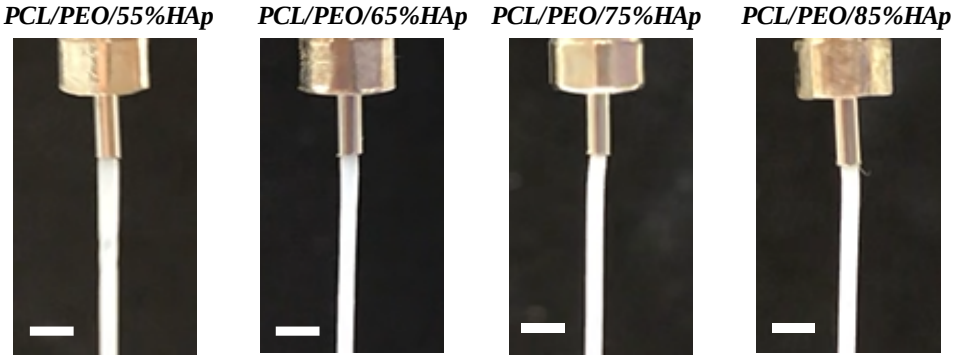

Figure 6.1: Filament formation test with manual dispensing of PCL/PEO/HAp inks with HAp concentrations from 55% to 85% w/w. The scale bar represents 1 mm.

6.2.2 Ink rheology

Routine rheology measurements were performed to characterize the shear rate-dependent viscosity and recovery behaviour of the formulated inks. The viscosity of the PCL/PEO/HAp inks with HAp concentrations from 55 to 85% w/w were evaluated through steady-state shear viscosity measurements as shown in Figure 6.2 (a). By applying the power-law model to fit the shear rate-viscosity profiles, the degree of shear-thinning was determined by calculating the consistency index and power-law index (Morrison et al., 2001), which is given by Equation 6.1:

$$\eta(\gamma) = m\gamma^{n-1} \tag{6.1}$$

where m is the consistency index and n is the power law index The value of m is associated with the magnitude of the viscosity and the value of n defines the viscosity behaviour: (i) shear-thinning if $n < 1$, (ii) shear-thickening if $n > 1$, or (iii) Newtonian if $n = 1$. The curve of $\ln\eta - \ln\gamma$ was obtained based on the ink viscosity curves. The consistency index m and power law index n for the PCL/PEO/HAp inks were obtained by fitting the slope and intercept.

Figure 6.2 (b) summarises the n and m values of PCL/PEO/HAp inks; their correlation coefficients (R^2) were greater than 0.99. The n values for all of the inks were

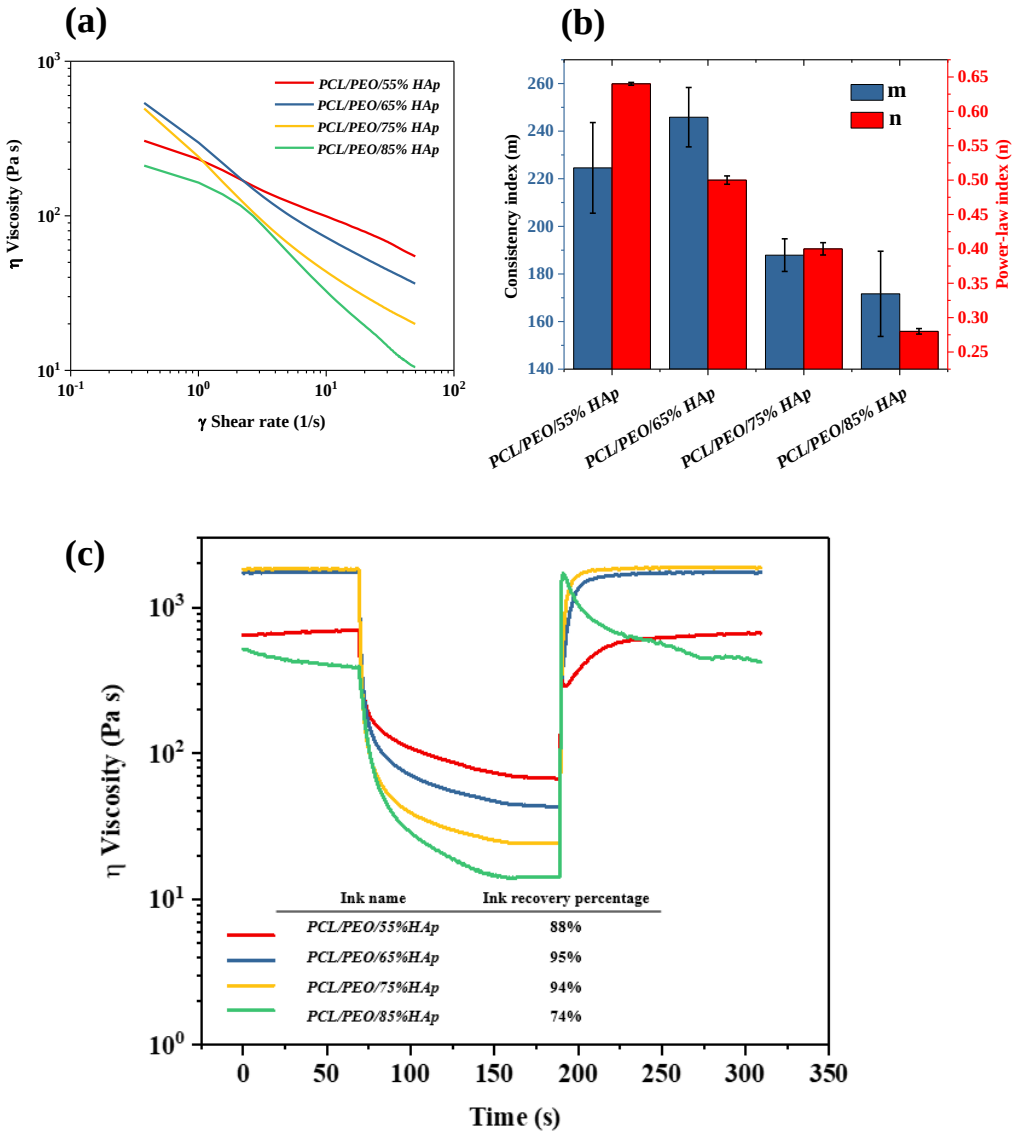

Figure 6.2: (a) The shear rate-viscosity flow curves. (b) Power law model fitting parameters - consistency index (*m*) and power-law index (*n*) for inks of *PCL/PEO/55%HAp*, *PCL/PEO/65%HAp*, *PCL/PEO/75%HAp*, and *PCL/PEO/85%HAp*. (c) Viscosity as a function of the time for the creep recovery test among PCL/PEO/HAp inks. The inserted table was the viscosity recovery percentages were calculated from the creep recovery test.

less than 1, indicating that all of inks are non-Newtonian fluids with shear-thinning behaviour. The larger the deviation of n from 1, the more non-Newtonian the behaviour of the fluid (Blair et al., 1939). The power law index (n) decreased with an increase in the HAp concentration from 55 to 85% w/w for the PCL/PEO/HAp inks, which indicates a more prevalent shear-thinning property.

Then, the ink viscosity recovery behaviour was examined using the creep recovery test. This test corresponded to the DIW printing process: (a) inks tend to become oriented in the flow direction when inks flow through the nozzle tip; (b) the viscosity decreases and stays constant in the load-interval; (c) the viscosity recovery occurs with time after removal of the high shear rate. Peak et al. (2018) indicated that the inks with an initial viscosity recovery higher than 80% could be used for 3D printing. The result of the ink viscosity recovery test is presented in Figure 6.2 (c). For inks of *PCL/PEO/55%HAp*, *PCL/PEO/65%HAp*, *PCL/PEO/75%HAp*, and *PCL/PEO/85%HAp*, the recovery percentages were 88%, 95%, 94% and 74%, respectively, at 300 s. These results indicate that all of the formulated inks could meet the second requirement for DIW printability: low viscosity values at high shear rates and high viscosity values at the low shear rate. However, considering that the ink recovery percentage should be high enough (at least 80%) to maintain ink continuity and consistency during DIW printing, the *PCL/PEO/55%HAp*, *PCL/PEO/65%HAp*, and *PCL/PEO/75%HAp* inks are more suitable for DIW printing.

6.3 Mathematical analysis of ink flow within a printing nozzle

The theoretical extrusion behaviour of inks within a printing nozzle was analysed using the mathematical model as described by Equations from 3.1 to 3.3. The spatial distributions of extrusion rate, printing velocity, and shear rate were predicted for PCL/PEO/HAp inks with HAp concentrations from 55 to 85% w/w. The profiles of velocity in the Z direction (V_z) of inks along a radial axis of 301.5 μm nozzle

were calculated using Equation 3.3 as shown in Figures 6.3 (a-d). When the fluid extrusion rate increased from 0.8 to 2.4 mm^3/s, the extrusion pressure (ΔP) and generated wall shear rate ($\dot{\gamma}$) within a printing nozzle were raised; the velocity profile along with the needle nozzle in the Z direction (V_z) decreased towards the needle wall. This result is similar to a fully developed parabolic fluid profile within a pipe, and internal friction in the fluid would resist flow motion (Chen et al., 2019a; Zhang et al., 2020b). When a fluid is in contact with a static solid surface (i.e., the needle wall), adhesion can slow the fluid flow. Meanwhile, A fluid with high viscosity has a large amount of internal friction.

In Figures 6.3 (a), the results indicate that the velocity profile of *PCL/PEO/55%HAp* ink gradually decreased from the middle of the printing needle to the needle wall. In Figure 6.3 (d), the velocity (V_z) of *PCL/PEO/85%HAp* ink kept a constant level within the needle until r = 0.15 mm, decreased gradually (r > 0.15 mm), then reached 0 at the nozzle wall (r = 0.3 mm). This result could be related to the strong shear-thinning behaviour of the *PCL/PEO/85%HAp* ink, which maintained a higher viscosity under a low shear rate than the *PCL/PEO/55%HAp* ink.

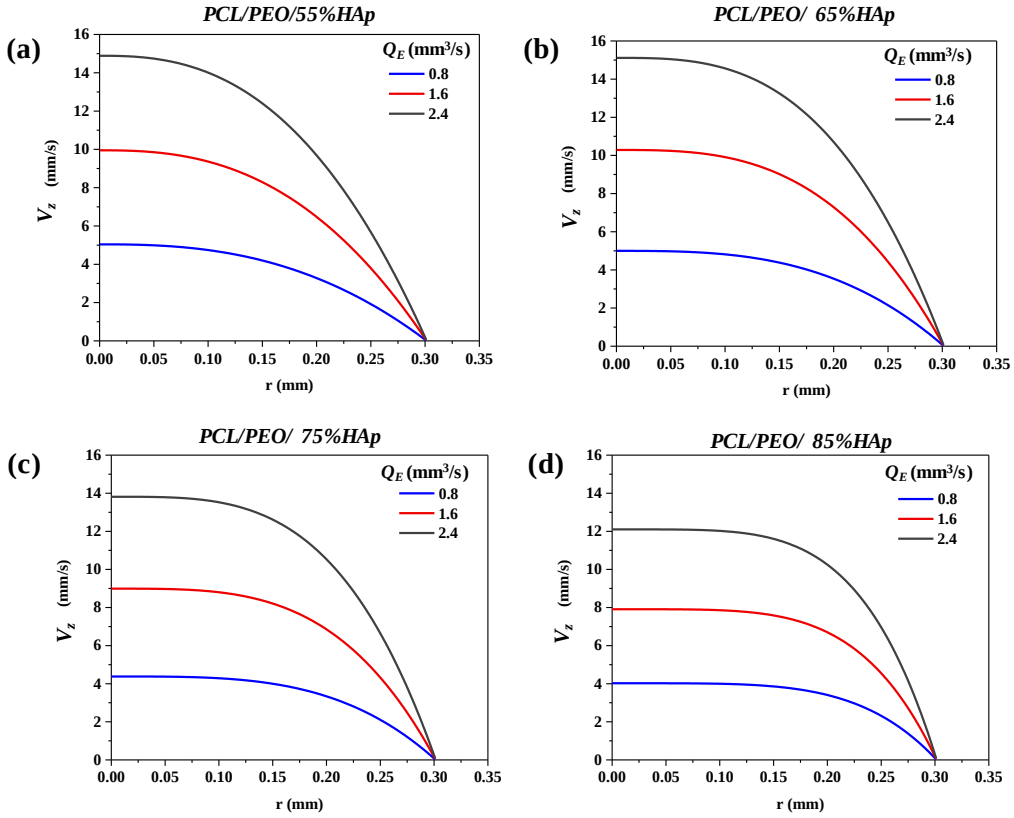

Figure 6.3: The ink velocity (Z direction) (V_z) profile inside a printing nozzle for inks of *PCL/PEO/55%HAp* (a), *PCL/PEO/65%HAp* (b), *PCL/PEO/75%HAp* (c) and *PCL/PEO/85%HAp* (d).

Figures 6.4 (a, b, c, d) show that the shear rate of four inks experienced linearly increase as a function of the extrusion flow rate (Q_E). The ink shear-thinning behaviour under extrusion allows decrease of the ink viscosity and thereby ink would flow out. When under the extrusion rate of 0.8 mm^3/s, the predicted shear rate that inks of *PCL/PEO/55%HAp*, *PCL/PEO/65%HAp*, *PCL/PEO/75%HAp*, and *PCL/PEO/85%HAp* experienced are 42.2 s^{-1}, 46.2 s^{-1}, 50.9 s^{-1}, and 60.8 s^{-1}, respectively. *PCL/PEO/85%HAp* ink exhibited approximately 1.4 times more shear rate than that of *PCL/PEO/55%HAp* ink. The higher shear rate for the *PCL/PEO/85%HAp* ink, as well as the lower recovery percentage after removing from a high shear rate (i.e. 50 s^{-1}) in the creep recovery test, which could lead the *PCL/PEO/85%HAp* ink prone to printing failure while other inks could be more suitable for successful DIW printing extrusion.

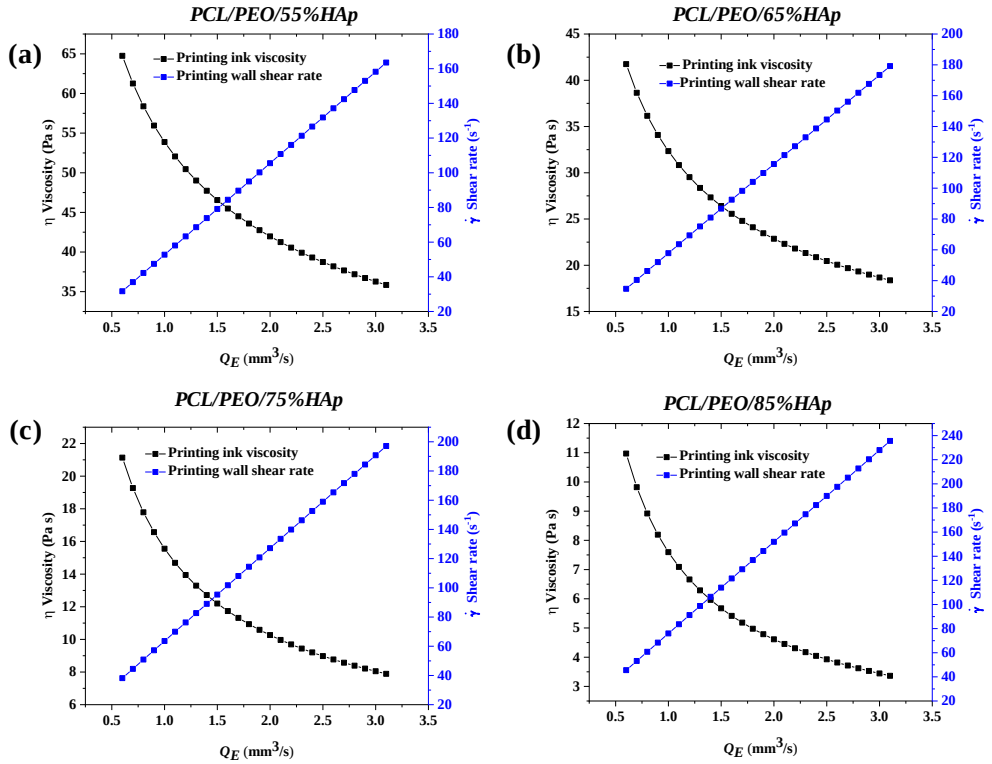

Figure 6.4: DIW printing viscosity (η) and wall shear rate ($\dot{\gamma}$) as a function of the extrusion fluid rate (Q_E) for the inks of *PCL/PEO/55%HAp* (a), *PCL/PEO/65%HAp* (b), *PCL/PEO/75%HAp* (c), and *PCL/PEO/85%HAp* (d).

6.4 Shape fidelity analysis

6.4.1 Effect of operational parameters

The extrusion rate (Q_E) and printing speed in the XY plane (V_{xy}) directly influence the shape fidelity for filament deposition. As shown in Figure 6.5 (a) for *PCL/PEO/55%HAp* ink, the printed filament width was varied by changing the printing speed (V_{xy}) when the extrusion rate was 0.8 mm^3/s. The printed filament width was 620 ± 3 µm when the print speed was 2.5 mm/s; this value was wider than the nozzle diameter (d = 603 µm). When the printing speed was 5 mm/s, the printed filament width was similar to the nozzle diameter; the width of the deposited filament was 600 ± 8 µm. When the velocity increased to 12.5 mm/s, the printed filament width was 420 ± 7 µm which was lower than the nozzle diameter.

Figure 6.5 (b, c, d, e) shows the DIW printed filament width of four types of PCL/PEO/HAp inks under various extrusion fluid rates (Q_E) from 0.8 to 2.4 mm^3/s) as well as the printing speeds (V_{xy}) from 2.5 to 12.5 mm/s. The first layer of the 3D construct (Figure 3.5(b)) was printed to access the relationship between filament width and printing parameters (i.e. extrusion rate and printing speed). The DIW printed filament width increased with a decrease in print velocity (V_{xy}) or an increase in fluid extrusion rate (Q_E), and vice versa. It would not able to measure the filament width once the printed filament width would exceed interfilament distance.

The relative filament deviation index ($\sigma_{filament}$) was used to evaluate the shape fidelity of the DIW printed filaments as calculated from Equation 3.6. The $\sigma_{filament}$ approached 0 when the filament width ($W_{filament}$) matched the nozzle diameter (d). The relative filament deviation indexes at various extrusion fluid rate (Q_E) and print velocity (V_{xy}) values were compared in Figure 6.6 (a, b, c, d). Optimisation of the shape fidelity ($\sigma_{filament}$ was closest to 0) was demonstrated at a printing speed V_{xy} of 5 mm/s and a fluid extrusion rate Q_E of 0.8 mm^3/s for the inks *PCL/PEO/55%HAp* and *PCL/PEO/65%HAp*. Similarly, a printing speed (V_{xy}) of 7.5 mm/s and an extrusion fluid rate (Q_E) of 0.8 mm^3/s were optimal for the inks *PCL/PEO/75%HAp* and *PCL/PEO/85%HAp*. These operation parameters were subsequently used to build the 3D scaffolds in a layer by layer manner.

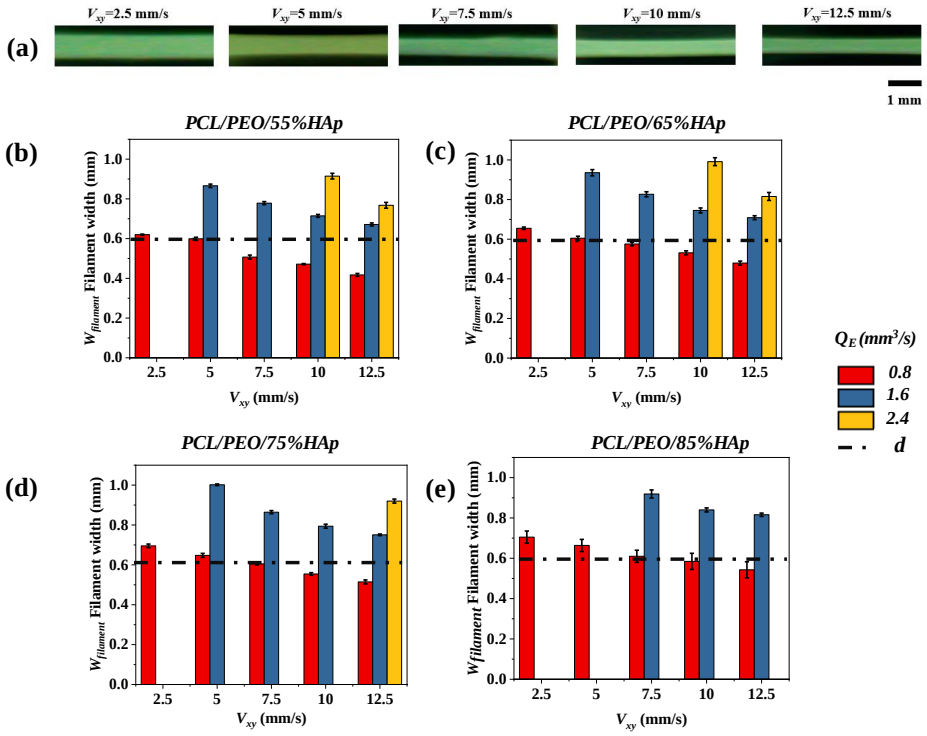

Figure 6.5: (a) The printed filament width of ink *PCL/PEO/55%HAp* decreases with the increased print speed V_{xy} when the extrusion rate Q_E as 0.8 mm^3/s, the scale bar is 1 mm. The DIW printed filament width compares with the applied nozzle diameter (d=603 μm) under the designated printing speed (V_{xy}) and extrusion rate (Q_E) with inks of *PCL/PEO/55%HAp* (b), *PCL/PEO/65%HAp* (c), *PCL/PEO/75%HAp* (d), and *PCL/PEO/85%HAp* (e).

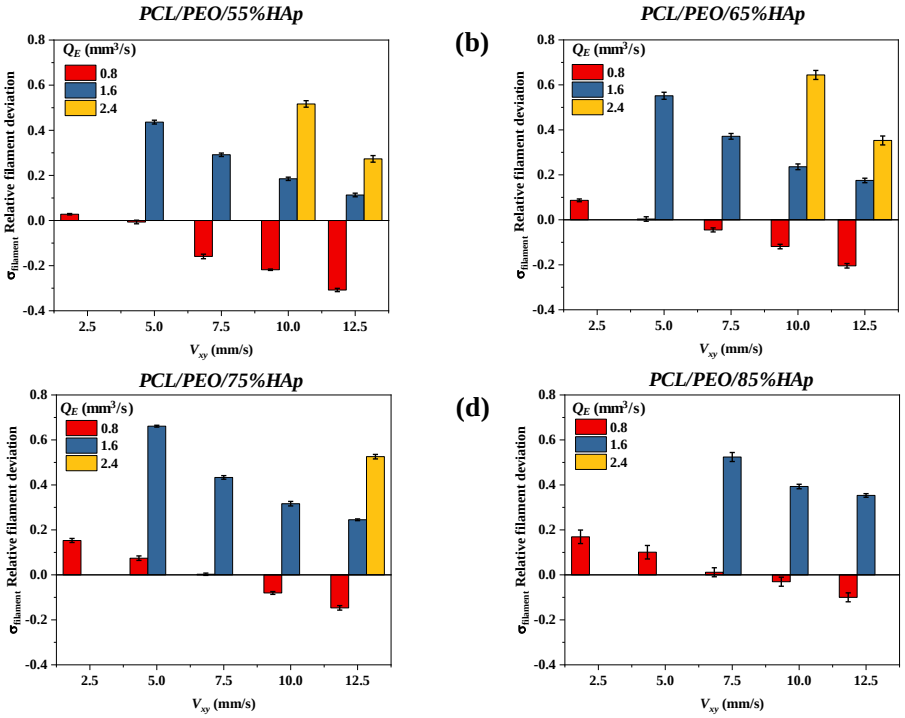

Figure 6.6: Relative filament deviation ($\sigma_{filament}$) as an index to evaluate the DIW printed filament width under the designated printing speed (V_{xy}) and extrusion rate (Q_E) with inks of *PCL/PEO/55%HAp* (a), *PCL/PEO/65%HAp* (b), *PCL/PEO/75%HAp* (c), and *PCL/PEO/85%HAp* (d).

6.4.2 3D constructs

The printed 3D scaffolds *PCL/PEO/55%HAp*, *PCL/PEO/65%HAp*, *PCL/PEO/75%HAp*, and *PCL/PEO/85%HAp* were built in a layer by layer manner. The images of the printed samples, showing 12 layers, are provided in Figure 6.7 (a). In Table 6.1, the printed dimensions (width, length, and thickness) of the scaffolds were smaller than the CAD theoretical values. Previous studies (Roopavath et al., 2019; Lin et al., 2019) also show similar results and reflected the shrinkage issue of the DIW printed scaffolds. With the increase in HAp concentration, the difference between the theoretical values and experimental values in terms of width, length, and thickness gradually decreased. This result indicates that adding HAp nanoparticles relieves the shrinkage issue. The filament width ($W_{filament}$) of the top layer of the DIW printed scaffolds were compared with the applied nozzle diameter (d) in Figure 6.7

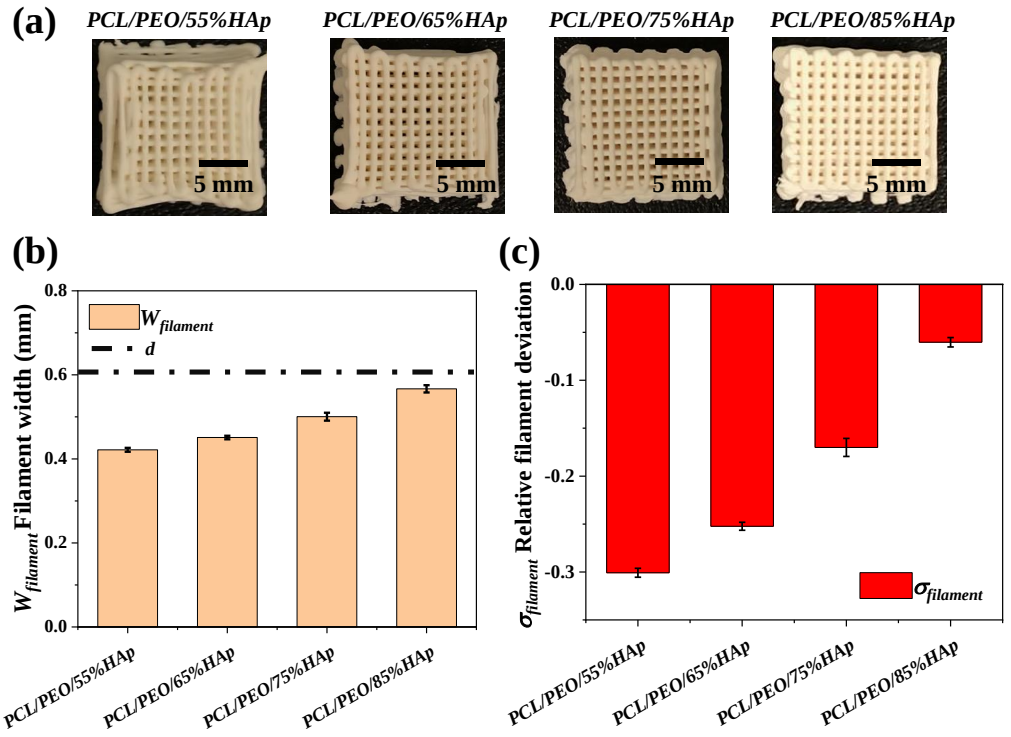

Figure 6.7: Scaffold image (a), the measured filament width ($W_{filament}$) compares with the applied nozzle diameter (d=603 μm) (b) and relative filament deviation ($\sigma_{filament}$) (c) of DIW printed 3D scaffolds - *PCL/PEO/55%HAp*, *PCL/PEO/65%HAp*, *PCL/PEO/75%HAp*, and *PCL/PEO/85%HAp*.

(b). A comparison of the relative filament deviation indexes ($\sigma_{filament}$) from the top layers of all of the DIW printed samples is shown in Figure 6.7 (c). This result confirms that all of the samples have shrinkage due to relative filament deviation indexes ($\sigma_{filament}$) that were less than 0. The printed filament of *PCL/PEO/85%HAp* was most closely matched to the nozzle diameter (d); the $\sigma_{filament}$ was the closest to 0.

6.5 Mechanical property

6.5.1 The influence of HAp concentration

The compressive test was applied to evaluate the mechanical property of DIW printed samples - *PCL/PEO/55%HAp*, *PCL/PEO/65%HAp*, *PCL/PEO/75%HAp*,

Table 6.1: The comparison of designed theoretical values of CAD structures and DIW printed 3D scaffolds, ($n = 3$).

	Width (mm)	Length (mm)	Thickness (mm)
Theoretical value	14	14	5
Experimental value			
PCL/PEO/55%HAp	12.65 ± 0.23	12.50 ± 0.20	4.24 ± 0.03
PCL/PEO/65%HAp	12.89 ± 0.24	12.95 ± 0.16	4.43 ± 0.08
PCL/PEO/75%HAp	13.53 ± 0.10	13.55 ± 0.26	4.64 ± 0.09
PCL/PEO/85%HAp	13.95 ± 0.03	13.83 ± 0.10	4.67 ± 0.06

and *PCL/PEO/85%HAp*. The schematic compressive setting up, as shown in Figure 6.8 (a). To analyse the results, the area of 14 mm x 14 mm was assumed (area = 196 mm^2) to calculate stress for all samples. The strain was also calculated by the displacement divide the thickness of printed samples. The elastic modulus was taken as the slope of a linear region of the stress-strain curve before the yield point. In Figure 6.8 (b), the compression experiment results indicate elastic modulus of PCL/PEO/HAp scaffolds increased when the HAp concentration increased from 55% to 65% w/w, which was 7.20 ± 0.87 MPa and 10.75 ± 0.31 MPa, respectively. However, elastic modulus decreased when the HAp concentration was rising from 65% to 85% w/w. The elastic modulus of samples of *PCL/PEO/75%HA* and *PCL/PEO/85%HA* were 4.44 ± 0.55 MPa and 3.56 ± 0.32 MPa, respectively. This could be explained by the fact that the HAp nanoparticles and polymers were physically blend, the increasing concentrations of HAp particles would cause the brittleness of printed filament and further lead to the decrease of elastic modulus of scaffolds. As shown in Figure 6.8 (c), the SEM micrographs of the surface morphology of the DIW printed scaffolds indicate that small cracks started to appear on top of the filament surface of sample *PCL/PEO/75%HAp* and *PCL/PEO/85%HAp*.

The yield strength values had the same trend as the elastic modulus values; yield strength values of 0.77 ± 0.03, 0.97 ± 0.03, 0.42 ± 0.02, 0.35 ± 0.05 MPa were obtained for the samples *PCL/PEO/55%HAp*, *PCL/PEO/65%HAp*, *PCL/PEO/75%HAp*, and *PCL/PEO/85%HAp*, respectively. The result indicates that the scaffold *PCL/PEO/65%HA* had the best elastic modulus and yield strength.

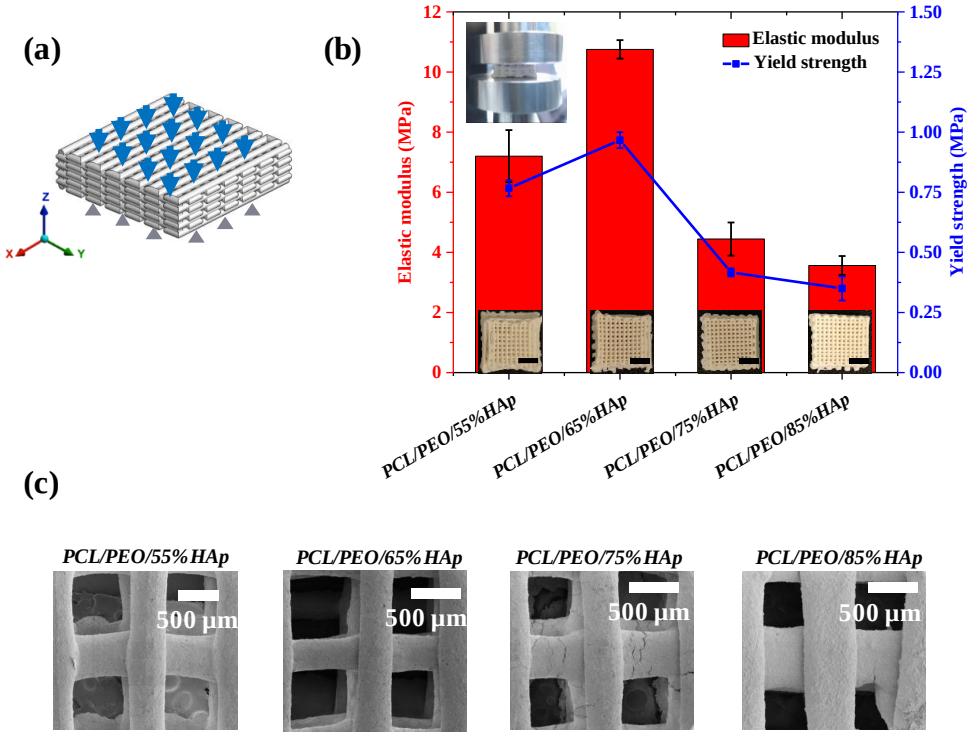

Figure 6.8: (a) The schematic of setup for the compressive test, an example of compressive loading in the *Z* direction is shown - the bottom plate is fixed, and the top plate moves downwards in the *Z* direction. (b) The elastic modulus and yield strength of DIW printed scaffolds, the inserted images are the DIW printed PCL/PEO/HAp scaffolds - *PCL/PEO/55%HAp*, *PCL/PEO/65%HAp*, *PCL/PEO/75%HAp*, and *PCL/PEO/85%HAp* (n=4), the scale bar is 5 mm. (c) The corresponding SEM micrographs of the surface morphology of the DIW printed scaffolds. The SEM images were collected on the pristine DIW printed samples, i.e. before mechanical testing.

6.5.2 The influence of scaffold pore geometries

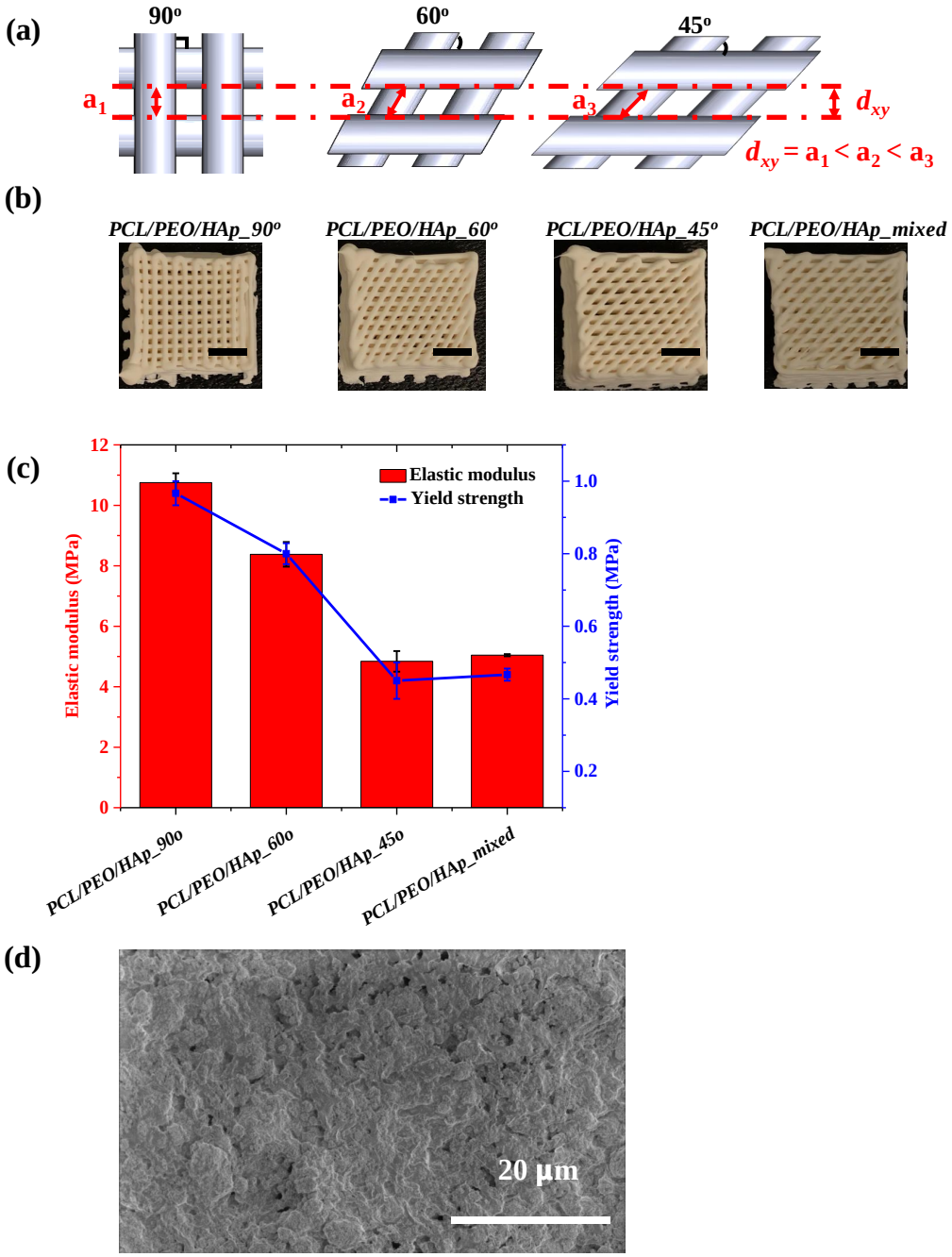

Figure 6.9: (a) The unit cells of various lay-down angles of CAD scaffolds in the *XY* plane. (b) The DIW printed PCL/PEO/HAp scaffolds with HAp concentrations of 65% w/w - *PCL/PEO/HAp_90°*, *PCL/PEO/HAp_60°*, *PCL/PEO/HAp_45°*, and *PCL/PEO/HAp_mixed*; the scale bar is 5 mm. (c) The elastic modulus and yield strength of DIW printed PCL/PEO/HAp scaffolds (n=4). (d) The SEM image of the filament surface morphology of *PCL/PEO/65%HAp* scaffold.

The PCL/PEO/HAp ink with 65% w/w HAp concentration was applied to fabricate the scaffold with different pore geometries (intersection angles of 90°, 60°, 45°, and mixed angles). Figure 6.9 (a) shows the design of the unit geometry of the scaffold structure. For all structures, their pore widths (d_{xy}) were all 500 μm. Their porosity of CAD design (47%) was the same as that calculated from Equation 3.4 and 3.5. Their edge length of pore (a_1, a_2, a_3) for samples of *PCL/PEO/HAp_90°*, *PCL/PEO/HAp_60°*, *PCL/PEO/HAp_45°* had the relationship as $a_1 < a_2 < a_3$. The DIW printed scaffold is shown in Figure 6.9 (b). Figure 6.9 (c) shows the elastic modulus and yield strength of those printed samples. The results indicate that the *PCL/PEO/HAp_90°* had the highest elastic modulus and yield strength, which were 10.75 ± 0.31 MPa and 0.97 ± 0.03 MPa, respectively. Scaffold *PCL/PEO/HAp_60°* was the second, its elastic modulus and yield strength were 8.38 ± 0.41 MPa, and 0.8 ± 0.03 MPa. The elastic modulus and yield strength for scaffold *PCL/PEO/HAp_45°* were the smallest, and they were 4.84 ± 0.34 MPa, and 0.45 ± 0.05 MPa, respectively. The elastic modulus and yield strength of mixed angles sample (*PCL/PEO/HAp_mixed*) were slightly higher than the *PCL/PEO/HAp_45°* sample, which were 5.04 ± 0.04 MPa, and 0.47 ± 0.02 MPa. One of the reasons for the gradually decreased elastic modulus and yield strength of *PCL/PEO/HAp_90°*, *PCL/PEO/HAp_60°*, *PCL/PEO/HAp_45°* is the increased edge length of the ($a_1 < a_2 < a_3$). As shown in Figure 6.9 (d), there are micro and nanopores on top of the filament surface of the printed scaffolds, and thus those pores could make the scaffold reach their yield strength easily under the compressive load when the scaffolds with a larger edge length. For those scaffolds with mixed angles - the overlay structures with three angles (90°, 60°, 45°), the smaller edge lengths from 90° structure could cancel out the disadvantage influence that brought from the larger edge length of filament from 45° angle structure. This could be the reason that the mechanical property of *PCL/PEO/HAp_mixed* was slightly better than the sample of *PCL/PEO/HAp_45°*.

6.6 Wettability

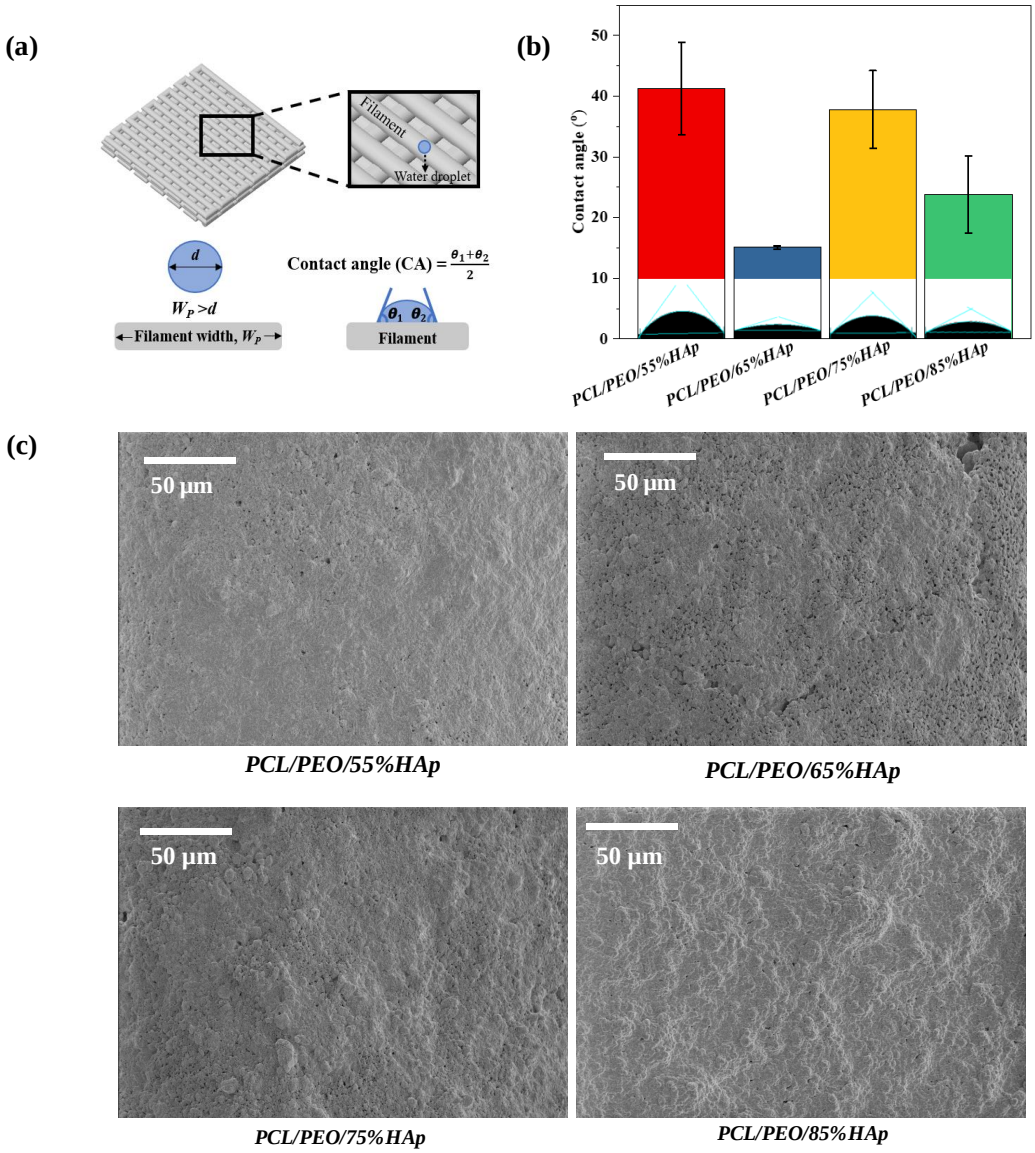

Figure 6.10: (a) The schematic diagram of contact angle. (b) The initial CA results on the DIW printed filament surface ($n = 3$). (c) SEM images of the surface morphology of the DIW printed samples - *PCL/PEO/55%HAp*, *PCL/PEO/65%HAp*, *PCL/PEO/75%HAp*, and *PCL/PEO/85%HAp*.

Contact angle (CA) is a measure of surface wettability, which indicates whether the material is hydrophilic (< 90°) or hydrophobic (> 90°) (Dubey et al., 2015). The CA value from the top layer filament of DIW printed samples are shown in Figure 6.10 (a). A droplet volume of 4×10^{-3} µL was applied for the CA measurement; the

droplet diameter was approximately 200 µm, which was smaller than the filament width (ranging from 420 to 570 µm). Thus, the CA approach was able to place the water droplets on top of a single filament.

Figure 6.10 (b) shows the initial contact point of a droplet on the top layer filament of DIW printed samples. The CA values were $41.3 \pm 7.6°$, $15.1 \pm 0.3°$, $37.8 \pm 6.4°$ and $23.8 \pm 6.3°$ for *PCL/PEO/55%HAp*, *PCL/PEO/65%HAp*, *PCL/PEO/75%HAp*, and *PCL/PEO/85%HAp*, respectively (n=3). After 500 ms, the droplets infiltrated through the *PCL/PEO/65%HAp* samples, and the CA values become 0, thus indicating that the filaments of *PCL/PEO/65%HAp* wetted entirely within less than 500 ms. For the other samples, *PCL/PEO/55%HAp*, *PCL/PEO/75%HAp*, and *PCL/PEO/85%HAp*, the CA values were $32.5 \pm 5.5°$, $27.5 \pm 3.7°$, $15.3 \pm 5.1°$, respectively, at 10 s. The sample *PCL/PEO/55%HAp* provided the largest CA values on the printed samples ($p < 0.05$). The results suggest that the surface wettability of DIW printed samples is affected by the addition of HAp. The samples of *PCL/PEO/65%HAp* had the smallest CA values; the materials also contained more micro and nanopores on top of the filament surface as indicated in Figure 6.10 (c).

6.7 Material characterisation

FTIR was used to identify molecular bands of PCL, PEO, HAp, and PCL/PEO/HAp composite scaffolds as shown in Figure 6.11 (a-d). The FTIR spectra of DIW printed vancomycin-loaded PCL/PEO/HAp scaffolds Figure 6.11 (e, f) and vancomycin (VAN) Figure 6.11 (g) were also obtained. As shown in the inserted image of Figure 6.11, VAN showed three peaks at 1506 cm^{-1}, related to aromatic rings; features at 1588 cm^{-1} and 1652 cm^{-1} correspond to the peaks of amide I, and amide II, respectively. The intensity of the peaks at 1652 cm^{-1} was found to increase with increasing VAN concentration. These features were not observed in PCL/PEO/HAp scaffolds without VAN. Additionally, 1506 cm^{-1} and 1588 cm^{-1} peaks were detected only in scaffolds with higher VAN content (9% w/w) as shown

in Figure 6.11 (f).

The interaction between VAN and either PCL or PEO potentially occurs via hydrogen bond formation. The N-H moiety in vancomycin molecule is capable of forming hydrogen bonds with the C-O-C moiety in PCL and PEO. The intensities of peaks at 1187 cm^{-1}, 1168 cm^{-1} and 1095 cm^{-1}, attributed to OC-O stretching, symmetrical COC stretching, and C-O-C stretching vibration, were reduced. The reduced intensities of these peaks could indicate that OC-O and C-O stretching of PCL and PEO monomers were diminished, which may be caused by hydrogen bond formation between PCL and VAN. The FTIR spectra of drug-loaded scaffolds showed no visible peak shifts compared with the unloaded scaffold (Figure 6.11). This result indicated that drug-composite interactions were weak after the DIW process. The PCL/PEO/HAp composite scaffold shows the main characteristic absorption bands of PCL, PEO, and HAp. The FTIR spectra also confirmed the presence of VAN in the DIW printed composite scaffold, suggesting that VAN was successfully encapsulated by DIW printing method to produce a drug/polymer/ceramic composite scaffold.

PXRD was used to determine the phase structure of the PCL/PEO/HAp composites. Figure 6.12 shows the PXRD pattern of the printed PCL/PEO/HAp scaffold. The peaks at angles $2\theta = 21.4°$ and 23.8° correspond to the (110) and (200) crystallographic planes of the semi-crystalline nature of the PCL biopolymer (Abdelrazek et al., 2016). PEO exhibits two characteristic peaks at angles around $2\theta = 23°$, and 19° (Nasir et al., 2005). HAp exhibits broad peaks, suggesting that the nanoparticle size is very small (Ragu et al., 2014). The characteristic of peaks of PCL, PEO and HAp were unchanged in the PCL/PEO/HAp blends.

Additionally, a broad feature was observed in the PXRD pattern of vancomycin from 2θ of 10° to 35° as shown in Figure 6.12; this result indicates that VAN is amorphous (Zarif et al., 2012). The PXRD patterns of the VAN loaded PCL/PEO/HAp samples - *PCL/PEO/HAp_3%VAN* and *PCL/PEO/HAp_9%VAN* were similar to that of *PCL/PEO/HAp_without VAN*. These results suggest that the

crystallinity of the PCL/PEO/HAp was maintained after loading with VAN.

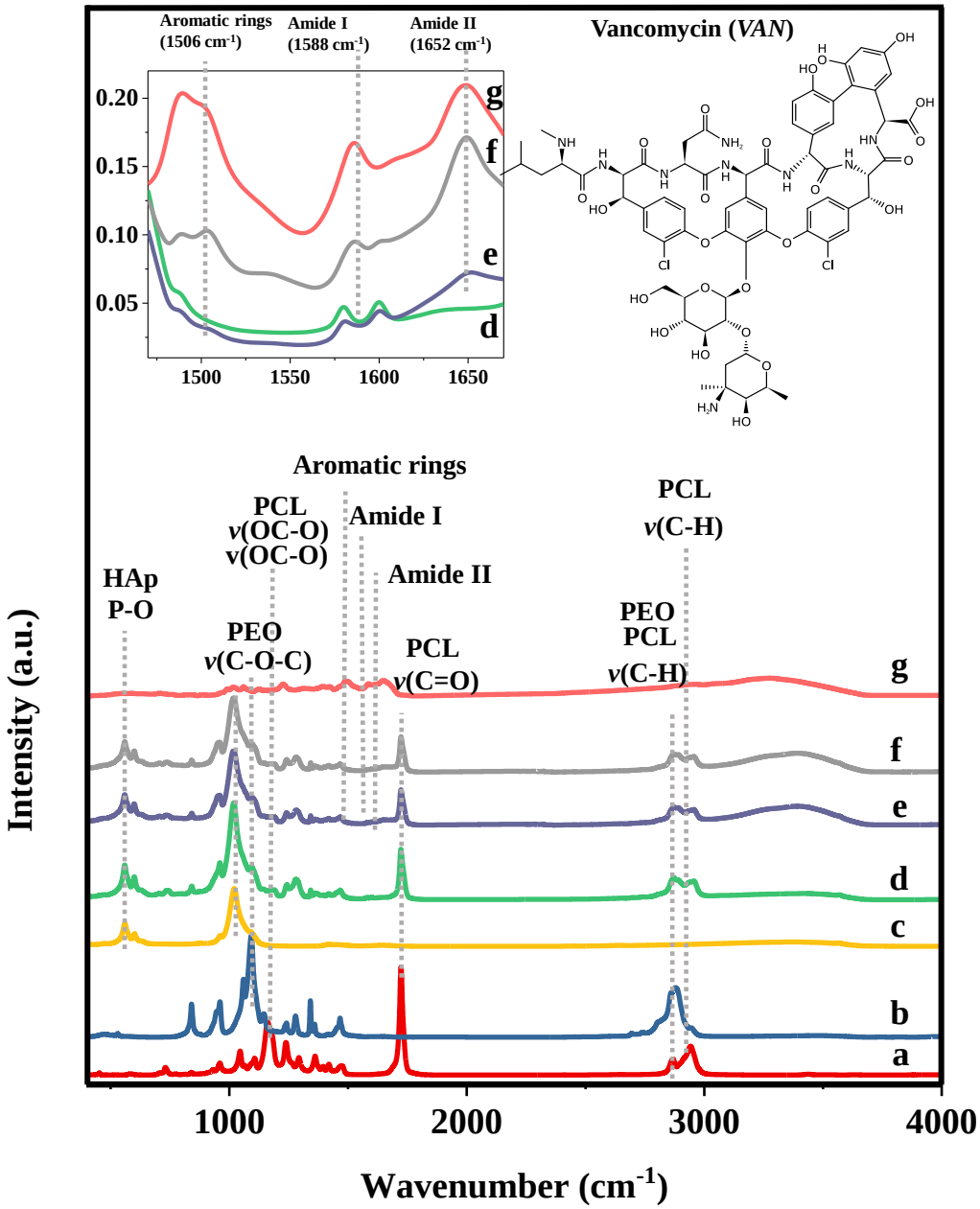

Figure 6.11: FTIR spectra of PCL (a), PEO (b), HAp (c), DIW printed *PCL/PEO/65%HAp scaffold* (d), *PCL/PEO/HAp_3%VAN* scaffold (e), *PCL/PEO/HAp_9%VAN* scaffold (f) and VAN (g). The insert image represents stacked spectra of VAN drug and PCL/PEO/HAp scaffold with and without VAN: the intensity of the VAN peak at 1662 cm^{-1} increases with increasing VAN content.

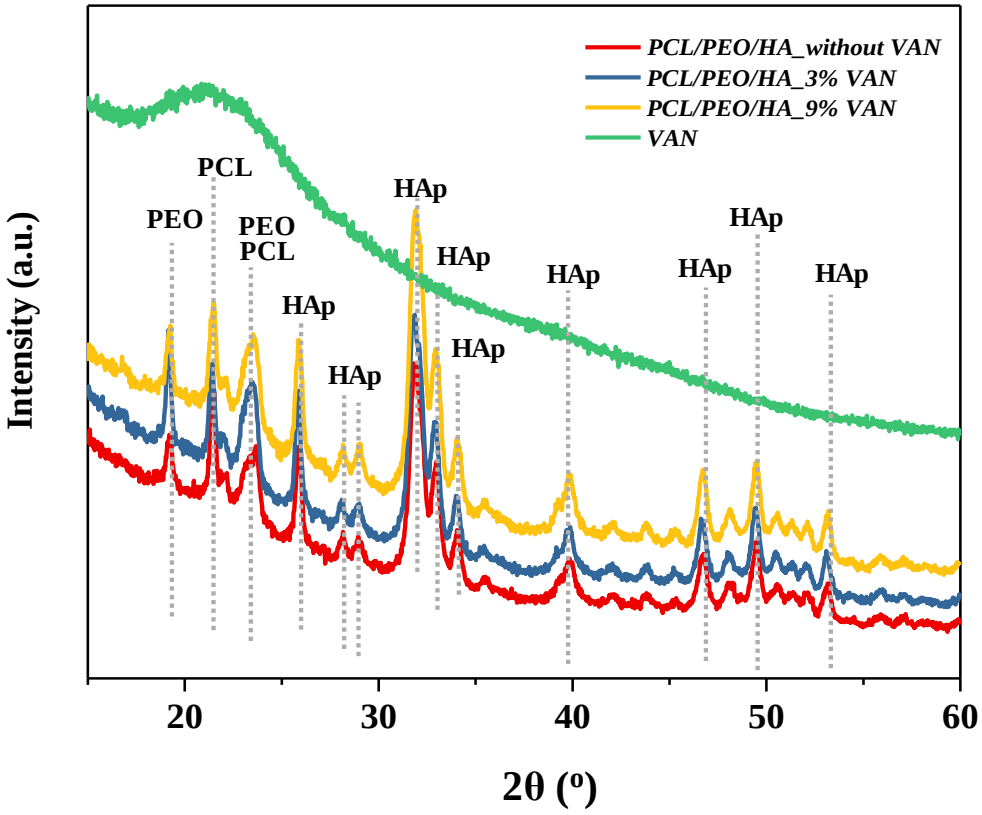

Figure 6.12: PXRD patterns of the DIW printed *PCL/PEO/65%HA scaffold* (i.e. *PCL/PEO/HAp_without VAN*), *PCL/PEO/HAp_3%VAN scaffold*, *PCL/PEO/HAp_9%VAN* scaffold and VAN powder: VAN amounts does not affect the crystallinity of DIW printed PCL/PEO/HAp scaffold.

6.8 Drug loaded 3D scaffolds

6.8.1 In vitro dissolution test

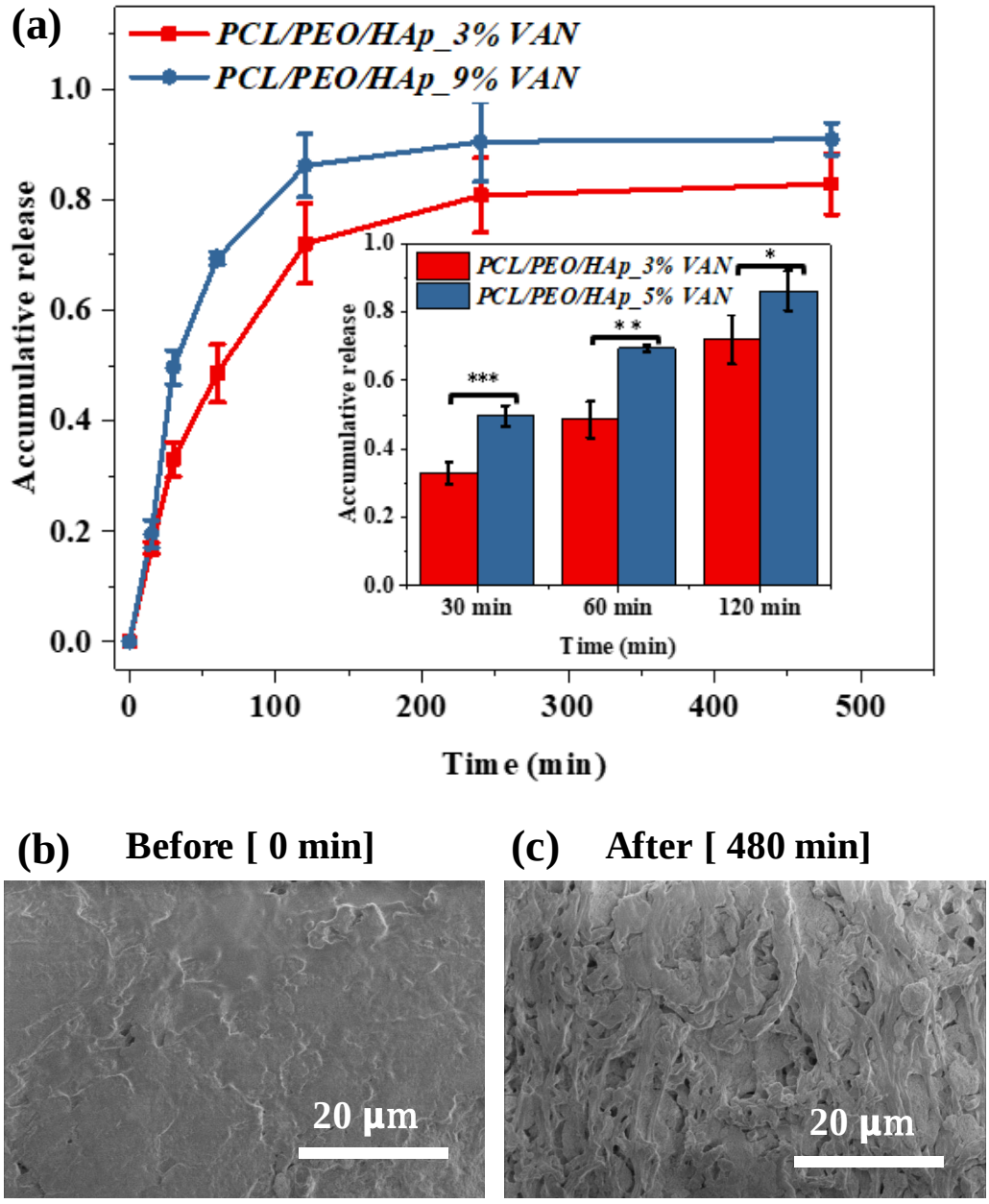

Figure 6.13: (a) VAN release profiles from DIW printed samples - *PCL/PEO/HAp_3%VAN* and *PCL/PEO/HAp_9%VAN* (n=3) in PBS (pH=7.4) with temperature set at 37°C. SEM micrographs before (b) and after (c) release studies of *PCL/PEO/HAp_9%VAN*.

The release kinetics of DIW printed PCL/PEO/HAp samples containing low and high VAN loading (3% and 9% w/w) were determined in vitro; the effect of drug loading on release profile was examined. The accumulative release profiles of VAN from the DIW printed constructs is shown in Figure 6.13. Total release values of $82.67 \pm 0.06\%$ and $91 \pm 0.03\%$ were obtained for *PCL/PEO/HAp_3%VAN* and *PCL/PEO/HAp_9%VAN*, respectively, after 480 min. The in vitro release profile results were in line with the literature data reporting an initial burst release of the incorporated drug followed by a slow-release phase (Potrč et al., 2015; Rychter et al., 2018). Additionally, the release profiles revealed the formulation with a higher VAN loading released VAN faster than the formation with a lower drug loading, especially for the time points of 30 min, 60 min, and 120 min; the drug release results were 33.01%, 48.57%, 72.06% at 30 min, 60 min, and 120 min for *PCL/PEO/HAp_3%VAN* and 49.66%, 69.39%, 86.18% at 30 min, 60 min, and 120 min for *PCL/PEO/HAp_9%VAN*. SEM micrographs (Figure 6.13 (b) and (c)) show the surface morphology of the drug-loaded scaffold before and after the release study of sample *PCL/PEO/HAp_3%VAN*.

6.8.2 Agar diffusion test

The agar diffusion test was used to examine the antibacterial activity of PCL/PEO/HAp scaffold, with low (3% w/w) and high (9% w/w) VAN concentrations against both *S. aureus* (Gram-positive) and *P. aeruginosa* (Gram-negative) bacteria. The inhibition zone values of drug loaded PCL/PEO/HAp scaffolds were calculated based on Equation 3.7. At 24 h after treatment, it was found that the inhibition zone values for samples *PCL/PEO/HAp_3%VAN*, and *PCL/PEO/HAp_9%VAN* on the *S. aureus* (Gram-positive) inoculated plates were 15.82 ± 0.25 and 20.06 ± 0.25 mm, respectively (Figure 6.14 a, c).

Figure 6.14 (b) shows the antimicrobial activity on *P. aeruginosa* (Gram-negative) bacteria, which indicates that there was growth on the surface of scaffold and no zone of inhibition for *PCL/PEO/HAp_without VAN*; there was no growth on the surface of the scaffold and no zone of inhibition for *PCL/PEO/HAp_3%VAN*;

on the other hand, the zone of inhibition was 3.58 ± 0.18 mm for sample *PCL/PEO/HAp_9%VAN*. Thus, based on the analysis of the zone of inhibition, it can be concluded that the addition of VAN provided the PCL/PEO/HAp scaffold with potent antibacterial activity.

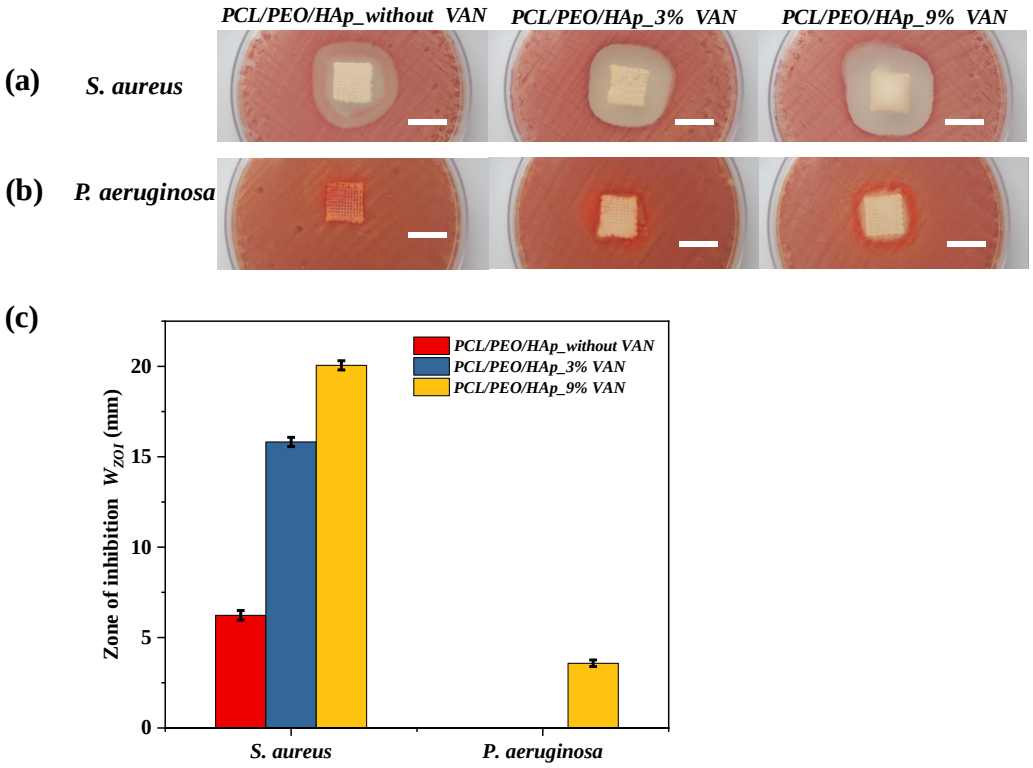

Figure 6.14: Photographic images for the inhibition zone of sample *PCL/PEO/HAp_without VAN*, *PCL/PEO/HAp_3%VAN*, and *PCL/PEO/HAp_9%VAN* against *S. aureus* (Gram-positive) (a) and *P. aeruginosa* (Gram-negative) (b), and the quantitative data analysis zone of inhibition (c).

6.9 Discussion

An increase in the HAp concentration in PCL/PEO/HAp inks had a noteworthy impact on the ink rheological properties. The initial viscosity (when shear rate as 0.05 s^{-1}) of *PCL/PEO/65%HAp* inks were the highest, and the initial viscosity of the *PCL/PEO/85%HAp* inks were the lowest. This result may be due to the greater interchain bonding in the polymers within *PCL/PEO/65%HAp* inks than in the *PCL/PEO/85%HAp* inks, which in turn lead to higher viscosity values for

the *PCL/PEO/65%HAp* inks at rest or low shear strains. This phenomenon also can be correlated with ink recovery behaviour results. At the high shear rate (50 s^{-1}), the *PCL/PEO/65%HAp* inks had the highest recovery percentage (95%); the *PCL/PEO/85%HAp* inks had the lowest recovery percentage (74%). Moreover, the power law index (n) of PCL/PEO/HAp inks decreased with the increase in the HAp concentration from 55% to 85% w/w. This result could be due to the difference in solute polarity between the polymer molecules and HAp particles. All inks showed the shear-thinning non-Newtonian behaviour; however, an adequate recovery percentage of viscosity (> 80%) with a time-dependent increase were only possible with the *PCL/PEO/55%HAp*, *PCL/PEO/65%HAp*, and *PCL/PEO/75%HAp* inks. This result implies that inks with a HAp concertation greater than 75% (such as *PCL/PEO/85%HAp* ink) would not be an ideal printable material for DIW printing.

The elastic modulus and yield strength values are greater when HAp concentration increases from 55% to 65% w/w. Similar results also can be found in other studies (Arunkumar et al., 2019; Liu et al., 2019). However, when the HAp content increased up to 75% w/w, the elastic modulus and yield strength decreased. One possible reason could be related to the ink recovery behaviour. The mechanical property results of the PCL/PEO/HAp scaffold were in line with the ink recovery percentage. Another possible reason is that small cracks were observed from the SEM images on the surface of DIW printed samples with more than 75% HAp content. There was an increase of polymer and ceramic molecule bonding when the concentration of HAp was increased from 55% to 65% w/w. However, when the HAp concentration was increased to 75% and 85% w/w, the additional HAp particles did not bond with polymer molecules and directly attached on top of the filament surface to form small cracks. Thus, the mechanical properties of *PCL/PEO/75%HAp* and *PCL/PEO/85%HAp* scaffold were inferior to those of *PCL/PEO/65%HAp*. From this perspective, the *PCL/PEO/65%HAp* ink is the most suitable formulation for the DIW fabrication 3D scaffolds.

Additionally, the mechanical property of scaffolds with different pore geometries was compared, and the results indicate that the sample *PCL/PEO/HAp_90°* had

the highest elastic modulus (10.75 MPa) and yield strength (0.97 MPa). Their elastic modulus and yield strength were decreased when the pore geometries change from 90° to 45°. Meanwhile, a scaffold should ideally exhibit mechanical properties (i.e., yield strength and elastic modulus) that are similar to those of human bone tissue. Table 6.2 shows the compressive yield strength and elastic modulus of human cortical and cancellous bones. The elastic modulus and yield strength of PCL/PEO/HAp scaffolds fabricated in this study were in the range of 3.56 to 10.75 MPa, and 0.97 to 0.35 MPa, depending on the HAp concentration. Those results were in the range of the mechanical properties of human cancellous bones.

Table 6.2: Mechanical properties of human cortical and cancellous bones (Athanasiou et al., 1994; Boschetti et al., 2004; Gibson, 1985; Sabree et al., 2015; Antons et al., 2018; Oladapo et al., 2019).

	Compressive yield strength (MPa)	Compressive elastic modulus (GPa)
Cancellous bone	0.1-10	0.001-0.9
Cortical bone	100 - 230	7-30

The VAN drug was successfully loaded into the DIW printed PCL/PEO/HAp composite scaffolds. The VAN loaded PCL/PEO/HAp scaffolds exhibited an initial burst pattern within the first hour drug dissolution. The initial burst phenomenon was more prominent for *PCL/PEO/HAp_9%VAN* than for *PCL/PEO/HAp_3%VAN*. A similar trend was found in previous studies (Kim et al., 2005; Weng et al., 2017; Parker et al., 2012). This result may be attributed to the hydrophilic nature of VAN. The vancomycin molecules do not have a specific binding affinity to the components of the PCL/PEO/HAp scaffold. The VAN was distributed on the surface of filament before the release study as seen in the SEM image of Figure 6.13 (b); this initial burst release in the initial phase may be attributed to this morphology. Figure 6.13 (c) shows the surface morphology of scaffold after release revealed that VAN was almost entirely eluted. Meanwhile, the higher drug content would create a higher concentration gradient between the construct and the outer dissolution media to drive the drug release, in comparison to the construct with lower drug loading.Thus, the drug release results showed sudden drug release within a short period, particularly for the scaffold with a higher VAN concentration.

S. aureus (Gram-positive) and *P. aeruginosa* (Gram-negative) bacteria were selected in this study due to these strains infections account for approximately 80% of clinical orthopedic infections (DeLeon et al., 2014; Grayson et al., 2010). It is noteworthy that the antibacterial activity of the VAN loaded PCL/PEO/HAp composite scaffolds against *S. aureus* (Gram-positive) bacteria were higher than against *P. aeruginosa* (Gram-negative) bacteria. Similar results were also described in other studies (Savitskaya et al., 2019; Mai-Prochnow et al., 2016). The structure of Gram-positive bacteria does not include an outer cell membrane, which can be found in Gram-negative bacteria. As such, Gram-negative bacteria are more resistant to antibiotics since they have a largely impermeable cell wall. However, the inhibition zone of both *S. aureus* and *P. aeruginosa* increased and antibacterial activity improved with the addition of VAN for the drug loaded PCL/PEO/HAp scaffolds.

6.10 Conclusions

This chapter demonstrates the processing of biocomposite PCL/PEO/HAp inks with HAp concentrations from 55% to 85% w/w; woodpile scaffold structures with the formulated composite inks were successfully fabricated. The ink rheology properties, scaffold material properties, surface properties, and mechanical properties of the scaffold structures were investigated. The rheological data indicate that upon increasing the concentration of HAp, more marked shear-thinning behaviour was observed. Based on the mathematical modelling analysis of ink conditions within the printing needle, the shear rate of the *PCL/PEO/85%HAp* ink was the higher than that of other types of inks; while it had the lowest ink recover rate. Thus, the results suggest HAp concentration should be not higher 75% w/w in PCL/PEO/HAp composite inks for scaffold fabrication using DIW printing.

The *PCL/PEO/65%HAp* scaffold had a better wettability and higher mechanical properties compared to others. Also 65% w/w HAp concentration is close to the inorganic composition of natural bone tissue. The obtained elastic modulus and yield strength of the DIW printed scaffolds were in the range of the mechanical

properties of human cancellous bones. Furthermore, in vitro drug release and agar diffusion data demonstrated that the VAN-loaded scaffolds were capable of releasing VAN and antibacterial activity. Combining these outcomes, the PCL/PEO/HAp composite developed in this study offers a new ink for the DIW printing technique for the fabrication of 3D scaffolds with tunable mechanical properties and antibacterial activity for biomedical applications.

Chapter 7

Conclusions and Future work

7.1 Overview

In this thesis, PCL-based inks were formulated for tissue scaffold fabrication using DIW with controllable material compositions, structures, and mechanical properties. A critical review of previous research and projects in this field has highlighted the potentials of using DIW for tissue scaffold fabrication with constraints and challenges addressed. It was found that there is a lack of composite inks, particularly for hydrophobic-based biomaterials that are not water-soluble. This thesis details the development methodology of hydrophobic material (i.e. PCL-base ink) and fabrication of the scaffolds with designed structures using DIW method.

7.2 Summary of the thesis

In Chapter 4, lattice scaffolds with porosities ranging from 35% to 75% were proposed by varying the interfilamentous spacing, filament diameter, and overlap spacing. Keeping those parameters as constants, several lay-down angles (90°, 75°, 60°, 45°, 30°, and 15°) were designed to achieve pore shapes. The finite element method (FEM) was used to investigate the elastic modulus and yield strength of those de-

signed scaffolds.

The FEM analysis results show that elastic modulus of scaffolds decreased linearly with the increase of scaffold porosity. Meanwhile, a range of elastic modulus was obtained from FEM covering the range of elastic modulus values of natural osteochondral interfacial tissue. Those results suggest that by tuning the parameters used to design the scaffolds, the desired elastic modulus of the scaffold can be customized to match specific osteochondral tissue.

The FEM analysis results of a single lay-down angle from 15° to 90° show that the orthotropic effect increases when the lay-down angle decreases from 90° to 15°. This indicates that the lattice scaffold can be adapted to different requirements of anisotropic by rotating the orientation of filaments. Moreover, a complex scaffold was created by assembling individual sections of six different lay-down angles, i.e. 15°, 30°, 45°, 60°, 75°, and 90°. The FEM analysis results indicate that the assembled complex structure retained the anisotropic nature of a single lay-down angle scaffold. The anisotropic property of the complex structure was analysed from a strain distribution perspective. The results indicate that the strain magnitudes in transverse directions highly depend on the angle between the direction of compressive loading and the filament orientation. The strain was greater when this angle approaches 0° and decreases when this angle approaches 90°. Literature indicates that the strains generated from mechanical loading can transmit to cells attached on the surface of the scaffold and cause various types of cell differentiation according to the deformation magnitude. Therefore, it is imposed that by using an assembled scaffold with multiple lay-down angels, various strain magnitudes and hierarchical/gradient transitions can be achieved within a single construct.

Chapter 5 introduced the formulation of PCL-based inks for scaffold fabrication using DIW printing. Due to PCL is hydrophilic and not water-soluble, the selection of organic solvents was important for the development of inks. The influences of two solvents, i.e. acetone (ACE) and dichloromethane (DCM), were compared in terms of their ink rheology behaviour, printing process parameter, mate-

rial characterisation, thermal characterisation, and surface wettability of the printed scaffolds.

The ink rheology behaviour results indicate that ACE inks have more pronounced shear-thinning behaviour than those of DCM inks. However, the ink recovery behaviour of ACE is inferior to DCM inks. Additionally, the process parameters within the needle using mathematical modelling were analysed. The result suggests that under the same extrusion condition, the shear rate of the ACE based ink was ten times higher than that of the DCM based one, which could lead low ink yield stress, thus causing printing failure. The shape fidelity of the printed constructs result indicates that compared to the ACE based printing of PCL/PEO 3D construct, the structure printed with DCM-based ink had a closer match to the designed structure. Additionally, the printed filaments from DCM based inks are more uniform than those from ACE based inks. This result could be attributed to that the ink recovery rate of ACE ink is lower, which might lead to an associated inherent variability of the extrusion printing process.

Moreover, the wettability property results indicate that the DCM based inks printed constructs resulted in smaller contact angles (CAs) than those from ACE based inks. Also, the incorporation of PEO reduced the CAs for both solvents. This could be attributed to the higher O/C ratios measured from XPS. In comparison with other 3D printing fabrication methods such as fused deposition modelling (FDM), the DIW process has the tendency of producing PCL-based constructs with enhanced wettability. This could be particularly useful for biomedical applications as the hydrophobicity of PCL is often regarded as the weak spot. Therefore, combining these aspects, the DIW technique offers a new toolkit to develop a 3D construct with tunable surface characteristics for biomedical applications.

Chapter 6 detailed the development of another new ink by formulating the composites of PCL and PEO with hydroxyapatite (HAp) to close mimic the natural bone tissue. The influence of HAp concentrations (from 55% to 85% w/w) on ink rheology behaviour, fabrication process, material characterisation, surface properties,

and mechanical properties of the DIW printed constructs were investigated.

The ink rheology results suggest that upon increasing the HAp concentrations, there was more prevalent shear shinning behaviour. Meanwhile, the PCL/PEO/HAp inks with 65% w/w of HAp concentration had the highest ink recovery behaviour, whereas the lowest one was when the HAp concentration of 85% w/w. This could be due to the HAp amount was overloaded and cannot properly interact with polymers chains. Meanwhile, compared to PCL/PEO/HAp inks with 55% w/w HAp concentration, the ink recovery behaviour increased for the one with 65% w/w HAp concentration. This observation imposes that a feasible amount of subsidiary nanoparticle such as HAp can aid the scaffold fabrication using the DIW printing.

The mechanical properties of the printed scaffold with HAp from 55%w/w to 85%w/w were evaluated, the results indicate that elastic modulus and yield strength of PCL/PEO/HAp scaffolds increased when the HAp concentration increased from 55% to 65% w/w, while those values start to decrease when the HAp concentration was rising from 65% to 85% w/w. The trends of elastic modulus and yield stress (highest when the HAp concentration was 65% w/w) were in line with the results of ink recovery test. Further, ink *PCL/PEO/65%HAp* was applied to print the scaffold structure with different pore geometries designed in Chapter 4. The mechanical property of those DIW printed structures were compared, and the results indicate that 90° structure had the highest elastic modulus and yield strength, while the 45° one had the lowest. This result matches the FEM simulation results in Chapter 4. Furthermore, VAN drug was successfully loaded in PCL/PEO/HAp scaffold. The results of drug release and agar diffusion indicate that the VAN-loaded scaffolds have the capability of releasing VAN and anti-bacteria function.

In summary, this thesis has proposed a novel scaffold structure assembled by pore geometries changing from 90° to 15°. The analysis of FEA modelling suggested that the strain within the complex structure changed gradually. PCL-based inks were formulated, their rheology behaviour and the application for the scaffold fabrication using DIW were compared. The optimised inks were selected to fab-

ricate the predesigned novel structure. Combining these outcomes, this study has designed a new complex structure and offered two new inks for the DIW printing technique for the fabrication of 3D scaffolds with tunable surface characteristics and mechanical properties for biomedical applications.

7.3 Summary of contributions

As stated in Chapter 1, this thesis focuses on developing composite material inks to build predesigned scaffold structures using DIW technique. By analysing and summarising the work, the research aim has been achieved through the following aspects:

- **Development of a novel structure that can form gradient mechanical properties**: FEA modelling method was applied to investigate the magnitude and distribution of elastic modulus, yield strength, and principal strain within the designed scaffold structure under compressive loadings.

- **Formulation of PCL-based polymeric inks and comparison of the solvent influence**: PCL and PCL/PEO inks were formulated by dissolving PCL and PCL/PEO polymers into two types of solvents – ACE and DCM. By comparing the ink rheology behaviour, printing quality, and wettability, it was concluded that the DCM based PCL/PEO ink was the most feasible inks that can be used for DIW printing.

- **Formulation of PCL-based composite inks and comparison of the hydroxyapatite (HAp) influence**: to close mimic natural bone tissue, various concentrations of HAp (from 55% to 85% w/w) were incorporated in the DCM-based PCL/PEO inks to formulate the PCL/PEO/HAp composite inks. By comparing the ink rheology behaviour, mechanical property, and wettability, it was concluded that the PCL/PEO/HAp with 65% w/w HAp concentration was the most feasible inks for the fabrication of the predesigned scaffold using DIW printing. It is noteworthy that 65% w/w HAp concentration is

close to the inorganic composition of natural bone tissue.

The contributions of this research are twofold. First, a novel structure of tissue scaffold was designed and the FEM simulations verified that this structure has created gradient mechanical properties. Second, two new inks were developed for scaffold fabrication using DIW. The PCL/PEO scaffold was developed to mimic the soft tissue layer of the OC tissue, while the PCL/PEO/HAp scaffold was developed to mimic the hard tissue layer of the OC tissue, which aims for the gradient property from soft to hard tissue. Those newly formulated PCL-based inks were applied to fabricate the designed novel structure using DIW printing, which has the potential capability to produce tissue scaffold for interfacial tissue engineering. In future work, more suitable ink materials and scaffold geometries could be developed; optimal combinations of materials and geometries could be selected to achieve the gradient property of interfacial tissue.

7.4 Recommendations for future work

7.4.1 Overlap spacing and solidification optimisation

The overlap spacing for 3D constructs printed by DIW layer-by-layer was set based on the smallest distance that the nozzle tip would not touch and affect the previous layer. However, the overlap spacing should not always be constant due to the scaffold would shrink with time. The results from this study suggest that the scaffold has a shrinking issue after drying, which is in line with other studies (Roopavath et al., 2019; Li et al., 2017). This is an inevitable problem for solvent-based 3D printing due to the solvent would evaporate when scaffold is printed layer-by-layer. The overlap distance needs to be adjusted correspondingly, particularly when organic solvents are used. Therefore, it would be interesting to investigate the evaporation mechanisms of solvents from the composite inks to predict the setting parameters for overlap spacing.

7.4.2 Pore geometry effects on cells under static culture in vitro

The 2D pore geometry of scaffold has been explored by some studies as a factor to affect cell proliferation, differentiation, and biological response (Rumpler et al., 2008; Knychala et al., 2013; Bidan et al., 2013). Their results suggest that the local growth rate of tissue formed by osteoblasts is strongly influenced by 2D pore geometries. However, cell response within 3D pore shape has not been systematically investigated yet. It would be meaningful to investigate the influence of those 3D pore shape on the local growth rate of tissue formed by osteoblasts.

7.4.3 Pore geometry effects on cells under dynamic culture in vitro

As indicated in the literature review of the thesis, cells sense mechanical stimulus and emit signals that stimulate cell expression and cell or tissue differentiation (Prendergast et al., 1997; Lacroix and Prendergast, 2002). So far, most of the theories related to the relationship between mechanical stimulus and tissue regeneration are based on the fracture healing of the bone tissue in vivo. However, considering the difference of tissue regeneration between in vivo and in vitro, a theory about mechanic-regulation model describes the effects of mechanical stimulus on cells and tissues in vitro should be developed. In this study, the FEM result indicates that there was a gradient distribution of principal strain under compressive loading within the developed novel scaffold. Therefore, it is recommended to investigate the research question of how those gradient changes of principle strain could cause tissue differentiation in vitro. A suitable dynamic cultural environment that can provide feasible compressive loading could be developed to help with the investigation of mechanical stimulus resulted from compressive strain on tissue growth.

References

Abarrategi, A., Lópiz-Morales, Y., Ramos, V., Civantos, A., López-Durán, L., Marco, F., and López-Lacomba, J. L. Chitosan scaffolds for osteochondral tissue regeneration. *Journal of Biomedical Materials Research Part A*, 95(4):1132–1141, 2010.

Abdelrazek, E., Hezma, A., El-Khodary, A., and Elzayat, A. Spectroscopic studies and thermal properties of pcl/pmma biopolymer blend. *Egyptian Journal of Basic and Applied Sciences*, 3(1):10–15, 2016.

Abrahamsson, C. K., Yang, F., Park, H., Brunger, J. M., Valonen, P. K., Langer, R., Welter, J. F., Caplan, A. I., Guilak, F., and Freed, L. E. Chondrogenesis and mineralization during in vitro culture of human mesenchymal stem cells on three-dimensional woven scaffolds. *Tissue Engineering Part A*, 16(12):3709–3718, 2010.

Ali, D. and Sen, S. Finite element analysis of mechanical behavior, permeability and fluid induced wall shear stress of high porosity scaffolds with gyroid and lattice-based architectures. *Journal of the mechanical behavior of biomedical materials*, 75:262–270, 2017.

Ansari, S., Khorshidi, S., and Karkhaneh, A. Engineering of gradient osteochondral tissue: From nature to lab. *Acta biomaterialia*, 2019.

Antons, J., Marascio, M. G. M., Nohava, J., Martin, R., Applegate, L., Bourban, P., and Pioletti, D. Zone-dependent mechanical properties of human articular

cartilage obtained by indentation measurements. *Journal of Materials Science: Materials in Medicine*, 29(5):57, 2018.

Arunkumar, P., Dougherty, J. A., Weist, J., Kumar, N., Angelos, M. G., Powell, H. M., and Khan, M. Sustained release of basic fibroblast growth factor (bfgf) encapsulated polycaprolactone (pcl) microspheres promote angiogenesis in vivo. *Nanomaterials*, 9(7):1037, 2019.

Athanasiou, K., Agarwal, A., and Dzida, F. Comparative study of the intrinsic mechanical properties of the human acetabular and femoral head cartilage. *Journal of Orthopaedic Research*, 12(3):340–349, 1994.

Azad, M. A., Olawuni, D., Kimbell, G., Badruddoza, A. Z. M., Hossain, M., Sultana, T., et al. Polymers for extrusion-based 3d printing of pharmaceuticals: A holistic materials–process perspective. *Pharmaceutics*, 12(2):124, 2020.

Bailie, G. R. and Neal, D. Vancomycin ototoxicity and nephrotoxicity. *Medical toxicology and adverse drug experience*, 3(5):376–386, 1988.

Baker, B. M., Shah, R. P., Silverstein, A. M., Esterhai, J. L., Burdick, J. A., and Mauck, R. L. Sacrificial nanofibrous composites provide instruction without impediment and enable functional tissue formation. *Proceedings of the National Academy of Sciences*, 109(35):14176–14181, 2012.

Barry III, R. A., Shepherd, R. F., Hanson, J. N., Nuzzo, R. G., Wiltzius, P., and Lewis, J. A. Direct-write assembly of 3d hydrogel scaffolds for guided cell growth. *Advanced materials*, 21(23):2407–2410, 2009.

Bauer, T. W. and Muschler, G. F. Bone graft materials: an overview of the basic science. *Clinical Orthopaedics and Related Research®*, 371:10–27, 2000.

Bauer, T. W. and Schils, J. The pathology of total joint arthroplasty. *Skeletal radiology*, 28(9):483–497, 1999.

Bayrak, E. and Yilgor Huri, P. Engineering musculoskeletal tissue interfaces. *Frontiers in Materials*, 5:24, 2018.

Betts, G., Desaix, P., Johnson, E., Korol, O., Kruse, D., Poe, B., et al. Human anatomy and physiology. *OpenStax College: Houston, TX, USA*, 2013.

Bidan, C. M., Kommareddy, K. P., Rumpler, M., Kollmannsberger, P., Fratzl, P., and Dunlop, J. W. Geometry as a factor for tissue growth: towards shape optimization of tissue engineering scaffolds. *Advanced healthcare materials*, 2(1):186–194, 2013.

Bittner, S. M., Smith, B. T., Diaz-Gomez, L., Hudgins, C. D., Melchiorri, A. J., Scott, D. W., Fisher, J. P., and Mikos, A. G. Fabrication and mechanical characterization of 3d printed vertical uniform and gradient scaffolds for bone and osteochondral tissue engineering. *Acta biomaterialia*, 90:37–48, 2019.

Blaeser, A., Duarte Campos, D. F., Puster, U., Richtering, W., Stevens, M. M., and Fischer, H. Controlling shear stress in 3d bioprinting is a key factor to balance printing resolution and stem cell integrity. *Advanced healthcare materials*, 5(3): 326–333, 2016.

Blair, G. S., Hening, J., and Wagstaff, A. The flow of cream through narrow glass tubes. *Journal of physical chemistry*, 43(7):853–864, 1939.

Boschetti, F., Pennati, G., Gervaso, F., Peretti, G. M., and Dubini, G. Biomechanical properties of human articular cartilage under compressive loads. *Biorheology*, 41 (3-4):159–166, 2004.

Bruyas, A., Lou, F., Stahl, A. M., Gardner, M., Maloney, W., Goodman, S., and Yang, Y. P. Systematic characterization of 3d-printed pcl/β-tcp scaffolds for biomedical devices and bone tissue engineering: influence of composition and porosity. *Journal of materials research*, 33(14):1948–1959, 2018.

Brynk, T., Hellmich, C., Fritsch, A., Zysset, P., and Eberhardsteiner, J. Experimental poromechanics of trabecular bone strength: role of terzaghi's effective stress and of tissue level stress fluctuations. *Journal of biomechanics*, 44(3):501–508, 2011.

Buxton, A. N., Bahney, C. S., Yoo, J. U., and Johnstone, B. Temporal exposure to chondrogenic factors modulates human mesenchymal stem cell chondrogenesis in hydrogels. *Tissue Engineering Part A*, 17(3-4):371–380, 2011.

Byers, B. A., Mauck, R. L., Chiang, I. E., and Tuan, R. S. Transient exposure to transforming growth factor beta 3 under serum-free conditions enhances the biomechanical and biochemical maturation of tissue-engineered cartilage. *Tissue Engineering Part A*, 14(11):1821–1834, 2008.

Byrne, D. P., Lacroix, D., Planell, J. A., Kelly, D. J., and Prendergast, P. J. Simulation of tissue differentiation in a scaffold as a function of porosity, young's modulus and dissolution rate: application of mechanobiological models in tissue engineering. *Biomaterials*, 28(36):5544–5554, 2007.

Cahill, S., Lohfeld, S., and McHugh, P. E. Finite element predictions compared to experimental results for the effective modulus of bone tissue engineering scaffolds fabricated by selective laser sintering. *Journal of Materials Science: Materials in Medicine*, 20(6):1255–1262, 2009.

Carter, D. R., Wong, M., and Orr, T. E. Musculoskeletal ontogeny, phylogeny, and functional adaptation. *Journal of Biomechanics*, 24:3–16, 1991.

Carter, D., Blenman, P., and Beaupre, G. Correlations between mechanical stress history and tissue differentiation in initial fracture healing. *Journal of Orthopaedic Research*, 6(5):736–748, 1988.

Chen, D. X., Chen, and Glaser. *Extrusion Bioprinting of Scaffolds for Tissue Engineering Applications*. Springer, 2019a.

Chen, D., Wei, J., Deng, Y., Xu, H., Li, Z., Meng, H., Han, X., Wang, Y., Wan, J., Yan, T., et al. Virtual stenting with simplex mesh and mechanical contact analysis for real-time planning of thoracic endovascular aortic repair. *Theranostics*, 8(20): 5758, 2018.

Chen, J., Chen, H., Li, P., Diao, H., Zhu, S., Dong, L., Wang, R., Guo, T., Zhao, J., and Zhang, J. Simultaneous regeneration of articular cartilage and subchondral bone in vivo using mscs induced by a spatially controlled gene delivery system in bilayered integrated scaffolds. *Biomaterials*, 32(21):4793–4805, 2011a.

Chen, L., Deng, C., Li, J., Yao, Q., Chang, J., Wang, L., and Wu, C. 3d printing of a lithium-calcium-silicate crystal bioscaffold with dual bioactivities for osteochondral interface reconstruction. *Biomaterials*, 196:138–150, 2019b.

Chen, Y., Feng, B., Zhu, Y., Weng, J., Wang, J., and Lu, X. Preparation and characterization of a novel porous titanium scaffold with 3d hierarchical porous structures. *Journal of Materials Science: Materials in Medicine*, 22(4):839–844, 2011b.

Cheng, Y., Qin, H., Acevedo, N. C., Jiang, X., and Shi, X. 3d printing of extended-release tablets of theophylline using hydroxypropyl methylcellulose (hpmc) hydrogels. *International Journal of Pharmaceutics*, 591:119983, 2020.

Chiang, H. and Jiang, C.-C. Repair of articular cartilage defects: review and perspectives. *Journal of the Formosan Medical Association*, 108(2):87–101, 2009.

Chin, S. Y., Dikshit, V., Meera Priyadarshini, B., and Zhang, Y. Powder-based 3d printing for the fabrication of device with micro and mesoscale features. *Micromachines*, 11(7):658, 2020.

Choi, S.-W., Zhang, Y., and Xia, Y. Three-dimensional scaffolds for tissue engineering: the importance of uniformity in pore size and structure. *Langmuir*, 26 (24):19001–19006, 2010.

Christensen, B. B., Foldager, C. B., Jensen, J., Jensen, N. C., and Lind, M. Poor osteochondral repair by a biomimetic collagen scaffold: 1-to 3-year clinical and radiological follow-up. *Knee surgery, sports traumatology, arthroscopy*, 24(7): 2380–2387, 2016.

Claes, L. E., Heigele, C. A., Neidlinger-Wilke, C., Kaspar, D., Seidl, W., Margevicius, K. J., and Augat, P. Effects of mechanical factors on the fracture healing process. *Clinical Orthopaedics and Related Research®*, 355:S132–S147, 1998.

Comper, W. D. *Extracellular matrix*, volume 1. Crc Press, 1996.

Cui, Z., Nelson, B., Peng, Y., Li, K., Pilla, S., Li, W.-J., Turng, L.-S., and Shen, C. Fabrication and characterization of injection molded poly (ε-caprolactone) and poly (ε-caprolactone)/hydroxyapatite scaffolds for tissue engineering. *Materials Science and Engineering: C*, 32(6):1674–1681, 2012.

Dash, M., Chiellini, F., Ottenbrite, R. M., and Chiellini, E. Chitosan—a versatile semi-synthetic polymer in biomedical applications. *Progress in polymer science*, 36(8):981–1014, 2011.

Dávila, J. L. and d'Ávila, M. A. Rheological evaluation of laponite/alginate inks for 3d extrusion-based printing. *The International Journal of Advanced Manufacturing Technology*, 101(1-4):675–686, 2019.

Delaine-Smith, R. M. and Reilly, G. C. The effects of mechanical loading on mesenchymal stem cell differentiation and matrix production. In *Vitamins & Hormones*, volume 87, pages 417–480. Elsevier, 2011.

DeLeon, S., Clinton, A., Fowler, H., Everett, J., Horswill, A. R., and Rumbaugh, K. P. Synergistic interactions of pseudomonas aeruginosa and staphylococcus aureus in an in vitro wound model. *Infection and immunity*, 82(11):4718–4728, 2014.

Dell'Osso, G., Bottai, V., Bugelli, G., Manisco, T., Cazzella, N., Celli, F., Guido, G., and Giannotti, S. The biphasic bioresorbable scaffold (trufit®) in the osteochondral knee lesions: long-term clinical and mri assessment in 30 patients. *Musculoskeletal surgery*, 100(2):93–96, 2016.

Di Luca, A., Van Blitterswijk, C., and Moroni, L. The osteochondral interface as a gradient tissue: from development to the fabrication of gradient scaffolds for

regenerative medicine. *Birth Defects Research Part C: Embryo Today: Reviews*, 105(1):34–52, 2015.

Diego, R. B., Estellés, J. M., Sanz, J. A., García-Aznar, J. M., and Sánchez, M. S. Polymer scaffolds with interconnected spherical pores and controlled architecture for tissue engineering: fabrication, mechanical properties, and finite element modeling. *Journal of Biomedical Materials Research Part B: Applied Biomaterials: An Official Journal of The Society for Biomaterials, The Japanese Society for Biomaterials, and The Australian Society for Biomaterials and the Korean Society for Biomaterials*, 81(2):448–455, 2007.

Dillon, B., Doran, P., Fuenmayor, E., Healy, A. V., Gately, N. M., Major, I., and Lyons, J. G. The influence of low shear microbore extrusion on the properties of high molecular weight poly (l-lactic acid) for medical tubing applications. *Polymers*, 11(4):710, 2019.

Do, A.-V., Khorsand, B., Geary, S. M., and Salem, A. K. 3d printing of scaffolds for tissue regeneration applications. *Advanced healthcare materials*, 4(12):1742–1762, 2015.

Domingos, M., Intranuovo, F., Russo, T., De Santis, R., Gloria, A., Ambrosio, L., Ciurana, J., and Bartolo, P. The first systematic analysis of 3d rapid prototyped poly (ε-caprolactone) scaffolds manufactured through biocell printing: the effect of pore size and geometry on compressive mechanical behaviour and in vitro hmsc viability. *Biofabrication*, 5(4):045004, 2013.

Dong, L., Wang, S.-J., Zhao, X.-R., Zhu, Y.-F., and Yu, J.-K. 3d-printed poly (ε-caprolactone) scaffold integrated with cell-laden chitosan hydrogels for bone tissue engineering. *Scientific reports*, 7(1):1–9, 2017.

Dorcemus, D. L. and Nukavarapu, S. P. Novel and unique matrix design for osteochondral tissue engineering. *MRS Online Proceedings Library Archive*, 1621: 17–23, 2014.

Dorj, B., Won, J.-E., Kim, J.-H., Choi, S.-J., Shin, U. S., and Kim, H.-W. Robocasting nanocomposite scaffolds of poly (caprolactone)/hydroxyapatite incorporating modified carbon nanotubes for hard tissue reconstruction. *Journal of Biomedical Materials Research Part A*, 101(6):1670–1681, 2013.

Dormer, N. H., Singh, M., Wang, L., Berkland, C. J., and Detamore, M. S. Osteochondral interface tissue engineering using macroscopic gradients of bioactive signals. *Annals of biomedical engineering*, 38(6):2167–2182, 2010.

Drummer, D., Rietzel, D., and Kühnlein, F. Development of a characterization approach for the sintering behavior of new thermoplastics for selective laser sintering. *Physics Procedia*, 5:533–542, 2010.

Du, M., Chen, B., Meng, Q., Liu, S., Zheng, X., Zhang, C., Wang, H., Li, H., Wang, N., and Dai, J. 3d bioprinting of bmsc-laden methacrylamide gelatin scaffolds with cbd-bmp2-collagen microfibers. *Biofabrication*, 7(4):044104, 2015.

Du, Y., Liu, H., Yang, Q., Wang, S., Wang, J., Ma, J., Noh, I., Mikos, A. G., and Zhang, S. Selective laser sintering scaffold with hierarchical architecture and gradient composition for osteochondral repair in rabbits. *Biomaterials*, 137:37–48, 2017.

Duan, B., Kapetanovic, E., Hockaday, L. A., and Butcher, J. T. Three-dimensional printed trileaflet valve conduits using biological hydrogels and human valve interstitial cells. *Acta biomaterialia*, 10(5):1836–1846, 2014.

Dubey, P., Bhushan, B., Sachdev, A., Matai, I., Uday Kumar, S., and Gopinath, P. Silver-nanoparticle-incorporated composite nanofibers for potential wound-dressing applications. *Journal of Applied Polymer Science*, 132(35), 2015.

Dwivedi, R., Kumar, S., Pandey, R., Mahajan, A., Nandana, D., Katti, D. S., and Mehrotra, D. Polycaprolactone as biomaterial for bone scaffolds: Review of literature. *Journal of Oral Biology and Craniofacial Research*, 10(1):381–388, 2020.

Eltom, A., Zhong, G., and Muhammad, A. Scaffold techniques and designs in tissue engineering functions and purposes: a review. *Advances in Materials Science and Engineering*, 2019, 2019.

Engler, A. J., Sen, S., Sweeney, H. L., and Discher, D. E. Matrix elasticity directs stem cell lineage specification. *Cell*, 126(4):677–689, 2006.

Entezari, A., Zhang, Z., Sue, A., Sun, G., Huo, X., Chang, C.-C., Zhou, S., Swain, M. V., and Li, Q. Nondestructive characterization of bone tissue scaffolds for clinical scenarios. *Journal of the Mechanical Behavior of Biomedical Materials*, 89:150–161, 2019.

Eshraghi, S. and Das, S. Mechanical and microstructural properties of polycaprolactone scaffolds with one-dimensional, two-dimensional, and three-dimensional orthogonally oriented porous architectures produced by selective laser sintering. *Acta biomaterialia*, 6(7):2467–2476, 2010.

Espinoza, S. M., Patil, H. I., San Martin Martinez, E., Casañas Pimentel, R., and Ige, P. P. Poly-ε-caprolactone (pcl), a promising polymer for pharmaceutical and biomedical applications: Focus on nanomedicine in cancer. *International Journal of Polymeric Materials and Polymeric Biomaterials*, 69(2):85–126, 2020.

Farto-Vaamonde, X., Auriemma, G., Aquino, R. P., Concheiro, A., and Alvarez-Lorenzo, C. Post-manufacture loading of filaments and 3d printed pla scaffolds with prednisolone and dexamethasone for tissue regeneration applications. *European Journal of Pharmaceutics and Biopharmaceutics*, 141:100–110, 2019.

Fazli, N., Nasir, M., Norita, M. Z., Raha, M. G., and Nahrizul Adib, K. Characterization of chitosan-poly (ethylene oxide) blends as haemodialysis membrane. 2005.

Feng, P., Niu, M., Gao, C., Peng, S., and Shuai, C. A novel two-step sintering for nano-hydroxyapatite scaffolds for bone tissue engineering. *Scientific reports*, 4: 5599, 2014.

Feng, P., Wu, P., Gao, C., Yang, Y., Guo, W., Yang, W., and Shuai, C. A multimaterial scaffold with tunable properties: toward bone tissue repair. *Advanced science*, 5(6):1700817, 2018.

Feng, P., Kong, Y., Yu, L., Li, Y., Gao, C., Peng, S., Pan, H., Zhao, Z., and Shuai, C. Molybdenum disulfide nanosheets embedded with nanodiamond particles: co-dispersion nanostructures as reinforcements for polymer scaffolds. *Applied Materials Today*, 17:216–226, 2019.

for Disease Control (CDC, C. et al. Transmission of hiv through bone transplantation: case report and public health recommendations. *MMWR. Morbidity and mortality weekly report*, 37(39):597, 1988.

Fritsch, A., Dormieux, L., Hellmich, C., and Sanahuja, J. Mechanical behavior of hydroxyapatite biomaterials: an experimentally validated micromechanical model for elasticity and strength. *Journal of Biomedical Materials Research Part A: An Official Journal of The Society for Biomaterials, The Japanese Society for Biomaterials, and The Australian Society for Biomaterials and the Korean Society for Biomaterials*, 88(1):149–161, 2009.

Fritsch, A., Hellmich, C., and Dormieux, L. The role of disc-type crystal shape for micromechanical predictions of elasticity and strength of hydroxyapatite biomaterials. *Philosophical Transactions of the Royal Society A: Mathematical, Physical and Engineering Sciences*, 368(1917):1913–1935, 2010.

Gadjanski, I. Mimetic hierarchical approaches for osteochondral tissue engineering. In *Osteochondral Tissue Engineering*, pages 143–170. Springer, 2018.

Gao, F., Xu, Z., Liang, Q., Liu, B., Li, H., Wu, Y., Zhang, Y., Lin, Z., Wu, M., Ruan, C., et al. Direct 3d printing of high strength biohybrid gradient hydrogel scaffolds for efficient repair of osteochondral defect. *Advanced Functional Materials*, 28 (13):1706644, 2018.

Gao, G., Yonezawa, T., Hubbell, K., Dai, G., and Cui, X. Inkjet-bioprinted acrylated peptides and peg hydrogel with human mesenchymal stem cells promote robust

bone and cartilage formation with minimal printhead clogging. *Biotechnology journal*, 10(10):1568–1577, 2015.

Gao, L.-L., Zhang, C.-Q., Gao, H., Liu, Z.-D., and Xiao, P.-P. Depth and rate dependent mechanical behaviors for articular cartilage: experiments and theoretical predictions. *Materials Science and Engineering: C*, 38:244–251, 2014.

Geris, L., Andreykiv, A., Van Oosterwyck, H., Vander Sloten, J., Van Keulen, F., Duyck, J., and Naert, I. Numerical simulation of tissue differentiation around loaded titanium implants in a bone chamber. *Journal of biomechanics*, 37(5): 763–769, 2004.

Gervaso, F., Sannino, A., and Peretti, G. M. The biomaterialist's task: scaffold biomaterials and fabrication technologies. *Joints*, 1(3):130, 2013.

Ghosh, S., Parker, S. T., Wang, X., Kaplan, D. L., and Lewis, J. A. Direct-write assembly of microperiodic silk fibroin scaffolds for tissue engineering applications. *Advanced Functional Materials*, 18(13):1883–1889, 2008.

Giannoni, P., Lazzarini, E., Ceseracciu, L., Barone, A. C., Quarto, R., and Scaglione, S. Design and characterization of a tissue-engineered bilayer scaffold for osteochondral tissue repair. *Journal of tissue engineering and regenerative medicine*, 9(10):1182–1192, 2015.

Gibson, L. The mechanical behaviour of cancellous bone. *Journal of biomechanics*, 18(5):317–328, 1985.

Gill, T. J., Asnis, P. D., and Berkson, E. M. The treatment of articular cartilage defects using the microfracture technique. *Journal of Orthopaedic & Sports Physical Therapy*, 36(10):728–738, 2006.

Gittard, S. D. and Narayan, R. J. Laser direct writing of micro-and nano-scale medical devices. *Expert review of medical devices*, 7(3):343–356, 2010.

Gleadall, A., Visscher, D., Yang, J., Thomas, D., and Segal, J. Review of additive manufactured tissue engineering scaffolds: relationship between geometry and performance. *Burns & trauma*, 6(1), 2018.

Gloria, A., Russo, T., De Santis, R., and Ambrosio, L. 3d fiber deposition technique to make multifunctional and tailor-made scaffolds for tissue engineering applications. *Journal of Applied Biomaterials and Biomechanics*, 7(3):141–152, 2009.

Gómez, S., Vlad, M., López, J., and Fernández, E. Design and properties of 3d scaffolds for bone tissue engineering. *Acta biomaterialia*, 42:341–350, 2016.

Gómez, S., Vlad, M. D., López, J., Navarro, M., and Fernández, E. Characterization and three-dimensional reconstruction of synthetic bone model foams. *Materials Science and Engineering: C*, 33(6):3329–3335, 2013.

Goncalves, E. M., Oliveira, F. J., Silva, R. F., Neto, M. A., Fernandes, M. H., Amaral, M., Vallet-Regí, M., and Vila, M. Three-dimensional printed pcl-hydroxyapatite scaffolds filled with cnt s for bone cell growth stimulation. *Journal of Biomedical Materials Research Part B: Applied Biomaterials*, 104(6): 1210–1219, 2016.

Gong, T., Xie, J., Liao, J., Zhang, T., Lin, S., and Lin, Y. Nanomaterials and bone regeneration. *Bone research*, 3:15029, 2015.

Grayson, W. L., Fröhlich, M., Yeager, K., Bhumiratana, S., Chan, M. E., Cannizzaro, C., Wan, L. Q., Liu, X. S., Guo, X. E., and Vunjak-Novakovic, G. Engineering anatomically shaped human bone grafts. *Proceedings of the National Academy of Sciences*, 107(8):3299–3304, 2010.

Guo, L., Vardakis, J. C., Lassila, T., Mitolo, M., Ravikumar, N., Chou, D., Lange, M., Sarrami-Foroushani, A., Tully, B. J., Taylor, Z. A., et al. Subject-specific multi-poroelastic model for exploring the risk factors associated with the early stages of alzheimer's disease. *Interface focus*, 8(1):20170019, 2018.

Guo, L., Vardakis, J. C., Chou, D., and Ventikos, Y. A multiple-network poroelastic model for biological systems and application to subject-specific modelling of cerebral fluid transport. *International Journal of Engineering Science*, 147: 103204, 2020.

Hadjidakis, D. J. and Androulakis, I. I. Bone remodeling. *Annals of the New York Academy of Sciences*, 1092(1):385–396, 2006.

Han, Y., Li, X., Zhang, Y., Han, Y., Chang, F., and Ding, J. Mesenchymal stem cells for regenerative medicine. *Cells*, 8(8):886, 2019.

Hansen, C. M. *Hansen solubility parameters: a user's handbook*. CRC press, 2007.

He, Y., Yang, F., Zhao, H., Gao, Q., Xia, B., and Fu, J. Research on the printability of hydrogels in 3d bioprinting. *Scientific reports*, 6:29977, 2016.

Heinegård, D. and Saxne, T. The role of the cartilage matrix in osteoarthritis. *Nature Reviews Rheumatology*, 7(1):50, 2011.

Helguero, C. G., Mustahsan, V. M., Parmar, S., Pentyala, S., Pfail, J. L., Kao, I., Komatsu, D. E., and Pentyala, S. Biomechanical properties of 3d-printed bone scaffolds are improved by treatment with crfp. *Journal of orthopaedic surgery and research*, 12(1):195, 2017.

Hellmich, C., Ulm, F.-J., and Dormieux, L. Can the diverse elastic properties of trabecular and cortical bone be attributed to only a few tissue-independent phase properties and their interactions? *Biomechanics and modeling in mechanobiology*, 2(4):219–238, 2004.

Hench, L. L. The story of bioglass®. *Journal of Materials Science: Materials in Medicine*, 17(11):967–978, 2006.

Hendrikson, W. J., Deegan, A. J., Yang, Y., van Blitterswijk, C. A., Verdonschot, N., Moroni, L., and Rouwkema, J. Influence of additive manufactured scaffold architecture on the distribution of surface strains and fluid flow shear stresses

and expected osteochondral cell differentiation. *Frontiers in bioengineering and biotechnology*, 5:6, 2017.

Huang, J., Best, S., Bonfield, W., and Buckland, T. Development and characterization of titanium-containing hydroxyapatite for medical applications. *Acta biomaterialia*, 6(1):241–249, 2010.

Huiskes, R., Van Driel, W., Prendergast, P., and Søballe, K. A biomechanical regulatory model for periprosthetic fibrous-tissue differentiation. *Journal of materials science: Materials in medicine*, 8(12):785–788, 1997.

Hulbert, S., Young, F., Mathews, R., Klawitter, J., Talbert, C., and Stelling, F. Potential of ceramic materials as permanently implantable skeletal prostheses. *Journal of biomedical materials research*, 4(3):433–456, 1970.

Hung, C. T., Mauck, R. L., Wang, C. C.-B., Lima, E. G., and Ateshian, G. A. A paradigm for functional tissue engineering of articular cartilage via applied physiologic deformational loading. *Annals of biomedical engineering*, 32(1):35–49, 2004.

Hutmacher, D. W. and Williams, D. Scaffolds in tissue engineering bone and cartilage. the biomaterials: Silver jubilee compendium, 2006.

Hutmacher, D. and Cool, S. Concepts of scaffold-based tissue engineering—the rationale to use solid free-form fabrication techniques. *Journal of cellular and molecular medicine*, 11(4):654–669, 2007.

Hwang, H. H., Zhu, W., Victorine, G., Lawrence, N., and Chen, S. 3d-printing of functional biomedical microdevices via light-and extrusion-based approaches. *Small methods*, 2(2):1700277, 2018.

Jakob, R. P., Franz, T., Gautier, E., and Mainil-Varlet, P. Autologous osteochondral grafting in the knee: indication, results, and reflections. *Clinical Orthopaedics and Related Research®*, 401:170–184, 2002.

Jakus, A. E., Rutz, A. L., Jordan, S. W., Kannan, A., Mitchell, S. M., Yun, C., Koube, K. D., Yoo, S. C., Whiteley, H. E., Richter, C.-P., et al. Hyperelastic "bone": A highly versatile, growth factor–free, osteoregenerative, scalable, and surgically friendly biomaterial. *Science translational medicine*, 8(358): 358ra127–358ra127, 2016.

Jang, J., Park, J. Y., Gao, G., and Cho, D.-W. Biomaterials-based 3d cell printing for next-generation therapeutics and diagnostics. *Biomaterials*, 156:88–106, 2018.

Jeon, H., Lee, H., and Kim, G. A surface-modified poly (ε-caprolactone) scaffold comprising variable nanosized surface-roughness using a plasma treatment. *Tissue Engineering Part C: Methods*, 20(12):951–963, 2014.

Jiang, J., Tang, A., Ateshian, G. A., Guo, X. E., Hung, C. T., and Lu, H. H. Bioactive stratified polymer ceramic-hydrogel scaffold for integrative osteochondral repair. *Annals of biomedical engineering*, 38(6):2183–2196, 2010.

Jiao, Z., Luo, B., Xiang, S., Ma, H., Yu, Y., and Yang, W. 3d printing of ha/pcl composite tissue engineering scaffolds. *Advanced Industrial and Engineering Polymer Research*, 2(4):196–202, 2019.

Jones, D. S., Djokic, J., McCoy, C. P., and Gorman, S. P. Poly (ε-caprolactone) and poly (ε-caprolactone)-polyvinylpyrrolidone-iodine blends as ureteral biomaterials: characterisation of mechanical and surface properties, degradation and resistance to encrustation in vitro. *Biomaterials*, 23(23):4449–4458, 2002.

Jones, D. G. and Peterson, L. Autologous chondrocyte implantation. *JBJS*, 88(11): 2501–2520, 2006.

Kalia, P., Vizcay-Barrena, G., Fan, J. P., Warley, A., Di Silvio, L., and Huang, J. Nanohydroxyapatite shape and its potential role in bone formation: an analytical study. *Journal of The Royal Society Interface*, 11(93):20140004, 2014.

Kang, H., Zeng, Y., and Varghese, S. Functionally graded multilayer scaffolds for in vivo osteochondral tissue engineering. *Acta biomaterialia*, 78:365–377, 2018.

Kaplan, S. J., Hayes, W. C., Stone, J. L., and Beaupré, G. S. Tensile strength of bovine trabecular bone. *Journal of biomechanics*, 18(9):723–727, 1985.

Karageorgiou, V. and Kaplan, D. Porosity of 3d biomaterial scaffolds and osteogenesis. *Biomaterials*, 26(27):5474–5491, 2005.

Kariem, H., Pastrama, M.-I., Roohani-Esfahani, S. I., Pivonka, P., Zreiqat, H., and Hellmich, C. Micro-poro-elasticity of baghdadite-based bone tissue engineering scaffolds: a unifying approach based on ultrasonics, nanoindentation, and homogenization theory. *Materials Science and Engineering: C*, 46:553–564, 2015.

Kaul, H., Hall, B. K., Newby, C., and Ventikos, Y. Synergistic activity of polarised osteoblasts inside condensations cause their differentiation. *Scientific reports*, 5 (1):1–19, 2015.

Khanarian, N. T., Haney, N. M., Burga, R. A., and Lu, H. H. A functional agarose-hydroxyapatite scaffold for osteochondral interface regeneration. *Biomaterials*, 33(21):5247–5258, 2012.

Kim, H.-W., Knowles, J. C., and Kim, H.-E. Hydroxyapatite porous scaffold engineered with biological polymer hybrid coating for antibiotic vancomycin release. *Journal of materials science: materials in medicine*, 16(3):189–195, 2005.

Kim, K., Yeatts, A., Dean, D., and Fisher, J. P. Stereolithographic bone scaffold design parameters: osteogenic differentiation and signal expression. *Tissue Engineering Part B: Reviews*, 16(5):523–539, 2010.

Klein, T. J., Rizzi, S. C., Reichert, J. C., Georgi, N., Malda, J., Schuurman, W., Crawford, R. W., and Hutmacher, D. W. Strategies for zonal cartilage repair using hydrogels. *Macromolecular bioscience*, 9(11):1049–1058, 2009.

Knychala, J., Bouropoulos, N., Catt, C., Katsamenis, O., Please, C., and Sengers, B. Pore geometry regulates early stage human bone marrow cell tissue formation and organisation. *Annals of biomedical engineering*, 41(5):917–930, 2013.

Kon, E., Filardo, G., Di Martino, A., Busacca, M., Moio, A., Perdisa, F., and Marcacci, M. Clinical results and mri evolution of a nano-composite multilayered biomaterial for osteochondral regeneration at 5 years. *The American journal of sports medicine*, 42(1):158–165, 2014a.

Kon, E., Filardo, G., Perdisa, F., Di Martino, A., Busacca, M., Balboni, F., Sessa, A., and Marcacci, M. A one-step treatment for chondral and osteochondral knee defects: clinical results of a biomimetic scaffold implantation at 2 years of follow-up. *Journal of Materials Science: Materials in Medicine*, 25(10):2437–2444, 2014b.

Korpayev, S., Kaygusuz, G., Şen, M., Orhan, K., Oto, Ç., and Karakeçili, A. Chıtosan/collagen based biomimetic osteochondral tissue constructs: A growth factor-free approach. *International Journal of Biological Macromolecules*, 2020.

Kosik-Kozioł, A., Heljak, M., and Święszkowski, W. Mechanical properties of hybrid triphasic scaffolds for osteochondral tissue engineering. *Materials Letters*, 261:126893, 2020.

La Carrubba, V., Pavia, F. C., De Luca, A., and Giavaresi, G. Composite scaffolds with a hydrohyapatite spatial gradient for osteochondral defect repair. In *2018 IEEE 4th International Forum on Research and Technology for Society and Industry (RTSI)*, pages 1–4. IEEE, 2018.

Lacroix, D. and Prendergast, P. A mechano-regulation model for tissue differentiation during fracture healing: analysis of gap size and loading. *Journal of biomechanics*, 35(9):1163–1171, 2002.

Lacroix, D., Chateau, A., Ginebra, M.-P., and Planell, J. A. Micro-finite element models of bone tissue-engineering scaffolds. *Biomaterials*, 27(30):5326–5334, 2006.

Lee, P., Manoukian, O. S., Zhou, G., Wang, Y., Chang, W., Yu, X., and Kumbar, S. G. Osteochondral scaffold combined with aligned nanofibrous scaffolds for cartilage regeneration. *RSC advances*, 6(76):72246–72255, 2016.

Lee, S., Porter, M., Wasko, S., Lau, G., Chen, P.-Y., Novitskaya, E. E., Tomsia, A. P., Almutairi, A., Meyers, M. A., and McKittrick, J. Potential bone replacement materials prepared by two methods. *MRS Online Proceedings Library Archive*, 1418, 2012.

Lee, W., Debasitis, J. C., Lee, V. K., Lee, J.-H., Fischer, K., Edminster, K., Park, J.-K., and Yoo, S.-S. Multi-layered culture of human skin fibroblasts and keratinocytes through three-dimensional freeform fabrication. *Biomaterials*, 30(8): 1587–1595, 2009.

Levingstone, T. J., Matsiko, A., Dickson, G. R., O'Brien, F. J., and Gleeson, J. P. A biomimetic multi-layered collagen-based scaffold for osteochondral repair. *Acta biomaterialia*, 10(5):1996–2004, 2014.

Lewis, J. A. and Gratson, G. M. Direct writing in three dimensions. *Materials today*, 7(7-8):32–39, 2004.

Li, G., Yin, J., Gao, J., Cheng, T. S., Pavlos, N. J., Zhang, C., and Zheng, M. H. Subchondral bone in osteoarthritis: insight into risk factors and microstructural changes. *Arthritis research & therapy*, 15(6):223, 2013.

Li, L., Lin, Q., Tang, M., Duncan, A. J., and Ke, C. Advanced polymer designs for direct-ink-write 3d printing. *Chemistry–A European Journal*, 25(46):10768–10781, 2019.

Li, V. C.-F., Dunn, C. K., Zhang, Z., Deng, Y., and Qi, H. J. Direct ink write (diw) 3d printed cellulose nanocrystal aerogel structures. *Scientific reports*, 7(1):1–8, 2017.

Li, X., Ding, J., Wang, J., Zhuang, X., and Chen, X. Biomimetic biphasic scaffolds for osteochondral defect repair. *Regenerative biomaterials*, 2(3):221–228, 2015.

Li, Y., Wu, Z.-g., Li, X.-k., Guo, Z., Wu, S.-h., Zhang, Y.-q., Shi, L., Teoh, S.-h., Liu, Y.-c., and Zhang, Z.-y. A polycaprolactone-tricalcium phosphate composite

scaffold as an autograft-free spinal fusion cage in a sheep model. *Biomaterials*, 35(22):5647–5659, 2014.

Li, Z., Jia, S., Xiong, Z., Long, Q., Yan, S., Hao, F., Liu, J., and Yuan, Z. 3d-printed scaffolds with calcified layer for osteochondral tissue engineering. *Journal of bioscience and bioengineering*, 126(3):389–396, 2018.

Liao, C.-T. and Ho, M.-H. The fabrication of biomimetic chitosan scaffolds by using sbf treatment with different crosslinking agents. *Membranes*, 1(1):3–12, 2011.

Lin, H., Lozito, T. P., Alexander, P. G., Gottardi, R., and Tuan, R. S. Stem cell-based microphysiological osteochondral system to model tissue response to interleukin-1β. *Molecular pharmaceutics*, 11(7):2203–2212, 2014.

Lin, K., Sheikh, R., Romanazzo, S., and Roohani, I. 3d printing of bioceramic scaffolds—barriers to the clinical translation: From promise to reality, and future perspectives. *Materials*, 12(17):2660, 2019.

Liu, J., Li, L., Suo, H., Yan, M., Yin, J., and Fu, J. 3d printing of biomimetic multi-layered gelma/nha scaffold for osteochondral defect repair. *Materials & Design*, 171:107708, 2019.

Liu, W., Zhang, Y. S., Heinrich, M. A., De Ferrari, F., Jang, H. L., Bakht, S. M., Alvarez, M. M., Yang, J., Li, Y.-C., Trujillo-de Santiago, G., et al. Rapid continuous multimaterial extrusion bioprinting. *Advanced materials*, 29(3):1604630, 2017.

Liu, X. and Niebur, G. L. Bone ingrowth into a porous coated implant predicted by a mechano-regulatory tissue differentiation algorithm. *Biomechanics and modeling in mechanobiology*, 7(4):335, 2008.

Loh, Q. L. and Choong, C. Three-dimensional scaffolds for tissue engineering applications: role of porosity and pore size. *Tissue Engineering Part B: Reviews*, 19(6):485–502, 2013.

Longley, R., Ferreira, A. M., and Gentile, P. Recent approaches to the manufacturing of biomimetic multi-phasic scaffolds for osteochondral regeneration. *International journal of molecular sciences*, 19(6):1755, 2018.

Loozen, L. D., Wegman, F., Öner, F. C., Dhert, W. J., and Alblas, J. Porous bioprinted constructs in bmp-2 non-viral gene therapy for bone tissue engineering. *Journal of Materials Chemistry B*, 1(48):6619–6626, 2013.

Luczynski, K. W., Brynk, T., Ostrowska, B., Swieszkowski, W., Reihsner, R., and Hellmich, C. Consistent quasistatic and acoustic elasticity determination of poly-l-lactide-based rapid-prototyped tissue engineering scaffolds. *Journal of Biomedical Materials Research Part A*, 101(1):138–144, 2013.

Luczynski, K., Dejaco, A., Lahayne, O., Jaroszewicz, J., Swieszkowski, W., and Hellmich, C. Microct/micromechanics-based finite element models and quasistatic unloading tests deliver consistent values for young's modulus of rapid-prototyped polymer-ceramic tissue engineering scaffold. *Computer Modeling in Engineering & Sciences(CMES)*, 87(6):505–528, 2012.

Ma, P. X., Zhang, R., Xiao, G., and Franceschi, R. Engineering new bone tissue in vitro on highly porous poly (α-hydroxyl acids)/hydroxyapatite composite scaffolds. *Journal of Biomedical Materials Research: An Official Journal of The Society for Biomaterials and The Japanese Society for Biomaterials*, 54(2):284–293, 2001.

Macosko, C. W. and Larson, R. G. Rheology: principles, measurements, and applications. 1994.

Mai-Prochnow, A., Clauson, M., Hong, J., and Murphy, A. B. Gram positive and gram negative bacteria differ in their sensitivity to cold plasma. *Scientific reports*, 6:38610, 2016.

Malda, J., Visser, J., Melchels, F. P., Jüngst, T., Hennink, W. E., Dhert, W. J., Groll, J., and Hutmacher, D. W. 25th anniversary article: engineering hydrogels for biofabrication. *Advanced materials*, 25(36):5011–5028, 2013.

Maleki, H., Gharehaghaji, A., Moroni, L., and Dijkstra, P. J. Influence of the solvent type on the morphology and mechanical properties of electrospun plla yarns. *Biofabrication*, 5(3):035014, 2013.

Malikmammadov, E., Tanir, T. E., Kiziltay, A., Hasirci, V., and Hasirci, N. Pcl and pcl-based materials in biomedical applications. *Journal of Biomaterials science, Polymer edition*, 29(7-9):863–893, 2018.

March, L., Cross, M., Lo, C., Arden, N., Gates, L., Leyland, K., Hawker, G., and King, L. Osteoarthritis: a serious disease. *OARSI. org*, 2016.

Markstedt, K., Mantas, A., Tournier, I., Hector, M. A., Hagg, D., and Gatenholm, P. 3d bioprinting human chondrocytes with nanocellulose–alginate bioink for cartilage tissue engineering applications. *Biomacromolecules*, 16(5):1489–1496, 2015.

Marrella, A., Lee, T. Y., Lee, D. H., Karuthedom, S., Syla, D., Chawla, A., Khademhosseini, A., and Jang, H. L. Engineering vascularized and innervated bone biomaterials for improved skeletal tissue regeneration. *Materials Today*, 21 (4):362–376, 2018.

Martín, A. R., Patel, J. M., Zlotnick, H. M., Carey, J. L., and Mauck, R. L. Emerging therapies for cartilage regeneration in currently excluded 'red knee'populations. *NPJ Regenerative medicine*, 4(1):1–11, 2019.

Martin, I., Miot, S., Barbero, A., Jakob, M., and Wendt, D. Osteochondral tissue engineering. *Journal of biomechanics*, 40(4):750–765, 2007.

McCullen, S. D., Miller, P. R., Gittard, S. D., Gorga, R. E., Pourdeyhimi, B., Narayan, R. J., and Loboa, E. G. In situ collagen polymerization of layered cell-seeded electrospun scaffolds for bone tissue engineering applications. *Tissue Engineering Part C: Methods*, 16(5):1095–1105, 2010.

Melchels, F. P., Bertoldi, K., Gabbrielli, R., Velders, A. H., Feijen, J., and Grijpma,

D. W. Mathematically defined tissue engineering scaffold architectures prepared by stereolithography. *Biomaterials*, 31(27):6909–6916, 2010.

Melchels, F. P., Tonnarelli, B., Olivares, A. L., Martin, I., Lacroix, D., Feijen, J., Wendt, D. J., and Grijpma, D. W. The influence of the scaffold design on the distribution of adhering cells after perfusion cell seeding. *Biomaterials*, 32(11): 2878–2884, 2011.

Meyer, U., Büchter, A., Nazer, N., and Wiesmann, H. Design and performance of a bioreactor system for mechanically promoted three-dimensional tissue engineering. *British Journal of Oral and Maxillofacial Surgery*, 44(2):134–140, 2006.

Michalopoulos, E., Knight, R. L., Korossis, S., Kearney, J. N., Fisher, J., and Ingham, E. Development of methods for studying the differentiation of human mesenchymal stem cells under cyclic compressive strain. *Tissue Engineering Part C: Methods*, 18(4):252–262, 2012.

Minas, T. Autologous chondrocyte implantation for focal chondral defects of the knee. *Clinical Orthopaedics and Related Research®*, 391:S349–S361, 2001.

Miranda, P., Pajares, A., Saiz, E., Tomsia, A. P., and Guiberteau, F. Mechanical properties of calcium phosphate scaffolds fabricated by robocasting. *Journal of Biomedical Materials Research Part A: An Official Journal of The Society for Biomaterials, The Japanese Society for Biomaterials, and The Australian Society for Biomaterials and the Korean Society for Biomaterials*, 85(1):218–227, 2008.

Miron, R. J., Sculean, A., Shuang, Y., Bosshardt, D. D., Gruber, R., Buser, D., Chandad, F., and Zhang, Y. Osteoinductive potential of a novel biphasic calcium phosphate bone graft in comparison with autographs, xenografts, and dfdba. *Clinical oral implants research*, 27(6):668–675, 2016.

Mobasheri, A., Kalamegam, G., Musumeci, G., and Batt, M. E. Chondrocyte and mesenchymal stem cell-based therapies for cartilage repair in osteoarthritis and related orthopaedic conditions. *Maturitas*, 78(3):188–198, 2014.

Mohan, N., Dormer, N. H., Caldwell, K. L., Key, V. H., Berkland, C. J., and Detamore, M. S. Continuous gradients of material composition and growth factors for effective regeneration of the osteochondral interface. *Tissue Engineering Part A*, 17(21-22):2845–2855, 2011.

Molino, G., Palmieri, M. C., Montalbano, G., Fiorilli, S., and Vitale-Brovarone, C. Biomimetic and mesoporous nano-hydroxyapatite for bone tissue application: a short review. *Biomedical Materials*, 15(2):022001, 2020.

Morrison, F. A. et al. *Understanding rheology*. Oxford University Press, USA, 2001.

Morrison, R. J., Hollister, S. J., Niedner, M. F., Mahani, M. G., Park, A. H., Mehta, D. K., Ohye, R. G., and Green, G. E. Mitigation of tracheobronchomalacia with 3d-printed personalized medical devices in pediatric patients. *Science translational medicine*, 7(285):285ra64–285ra64, 2015.

Mozafari, M., Kargozar, S., De Santiago, G., Mohammadi, M. R., Milan, P., Foroutan Koudehi, M., Aghabarari, B., and Nourani, M. Synthesis and characterisation of highly interconnected porous poly (ε-caprolactone)-collagen scaffolds: a therapeutic design to facilitate tendon regeneration. *Materials technology*, 33 (1):29–37, 2018.

Müller, M., Becher, J., Schnabelrauch, M., and Zenobi-Wong, M. Nanostructured pluronic hydrogels as bioinks for 3d bioprinting. *Biofabrication*, 7(3):035006, 2015.

Naghieh, S., Ravari, M. K., Badrossamay, M., Foroozmehr, E., and Kadkhodaei, M. Numerical investigation of the mechanical properties of the additive manufactured bone scaffolds fabricated by fdm: the effect of layer penetration and post-heating. *Journal of the mechanical behavior of biomedical materials*, 59: 241–250, 2016.

Naghieh, S., Karamooz-Ravari, M. R., Sarker, M., Karki, E., and Chen, X. Influence of crosslinking on the mechanical behavior of 3d printed alginate scaffolds:

Experimental and numerical approaches. *Journal of the mechanical behavior of biomedical materials*, 80:111–118, 2018.

Nasir, N. M., Zain, N. M., Raha, M., and Kadri, N. Characterization of chitosan-poly (ethylene oxide) blends as haemodialysis membrane. *American Journal of Applied Sciences*, 2(12):1578–1583, 2005.

Ng, H. Y., Lee, K.-X. A., and Shen, Y.-F. Articular cartilage: Structure, composition, injuries and repair. *JSM Bone and Joint Dis*, 1(2):1010, 2017.

Nikolov, S. and Raabe, D. Hierarchical modeling of the elastic properties of bone at submicron scales: the role of extrafibrillar mineralization. *Biophysical journal*, 94(11):4220–4232, 2008.

Ning, L., Guillemot, A., Zhao, J., Kipouros, G., and Chen, X. Influence of flow behavior of alginate–cell suspensions on cell viability and proliferation. *Tissue Engineering Part C: Methods*, 22(7):652–662, 2016.

Nooeaid, P., Salih, V., Beier, J. P., and Boccaccini, A. R. Osteochondral tissue engineering: scaffolds, stem cells and applications. *Journal of cellular and molecular medicine*, 16(10):2247–2270, 2012.

Nooeaid, P., Roether, J. A., Weber, E., Schubert, D. W., and Boccaccini, A. R. Technologies for multilayered scaffolds suitable for interface tissue engineering. *Advanced Engineering Materials*, 16(3):319–327, 2014.

Nowicki, M., Zhu, W., Sarkar, K., Rao, R., and Zhang, L. G. 3d printing multiphasic osteochondral tissue constructs with nano to micro features via pcl based bioink. *Bioprinting*, 17:e00066, 2020.

Nowicki, M. A., Castro, N. J., Plesniak, M. W., and Zhang, L. G. 3d printing of novel osteochondral scaffolds with graded microstructure. *Nanotechnology*, 27 (41):414001, 2016.

Oladapo, B. I., Zahedi, S., and Adeoye, A. 3d printing of bone scaffolds with hybrid biomaterials. *Composites Part B: Engineering*, 158:428–436, 2019.

Olivares, A. L., Marsal, È., Planell, J. A., and Lacroix, D. Finite element study of scaffold architecture design and culture conditions for tissue engineering. *Biomaterials*, 30(30):6142–6149, 2009.

Panadero, J., Lanceros-Mendez, S., and Ribelles, J. G. Differentiation of mesenchymal stem cells for cartilage tissue engineering: Individual and synergetic effects of three-dimensional environment and mechanical loading. *Acta biomaterialia*, 33:1–12, 2016.

Parisi, C., Salvatore, L., Veschini, L., Serra, M. P., Hobbs, C., Madaghiele, M., Sannino, A., and Di Silvio, L. Biomimetic gradient scaffold of collagen–hydroxyapatite for osteochondral regeneration. *Journal of Tissue Engineering*, 11:2041731419896068, 2020.

Park, S. A., Lee, S. H., and Kim, W. D. Fabrication of porous polycaprolactone/hydroxyapatite (pcl/ha) blend scaffolds using a 3d plotting system for bone tissue engineering. *Bioprocess and biosystems engineering*, 34(4):505–513, 2011.

Park, S. A., Lee, S. J., Seok, J. M., Lee, J. H., Kim, W. D., and Kwon, I. K. Fabrication of 3d printed pcl/peg polyblend scaffold using rapid prototyping system for bone tissue engineering application. *Journal of Bionic Engineering*, 15(3): 435–442, 2018.

Parker, T., Davé, V., Falotico, R., Zhao, J., Nguyen, T., He, S., Sun, Y.-P., and Rogers, C. Control of cilostazol release kinetics and direction from a stent using a reservoir-based design. *Journal of Biomedical Materials Research Part B: Applied Biomaterials*, 100(3):603–610, 2012.

Patel, S., Caldwell, J.-M., Doty, S. B., Levine, W. N., Rodeo, S., Soslowsky, L. J., Thomopoulos, S., and Lu, H. H. Integrating soft and hard tissues via interface tissue engineering. *Journal of Orthopaedic Research®*, 36(4):1069–1077, 2018.

Pauwels, F. Basic biomechanics of fracture healing. 34th congress of the german

orthopedic society ferdinand enke verlag, stuttgart (1980) (biomechanics of the locomotor apparatus). p. manquet and r. furlong, 1941.

Paxton, N., Smolan, W., Böck, T., Melchels, F., Groll, J., and Jungst, T. Proposal to assess printability of bioinks for extrusion-based bioprinting and evaluation of rheological properties governing bioprintability. *Biofabrication*, 9(4):044107, 2017.

Peak, C. W., Stein, J., Gold, K. A., and Gaharwar, A. K. Nanoengineered colloidal inks for 3d bioprinting. *Langmuir*, 34(3):917–925, 2018.

Perren, S. Physical and biological aspects of fracture healing with special reference to internal fixation. *Clinical orthopaedics and related research*, (138):175–196, 1979.

Phillippi, J. A., Miller, E., Weiss, L., Huard, J., Waggoner, A., and Campbell, P. Microenvironments engineered by inkjet bioprinting spatially direct adult stem cells toward muscle-and bone-like subpopulations. *Stem cells*, 26(1):127–134, 2008.

Potrč, T., Baumgartner, S., Roškar, R., Planinšek, O., Lavrič, Z., Kristl, J., and Kocbek, P. Electrospun polycaprolactone nanofibers as a potential oromucosal delivery system for poorly water-soluble drugs. *European Journal of Pharmaceutical Sciences*, 75:101–113, 2015.

Prendergast, P., Huiskes, R., and Søballe, K. Biophysical stimuli on cells during tissue differentiation at implant interfaces. *Journal of biomechanics*, 30(6):539–548, 1997.

Qiu, Z., Ikehara, T., and Nishi, T. Miscibility and crystallization of poly (ethylene oxide) and poly (ε-caprolactone) blends. *Polymer*, 44(10):3101–3106, 2003.

Qu, F., Holloway, J. L., Esterhai, J. L., Burdick, J. A., and Mauck, R. L. Programmed biomolecule delivery to enable and direct cell migration for connective tissue repair. *Nature communications*, 8(1):1–11, 2017.

Qu, H., Fu, H., Han, Z., and Sun, Y. Biomaterials for bone tissue engineering scaffolds: a review. *RSC advances*, 9(45):26252–26262, 2019.

Raghunath, J., Rollo, J., Sales, K. M., Butler, P. E., and Seifalian, A. M. Biomaterials and scaffold design: key to tissue-engineering cartilage. *Biotechnology and applied biochemistry*, 46(2):73–84, 2007.

Ragu, A., Senthilarasan, K., and Sakthivel, P. Synthesis and characterization of nano hydroxyapatite with poly vinyl pyrrolidone nano composite for bone tissue regeneration. *Int. J. Eng. Res. Appl*, 4(10):50–54, 2014.

Rai, A., Senapati, S., Saraf, S. K., and Maiti, P. Biodegradable poly (ε-caprolactone) as a controlled drug delivery vehicle of vancomycin for the treatment of mrsa infection. *Journal of Materials Chemistry B*, 4(30):5151–5160, 2016.

Raney, J. R. and Lewis, J. A. Printing mesoscale architectures. *Mrs Bulletin*, 40 (11):943, 2015.

Rao, R. T., Browe, D. P., Lowe, C. J., and Freeman, J. W. An overview of recent patents on musculoskeletal interface tissue engineering. *Connective tissue research*, 57(1):53–67, 2016.

Rebollar, E., Cordero, D., Martins, A., Chiussi, S., Reis, R. L., Neves, N. M., and León, B. Improvement of electrospun polymer fiber meshes pore size by femtosecond laser irradiation. *Applied Surface Science*, 257(9):4091–4095, 2011.

Reichert, J. C., Wullschleger, M. E., Cipitria, A., Lienau, J., Cheng, T. K., Schütz, M. A., Duda, G. N., Nöth, U., Eulert, J., and Hutmacher, D. W. Custom-made composite scaffolds for segmental defect repair in long bones. *International orthopaedics*, 35(8):1229–1236, 2011.

Remya, K., Chandran, S., Mani, S., John, A., and Ramesh, P. Hybrid polycaprolactone/polyethylene oxide scaffolds with tunable fiber surface morphology, improved hydrophilicity and biodegradability for bone tissue engineering appli-

cations. *Journal of Biomaterials science, Polymer edition*, 29(12):1444–1462, 2018.

Rezwan, K., Chen, Q., Blaker, J. J., and Boccaccini, A. R. Biodegradable and bioactive porous polymer/inorganic composite scaffolds for bone tissue engineering. *Biomaterials*, 27(18):3413–3431, 2006.

Rodrigues, M. T., Gomes, M. E., and Reis, R. L. Current strategies for osteochondral regeneration: from stem cells to pre-clinical approaches. *Current opinion in biotechnology*, 22(5):726–733, 2011.

Rodríguez-Montaño, Ó. L., Cortés-Rodríguez, C. J., Uva, A. E., Fiorentino, M., Gattullo, M., Monno, G., and Boccaccio, A. Comparison of the mechanobiological performance of bone tissue scaffolds based on different unit cell geometries. *Journal of the mechanical behavior of biomedical materials*, 83:28–45, 2018.

Roopavath, U. K., Malferrari, S., Van Haver, A., Verstreken, F., Rath, S. N., and Kalaskar, D. M. Optimization of extrusion based ceramic 3d printing process for complex bony designs. *Materials & Design*, 162:263–270, 2019.

Rumpler, M., Woesz, A., Dunlop, J. W., Van Dongen, J. T., and Fratzl, P. The effect of geometry on three-dimensional tissue growth. *Journal of the Royal Society Interface*, 5(27):1173–1180, 2008.

Rychter, M., Baranowska-Korczyc, A., Milanowski, B., Jarek, M., Maciejewska, B. M., Coy, E. L., and Lulek, J. Cilostazol-loaded poly (ε-caprolactone) electrospun drug delivery system for cardiovascular applications. *Pharmaceutical research*, 35(2):32, 2018.

Sabree, I., Gough, J. E., and Derby, B. Mechanical properties of porous ceramic scaffolds: influence of internal dimensions. *Ceramics International*, 41(7):8425–8432, 2015.

Salerno, A., Zeppetelli, S., Di Maio, E., Iannace, S., and Netti, P. Processing/structure/property relationship of multi-scaled pcl and pcl–ha composite scaf-

folds prepared via gas foaming and nacl reverse templating. *Biotechnology and bioengineering*, 108(4):963–976, 2011.

San Cheong, V., Fromme, P., Mumith, A., Coathup, M. J., and Blunn, G. W. Novel adaptive finite element algorithms to predict bone ingrowth in additive manufactured porous implants. *Journal of the mechanical behavior of biomedical materials*, 87:230–239, 2018.

Sandino, C., Planell, J., and Lacroix, D. A finite element study of mechanical stimuli in scaffolds for bone tissue engineering. *Journal of biomechanics*, 41(5): 1005–1014, 2008.

Savitskaya, I., Shokatayeva, D., Kistaubayeva, A., Ignatova, L., and Digel, I. Antimicrobial and wound healing properties of a bacterial cellulose based material containing b. subtilis cells. *Heliyon*, 5(10):e02592, 2019.

Schacht, K., Jüngst, T., Schweinlin, M., Ewald, A., Groll, J., and Scheibel, T. Biofabrication of cell-loaded 3d spider silk constructs. *Angewandte Chemie International Edition*, 54(9):2816–2820, 2015.

Schaefer, D., Martin, I., Shastri, P., Padera, R., Langer, R., Freed, L., and Vunjak-Novakovic, G. In vitro generation of osteochondral composites. *Biomaterials*, 21(24):2599–2606, 2000.

Schek, R. M., Taboas, J. M., Segvich, S. J., Hollister, S. J., and Krebsbach, P. H. Engineered osteochondral grafts using biphasic composite solid free-form fabricated scaffolds. *Tissue Engineering*, 10(9-10):1376–1385, 2004.

Schipani, R., Nolan, D. R., Lally, C., and Kelly, D. J. Integrating finite element modelling and 3d printing to engineer biomimetic polymeric scaffolds for tissue engineering. *Connective Tissue Research*, 61(2):174–189, 2020.

Schroeder, J. E. and Mosheiff, R. Tissue engineering approaches for bone repair: concepts and evidence. *Injury*, 42(6):609–613, 2011.

Seidi, A., Ramalingam, M., Elloumi-Hannachi, I., Ostrovidov, S., and Khademhosseini, A. Gradient biomaterials for soft-to-hard interface tissue engineering. *Acta biomaterialia*, 7(4):1441–1451, 2011.

Serra, T., Planell, J. A., and Navarro, M. High-resolution pla-based composite scaffolds via 3-d printing technology. *Acta biomaterialia*, 9(3):5521–5530, 2013.

Shaqour, B., Samaro, A., Verleije, B., Beyers, K., Vervaet, C., and Cos, P. Production of drug delivery systems using fused filament fabrication: a systematic review. *Pharmaceutics*, 12(6):517, 2020.

Shenoy, S. L., Bates, W. D., Frisch, H. L., and Wnek, G. E. Role of chain entanglements on fiber formation during electrospinning of polymer solutions: good solvent, non-specific polymer–polymer interaction limit. *Polymer*, 46(10):3372–3384, 2005.

Shi, D., Shen, J., Zhang, Z., Shi, C., Chen, M., Gu, Y., and Liu, Y. Preparation and properties of dopamine-modified alginate/chitosan–hydroxyapatite scaffolds with gradient structure for bone tissue engineering. *Journal of Biomedical Materials Research Part A*, 107(8):1615–1627, 2019.

Shin, J. H. and Kang, H.-W. The development of gelatin-based bio-ink for use in 3d hybrid bioprinting. *International Journal of Precision Engineering and Manufacturing*, 19(5):767–771, 2018.

Shirazi, S. F. S., Gharehkhani, S., Mehrali, M., Yarmand, H., Metselaar, H. S. C., Kadri, N. A., and Osman, N. A. A. A review on powder-based additive manufacturing for tissue engineering: selective laser sintering and inkjet 3d printing. *Science and technology of advanced materials*, 2015.

Shor, L., Güçeri, S., Wen, X., Gandhi, M., and Sun, W. Fabrication of three-dimensional polycaprolactone/hydroxyapatite tissue scaffolds and osteoblast-scaffold interactions in vitro. *Biomaterials*, 28(35):5291–5297, 2007.

Shuai, C., Feng, P., Wu, P., Liu, Y., Liu, X., Lai, D., Gao, C., and Peng, S. A combined nanostructure constructed by graphene and boron nitride nanotubes reinforces ceramic scaffolds. *Chemical Engineering Journal*, 313:487–497, 2017.

Shuai, C., Guo, W., Wu, P., Yang, W., Hu, S., Xia, Y., and Feng, P. A graphene oxide-ag co-dispersing nanosystem: dual synergistic effects on antibacterial activities and mechanical properties of polymer scaffolds. *Chemical Engineering Journal*, 347:322–333, 2018.

Shuai, C., Liu, G., Yang, Y., Yang, W., He, C., Wang, G., Liu, Z., Qi, F., and Peng, S. Functionalized batio3 enhances piezoelectric effect towards cell response of bone scaffold. *Colloids and Surfaces B: Biointerfaces*, 185:110587, 2020a.

Shuai, C., Zan, J., Yang, Y., Peng, S., Yang, W., Qi, F., Shen, L., and Tian, Z. Surface modification enhances interfacial bonding in plla/mgo bone scaffold. *Materials Science and Engineering: C*, 108:110486, 2020b.

Siddiqui, N., Asawa, S., Birru, B., Baadhe, R., and Rao, S. Pcl-based composite scaffold matrices for tissue engineering applications. *Molecular biotechnology*, 60(7):506–532, 2018.

Song, R., Murphy, M., Li, C., Ting, K., Soo, C., and Zheng, Z. Current development of biodegradable polymeric materials for biomedical applications. *Drug design, development and therapy*, 12:3117, 2018.

Sophia Fox, A. J., Bedi, A., and Rodeo, S. A. The basic science of articular cartilage: structure, composition, and function. *Sports health*, 1(6):461–468, 2009.

Steele, J., McCullen, S., Callanan, A., Autefage, H., Accardi, M., Dini, D., and Stevens, M. Combinatorial scaffold morphologies for zonal articular cartilage engineering. *Acta biomaterialia*, 10(5):2065–2075, 2014.

Stratton, S., Shelke, N. B., Hoshino, K., Rudraiah, S., and Kumbar, S. G. Bioactive polymeric scaffolds for tissue engineering. *Bioactive materials*, 1(2):93–108, 2016.

Sumanasinghe, R. D., Bernacki, S. H., and Loboa, E. G. Osteogenic differentiation of human mesenchymal stem cells in collagen matrices: effect of uniaxial cyclic tensile strain on bone morphogenetic protein (bmp-2) mrna expression. *Tissue engineering*, 12(12):3459–3465, 2006.

Sun, L., Parker, S. T., Syoji, D., Wang, X., Lewis, J. A., and Kaplan, D. L. Direct-write assembly of 3d silk/hydroxyapatite scaffolds for bone co-cultures. *Advanced healthcare materials*, 1(6):729–735, 2012.

Sung, H.-J., Meredith, C., Johnson, C., and Galis, Z. S. The effect of scaffold degradation rate on three-dimensional cell growth and angiogenesis. *Biomaterials*, 25 (26):5735–5742, 2004.

Sutcu, M. Orthotropic and transversely isotropic stress-strain relations with built-in coordinate transformations. *International journal of solids and structures*, 29(4): 503–518, 1992.

Szlazak, K., Vass, V., Hasslinger, P., Jaroszewicz, J., Dejaco, A., Idaszek, J., Scheiner, S., Hellmich, C., and Swieszkowski, W. X-ray physics-based ct-to-composition conversion applied to a tissue engineering scaffold, enabling multi-scale simulation of its elastic behavior. *Materials Science and Engineering: C*, 95:389–396, 2019.

Tamaddon, M., Wang, L., Liu, Z., and Liu, C. Osteochondral tissue repair in osteoarthritic joints: clinical challenges and opportunities in tissue engineering. *Bio-design and manufacturing*, 1(2):101–114, 2018.

Tang, Z., Black, R., Curran, J., Hunt, J., Rhodes, N., and Williams, D. Surface properties and biocompatibility of solvent-cast poly [ε-caprolactone] films. *Biomaterials*, 25(19):4741–4748, 2004.

Tibor, L. M. and Weiss, J. A. Hip cartilage restoration: Overview. *Hip Arthroscopy and Hip Joint Preservation Surgery*, pages 1–19, 2013.

Trachtenberg, J. E., Placone, J. K., Smith, B. T., Fisher, J. P., and Mikos, A. G. Extrusion-based 3d printing of poly (propylene fumarate) scaffolds with hydroxyapatite gradients. *Journal of Biomaterials science, Polymer edition*, 28(6):532–554, 2017.

Tripathy, N., Perumal, E., Ahmad, R., Song, J. E., and Khang, G. Hybrid composite biomaterials. In *Principles of Regenerative Medicine*, pages 695–714. Elsevier, 2019.

Truby, R. L. and Lewis, J. A. Printing soft matter in three dimensions. *Nature*, 540 (7633):371–378, 2016.

Turner-Walker, G. H. *The characterisation of fossil bone*. PhD thesis, Durham University, 1993.

Vacanti, J. P. and Langer, R. Tissue engineering: the design and fabrication of living replacement devices for surgical reconstruction and transplantation. *The lancet*, 354:S32–S34, 1999.

Van Bael, S., Chai, Y. C., Truscello, S., Moesen, M., Kerckhofs, G., Van Oosterwyck, H., Kruth, J.-P., and Schrooten, J. The effect of pore geometry on the in vitro biological behavior of human periosteum-derived cells seeded on selective laser-melted ti6al4v bone scaffolds. *Acta biomaterialia*, 8(7):2824–2834, 2012.

Van Rietbergen, B., Müller, R., Ulrich, D., Rüegsegger, P., and Huiskes, R. Tissue stresses and strain in trabeculae of a canine proximal femur can be quantified from computer reconstructions. *Journal of biomechanics*, 32(2):165–173, 1999.

Verhaegen, J., Clockaerts, S., Van Osch, G., Somville, J., Verdonk, P., and Mertens, P. Trufit plug for repair of osteochondral defects—where is the evidence? systematic review of literature. *Cartilage*, 6(1):12–19, 2015.

Walther, A., Hoyer, B., Springer, A., Mrozik, B., Hanke, T., Cherif, C., Pompe, W., and Gelinsky, M. Novel textile scaffolds generated by flock technology for tissue engineering of bone and cartilage. *Materials*, 5(3):540–557, 2012.

Wang, C., Feng, N., Chang, F., Wang, J., Yuan, B., Cheng, Y., Liu, H., Yu, J., Zou, J., Ding, J., et al. Injectable cholesterol-enhanced stereocomplex polylactide thermogel loading chondrocytes for optimized cartilage regeneration. *Advanced healthcare materials*, 8(14):1900312, 2019.

Wang, H., Su, K., Su, L., Liang, P., Ji, P., and Wang, C. The effect of 3d-printed ti6al4v scaffolds with various macropore structures on osteointegration and osteogenesis: A biomechanical evaluation. *Journal of the mechanical behavior of biomedical materials*, 88:488–496, 2018.

Wang, W., Caetano, G., Ambler, W. S., Blaker, J. J., Frade, M. A., Mandal, P., Diver, C., and Bártolo, P. Enhancing the hydrophilicity and cell attachment of 3d printed pcl/graphene scaffolds for bone tissue engineering. *Materials*, 9(12):992, 2016.

Wang, Y., Meng, H., Yuan, X., Peng, J., Guo, Q., Lu, S., and Wang, A. Fabrication and in vitro evaluation of an articular cartilage extracellular matrix-hydroxyapatite bilayered scaffold with low permeability for interface tissue engineering. *Biomedical engineering online*, 13(1):80, 2014.

Wang, Y., Blasioli, D. J., Kim, H.-J., Kim, H. S., and Kaplan, D. L. Cartilage tissue engineering with silk scaffolds and human articular chondrocytes. *Biomaterials*, 27(25):4434–4442, 2006.

Weng, W., Nie, W., Zhou, Q., Zhou, X., Cao, L., Ji, F., Cui, J., He, C., and Su, J. Controlled release of vancomycin from 3d porous graphene-based composites for dual-purpose treatment of infected bone defects. *RSC advances*, 7(5):2753–2765, 2017.

Williams, G. M., Chan, E. F., Temple-Wong, M. M., Bae, W. C., Masuda, K., Bugbee, W. D., and Sah, R. L. Shape, loading, and motion in the bioengineering design, fabrication, and testing of personalized synovial joints. *Journal of biomechanics*, 43(1):156–165, 2010.

Williams, J. and Lewis, J. Properties and an anisotropic model of cancellous bone from the proximal tibial epiphysis. 1982.

Woodfield, T., Blitterswijk, C. V., Wijn, J. D., Sims, T., Hollander, A., and Riesle, J. Polymer scaffolds fabricated with pore-size gradients as a model for studying the zonal organization within tissue-engineered cartilage constructs. *Tissue engineering*, 11(9-10):1297–1311, 2005.

Wu, G.-H. and Hsu, S.-h. polymeric-based 3d printing for tissue engineering. *Journal of medical and biological engineering*, 35(3):285–292, 2015.

Wüst, S., Müller, R., and Hofmann, S. Controlled positioning of cells in biomaterials—approaches towards 3d tissue printing. *Journal of functional biomaterials*, 2(3):119–154, 2011.

Wüst, S., Godla, M. E., Müller, R., and Hofmann, S. Tunable hydrogel composite with two-step processing in combination with innovative hardware upgrade for cell-based three-dimensional bioprinting. *Acta biomaterialia*, 10(2):630–640, 2014.

Xiao, H., Huang, W., Xiong, K., Ruan, S., Yuan, C., Mo, G., Tian, R., Zhou, S., She, R., Ye, P., et al. Osteochondral repair using scaffolds with gradient pore sizes constructed with silk fibroin, chitosan, and nano-hydroxyapatite. *International Journal of Nanomedicine*, 14:2011, 2019.

Xue, R., Chung, B., Tamaddon, M., Carr, J., Liu, C., and Cartmell, S. H. Osteochondral tissue coculture: An in vitro and in silico approach. *Biotechnology and bioengineering*, 116(11):3112–3123, 2019.

Yang, Y., Yuan, F., Gao, C., Feng, P., Xue, L., He, S., and Shuai, C. A combined strategy to enhance the properties of zn by laser rapid solidification and laser alloying. *Journal of the mechanical behavior of biomedical materials*, 82:51–60, 2018.

Yeo, M. G. and Kim, G. H. Preparation and characterization of 3d composite scaffolds based on rapid-prototyped pcl/β-tcp struts and electrospun pcl coated with collagen and ha for bone regeneration. *Chemistry of materials*, 24(5):903–913, 2012.

Yew, C. H. T., Azari, P., Choi, J. R., Muhamad, F., and Pingguan-Murphy, B. Electrospun polycaprolactone nanofibers as a reaction membrane for lateral flow assay. *Polymers*, 10(12):1387, 2018.

You, F., Wu, X., and Chen, X. 3d printing of porous alginate/gelatin hydrogel scaffolds and their mechanical property characterization. *International Journal of Polymeric Materials and Polymeric Biomaterials*, 66(6):299–306, 2017.

Yousefi, A.-M., Hoque, M. E., Prasad, R. G., and Uth, N. Current strategies in multiphasic scaffold design for osteochondral tissue engineering: a review. *Journal of biomedical materials research Part A*, 103(7):2460–2481, 2015.

Zanetti, A. S., Sabliov, C., Gimble, J. M., and Hayes, D. J. Human adipose-derived stem cells and three-dimensional scaffold constructs: A review of the biomaterials and models currently used for bone regeneration. *Journal of Biomedical Materials Research Part B: Applied Biomaterials*, 101(1):187–199, 2013.

Zarif, M., Afidah, A., Abdullah, J., and Shariza, A. Physicochemical characterization of vancomycin and its complexes with?-cyclodextrin. 2012.

Zhang, B., Cristescu, R., Chrisey, D. B., and Narayan, R. J. Solvent-based extrusion 3d printing for the fabrication of tissue engineering scaffolds. *International Journal of Bioprinting*, 6(1), 2020a.

Zhang, B., Guo, L., Chen, H., Ventikos, Y., Narayan, R. J., and Huang, J. Finite element evaluations of the mechanical properties of polycaprolactone/hydroxyapatite scaffolds by direct ink writing: Effects of pore geometry. *Journal of the Mechanical Behavior of Biomedical Materials*, 104:103665, 2020b.

Zhang, B., Huang, J., and Narayan, R. Nanostructured biomaterials for regenerative medicine: Clinical perspectives. In *Nanostructured Biomaterials for Regenerative Medicine*, pages 47–80. Elsevier, 2020c.

Zhang, L., Hu, J., and Athanasiou, K. A. The role of tissue engineering in articular cartilage repair and regeneration. *Critical Reviews™ in Biomedical Engineering*, 37(1-2), 2009.

Zhang, S., Chen, L., Jiang, Y., Cai, Y., Xu, G., Tong, T., Zhang, W., Wang, L., Ji, J., Shi, P., et al. Bi-layer collagen/microporous electrospun nanofiber scaffold improves the osteochondral regeneration. *Acta Biomaterialia*, 9(7):7236–7247, 2013.

Zhang, Y., Wang, F., Tan, H., Chen, G., Guo, L., and Yang, L. Analysis of the mineral composition of the human calcified cartilage zone. *International journal of medical sciences*, 9(5):353, 2012.

Zhao, C., Zhang, H., Cai, B., Wang, G., Fan, H., and Zhang, X. Preparation of porous plga/ti biphasic scaffold and osteochondral defect repair. *Biomaterials Science*, 1(7):703–710, 2013.

Zhou, G., Xu, C., Cheng, W., Zhang, Q., and Nie, W. Effects of oxygen element and oxygen-containing functional groups on surface wettability of coal dust with various metamorphic degrees based on xps experiment. *Journal of analytical methods in chemistry*, 2015, 2015.

Zhou, J., Xu, C., Wu, G., Cao, X., Zhang, L., Zhai, Z., Zheng, Z., Chen, X., and Wang, Y. In vitro generation of osteochondral differentiation of human marrow mesenchymal stem cells in novel collagen–hydroxyapatite layered scaffolds. *Acta biomaterialia*, 7(11):3999–4006, 2011.

Zhou, L., Ramezani, H., Sun, M., Xie, M., Nie, J., Lv, S., Cai, J., Fu, J., and He, Y. 3d printing of high-strength chitosan hydrogel scaffolds without any organic solvents. *Biomaterials Science*, 8(18):5020–5028, 2020.

Zhou, X., Esworthy, T., Lee, S.-J., Miao, S., Cui, H., Plesiniak, M., Fenniri, H., Webster, T., Rao, R. D., and Zhang, L. G. 3d printed scaffolds with hierarchical biomimetic structure for osteochondral regeneration. *Nanomedicine: Nanotechnology, Biology and Medicine*, 19:58–70, 2019.

Zhou, Z., Yao, Q., Li, L., Zhang, X., Wei, B., Yuan, L., and Wang, L. Antimicrobial activity of 3d-printed poly (ε-caprolactone)(pcl) composite scaffolds presenting vancomycin-loaded polylactic acid-glycolic acid (plga) microspheres. *Medical science monitor: international medical journal of experimental and clinical research*, 24:6934, 2018.

Appendix A

Scaffold property

A.1 Stress-strain curve

The value of Young's modulus (40 MPa) of the PCL/HAp bulk material was obtained from our mechanical compression tests of cylindrical specimens. A linear elastic region can be identified in the strain range of 2%-9% (dashed line in Figure A.1). The slope of this region is calculated as the Young's modulus for the bulk material (40 MPa), which is obtained as the average value of three specimens. The yield point was defined as the end of the linear stage.

A.2 Water absorption and swelling

Swelling ratio, as a percentage change in volume, was calculated using Equation A.1:

$$\text{Swelling ratio} = \frac{V_1 - V_2}{V_2} \tag{A.1}$$

where V_1 is volume after immersion, and V_2 is volume before immersion. Water absorption ratio, as a percentage change in weight was calculated using Equation A.2:

$$\text{Water absorption ratio} = \frac{W_1 - W_2}{W_2} \tag{A.2}$$

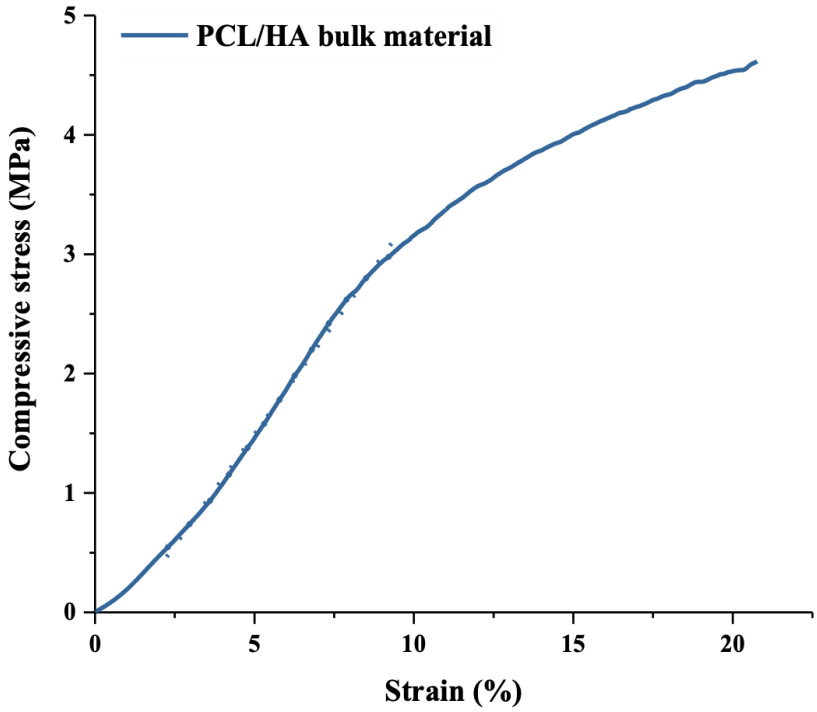

Figure A.1: Stress-strain relationship of the PCL/HAp bulk material (n=3).

where W_1 is volume after immersion, and W_2 is volume before immersion. Three replicates for each type of PCL/PEO/HAp scaffolds were immersed in phosphate buffer saline solution (PBS) at 37°C over 1 – 144 h time points. PBS was prepared by dissolving one tablet of PBS in 200 mL of deionised water to obtain a final pH of 7.4. At each time point, samples were removed, gently wiped with a blotting paper, and the dimensions measured using a vernier caliper. Additionally, the weight of the scaffolds was recorded using a high precision balance.

Changes in 3D scaffold weight and dimensions were monitored over 1-144 h in PBS. Four types of scaffolds - *PCL/PEO/55%HAp*, *PCL/PEO/65%HAp*, *PCL/PEO/75%HAp*, and *PCL/PEO/85%HAp*, were compared in terms of their water absorption and swelling property. As shown in Figure A.2 (a), sample *PCL/PEO/85%HAp* had a relatively large drop from 1-144 h. The reason for that is the structure of *PCL/PEO/85%HAp* start to collapse after immersing in the PBS and lose their weight during each measurement. The weight change ratios of the four types of scaffolds were calculated based on the Equation A.2.

PCL/PEO/75%HAp scaffolds were increased in weight changes at the first 4 hours and had the most weight change at 4 h, which was about $86.3 \pm 0.078\%$. While, samples *PCL/PEO/55%HAp*, and *PCL/PEO/65%HAp*, were $61.52 \pm 0.050\%$ and $76.2 \pm 0.089\%$, respectively. At 144 h, the weight change of *PCL/PEO/55%HAp*, *PCL/PEO/65%HAp*, *PCL/PEO/75%HAp*, and *PCL/PEO/85%HAp*, were $35.8 \pm 0.003\%$, $45.9 \pm 0.008\%$, $54.6 \pm 0.008\%$, and $15.41 \pm 0.15\%$. Interestingly, all samples weight overall higher than their initial weight after 144 h incubation.

Another parameter studied in scaffold morphology was its swelling capacity. Figure A.2 (b) shows the changes in scaffold dimensions among the four types of scaffolds. The swelling changes ratio of four types of scaffolds were calculated based on the Equation A.1 . *PCL/PEO/75%HAp* scaffold had the highest swelling ratio ($31.8 \pm 0.08\%$ at 4 hours), while other samples - *PCL/PEO/55%HAp*, *PCL/PEO/65%HAp*, *PCL/PEO/85%HAp*, were $26.6 \pm 0.03\%$, $30.5 \pm 0.05\%$, $18.6 \pm 0.06\%$, respectively. These results corroborate with the weight change ratio, in which similar trends were observed. At 48h, the swelling ratio of *PCL/PEO/85%HAp* start to become a negative value, which could possibly be due to the scaffold collapsed and lost their dimensions as indicated earlier. All samples start decreasing their dimensions after 144 h incubation in PBS. It was expected that the PCL/PEO/HAp scaffolds would swell when introduced in an aqueous environment due to osmotic exchange, which would encourage the break-down of the scaffold (Mozafari et al., 2018). Indirectly, the swelling ratio is related to the weight change ratio since scaffolds swelling is the result of water uptake and consequently means heavier scaffolds.

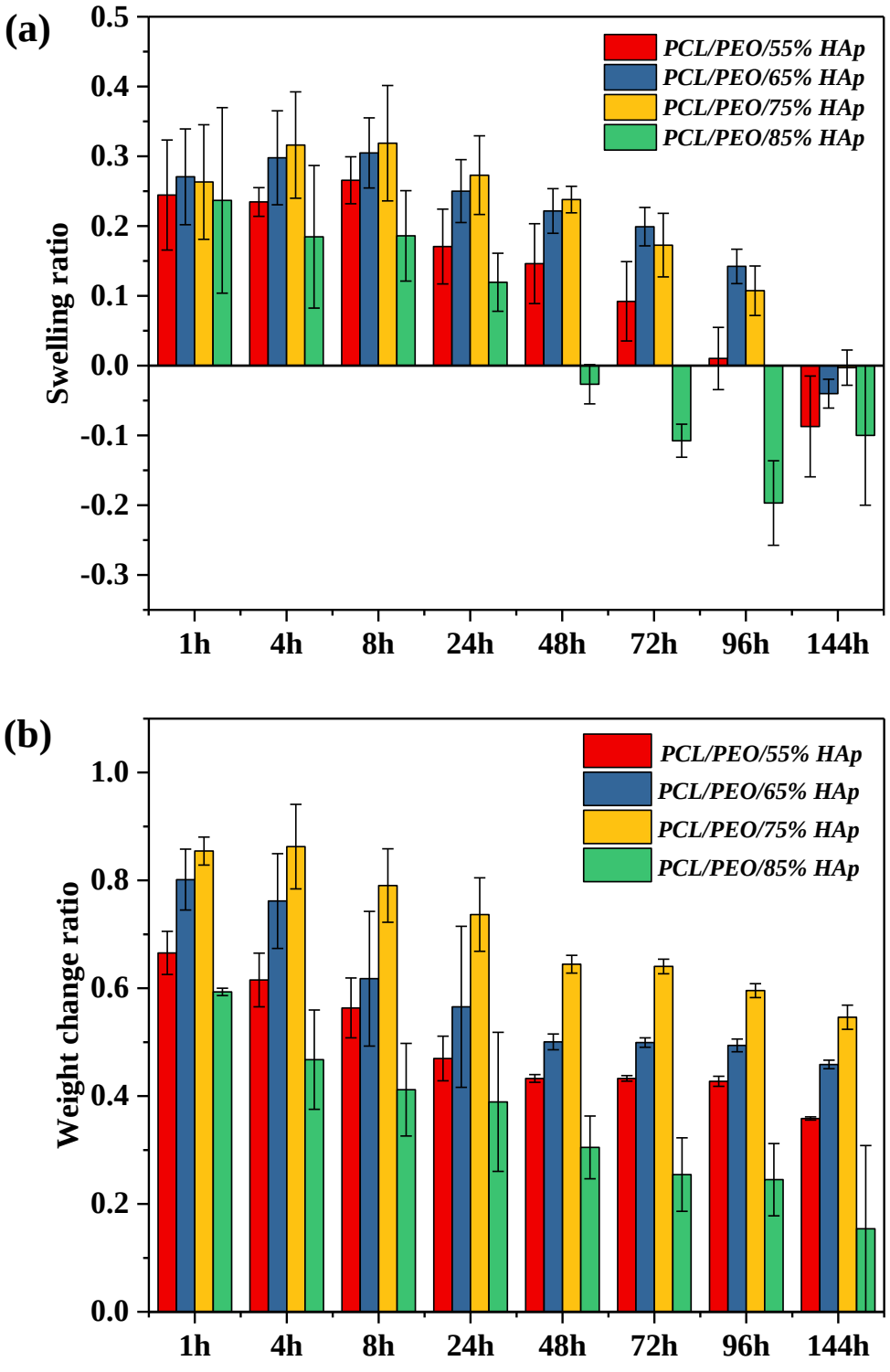

Figure A.2: Comparison of weight change ratio (a) and swelling ratio (b) for sample – *PCL/PEO/55%HAp*, *PCL/PEO/65%HAp*, *PCL/PEO/75%HAp*, and *PCL/PEO/85%HAp* in PBS at 1 – 144 hours incubation, (n = 3).

A.3 Degradation behaviour

The in vitro degradation rate of scaffolds was monitored in PBS. The equal dimension of scaffolds with HAp concentrations from 55%–85% w/w, were incubated in PBS at 37°C for six days and three replicates for each type of sample. At four days (96 h) and six days (144 h), the samples were removed, gently wiped with blotting paper and placed in a drying oven at 37°C for 48 h, and then weighed. The degradation ratio of the scaffold was calculated using Equation A.3. pH of the PBS was also recorded using pH meter (Mettler Toledo, Columbus, Ohio, USA).

$$\text{Degradation ratio} = \frac{W_0 - W_t}{W_0} \tag{A.3}$$

where W_0 is the weight before soaking, and W_t is the weight of the scaffold after soaking for t days.

The biodegradation behaviour of the scaffolds was evaluated by incubating them in PBS at 37°C for 144 h. The degradation ratio of four types of scaffolds were calculated based on the Equation A.3. As shown in Figure A.3 (a), apart from sample *PCL/PEO/85%HAp*, biodegradation ratio decreased when the concentration of HAp within scaffold increased. As shown in Figure A.3 (b), sample *PCL/PEO/85%HAp* had collapsed at the edge of the scaffold, which is the main reason that it has the highest degradation ratio. These results also demonstrate that *PCL/PEO/75%HAp* had minimal weight loss, confirming that the addition of HAp is essential to prevent rapid degradation of the scaffolds in aqueous environments and to maintain their structural integrity. Whereas, sample *PCL/PEO/55%HAp* had a relatively high degradation ratio, which could possibly be due to it had the highest polymer concentration, and PEO on top of filament surface was dissolved into the PBS after 144 hours. This explanation can be confirmed by the SEM images of dry samples (after soaking in PBS) in Figure A.3 (c), which indicates that there were more micro and nanopores on the filament of sample *PCL/PEO/55%HAp* comparing to other three types of samples.

Further, considering the release of acidic or basic substances during the degradation of the scaffold plays an important role in determining if the scaffolds are viable or harmful towards cells. The influence of scaffold degradation on buffer pH was investigated and compared among the scaffolds with various HAp concentrations. At the initial 1h, the pH levels remain relatively constant at pH 7.5 for all types of scaffolds, which was close to the PBS solution prepared at pH 7.4. After 96 h, as scaffold degradation ensued, pH levels in the buffer slightly increase for all samples. The results indicate that the pH value was 7.61 ± 0.01, 7.6 ± 0.003, 7.61 ± 0.003, and 7.61 ± 0.006 for scaffold *PCL/PEO/55%HAp*, *PCL/PEO/65%HAp*, *PCL/PEO/75%HAp*, and *PCL/PEO/85%HAp*. After 144 h, when the degradation ratio of scaffolds increases, the pH value for all samples was still constant (circa 7.6), which indicates that pH has reached a plateau for all samples. The result indicates that there is no significant influence of HAp concentration on the pH levels for all scaffolds. Although the final value of pH was 7.6, which was slightly higher than the PBS solution prepared at pH 7.4. Considering degradation rates and controlled environment (volume of 30 mL) in which the experiment was conducted, it would be expected that the effects of pH would be negligible if under an in vitro dynamic environment model.

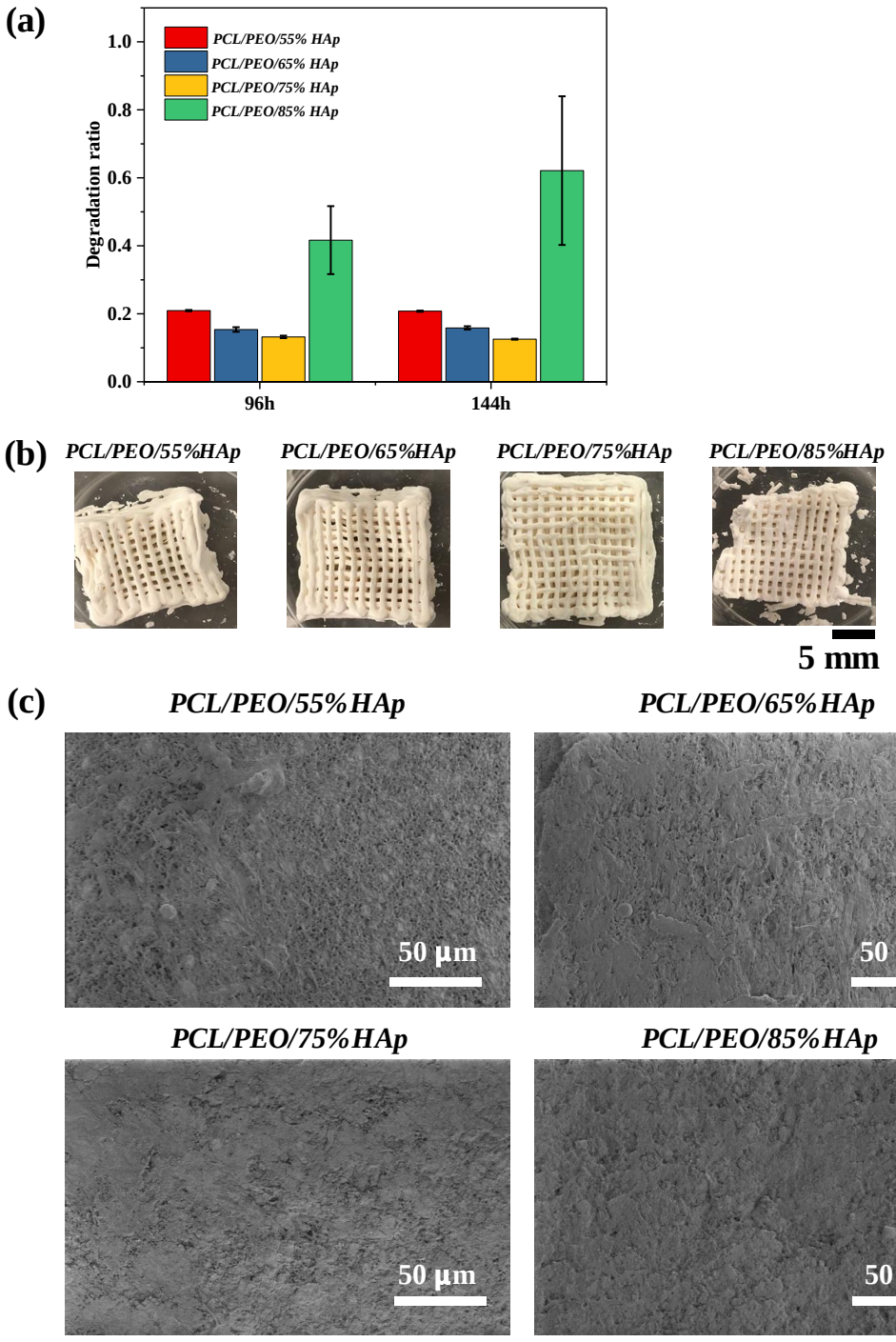

Figure A.3: Comparison in weight loss through degradation (a), the scaffold images (b) and SEM images (c) of dry samples after soaking in PBS (144 h) for samples - *PCL/PEO/55%HAp*, *PCL/PEO/65%HAp*, *PCL/PEO/75%HAp*, and *PCL/PEO/85%HAp*, (n = 3).